ADDITIVE MANUFACTURING AND SURFACE FUNCTIONALISATION OF Ti6Al4V COMPONENTS USING SELF-ASSEMBLED MONOLAYERS FOR BIOMEDICAL APPLICATIONS

Jayasheelan Vaithilingam, B.Tech., MSc.

Thesis submitted to the University of Nottingham for the degree of Doctor of Philosophy

July 2015

Abstract

The ability to provide mass customised and biocompatible implants is increasingly important to improve the quality of life. Additive manufacturing (AM) techniques have obtained increasing popularity and selective laser melting (SLM), a metal-based AM technique with an ability to build complex and well defined porous structures, has been identified as a route to fabricate customised biomedical implants. Surface modification of an implant with a biomolecule is used to improve its biocompatibility and to reduce post-implant complications. In this thesis, the potential of a novel approach to use self-assembled monolayers to modify SLM fabricated surfaces with therapeutic drugs has been evaluated.

Although there are numerous studies on the material development, process optimisation and mechanical testing of SLM fabricated parts, the surface chemistry of these parts is poorly understood. Initially, the surface chemistry of SLM as-fabricated (SLM-AF), SLM fabricated and mechanically polished (SLM-MP) and forged and mechanically polished (FGD-MP) parts made of Ti6Al4V was determined using an X-ray photoelectron spectrophotometer (XPS). Later the impact of laser power on the surface chemistry of the parts was also studied. A non-homogeneous surface chemistry was observed due to a change in the distribution of the alloying elements titanium, aluminium and vanadium on the surface oxide layer. Surface modification of the SLM fabricated component would be beneficial to obtain a homogenous surface chemistry, especially for biomedical application.

Coating of self-assembled monolayers (SAMs) onto SLM fabricated Ti6Al4V structures was performed to modify their surface chemistry. 16-phosphanohexadecanoic acid monolayers (16-PhDA) were used to modify SLM-AF and SLM-MP surfaces. XPS and static water contact angle measurements confirmed the chemisorption of monolayers on these surfaces. The obtained results confirmed that SAMs were stable on the Ti6Al4V surface for over 28 days before its desorption. It was also witnessed that the stability of monolayers on the rough SLM-AF and smooth SLM-MP surfaces were not

significantly different. Later, the 16-PhDA SAM coated Ti6Al4V SLM-MP surface was functionalised with a model drug, Paracetamol. An esterification reaction was performed to functionalise the phosphonic acid monolayers with Paracetamol. Surface characterisation revealed the sucessful attachment of Paracetamol to the SAMs.

Bacterial infections from biomedical implants and surgical devices are reported to be a major problem in orthopaedic, dental and vascular surgery. Hence, to further explore the potential of the proposed method, Ciprofloxacin® a broad spectrum antibiotic was immobilised to the SAMs, previously adsorbed on the SLM-MP Ti6Al4V surfaces. Using the proposed approach, approximately 1.12 $\mu g/cm^2$ of the drug was coated to the surface. Results showed that Ciprofloxacin® is highly stable under the oxidative conditions used in this study. Under in vitro condition, the drug was observed to release in a sustained manner. Antibacterial susceptibility tests revealed that the immobilised Ciprofloxacin® was therapeutically active upon its release. Thus, a novel methodology to fabricate customised and functionalised implants has been demonstrated for an improved biocompatibility and reduced post-implant complications.

List of Publications

Journals Published

1. Reika Sakai, Baiju John, Masami Okamoto, Jukka V. Seppälä, Jayasheelan Vaithilingam, Husnah Hussein and Ruth Goodridge (2012). Fabrication of poly-lactide based biodegradable thermoset scaffolds for tissue engineering applications. Macromolecular and Materials Engineering; 298, 45-52.
2. Jayasheelan Vaithilingam, Ruth D. Goodridge, Steven D.R. Christie, Steve Edmondson and Richard J.M. Hague (2014). Immobilisation of antibacterial drug – Ciprofloxacin® to Ti6Al4V components fabricated using selective laser melting. Applied Surface Science; 314, 642-654.
3. Jayasheelan Vaithilingam, Ruth D. Goodridge, Steven D.R. Christie, Steve Edmondson and Richard J.M. Hague (2015). Functionalisation of Ti6Al4V components fabricated using selective laser melting with a biomolecule. Materials Science and Engineering: C; 46, 52-61.

Book Chapter Published

1. Jayasheelan Vaithilingam, Ruth D. Goodridge, Steven D.R. Christie, Steve Edmondson and Richard J.M. Hague (2015). Additive manufacturing and surface modification of biomaterials using self-assembled monolayers. In: Dietmar W. Hutmacher and Wojciech Chrzanowski (eds), Biointerfaces: Where Material Meets Biology First Edition; Royal Society of Chemistry. 30-54 (ISBN: 9781849738767).

Manuscript Submitted

1. Jayasheelan Vaithilingam, Ruth D. Goodridge, Steven D.R. Christie, Steve Edmondson and Richard J.M. Hague. An investigation on the surface chemistry of selective laser melted and forged Ti6Al4V components. (Advanced Materials Engineering).

Manuscript In-preparation

1. Jayasheelan Vaithilingam, Ruth D. Goodridge, Steven D.R. Christie, Steve Edmondson and Richard J.M. Hague. The effect of laser re-melting on the surface chemistry of Ti6Al4V components fabricated by selective laser melting. (To be submitted to Surface Science).
2. Jayasheelan Vaithilingam, Ruth D. Goodridge, Steven D.R. Christie, Steve Edmondson and Richard J.M. Hague. Aging effect of Ti6Al4V powders during selective laser melting process. (To be submitted to Journal of Materials Processing Technology).
3. Jayasheelan Vaithilingam, Ruth D. Goodridge, Steven D.R. Christie, Steve Edmondson and Richard J.M. Hague. Electropolishing of tracheobronchial stents fabricated by selective laser melting. (To be submitted to Biomedical Materials Research Part B: Applied Biomaterials).

Selected Conference Presentations

List of Selected Oral Presentations

1. Jayasheelan Vaithilingam, Ruth D. Goodridge, Steven D.R. Christie, Steve Edmondson and Richard J.M. Hague, 2013. Anti-bacterial activity of Ciprofloxacin® immobilised to self-assembled monolayers; 25th European Society for Biomaterials Annual Conference, Madrid, Spain.
2. Jayasheelan Vaithilingam, Ruth D. Goodridge, Steven D.R. Christie, Steve Edmondson and Richard J.M. Hague, 2013. Delivery of an anti-bacterial drug from an additively manufactured surface; 24th International Conference on Solid Free-form Fabrication, Texas, USA.
3. Jayasheelan Vaithilingam, Ruth D Goodridge, Steven D Christie, Steve Edmondson and Richard JM Hague, 2012. Surface modification of selective laser melted structures using self-assembled monolayers for biomedical applications; 23rd Inter-national Conference on Solid Freeform Fabrication, Texas, USA. 316-325.
4. Jayasheelan Vaithilingam, Ruth D. Goodridge, Richard J.M. Hague, Steven D.R. Christie, and Steve Edmondson, 2012. Fabrication of

customised biomedical implants; 2nd Annual Research Student Conference, Health and Life Sciences Research School, Loughborough University, UK.

5. Jayasheelan Vaithilingam, Ruth D. Goodridge, Richard J.M. Hague, Steven D.R. Christie, and Steve Edmondson, 2012. Fabrication and surface modification of customised biomedical implants; In: East Midlands Universities Postgraduate Research Students Conference, University of Nottingham, Sutton Bonington, UK.
6. Jayasheelan Vaithilingam, Ruth D. Goodridge, Richard J.M. Hague, Steven D. Christie, and Steve Edmondson, 2012. Surface modification of selective laser melted Ti6Al4V structures using self-assembled monolayers; In: The UK Society for Biomaterials Annual Conference, University of Nottingham, UK.
7. Jayasheelan Vaithilingam, Ruth D. Goodridge, Richard J.M. Hague and Steven D Christie, 2012. Additive manufacturing and surface modification of tracheobronchial stents using self-assembled monolayers; 9th World Biomaterials Conference, Chengdu, China.

List of Selected Poster Presentations

1. Jayasheelan Vaithilingam, Ruth D. Goodridge, Steven D.R. Christie, Richard J.M. Hague and Steve Edmondson, 2013. Immobilisation of Ciprofloxacin® to an additively manufactured Ti6Al4V surface. 25th European Society for Biomaterials Annual Conference, Madrid, Spain.
2. Jayasheelan Vaithilingam, Ruth D. Goodridge, Richard J.M. Hague, Steven D.R. Christie, and Steve Edmondson, 2013. Revolutionising the fabrication of biomedical implants; Research Showcase Event, University of Nottingham, UK.
3. Jayasheelan Vaithilingam, Ruth D. Goodridge, Richard J.M. Hague, Steven D.R. Christie, and Steve Edmondson, 2013. A novel approach to engineer customised and functionalised biomedical implants; In: Engineering Postgraduate Research Event, Faculty of Engineering, University of Nottingham, UK **(Finalist)**.
4. Jayasheelan Vaithilingam, Ruth D. Goodridge, Richard J.M. Hague, Steven D.R. Christie, and Steve Edmondson, 2013. A novel approach

to engineer customised and functionalised biomedical implants; In: Science, Engineering and Technology for Britain **(SET for Britain)**, The House of Commons, Westminster, London, UK.

5. Jayasheelan Vaithilingam, Ruth D. Goodridge, Richard J.M. Hague, Steven D.R. Christie, and Steve Edmondson, 2012. Fabrication and functionalisation of customised biomedical implants; In: Loughborough Research That Matters: Annual Research Conference, Loughborough University, UK.
6. Jayasheelan Vaithilingam, Ruth D Goodridge, Richard J.M. Hague, Steven D.R. Christie, and Steve Edmondson, 2011. Fabrication of airway stents by selective laser melting; 1st Annual Research Student Conference, Health and Life Sciences Research School, Loughborough University, UK.

Acknowledgements

Right from the start of my research, I came across several great people and I strongly believe it would not be possible for me to progress to this stage of my research without the assistance and mentorship of such great people and here are few of them.

I am indebted to my supervisors Dr. Ruth Goodridge and Prof. Richard Hague, Additive Manufacturing and 3D Printing Research Group (AM & 3DPRG), Department of Mechanical, Materials and Manufacturing Engineering, University of Nottingham for their dedicated supervision, priceless guidance and advice during my research period. Technical assistance rendered by my supervisors kept me updated with the recent developments on mechanical & material processing. Without their continued support, motivation and assistance it would have been difficult for me to complete my PhD.

A special thanks to my supervisor Dr. Ruth Goodridge for her suggestions and helping me with research papers and thesis writing. Her motivations and understandings helped me to a lot during the course.

I am very thankful to Dr. Steven Christie, Department of Chemistry, Loughborough University for his co-supervision, constant technical support and motivation during my experimentations at the Department of Chemistry, Loughborough University. I also owe gratitude to Dr. Steve Edmondson, School of Materials, University of Manchester, for his co-supervision, guidance and technical assistance on surface characterisation and surface modification techniques. I am grateful to Dr. Chris Tuck, Prof. Ricky Wildman and Prof. David Grant, University of Nottingham for their valuable suggestions and assisting with my yearly assessments. I thank Prof. Wayne Hayes, University of Reading for assessing my thesis and for his valuable suggestions during my PhD viva.

I also would like to thank AM & 3DPRG technicians Mr. Mark East and Mr. Mark Hardy for their technical support and immense help during my experimental works *"Rapids Bro"*. I extend my humble thanks to the

technicians, Mr. Andy Sandaver, Mr. Jagpal Singh, Mrs. Pat Cropper, Dr. Keith Yendall and Mrs. Marion Dillon at Loughborough University for their technical support and wise suggestions during my experimentations.

I would like to thank all my colleagues and ex-colleagues of AM & 3DPRG members in particular Dave, Ajit, James, Helen, Martin, Mirela, Adedeji, Momo, Jiaming, Farhan, Marco, Belen, Joe, Chandra and Meisam for their help and assistance. I am also thankful to Sam, Andy, James, Tom and Nuria at the Department of Chemistry, Loughborough University for their help and support during my experimentations.

I also thank Prof. Nat Puri (Puri Foundation), Mr. Vydeswaran Murugesan, Dr. Bindhumadhavan Gururajan, Dr. Ayarivan Puratchikody, Prof. Zoltan Nagy, Dr. Aruna Palipana and Mr. Ramesh Kumar Muthusamy for their motivation, support and guidance.

I express my sincere thanks to my uncles Mr. Subramani Chidambaram, Mr. Palanivelu Chidambaram, Mr. Baskar Chidambaram, my aunties Mrs. Chitra Sivashanmugam, Mrs. Amsavalli Manohar and their family for all their help, support, care and everything they did for me.

I am grateful to my friends Sarvi, Lalitha, Alsu, Dipesh, Sushma, Shridharan, Pradeep, Sundar, Subash, Deepak, Ramji, Matt, Darren, Alun, Dave, Sonal, Sarah, Sophie, Andrea, John, Jodie and Jean for their help and support throughout my PhD.

I express my tremendous gratitude to my best friends Sabari, Manikandan, Ranjani, Santosh, Sanjeevi, Jayaraj, Dinakar Babu, Bharathi and Alex for all their help and support to me and my family. Friends like you are really hard to find.

Finally, I would like to thank the University of Nottingham, Loughborough University and Engineering and Physical Sciences Research Council (EPSRC), UK for funding my research.

Dedication

This thesis is dedicated to:

My mum, Jaya, my beloved dad, Mr. Vaithilingam Vaiyapuri and my paternal grand mum, Mrs. Sellammaal Vaiyapuri for their myriad sacrifices throughout their life for me. I am so proud and happy that I had you both in my life. Although you are not with me now physically, I know you both truly lived one and only for me. I would never say good bye to you cos, I know you will always be there in and around me. Your love, humbleness, kindness and your other numerous qualities instilled me and will reflect in each of my endeavours. Dear dad and grandma, "I MISS YOU" is not even the right word to express how I actually feel.

Mrs. Mariyayee Chidambaram, my maternal grand "mum" for her immense effort in bringing me up. I wouldn't be here in this position without all your sacrifices. I could never ask for a better grand mum than you. I LOVE YOU.

My teachers and supervisors (undergraduate, masters and PhD) for their huge support, guidance and advice throughout my life till now. Every one of you have given me the most precious time in my life that I cannot claim back anymore. I have learnt a lot of good qualities from you all and I certainly believe they will greatly profile my career.

Mr. Muruganantham Kanagasabai, Mr. Natarajan Subramanian, Dr. Ayarivan Puratchikody and Dr. Rajendran Ramasamy for fostering scientific temper in me and for their continued encouragement and support in all my endeavours.

My friend, Mr. Anbarasan Subramanian. Although I envisioned doing a PhD from my childhood, you are an important person who kindled my aim further.

My sisters Hemalatha Rajkumar, Deepa Vijayakumar and Sharmila Paul Reuben and their family who have given me the unconditional love and support in every possible way they could. I am very fortunate to have you all.

My wife and friend for life, Mrs. Ramya Jayasheelan. Thank you for your motivation, care, love and everything that you have given me. I LOVE YOU!

CONTENTS

List of Figures

List of Schemes

List of Tables

List of Symbols and Units

List of Symbols Used for Chemicals

Al	Aluminium	N	Nitrogen
Ba	Barium	O	Oxygen
C	Carbon	P	Phosphorous
Cl	Chlorine	S	Sulfur
Co	Cobalt	Si	Silica
Cr	Chromium	SS	Stainless Steel
F	Fluorine	Ti	Titanium
Mg	Magnesium	V	Vanadium

List of Units

°C	Degree Celsius	mL	Millilitre
λ	Wavelength	mm	Millimetre
µm	Micrometre	mm/s	Millimetre/second
µs	Microseconds	nm	Nanometre
amp	Ampere	mm^2	Square millimetre
cm	Centimetre	N	Newton
cm^2	Square centimetre	Pa	Pascal
eV	Electron volts	ppm	Parts per million
g	Gram	V	Volt
GPa	GigaPascal	W	Watts
MHz	Mega Hertz		

Special Characters

®	Registered
G+	Gram Positive
G-	Gram Negative

List of Acronyms

16-PhDA	16-phosphanonexadecanoic acid
3D	Three Dimensional
ACE	Acid Chloride Esterification
AFM	Atomic Force Microscope
AM	Additive Manufacturing
ASTM	American Society for Testing and Materials
ATCC	American Type Cell Collection
ATR	Attenuated Total Reflectance
CAD	Computer Aided Design
CARTIS	Centre for Applied Reconstructive Technologies in Surgery
CT	Computed Tomography
CNC	Computer Numeric Control
DCM	Dichloromethane
DC	Direct Current
DE	Direct Esterification
DES	Drug Eluting Stents
DHE	Direct Heat Esterification
EDM	Electrical Discharge Machining
EHT	Extra-high Tension
ESCA	Electron Spectroscopy for Chemical Analysis
FGD-MP	Mechanically Polished Forged Part
FTIR	Fourier Transform Infrared Spectroscopy
IGES	Initial Graphics Exchange System
IR	Infrared
MIC	Minimum Inhibitory Concentration

MRI	Magnetic Resonance Imaging
NIS	National Inpatient Sample
NIST	National Institute of Standards and Technology
NJR	National Joint Registry
NSK	No Skin Scan
ODPA	Octadecylphosphonic acid
PMMA	Polymethylmethaacrylate
SAMs	Self-assembled Monolayers
SE	Standard Error
SEM	Scanning Electron Microscope
SK	Skin Scan
SLM	Selective Laser Melting
SLM-AF	As-fabricated Selective Laser Melted Part
SLM-MP	Mechanically Polished Selective Laser Melted Part
THF	Tetrahydrofuran
Tris-HCl	Tris-hydrochloride
UK	United Kingdom
USA	United States of America
UV	Ultra-violet
UV-Vis	Ultra-violet Visible Spectroscopy
XPS	X-ray Photoelectron Spectroscopy

1. INTRODUCTION

1.1. Biomaterials

Biomaterials are natural or synthetic materials (other than drugs) that are used to evaluate, treat, augment or replace any damaged tissues/organs/function of the body [1]. The field of biomaterials is of major importance to mankind since their use has played a significant role in improving life expectancy and quality of life [2].

The use of biomaterials is not new; Egyptians and Romans used linen for sutures, gold and iron for dental applications and wood for toe replacements [3]. After the Second World War, nylon, teflon, silicone, stainless steel and titanium were some of the other materials introduced for biomedical applications. With recent advancements in human healthcare systems and with the availability of improved diagnostic tools, biomedical implants have found applications in almost all body functions (Figure 1-1). It is expected that virtually every individual will have contact with biomaterials and/or biomedical implants at some point of time during his or her life. This contact may occur in several ways including (i) permanent implantation (such as heart valves and total joint replacement); (ii) long-term applications (such as contact lenses, dental prostheses and fracture fixation devices) and (iii) transient applications (including needles for vaccination, wound healing dressings/sutures and cardiac assist systems).

Biomedical implants range from simple wires and screws for fracture plate fixation to joint prostheses for hips, knees, shoulders and so on. Depending on the requirement and load conditions, implants are made of natural and/or synthetic materials such as polymers, metals, ceramics or composites. For example, metals are generally preferred for load bearing implants and internal fixation devices whereas ceramics are preferred for skeletal and hard tissue repair [4]. Polymers have been found the optimal material class when requirements of little response to implantation, long-term stability in hostile environment, low material stiffness leading to high material flexibility, and

good electrical insulation of metallic conductors have to be combined in a single material [5].

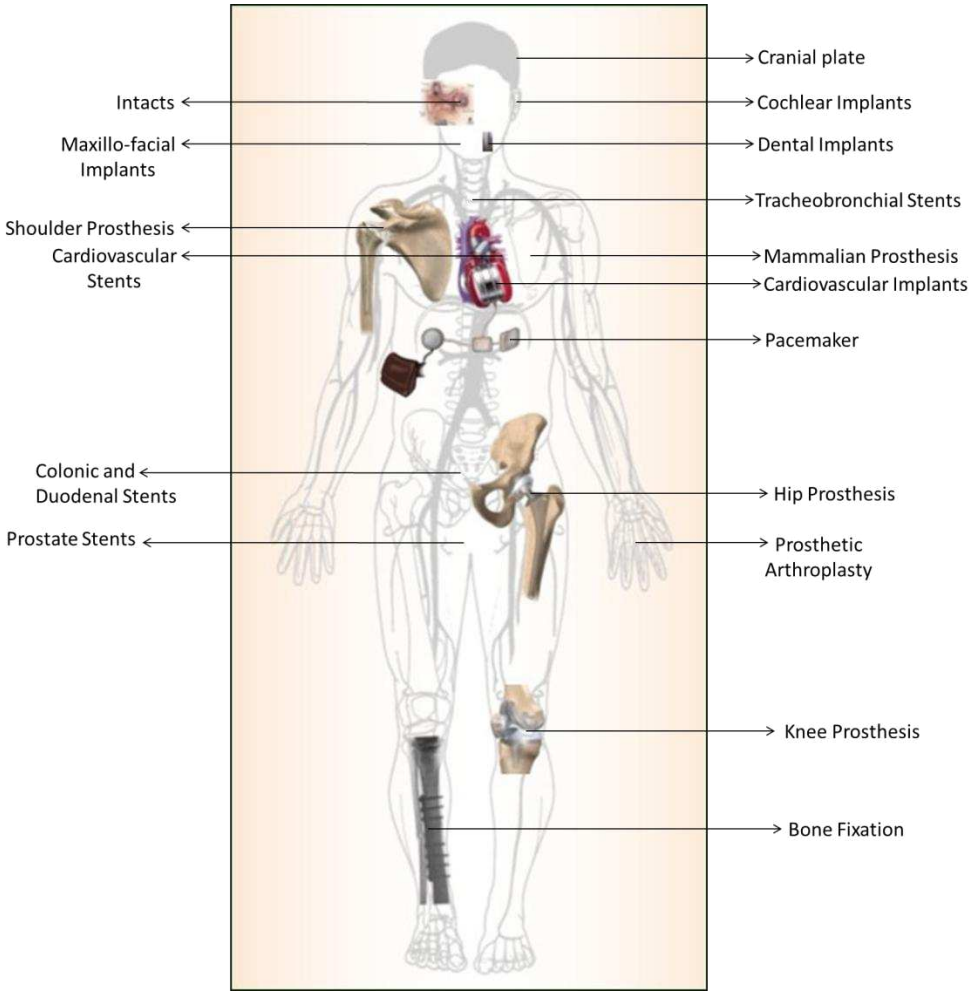

Figure 1-1 Biomedical implants for human application. Reproduced with kind permission from Bentham Open [3].

Biomedical implants are fabricated by employing one or more of the following conventional manufacturing techniques including forming, and/or subtractive manufacturing. In the forming technique, components are made in number of ways such as casting a liquid material to a mould or a die, joining of materials together by welding or knitting/braiding and by forging the material to obtain the desired shape. Laser or water jet cutting, milling, electrical discharge machining (EDM), computer numerical control (CNC) machining are some of the subtractive manufacturing processes used to fabricate most of the currently available implants for hip and knee replacements, vascular stents, dental and

maxillo-facial implants. These subtractive manufacturing methods are used on their own or in combination with other forming or casting techniques.

1.2. Market for Biomedical Implants

Implants available for various body systems and the material with which they are fabricated are tabulated in Table 1-1.

Table 1-1 Some of the materials used for the fabrication of biomedical implants [1, 4, 7, 8].

Application		Materials used
Skeletal system	Joint Replacements (hip, knee and shoulder)	Titanium, Ti-Al-V alloy, stainless steel and ultrahigh-molecular-weight polyethylene.
	Finger joints	Silicone.
	Bone plate for fracture fixation	Stainless steel and cobalt-chromium alloy.
	Bone cement	Poly(methyl methacrylate).
	Bony defect repair	Hydroxyapatite.
	Artificial tendon and ligament	Teflon and Dacron.
	Dental implant for tooth fixation	Gold, Titanium, Ti-Al-V alloy, stainless steel, polyethylene, alumina, and calcium phosphate.
	Maxillo-facial and cranial prostheses	Titanium, Ti-Al-V alloy, stainless steel, polydimethyl siloxane, polyurethane, polyvinylchloride and polyetherketoneketone.
Cardiovascular system and other vascular systems	Blood vessel prostheses	Dacron, Teflon and polyurethane.
	Heart valve	Reprocessed tissue, stainless steel and carbon.
	Catheter	Silicone rubber, Teflon and polyurethane.
	Stents	Stainless steel, Nitinol®, magnesium, Elgiloy®, tantalum, platinum-iridium alloys, Poly-L-lactic acid, poly-D,L-lactic acid, poly caprolactone and polyglycolic acid.
Organs	Artificial heart	Polyurethane.
	Skin repair template	Silicone-collagen composite.
	Artificial kidney	Cellulose and polyacrylonitrile.
	Heart-lung machine	Silicone rubber.
Senses	Cochlear replacement	Platinum electrodes.
	Intraocular lens	Poly(methyl methacrylate), silicone rubber and hydrogel.
	Contact lens	Silicone-acrylate and hydrogel.
	Corneal bandage	Collagen and hydrogel.
Other	Sutures	Polylactic and polyglycolic acid
	Gastrointestinal segments	Nylon, polyvinylchloride and silicone
	Breast enlargement	Silicone.

According to the National Joint Registry (NJR), UK's statistics for the year 2012 – 2013 (1st April – March 31st) in England, Wales and Northern Ireland, joint replacements including hip, knee, ankle, shoulder and elbow accounted for having the highest ever annual number of 196,403 [6]. Nationwide Inpatient Sample (NIS) in the United States of America (USA) shows that primary hip replacements increased by 48% and first time knee implants grew by 63% from 1997 to 2004. It is estimated that if these trends continue, the current estimated 600,000 hip and knee replacements will increase to 3.4 million by 2030 in the USA [7,8].

Bibb et al. (2010) reported that in excess of 64,000 facial prostheses are made annually worldwide. According to Datamonitor's report (2006), the USA accounts for 50% and Europe 30% of the total procedures worldwide [9]. The 2005 revenues for hip implants in the US were $2 billion and $1.4 billion in Europe, while knee implant revenues comprised $2.4 billion in the US and $774 million in Europe. According to Ratner et al. [1] the US market for biomaterials accounted for $9 billion. These figures show that the use of implants has become an integral part of our human health care system and a big rise in the biomedical sector over the last few decades.

1.3. Biological Response to an Implant

Understanding the mechanism by which cells respond to an implant is of major importance to achieve long-term success of the implant surgery [10]. Almost all biomaterials implanted in a living tissue/system undergo tissue responses within a few seconds after implantation [11]. On implantation, the implant is surrounded by water molecules, which trigger the host proteins. The surface property of an implant plays an important role at this stage on the extent and specific interaction of the implant's surface with this hydration layer. Based on this interaction, the host proteins respond to the implant surface and form a thin layer of extracellular matrix protein film [10].

The presence of proteins including albumin, fibrinogen, fibronectin, vitronectin, in the protein film modulates the host inflammatory cell interaction and adhesion [12]. Hence, the protein film is responsible for the control of subsequent biological reactions (such as inflammatory and wound healing

responses) at the implant-host interface [4]. Figure 1-2 schematically represents the sequential reactions that take place after the implantation of a biomaterial into a living system [4].

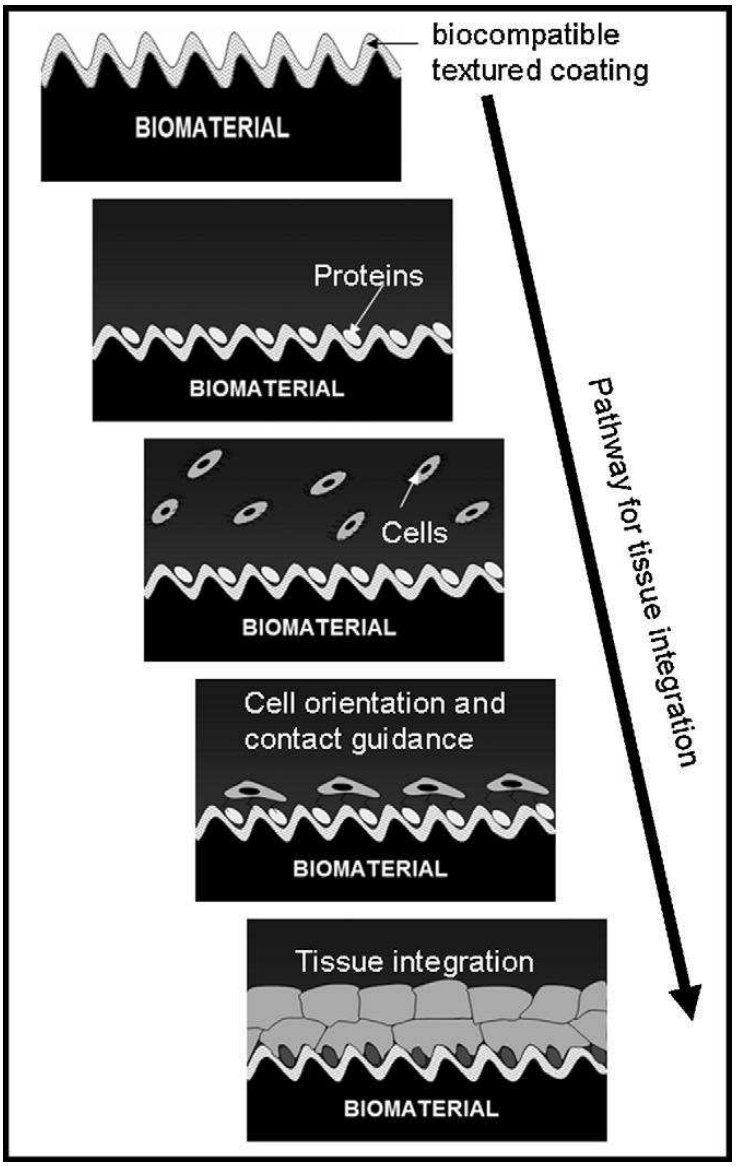

Figure 1-2 Schematic of the sequential reactions that take place after the implantation of a biomaterial. Figure reproduced with kind permission from Elsevier [4].

The adherence of different proteins, its concentration and conformations are controlled by the surface properties of the implanted biomaterial. The interaction of the adsorbed proteins with adhesion receptors such as (integrin) present on inflammatory cell populations constitutes the major cellular recognition system for implants [12]. The cell-protein interface formed after implantation will initiate cell adhesion, migration and differentiation. Some of

the factors that govern cell adhesion and growth are extracellular matrix proteins, cell-surface bound proteins and chemical characteristics and topography of the implant surface [13].

Since the surface properties of an implant is critical in determining the long-term success of the implant, there is a significant interest in optimising the implant-host interface by altering the surface properties specific to the site of implantation. For example, for cardio-vascular stent applications, haemocompatibility of the stent material would be advantageous whereas for the bone replacement applications, cytocompatibility of the implant would be beneficial. Surface modification of biomaterials is discussed in section 2.4.

The final stage of the body responses to an implant can last up to several decades. For example in an orthopaedic application, as a result of body responses, eventually a functionally active mineralised bone is formed surrounding the implant. Adverse reactions or post-implant complications such as fibrous capsule formation, granulation tissue formation, implant failure due to fracture and acute/chronic inflammation can happen at any time after implantation.

1.4. Issues with Current Biomedical Implants

Biomedical implants have significantly improved the quality of life for countless people; however, they still impose significant challenges on current manufacturing processes due to their need to function within a relatively harsh biological environment [2]. Customisation and fabrication of complex geometries, and the reduction of post-implant complications including implant migration, fracture and poor biocompatibility are major challenges to overcome.

1.4.1. Customisation and fabrication of complex geometries

Most off-the-shelf implants are available in a selection of dimensions to meet the patient requirement; however, they are not customised. Customisation is key in conditions such as where the patient's anatomy deviates from the standard sizes or is affected by individual defects. The primary objective of customisation is to fit the unique anatomy of a particular patient, especially

where the implant is not fixed. Personalised hearing aid shells for “in-the-ear” and “in-the-canal” devices are one example of a customised implant that has achieved superior fit compared to conventionally manufactured aids increasing both comfort and device functionality [14]. Orthopaedic implants usually perform better when they match exactly the anatomy of the patient, through the distribution and normalisation of the stresses incurred in the remaining skeletal system and reduction of migration and failure [15].

Migration of an implant is the movement of the implant from the actual or surgically positioned area and is mechanically triggered rather than a biological process [16]. Forces higher than expected may deteriorate fixation and cause implant migration. Migration of an implant to a more harmful anatomical space can sometimes be life threatening. Implant migration has been reported for a number of devices including total hip and knee replacement, dental, maxillo-facial and vascular implants [17–21]. Some of the factors that determine the rate of migration other than mechanical forces are implant design and fixation methods [16].

Cementing, screw retention of the implant, expanding the implant to conform to the walls and press fitting of the implant to the diseased/damaged area are some of the common fixation methods. However, all of these retention methods have advantages and limitations over the other methods and selection of an appropriate fixation method is key in long-term applications [22–25]. For example in orthopaedic surgery, polymeric cements such as polymethylmetha-acrylate (PMMA) is used to fix prosthesis due to its strong mechanical fixation. However, when using this PMMA cement fixation for long term application, loosening of implants due to a loss of mechanical fixation is observed. In recent years, bioresorbable bone cements are used to provide both mechanical fixation in the early stages leading to biological fixation [26]. Biological fixation is attained due to osseointegration after the resorption of the bone cement. Press-fit implants are considered as an option in hip replacements for patients with strong bone (since they are most likely to have a high possibility for biological fixation) and cement-retention are considered where there is a concern about bone quality. However, screw retention, press-

fit and cement restorations are practiced in dental applications depending on the need and medical conditions [27].

Fixation of implants may sometimes be difficult depending on the site and anatomy of the diseased/damaged part. In such cases, customisation may render improved fixation with the patient's anatomy and may normalise stresses thus preventing implant loosening and migration. However, the ability to achieve customised and complex geometries of biomedical implants using subtractive or formative manufacturing methods (such as moulding, die casting or subtractive processes) are limited and are often time consuming [27]. This is because these methods have limitations in the geometries that they can produce. Moulding and die casting methods require dies or moulds to fabricate the part. Hence, extra time for the manufacturing process is required in addition to fabricating the actual part. In addition, it is expensive to make a die or mould for a one-off-design. With subtractive manufacturing techniques such as computer numeric control (CNC) machining and laser cutting, parts with complex internal and external geometries are sometimes difficult to achieve.

1.4.2. Post-implant complications

In 2012 alone, among the total of 86,488 hip replacement procedures in England, Wales and Northern Ireland, over 10,000 were revision procedures [6]. This revision procedure accounts to 12% of total hip replacement in 2012 whereas in 2011 it was 11%. There are many reasons for the failure of an implant within the biological environment including manufacturing, chemical, mechanical, tribological and surgical failures [3]. The patient's health condition and the physician's experience could also be contributing factors. A variety of biomaterials (polymers, metals, ceramics and composites), fabrication techniques (such as compression moulding, die casting, bar stock milling and laser cutting) and surface modification techniques (biocompatible material coating, surface polishing and drug coating) have been employed to improve the mechanical and biological properties of the implant; however, there are still constraints in achieving this objective.

Even when using a biomaterial with suitable material and biological properties, there are possibilities for the failure of an implant due to faulty mechanical design or inappropriate application of the implant. Inadequate mechanical properties (e.g. elastic modulus, yield strength, tensile strength) can result in fracture leading to implant failure [17,28,29]. Elasticity modulus is the resistance offered by an object/substance when deformed elastically. Yield strength is the stress at which a material starts to deform plastically. Tensile strength is the maximum stress which the material can withstand before its failure. Fracture of an implant mainly occurs when the implant is not capable of bearing the load exerted on it. For example, the major purpose of orthopaedic implants is to restore the function of load bearing joints (such as hip or knee joints) that are subjected to high levels of mechanical stresses, wear and fatigue during the course of normal activity [4]. According to Wolff's law, the bone of a healthy human or an animal will adapt to the loads under which it is placed. For example, when there is an increase in loading of a particular bone, the bone will remodel itself over time to resist that load. The internal structure of the trabeculae will undergo adaptive changes, leading to secondary changes to the cortical portion of the bone. However, it should be noted that if the loading on a particular bone decreases, then the bone will become weak.

Although the mechanical properties of the bulk material, implant design and manufacturing process are considered to be the major factors determining implant fracture, corrosion of implants within the biological environment is also a crucial factor [3]. Before the advent of 316 stainless steel, metallic implants of various steel formulations failed dramatically due to tissue reactions [30]. 316L SS have a better corrosion resistance and relatively low carbon concentration in the alloy mixture compared to other steels. The presence of molybdenum increases the corrosion resistance of the alloy.

Implants corrode within the biological environment due to electrochemical attack by the electrolytes present in the hostile environment. Body pH can affect the corrosion resistance of implants. Although the pH value of the human body is normally maintained at pH 7, this might change from pH 3 – 9

depending on the imbalances in the biological system due to infections, diseases and other factors. The aqueous medium in the human body consist of anions including chloride, phosphate and bicarbonates, and cations including sodium, potassium, calcium and magnesium [3]. Leaching of metal ions from the implant surface due to corrosion will lead to erosion. The rate of corrosion is accelerated by increased surface area and loss of protective oxide film, later leading to fractures. Also, leaching of metal ions has been observed to induce acute and chronic effects. For example, the release of nickel from stainless steel was observed to affect the skin; cobalt was observed to cause anaemia which inhibits the absorption of iron into the blood stream; chromium was observed to cause ulcers and disturb the central nervous system; aluminium was reported to cause epileptic effects and Alzheimer's disease and leaching of vanadium in its elemental state was observed to be toxic [31]. The tolerable corrosion rate for metallic implants is 2.5×10^{-4} mm/year [3]. Hence, corrosion products formed as a result of implant-host interaction have a significant effect on the long term stability of the prosthesis and its cytocompatibility [32].

Biocompatibility, a requirement for all biomedical implants, is the property of a material to be compatible with the tissues in the human body by not producing a toxic, injurious or immunological response [4]. Chronic inflammations, lesions and scarring are some of the adverse reactions that may take place in the site if the implant is not biocompatible. To achieve better biocompatibility, two routes are often employed: (i) using biocompatible materials such as gold; (ii) fabrication of implants using off-the-shelf materials with application of a suitable biocompatible layer such as bio-active glass, calcium phosphate and protein coatings [15]. The corrosion resistance of titanium is better than other metals such as 316L SS due to the presence of a stable surface oxide layer (TiO_2) of approximately 10 nm. However, the thickness of this surface oxide layer can be enhanced by various surface modification methods including chemical etching and anodisation [30].

Contamination is another factor contributing towards an implant failure. Contamination of implants such as stents, dental, hip and knee implants by harmful microbes has been widely reported [33–36]. Bacterial infections due to

implants are one of the main risk factors in orthopaedic surgery leading to surgical removal of implants [17,37,38]. Contamination of an implant is possible due to non-sterile manufacturing and packing, during surgical placement and/or even due to the microbes present in the body after implantation into the body [38]. By entering the host through contaminated surfaces, bacteria multiply in the host environment and interfere with the host defence system leading to host tissue damage and inflammation [38]. Staphylococci species, including Staphylococcus aureus and Staphylococcus epidermidis are the more common cause of implant-associated infections [39].

Treatment measures available for bacterial infections include systemic, antibiotic loaded cements and antimicrobial coatings [37]. However, the release of drugs in a systemic therapy prevails as one of the major problems when conventional coating techniques are used. Slower release of antibiotics for a longer period of time is a potential cause of antibiotic resistance in the human body [40]. For example, in drug eluting stents (DES), to reduce the restenosis rate, the stents are coated with polymers containing a drug using simple techniques including dip/spray/spin coating or solvent casting [41,42]. After implantation, the DES is expanded to conform to the vessel wall. During this expansion, fractures, peeling of the polymeric coating and uneven release of the drug material were reported as some of the major problems with surface modified DES [43,44]. To address these issues, Mani et al. [45] adopted a coating technique by which the drug was directly loaded on to the implant surface. However, the amount of drug coated was very low (~ 5µg/cm^2) compared to the amount of drug coated on a commercially available drug-eluting systems (100 µg/cm^2). Polymer brushes were also used to coat implant surfaces with drugs [46]. Since these coating methods are in nano-scale, they add only a few nanometres to the implant surface and hence, peeling of drug coating is less likely to occur [47]. Also, implants coated with conventional coating techniques have drawbacks including surface heterogeneity in the type and distribution of functional groups, hydrophilic and hydrophobic domains and surface roughness [48].

1.5. Current Research

In order to address these prevailing challenges, a large amount of research is being performed worldwide aiming to reduce implant-associated complications and improve quality of life. Development of biocompatible and biodegradable materials, design optimisation of implants, the use of novel manufacturing and surface modification techniques are explored widely. With the properties of a material being a key factor in determining the success of an implant, there has been a considerable interest in material development. Currently the use of biodegradable materials, such as polycaprolactone and polyglycolic acid, is popular since their use reduces risks associated with implants being in the body for the rest of the patient's life. Implants fabricated using biodegradable materials can disintegrate after a pre-determined time interval which reduces the need for surgical removal of implants.

Optimisation of the implant designs to bear specific loads has been researched widely in recent years [49,50]. Optimisation methods allow the prediction of areas of fracture/failure of implants at specific loading conditions. Thus, implants can be designed to withstand the required load conditions with less material usage. Conventional manufacturing techniques used to fabricate biomedical implants have design constraints. Selective laser melting (SLM), a metal-based additive manufacturing (AM) technique, is of particular interest due to its capability to fabricate functional components having mechanical properties comparable to those of the bulk materials [51]. The ability of SLM to build complex parts from three dimensional (3D) computer designs (including well-defined porous structures) also offers the possibility of customisation of biomedical implants. The potential for using SLM to fabricate biomedical implants has been discussed in more detail in the literature review section.

Although customisation and mechanical properties of implants are very important for avoiding post-implant complications, surface properties including surface texture, surface chemistry and the stability of the surface oxide layer have also gained considerable attention [4,13]. In recent years, surface modifications have been performed not just to improve the surface

finish and corrosion resistance, but also to make the implant biocompatible and a drug carrier. Also for certain applications, surface modification is required to make an implant's surface specific-to the binding of extracellular matrix such as fibrinogen and laminin in order to promote cell adhesion and tissue regeneration [4]. There are numerous surface modification techniques (including coating with biocompatible materials or drug-eluting polymer) available to improve the corrosion-resistance, cytocompatibility, bone-tissue integration, drug delivery and reduce post-implant complications; however, most of them have limitations and do not have precise control over the surface chemistry [52–54]. Thus a coating technique that offers precise control on the location and orientation of chemical groups/biomolecules on the surface is essential to cater for current needs.

Self-assembled monolayers (SAMs) are composed of amphiphilic molecules with a head group which can attach to the surface to be modified and a tail group containing the functionality which is desired to be displayed on the surface. There are different types of SAMs including thiols, silanes and phosphonic acids. SAMs can be modified with various functionalities including drugs and proteins. Also, SAM coatings are usually in nano-scale and can be used to specifically modify a material's surface. The ability of SAMs to precisely control surface chemistry with relatively simple and inexpensive processing, has led to numerous suggested applications and biomedical applications is one among them [45,54–59]. A detailed explanation of SAMs, their types and formation are discussed in section 2.5.

1.6. Scope of the Research

The key to address the challenges with biomedical implants is to optimise the implant-host interface. It is envisaged that customised implant designs, due to their superior fit compared to traditional designs, can reduce post-implant complications by preventing implant migration. In addition, by modifying the surface chemistry of the implant with drug/protein molecules specific to the target site, biochemical interactions at the implant-host interface can be optimised and post-implant complications can be reduced. Previous research has demonstrated the use of SLM for producing biomedical implants with

customised and complex external and internal structures [60,61]. In addition SAMs, a form of nano-coating, have the ability to modify the surface chemistry of an implant precisely and specifically. This thesis will evaluate the potential to integrate SLM with SAMs-based surface modification to fabricate customised biomedical implants with functional properties.

1.7. Thesis Structure

Chapter 2 will discuss the available literature and help the reader to understand the background knowledge in additive manufacturing (AM), in particular the selective laser melting (SLM) process, as well as surface modification using self-assembled monolayers (SAMs). This chapter will critically analyse the literature and sets the aim and objectives for this research. Chapter 3 showcases the novelty, aim and objectives of this research. Chapter 4 describes the research methodology. It will list the materials, equipment, procedures and characterisation methods used in this study. Chapter 5 will present the results obtained for the fabrication and surface characterisation of parts produced using SLM. In this chapter the surface chemistry is investigated in detail by comparing the surface chemistry of a SLM fabricated part with a conventionally forged part. Further, the impact of laser power on the surface chemistry is also studied. Chapter 6 will describe the results for the surface modification of SLM structures using phosphonic acid monolayers. The stability of these monolayers under in vitro condition on both SLM as-fabricated and mechanically polished surfaces will be discussed. Chapter 7 will present the attachment of Paracetamol as a model drug to functionalise the SAMs and Chapter 8 will discuss the results obtained for the immobilisation, drug quantification, oxidative and in vitro stability and antibacterial susceptibility of Ciprofloxacin® attached to monolayers. Chapter 9 concludes the work with suggestions for future work.

2. LITERATURE REVIEW

2.1. Introduction

The purpose of this chapter is to introduce the reader to additive manufacturing (AM) methods (in particular selective laser melting) and surface modification using self-assembled monolayers (SAMs). This chapter begins by describing the standard definitions and manufacturing techniques belonging to AM. Later, SLM, a metal-based AM technique is introduced and previous literature on the SLM process, processing issues that exist and biomedical applications of SLM are discussed. In the second part of the literature review, issues with some of the current surface modification techniques are debated. An introduction to SAMs, their types, assembly methods and the advantages of phosphonic acid SAMs for biomedical applications are discussed in the later part. Finally from the literature, the knowledge gap in both of these SLM based manufacturing and SAMs based surface modification methods for biomedical applications is identified.

2.2. Additive Manufacturing

Additive Manufacturing (AM) has developed from the early days of rapid prototyping to enable the production of end-use parts. According to the American Society for Testing and Materials (ASTM), AM is defined as [62]:

"The process of joining materials to make objects from 3D model data, usually layer upon layer, as opposed to subtractive manufacturing *technologies".*

Although there are many terms used to describe AM, the most commonly used terms are free-form manufacturing, rapid manufacturing, additive fabrication, additive layered manufacturing and 3D printing.

AM was first developed for polymeric materials and now all types of materials including metals, ceramics and composites can be processed using these techniques to varying levels of success [63]. Currently there are many different AM processes available, most working on a layer-by-layer basis. However, they differ through the form of the starting material and the mechanism used to

consolidate it. Some of the consolidation methods used include the use of a laser or electron beam to selectively fuse polymer or metal powdered material; curing of liquid resin with ultraviolet (UV) light; extrusion of molten polymers from traversing nozzles; jetting of droplets from an array of nozzles, similar to inkjet printing and console`dation of sheets of materials using ultrasonic vibrations. Table 2-1 lists and defines the categories of AM processes in accordance with the ASTM International Committee F42 on Additive Manufacturing Technologies published in 2010 [62].

Table 2-1 Definitions of AM processes categories in accordance to the ASTM International Committee F42 on Additive Manufacturing Technologies (2010) [62].

Category	ASTM Definition
Vat Photopolymerisation	An additive manufacturing process in which liquid photopolymer in a vat is selectively cured by light-activated polymerization. Example: Stereolithography.
Material Jetting	An additive manufacturing process in which droplets of build material are selectively deposited. Example: PolyJet.
Binder Jetting	An additive manufacturing process in which a liquid bonding agent is selectively deposited to join powder materials. Example: ProJet 4500.
Material Extrusion	An additive manufacturing process in which material is selectively dispensed through a nozzle or orifice. Example: Fused deposition modelling.
Powder Bed Fusion	An additive manufacturing process in which thermal energy selectively fuses regions of a powder bed. Example: Selective laser melting.
Sheet Lamination	An additive manufacturing process in which sheets of material are bonded to form an object. Example: Ultrasonic consolidation.
Direct Energy Deposition	An additive manufacturing process in which focused thermal energy is used to fuse materials by melting as they are being deposited. Example: 3D laser cladding.

AM has gained considerable interest in recent years due to its ability to build parts of complex geometries from three-dimensional (3D) computer-aided design (CAD) model data [64]. AM is capable of building parts of almost any geometry in a single step regardless of the complexity of the part whereas conventional methods often need further steps and time or it is impossible to do so [65]. Furthermore, the use of AM speeds-up the whole development process since there is no need for dies/moulds and toolings [66]. Hence, the use of AM to fabricate customised one-off parts is faster and cheaper than

traditional methods. However, still there are issues in terms of the scalability of the AM processes to make large volume of parts due to its repeatability and the materials that are available. There are concerns over the mechanical properties such as hardness, ultimate tensile strength, surface roughness and density of the parts fabricated by AM. Also, the process is not currently cost-effective for large-scale production. Some of the active industries for AM include aerospace, automotive, medical, architectural, games, military, art, sport, construction and education; however, there has been particular interest for AM in aerospace and biomedical industries owing to the possibility for high performance parts where cost is not a main objective [64,67].

2.3. Selective Laser Melting

Selective laser melting (SLM) is an AM technique capable of fabricating metallic parts. Being an AM technique, increased geometrical freedom allows the fabrication of a part as envisioned without the manufacturing constraints prevailed with conventional techniques such as CNC machining, moulding and casting. Stainless steel (SS) was the initially used material when the SLM process was introduced in 1999. However after its introduction, a significant number of metals and alloys were developed for processing. Among stainless steel, 316L and 17-4PH are commonly prescribed for the use in a SLM process [68,69]. Badrossamay et al. [70] and Hauser et al. [71] have studied the use of tool steel to make highly dense parts. The use of aluminium alloys including AlSi10Mg [72] and AlSi12 [73] cobalt-chrome (ASTM75) [74], titanium and its alloys (Ti6Al4V, Ti24Nb4Zr8Sn and Ti6Al7Nb) [75], Inox 904L [76] and Inconel (625 and 718) [77] for SLM process were also reported in literature. Apart from these materials, magnesium [78] and nitinol (an alloy of nickel – titanium) [79] are also being researched to be processed in a SLM machine.

2.3.1. Generation of a CAD file and supports for SLM

In SLM, parts are built directly from 3D model data. Normally, the CAD file for the SLM process is designed using the commercially available design software including ProEngineer, Solidworks and Catia. For medical application, the CAD file of the implant to be fabricated is normally generated either by designing the part using CAD software packages or by reconstructing

the structure of the damaged part from magnetic resonance imaging (MRI) or computer tomography (CT) data. A set of CT/MRI data can be combined using commercially available software such as Mimics (Materialise NV) to convert the 2D DICOM files to a 3D surface tessellated (STL) file. During the STL file conversion from other formats such as initial graphics exchange specification (IGES), the geometry is converted to a triangular mesh, which represents the surface of the part. In some cases, CAD files can also be reverse engineered by laser scanning the damaged part.

SLM is capable of building net-shape parts with complex geometries; however, there might be some areas of the part that overhang and may need a support material during building. In such cases, supports should be generated in a way that they are easy to remove without damaging the part's quality during post-processing. For example, AM 250 (Renishaw Plc.) machines use the same material for supports as they do for fabricating the part (not only AM 250, all SLM systems use the same material for the build and its supports). However, they use a lower laser power for the supports than they use to fabricate the actual part so that the supports can be easily removed. Also it is important to position supports in a way that they can be removed easily and they cover all major overhangs. Supports are also used to stop warping of the part. Once the part is designed, the CAD file is then exported in STL format. Appropriate orientation is selected and supports are generated (where required) to the STL design. The machine interface software is then used to slice the STL file into several layers according to the predefined layer thickness along the Z direction.

2.3.2. Equipment and Principle of SLM

A schematic of the SLM process is shown in Figure 2-1. A typical SLM machine consists of a scanning laser (usually a fibre optic laser with wavelength λ=1070 nm) a hopper attached to a wiper (recoater), an elevator that lowers a build platform to adjust the layer thickness, and a lens that focuses the laser to the build area. Before starting the build, the chamber is made to be inert by pumping in an inert gas such as argon. The powder from which the part is to be fabricated is spread over the build platform from the

hopper to a pre-defined layer thickness. Depending on the surface quality and fabrication speed requirements, this layer thickness can be fixed to be between 20 µm and 100 µm.

Shortly after a layer of powder has been spread, the laser beam scans the powder in the areas specified by the layer of the model file and fuses them. Once the scan is complete, the build platform moves downwards by a pre-defined layer thickness for a new layer of powder to be spread over the previously scanned layer and this process continues until the part is completed. Once fabrication is complete, the build platform is raised and the part is removed from the substrate. The non-fused material on the build area can be sieved and recycled [63]. The part is normally sonicated with deionised water for 30 minutes to remove non-sintered particles.

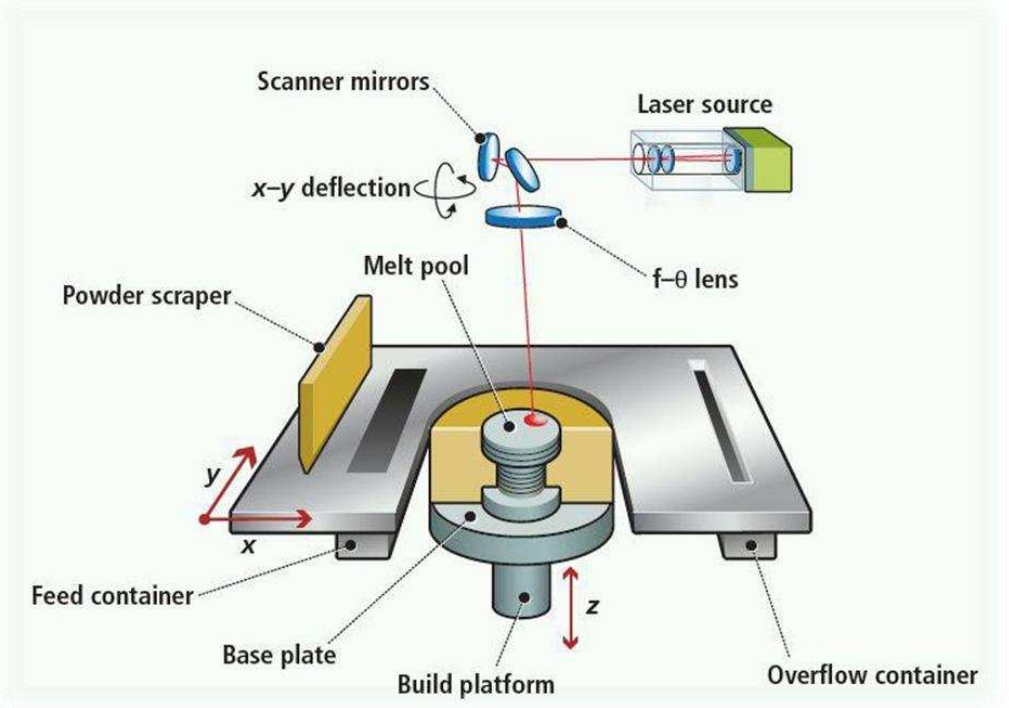

Figure 2-1 Schematic of the SLM process. Reproduced with kind permission from Vision Systems [80].

2.3.3. Factors governing the SLM process

The common factors that influence a part's physical and mechanical properties include material properties, powder bed property, laser energy input strategy,

part building strategy and atmosphere of the build chamber [81]. Most of these process parameters are variable but some are not. They are discussed below.

Material Properties

The SLM process uses powdered metal/alloys to produce parts. Although a range of metals can be processed using this technique, the material properties including particle shape and size distribution, absorptivity, reflectivity, melting and boiling point, conductivity and other thermal properties should be considered before processing of a powder material since they have a significant effect during the SLM process.

Particle shape and its size distribution have been shown to effect flowability, powder bed density and fluidity of the material [72]. This may lead to increased porosity as the larger particles melt or partially melt while the smaller particles vaporise during the process [82]. Kempen et al. [72] reported that varied powder morphology and its size distribution affected the SLM powder bed density by 1%. Particle size distribution of the material directly influences the powder bed density. In the SLM process, metal powder is spread by a wiper. As the wiper moves across the bed, it may deliver certain pressure on the powder bed increasing the powder bed density. Hence, the powder bed density in a SLM process may lie between apparent density and tapped density of the powder [81].

In the SLM process, a layer of powder should be evenly spread over the platform to a predefined thickness for the laser to scan and fuse the material. If the layer is uneven, it can have a significant effect on the melting process and in turn affect the part's quality. In order to achieve good flowability and powder bed density, spherical particles are preferred. A wider particle size range of 5 µm – 70 µm was observed to offer a higher powder bed density of 5.31 g/ml than the narrow size range of 20 µm – 50 µm (4.88 g/ml) [81]. This may have been due to the fact that the smaller particles filled in the gaps between the relatively large particle sizes. As the packing density was increased, porosity in the fabricated part reduced from 0.11% to 0.05% [83]. However, it should be noted that in addition to the particle size, morphology, distribution and powder bed density, the physical and chemical properties of

the material are also the major driving factors and are discussed in the later section. The use of fine powders may create a dust cloud and may potentially cause respiratory disorders. Hence, any operation with the fine powders should be performed in a closed chamber or controlled environment.

Optical Scanning system

An optical system in a SLM machine contains a short pulse or continuous wave of laser energy, a beam expander, a dual axis scanning mirror and an F-Theta focal length lens [77]. Commercially available SLM machines have laser powers normally ranging from 50 – 400 W and sometimes even higher in certain machines. Since metals have high reflectivity (the ratio of energy of a wave reflected from a surface to the energy possessed by the wave striking the surface) at long wavelengths of incident laser and reduce the process efficiency, lasers with short wavelengths (such as the fibre laser) are preferred for the SLM process. Most commercially available SLM machines use fibre laser with a wavelength (λ) 1070 nm – 1090 nm [84]. They also use fibre modulated continuous wave laser operated in a pulsed laser fashion. This is because a continuous laser will produce a continuous and a stable energy to heat and melt the material homogenously. This can build up heat and increase melt-pool width. In contrast, a pulsed laser produces burst(s) of energy to melt the target material and thus the laser energy is delivered in a way such that heat build-up and melt-pool width can be minimised [77]. The use of an F-Theta lens ensures that the delivered laser energy is constant regardless of position in the powder bed.

Previous studies on the SLM process have shown that the surface roughness, porosity, dimensional accuracy and microstructure of a part greatly depends on the laser processing parameters including laser power, scan speed, scan strategy, beam width or spot size and scan overlap [51]. Laser energy density [the ratio of incident laser power (W) to the scanning speed (mm/s) and the laser spot diameter (mm)] is a critical parameter in the SLM process. The incident laser power and scan speed are controlled by the machine controller and the beam spot size is controlled manually by adjusting the lens.

Laser scan strategy is one of the important factors that determine the part's quality. A list of other variable parameters used in the scan strategy is tabulated in Table 2-2. Figure 2-2 is a schematic representation of some of the variable parameters used in the laser scanning. Energy density of the laser is mainly affected by the scan speed in addition to the laser power. Scan speed of the laser beam can be calculated as the ratio of point distance (µm) to the exposure time (µs). By varying the range laser power and scan speed same energy density can be altered. However, depending on the powder properties, the effect of energy density will be variable.

Table 2-2 Variable parameters in laser scan strategy.

Parameter	Description
Exposure time	The time of laser exposure to each point
Hatch type	Scan strategy such as scan direction and scan type.
Hatch distance	The distance between two adjacent lines of the scan
Point distance	Each hatch line is divided into series of points. Point distance is the distance between two points of a hatch line.
Scan speed	The speed of laser beam movement while scanning.

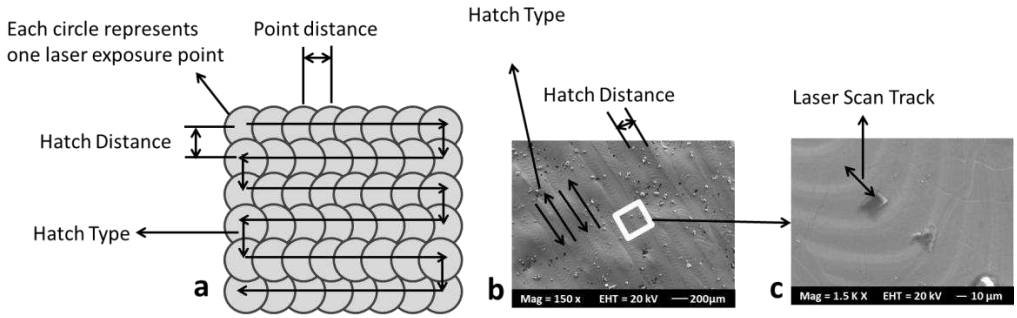

Figure 2-2 Schematic representation of laser scanning related input process parameters (a); SLM fabricated Ti6Al4V part showing actual laser scan track (b) and further magnified area depicting point distance of the laser scan(c).

The aim of optimising energy intensity is to make sure that the heat absorbed by the powder as a result of laser – powder interaction is enough to melt and produce fully dense part without overheating. Overheating of the powered material may lead to the formation of heat affect zones with mixed phases and may cause vaporisation and/or segregation of its alloying elements [51]. By reducing the laser power and increasing the hatch distance, the energy density can be reduced. Similarly when the scan speed is increased, the laser beam has

a short interaction time with the powder material and will lower the energy density.

Several laser scan strategies are available to consolidate the powders including uni-directional, bi-directional, alternating bi-directional, multi-directional and meander. Figure 2-3 shows a schematic representation of some of these scan strategies. The impact of scan strategies on the quality of the SLM parts has been discussed in the later section. Hence by altering the variable parameters of the optical system, highly dense parts with a better surface quality can be produced.

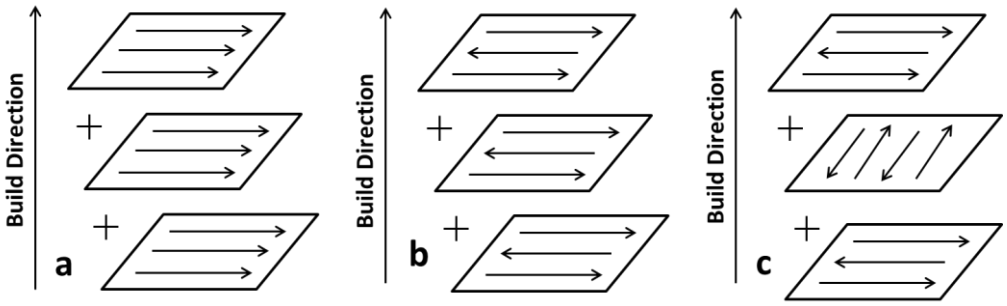

Figure 2-3 Schematic of some of the scan strategies typically used in a SLM process. Unidirectional (a); bi-directional (b) and alternating bi-directional (c).

Build atmosphere

Build atmosphere has a major part in determining the quality of the parts built in a SLM machine. In general, the build chamber atmosphere contains nitrogen, oxygen, carbon dioxide and inert gases. In an SLM process, the metal powders are melted and fused together at a very high temperature. During this process, the molten metals will react with the gases present in its atmosphere. If the SLM process is performed at atmospheric conditions, there is a high possibility for the metals to form its corresponding oxides, carbides and nitrides by reacting with the available oxygen, nitrogen and carbon in the atmosphere. For example, if SLM of titanium or magnesium is performed at atmospheric condition (in the presence of oxygen), since they are highly reactive, the metal will oxidise and burn/vaporise even before the melting point is reached. These reactions can have a significant impact on the next build layer causing porosity, delamination and reduction of the molten material's wettability which affects the fusion of successive layers, and possibly affects

the microstructure [84]. Also processing some metallic materials such as aluminium in atmospheric conditions can be problematic. Hence to avoid such adverse chemical reactions affecting the part's quality, the SLM process chamber is filled with an inert gas such as argon (99.99%). To aid in laser melting and remove moisture content from the powder material, the substrate/build platform is preheated to a certain temperature well below the melting point of the material. Marcu et al. studied the flowability of non-heat treated and heat treated (500 °C) Ti6Al7Nb particles (D90 = 56 µm) using Carney funnel flowmeter (5 mm diameter orifice). Their study accounted for an increased flowability (s) of 7 for the heat-treated Ti6Al7Nb whereas, no-flow of powders were observed for non-heat treated powders [85]. Thus pre-heating of powders is useful to improve the flowability. However, as mentioned in the material properties section, irregular particle shape and size can affect the packing density to 1%.

2.3.4. Heat Transfer in a SLM Process

Laser-material interaction in a SLM process is directly influenced by the ability of a material to absorb the incident radiation. However, during the SLM process, heat or energy input depends on numerous factors including material type, reflectivity, surface properties of the material (such as roughness and chemical composition), laser wavelength, direction of the incident radiation and temperature of the material.

Laser processing is usually a fast heating process. When the laser reaches the surface of a powder bed, the radiation is absorbed, reflected and transmitted through the bed. According to Fourier's theory of heat transfer, heat in a material flows via conduction due to the thermal gradients. In the SLM process, heat generated by the laser is absorbed by the metal powder and is then transferred to the particles in contact through conduction and convection.

Absorption of radiation in metals is influenced by various factors [84]. When the incident radiation is perpendicular to the metal surface, the absorptivity was observed to be low. Increased oxide layer film thickness of the metal, surface roughness and temperature were observed to increase the absorptivity of the corresponding metallic material. Some of the other factors affecting the

absorptivity of the material include material composition and surface contamination. Although most of the energy is conducted through the particles, some portion of the absorbed and reflected or transmitted energy is lost. During the laser scanning process, the energy is mainly lost due to reflectance of the beam and energy transfer to the powder bed. Whereas while melting, the heat energy is lost due to radiation, thermal diffusion and vaporisation [84].

When heat is conducted to a particle, it reaches to the core depending on its thermal conductivity. [81]. Thermal conductivity is a measure of rate of heat transfer through the material. When the heat conducted through is sufficient, it liquefies the metal particles and results in the formation of a melt pool [86]. Although the metallic powder materials have high conductivity, the powder's thermal conductivity depends on the metal's intrinsic properties and the number of contacts made between the particles. For example, the rate of heat transfer between the powders can be improved by increasing the powder bed density which makes more contacts between them. The bulk density of the metal powder itself can be a factor affecting the thermal conductivity [87].

2.3.5. Melt Pool Dynamics

A melt pool is formed when the absorbed energy is sufficient to change the solid phase of the metallic particles to liquid (Figure 2.4). As the laser scans the powder particles, the energy is absorbed and it is conducted to the surrounding particles in contact to melt them. After the laser moves from the scanned area, the melt pool is formed as a result of heat transfer between the particles. The shape of the melt pool in a SLM process tends to be flat [77]. However, this greatly depends on the wetting angle. When a high laser power is used, wettability is increased and a flat melt pool is obtained [77].

Wettability (the spreading behaviour of a liquid on a solid) is an important factor that determines the capillary stability of the melt pool. Liquid metals have poor wetting properties leading to capillary instability i.e. splitting of the molten metal into small entities in order to reduce surface tension variations [84]. This balling phenomenon is shown in Figure 2-4b. Balling is also referred as sphereodisation of the liquid melt pool [82]. Balling was observed to significantly cause weak inter-layer adhesion leading to the formation of non-

uniform layers. Further to this, balling was also observed to affect the part's quality by inducing porosity and increasing the surface roughness [77]. However, balling can be controlled by optimising the process parameters such as laser power, scan speed and hatch spacing [84].

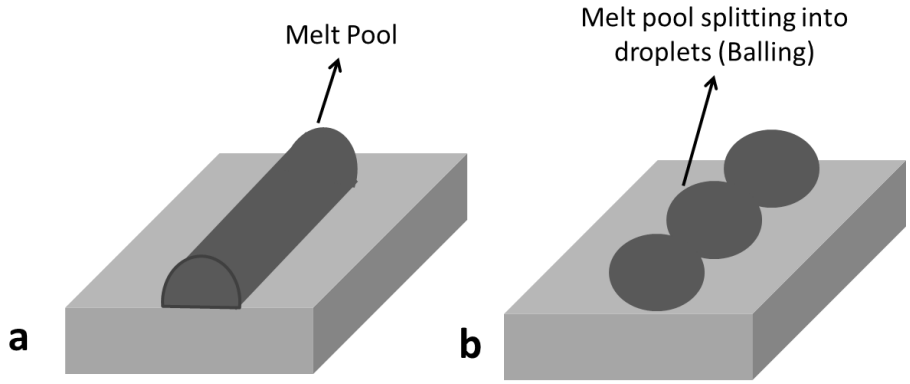

Figure 2-4 Schematic representation of melt pool (a) and splitting of melt pool resulting in balling phenomena (b).

2.3.6. Microstructural Development and Thermal Effects

As the laser scan is complete, the melt pool stabilises and solidifies with the release of thermal energy. In the SLM process, both the melting and cooling of the metal/alloy occurs rapidly [51]. Due to this, a non-homogenous nucleation is observed. Temperature gradients and heat transfer conditions determine the cooling rate, grain growth and the formation of microstructure [81]. The microstructure of the part fabricated by SLM determines the mechanical properties of the part such as hardness, elongation and fatigue behaviour. Altering the SLM process parameters can produce varied grain size, grain growth and distributions. For example, laser scan vector length was observed to influence microstructural features including the width of the prior β grains and the thickness of the α' laths. On comparing the microstructural features of meander and checkerboard laser scan strategies, the width of the prior β grain for Meander scan was 103 ± 32 µm whereas for the checkerboard strategy it was 383 ± 32 µm. The α lath thickness for meander scan was observed to be 0.5 ± 0.2 µm whereas for the checkerboard strategy, this was 0.9 ± 0.5 µm. [88].

During SLM, which is a rapid melting and cooling process compared to conventional forming processes, the metal stays in the liquid state for a fraction of second before solidifying. This short time and thermal cycle rate induces residual stresses in the fabricated part leading to dimensional inaccuracies, delamination of layers and solidification cracks [64]. Shiomi et al. reported residual stresses for parts built using chrome-molybdenum-steel alloy (JIS SCM 440) ranging from 300 – 400 MPa for laser scan speeds of 4 mm/s, 6 mm/s, 8 mm/s and 10 mm/s [89]. It was also reported in this study that, by heat treatment for an hour, 70% of the residual stress were relieved. Dimensional inaccuracies can be due to shrinkage of the part on solidification. The rate of cooling of the liquefied metal during the SLM process will contribute to the grain size distribution and microstructural pattern. Solidification cracks originate when the solidifying metal cannot accommodate the thermal shrinkage and this greatly depends on the material properties of the corresponding metal [84]. Solidification cracks generally originate between grain boundaries or at the interphase between different metals. The level of shrinkage can be controlled by optimising the process, such as preheating the powder bed and reducing the laser beam spot size. Preheating the powder bed is suggested to reduce solidification cracks and layer delamination. Residual stresses generated due to high thermal gradients can be relieved by post processing of the part [84].

2.3.7. Existing research on SLM

The SLM process developed at the Fraunhofer Institute (Germany) is believed to have been first commercialised by Fockele and Schwarze (Germany) in 1999. However, it is still considered a novel/innovative manufacturing technology and the process is constantly developing owing to its ability to make end-use parts and growing interest in diverse applications. Bridging SLM from research to mainstream manufacturing is not straightforward, as demanding industry standards and compliance need to be fulfilled. Material development, optimisation of processing methods to achieve better surface and mechanical properties, process economics, developing design rules for the process and exploring the use of SLM in various fields are some of the areas that researchers have concentrated on over the past decade.

As mentioned earlier in 2.3.3, the quality of a fabricated part greatly depends on the factors that govern the SLM process. Those governing factors can either be material based parameters (shape and size distribution of the particle; surface morphology, density of the particle and material composition) and/or equipment related parameters (such as laser power, scanning speed, scan strategy, beam/spot size, hatch distance, layer thickness, powder bed temperature and the atmosphere within the equipment) [76]. Manufacturing strategies including build orientation and scan numbers are also some important factors that can affect the quality of the part [74].

With SLM being a powder bed process, the material properties of the powders will play a significant role in determining the quality of the part. The manufacturing process of the powder, particle shape and size distribution, optical and heat transfer properties, chemical composition of the powder and thickness of the deposited layer for each fabrication cycle have all been observed to be important variables for SLM relating to the feed powder material [76].

Li et al. [68] studied the use of water atomised and gas atomised 316L stainless steel powders and reported that gas atomised powder rendered a denser structure when compared to the water atomised powder. This was due to the gas atomised powder having lower oxygen content than water atomised powder. The presence of high oxygen content can induce porosity, delamination and also affects the wettability of the molten metal. Since gas atomised powders have low oxygen content, they are preferred. The study also revealed that the gas atomised powder yielded a higher packing density than the water atomised powder since most of the gas atomised powder particles were spherical when compared to water atomised powder. However, it should be noted that internal pores may be present in gas atomised powders. The presence of these internal pores will lead to reduced apparent density and may cause gas bubbling when the laser beam scans the material [90]. Hence, this may also induce pores in the part fabricated by SLM. Presence of pores can affect the density of the fabricated part and are not favourable in applications where fabricating a dense part is the requirement.

Rombouts et al. [91] explored the effect of elements including iron, carbon, oxygen, copper, silicon and titanium on the quality of SLM fabricated parts. Their study revealed that the presence of oxygen in the build chamber increased the melt volume due to exothermic oxidation of iron and negatively affected the part's quality. Entrapment of carbon monoxide and carbon dioxide due to the oxidation of carbon was observed to induce porosity. Silicon and titanium were also observed to induce porosity due to their ability to form corresponding oxides and carbides. The energy absorption coefficient of oxides is higher than the metal and hence the oxides absorb more energy and increase the temperature of the metal, resulting in overheating. As the material is overheated, the rate of oxidation increases and affects the surface wettability. Since parts are produced additively in a SLM process, wettability of the previously scanned layer will have a significant impact on the density of a part [92].

The density of a component determines its mechanical properties. Similar to other manufacturing processes, the major goal of the SLM process is also usually to attain 100% dense parts. However, due to the lack of mechanical pressure (as found in the moulding process), this goal is difficult to achieve [51]. SLM is mainly characterised by temperature effects, gravity and capillary forces while processing. Entrapment of air bubbles due to low solubility of dissolved elements in the melt pool, oxidation of carbon present in the material, poor packing density of the successive layers and poor wettability of the molten material induces porosities that affect the part's density [91].

Studies conducted by Yadroitsev et al. [74] on 316L stainless steel (L in 316L represents low carbon in the alloy composition, i.e. 0.03% maximum) revealed that the production of highly dense parts is greatly dependent on the processing parameters such as laser power, scan speed and layer thickness. A balling phenomenon (splitting of the melt pool into small entities/droplets) was observed to significantly affect the densification behaviour in the SLM process [68]. Balling due to poor wetting of the melt pool was observed when low laser energy was used to melt a thick layer. As a result, agglomerates with pores between the metallic balls were observed as shown in Figure 2-5.

Pores are generated due to various other factors in addition to poor wettability. In SLM, high roughness peaks and valleys are formed after scanning every layer. When a fresh layer of powder is laid on this pre-melted and solidified layer, the peaks and valleys may prevent a homogenous distribution of the powder particles. As a result, gases are entrapped into the layer. When scanning such layers, the laser energy may not be sufficient to melt the layer completely due to the increased depth at certain locations caused by these peaks and valleys. If the powders are not evenly spread, entrapment of gases from the build atmosphere is possible. On laser scanning, the entrapped gas is superheated and expands rapidly removing the molten metal above it and thus inducing pores of sizes typically ranging from 2 – 50 µm [51]. Also when the hatch spacing is wide, pores were observed [84].

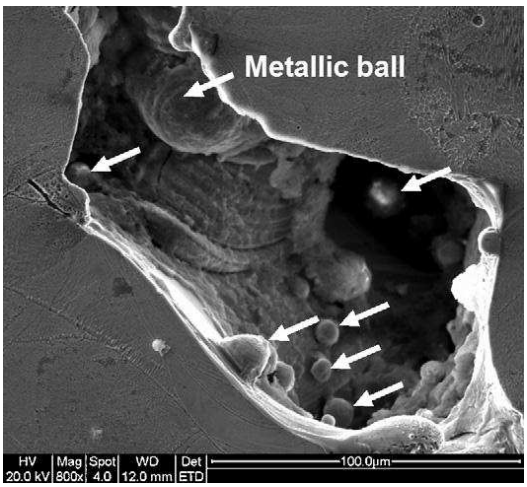

Figure 2-5 Micrograph showing a polished 316L SS surface depicting a balling induced pore. Reproduced with kind permission from Elsevier [68].

Morgan et al. [92] reported that the density of cubic parts fabricated using 316L SS in SLM increased with decreasing scan speed, when considering scan speeds between 100 - 200 mm/s. This is because, at a high scan speed, the energy per unit length will be less. Hence, less material will be consolidated and thereby porosity will be increased. Kruth et al. [51] studied various scan strategies (uni-directional, bi-directional and multi-directional) and reported that multi-directional scanning provided improved relative density. Also, the selective re-melting of each layer used in this study was observed to improve the part's density up to 98 – 99% for Ti6Al4V.

Li et al. [68] experimentally showed that at a high laser power, low scan speed with a narrow hatch spacing and thin layer thickness, highly dense parts can be obtained. Apart from laser power and scan speed, the quality of a part is also a function of beam size/width, pulse shape hatch distance hatch spacing and layer thickness. However, all of these process parameters are interrelated [76,77]. Yadroitsev et al. [74] studied the effects of processing parameters including laser power, scanning speed and powder layer thickness on the formation of single tracks. Their results concluded that, by choosing an optimal process window (layer thickness – 25 µm, laser power – 50W and scanning speed ranging from 80 – 200mm/s for 316L SS) and appropriate strategy of SLM, complex parts with mechanical properties comparable to wrought material can be manufactured. Optimisation of SLM process parameters has shown the potential to produce parts with mechanical properties comparable to their corresponding bulk material [93,94]. Researchers have optimised the SLM process parameters and obtained a relative density of up to 99% for AlSi10Mg and 316L SS [51,72]. Vandenbroucke et al. [95] reported that their optimised SLM parameters yielded part densities up to 99.98% for Ti6Al4V. Other than process optimisation, some post-processing (such as annealing, selective re-melting of the layers) is performed to improve the mechanical properties and surface quality of the SLM fabricated parts [93].

The mechanical properties of a SLM fabricated part not only depends on the material properties and density, but also the microstructure patterns and defects due to process parameters. Microstructures of the SLM fabricated parts were noted to differ in different directions due to the layer manufacturing. Since in SLM the metal powders are melted and cooled rapidly, the temperature gradient and heat transfer conditions determine the cooling rate, grain growth and the evolution of microstructures [81]. Rombouts et al. reported fine ferritic grains for Fe powder processed using SLM [91]. Simoneli et al. reported fine acicular α' grains throughout Ti6Al4V sample and prior β grain boundaries [88]. Li et al. [68] obtained a dense microstructure for a hatch spacing of 150 µm. More details on the microstructural patterns of SLM fabricated parts are recorded in the literature [51,68,91,96].

Defects such as porosity, delamination of layers and solidification cracks within a part can significantly deteriorate mechanical properties leading to the mechanical failure of the component [68]. Craeghs et al. [97] and Lott et al. [98] developed a feedback control system to monitor the effect of these parameters on the melt pool dynamics. Mathematical models were also developed to estimate the effect of process parameters on the local temperature distribution in the laser-material interaction zone to produce defect-free parts by SLM [99].

Although SLM has several advantages in terms of what it can do and what it can offer, poor surface quality of the SLM fabricated parts is of major concern [100]. Some of the major causes of surface roughness are the balling effect, partially melted and entrained powder particles that adhere to the outer edge of the solidified melt pool and the stepped profile observed due to layer-wise fabrication. The other contributing factor to the increased surface roughness is the surface temperature difference between the laser beam and the solidifying zone caused by the motion of the laser beam [86]. Kruth et al. [51] suggested selective re-melting of the top layer (Z axis) for a better surface finish. By surface re-melting, the average surface roughness (Ra) of 12 µm for non-laser re-melted surface reduced to 1.5 µm. However, it is still a challenge to obtain an even roughness profile all over the part. Post-processing methods such as mechanical (abrasive sand blasting and machining), chemical/electro-chemical (acid etching, oxidation and electro-polishing) and thermal processes (annealing, plasma spray) are performed to smoothen the SLM surface. Although an additional process is required to smoothen the surface profile, SLM offers the advantage of fabricating customised and complex designs in a single step that are almost difficult to fabricate with the subtractive or formative technique.

Although the advancement of SLM as a robust manufacturing process is held back by limitations including the availability of materials, surface finish, mechanical strength and repeatability, it has still established profound applications in diverse fields including automotive (customised structures), aerospace (fuel nozzles for jet engines made by General Electric company) and

biomedical (surgical guides, maxillofacial and porous implants for orthopaedic applications) where cost is not the prime concern [27,63,101,102].

2.3.8. Fabrication of medical devices using SLM

As discussed in section 1, customised manufacturing together with mass production is required to meet the growing demand of joint replacements [103]. The availability of customisation has been possible with advances in manufacturing technology, enabling low volume products to be achieved efficiently and AM is envisaged to be the enabler for many types of customisation [104]. The need for customisation of biomedical implants makes AM techniques such as SLM attractive for fabricating implants.

SLM not only has the ability to produce complex parts with desirable shape and structure but also has the advantage of establishing a closed process chain from scanning a damaged part of the body to design and manufacture. For example, bone replacement materials can be fabricated by scanning the bone defect using an MRI or CT, designing the implant structure, then directly manufacturing the individual implant. This closed process chain will have the potential to offer custom-fitting implants to the damaged part's anatomy [60].

Also the freedom of design offered by this technology enables the fabrication of complex geometries of the implants, in terms of both external and internal morphology. The challenges including the necessities to build complex parts with thin walled sections, customised implant design with micro-porous structures and the need to reduce the market time can be well addressed by SLM. SLM fabricated Ti6Al4V parts have also been reported to have good mechanical properties matching ASTM F136 standards concerning in vitro testing [60]. Inter-connected porosity offered by the SLM process is of significant interest for fabricating bone replacement implants [75]. With its advantages over conventional techniques that impose constraints on what can be moulded or machined, SLM will not only improve the product quality but could be a potential solution for some of the current biomedical issues including the fabrication of customised designs and complex geometries.

Development of porous metallic surfaces for load bearing orthopaedic applications is being researched since they promote bone ingrowth and osseointegration [105]. Osseointegration refers to a direct structural and functional connection between ordered living bone and the surface of a load-carrying implant. Porous structures are required to lower the elastic moduli of the component similar to that of bone. This is because metals exhibiting higher elastic moduli than that of bone have been identified as a major reason for the loosening of an implant [106]. For example the Young's modulus for bone is 20 GPa whereas for titanium it is 110GPa. Therefore several techniques are employed to fabricate porous structures and SLM is one of them.

To achieve improved cell adhesion, osseointegration and well-defined interconnectivity, pore size and the amount of pores on the implant surfaces are important. For example, pre-defined pores of a specific size and configuration that can be formed using SLM allow the growth of bone tissues through the implant in order to achieve a strong connection. For bone implants, a customised design with porous structure will increase the contact of the implant surface to the bone and increase the ability of bone regeneration [60].

The typical surface morphology of an implant fabricated using Ti6Al4V in an AM 250 (a SLM machine manufactured by Renishaw Plc.) is shown in Figure 2-6. As can be observed from the figure, the as-fabricated surface is porous due to partial melting of particles. Fabrication of porous scaffolds for bone tissue regeneration using SLM has been reported extensively in the literature [107–109]. Patanayak et al. [106] fabricated a titanium metal analogue to human cancellous bone using SLM. Traini et al. [110] fabricated a porous dental implant using Ti6Al4V by SLM and concluded that SLM is an efficient technique to fabricate porous dental implants that adapt better to the properties of a bone. Porosity is a measure of the void spaces in a material. Zieliński et al. [111] have fabricated porous structures using Ti alloy by SLM and deposited hydroxyapatite for improved osseointegration and lifetime of load-bearing implants. Although the SLM-produced surfaces will be highly advantageous in this context, care should be taken that the partially melted particles do not detach from the surface since this can potentially lead to acute and/or chronic effects depending on the biological response and site of implantation. For

example, in bronchial stents, peeling of these partially sintered particles may block the alveoli in the lungs. Similarly, for cardiovascular stents, the presence of rough surfaces can affect the flow of blood and peeling of these particles may block the artery and affect the blood flow.

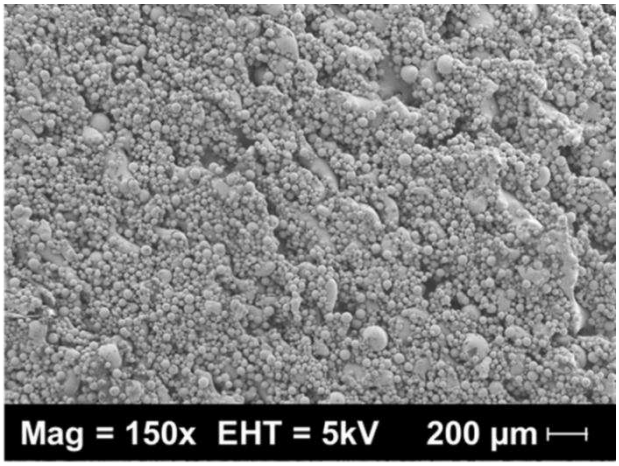

Figure 2-6 Typical surface morphology of a part fabricated using a Renishaw AM 250 machine. Note that the SEM micrograph is tilted to approximately 45° to the right to its build direction.

Wehmoller et al. [103] showed the ability of SLM to fabricate a lower jaw model (including teeth, the mandibular joint and the canal of the mandibular nerve), a spinal column model and a tubular bone femur. It was reported in their study that, to fabricate these implants in stainless steel, the production of the lower jaw required 24 hours, the spinal column required 25 hours and the bone femur took 26 hours. Although the time required to fabricate these parts in SLM may seem longer, due to the complexity of the part, it may be difficult to cast these models or fabricate using the subtractive/forming methods.

The Centre for Applied Reconstructive Technologies in Surgery, CARTIS UK, demonstrated the feasibility of the design and fabrication of a titanium cranioplasty plate and a successful implant to restore the orbital floor and rim produced in titanium by SLM. The implant was produced by the Centre for Rapid Prototyping and Manufacturing at the Central University of Technology, Bloemfontein, South Africa. Figures 2-7 and 2-8 show the demonstration cranioplasty implant and the implanted maxillofacial implant that were fabricated using the SLM process. Drstvenstek et al. [112] fabricated a bespoke angular implant using Ti6Al4V in a SLM machine to clinically treat a

patient with a congenital asymmetry of a facial bone. Their studies have also reported a clinical use of a mandibular implant fabricated by this technique.

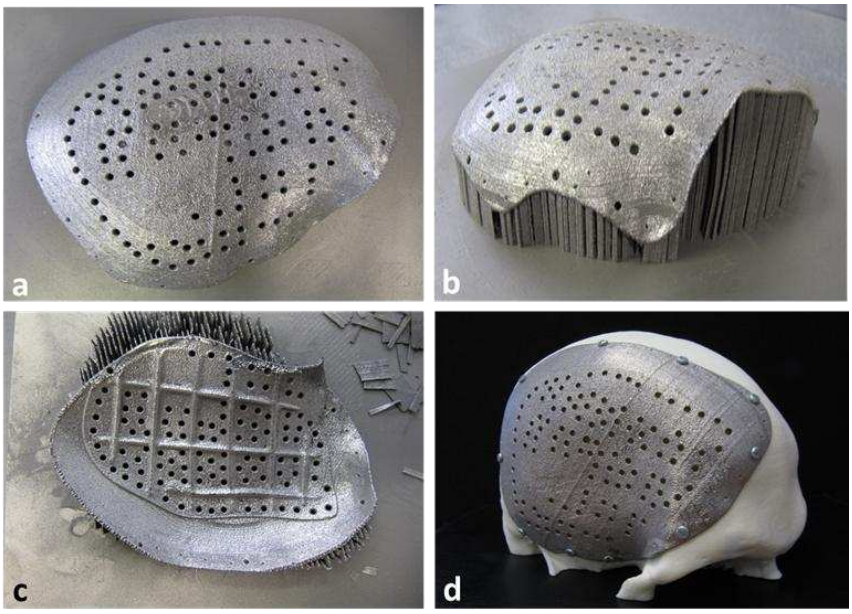

Figure 2-7 Customised cranial implant fabricated using the SLM process. SLM fabricated implant (a); Implant with support structures (b); Implant removed from support structure showing inner geometry (c) and custom-fitting of the implant to the skull (d). [Implant design and 3D model courtesy of CARTIS].

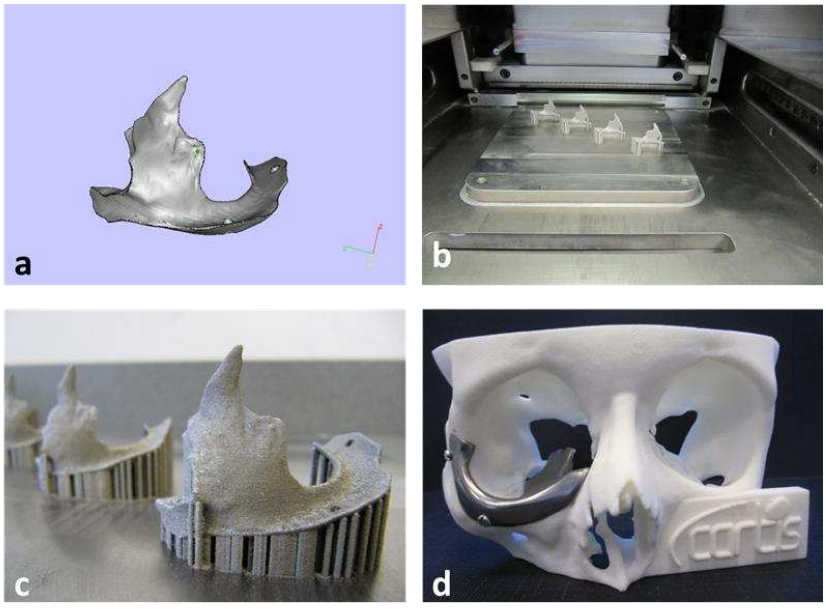

Figure 2-8 Customised maxillo facial implant fabricated using SLM. CAD design of a customised maxillo-facial implant (a); Implants fabricated in a SLM machine (b); Implant with its support structure (c); Custom fitting of implant to a model of the damaged part (d) [Implant design and 3D model courtesy of CARTIS].

Tolochko et al. [113] showed the possibility to fabricate dental root implants with the required structure, geometry and strength by SLM. A successful clinical use of a custom-made root analogue for a dental implant fabricated by this process has also been reported in literature. Almeida et al. [114] evaluated the reliability and failure modes of Ti6Al4V implant structure fabricated by two different technique, SLM and alumina blasted/acid etched. Their mechanical tests observed no significant differences in terms of reliability and fracture modes between these two approaches.

In summary, SLM has been shown to be able to fabricate 3D porous structures with customised, complex internal and external geometries which is difficult to achieve by conventional manufacturing [106]. Currently, LayerWise, Renishaw Plc and 3T RPD are some of the companies actively involved in the production of biomedical implants for cranial, maxillo-facial, orthopaedic and dental applications.

2.4. Surface Modification

Material selection is crucial for any application since the performance of a manufactured part will reflect the properties of the selected material. Finding a material with optimum bulk as well as the desired surface properties for any given application is rare and biomaterials are no exception [30]. Bulk alteration of a material is not generally preferred since it is expensive, time consuming and will impose limitations for the use of the material. Surface modification of a solid material at either atomic or molecular level is therefore performed to achieve the required surface properties without altering the key bulk properties of the material. Surface modification is required to reduce biological rejection and these can be attained by surface modifying an implant's surface with suitable body proteins as peptides.

Surface modification has wide applications including adhesive bonding enhancement, modifying wetting and non-wetting characteristics, creating micro-porous structures, altering the grain size and distribution, generating uniform three-dimensional structures on the surface and optimisation of surface chemistries of an engineered part. Although surface modification is

performed in a number of engineering disciplines, its application in the biomedical field is considered to be unique since it improves the quality of life of the patient. Several types of surface modification of biomedical implants such as morphological, physicochemical modification and biological modification using proteins and cells have been reviewed and reported by researchers [4,30,115–118].

2.4.1. Issues with current surface modification techniques

The ultimate aim of modern surface modification techniques is to make the implant surface biocompatible and to direct the biological healing response [115]. To address this goal, morphological, physico-chemical and biological modifications are performed. However, they all have limitations. In most cases, a single surface modification technique is not enough to achieve the desired surface property and hence two or more surface modifications are performed to achieve better biological properties. For example, Kim et al. [119] reported good adherence and spreading of human osteoblast cells for sand blasted and acid etched surface. Though the use of two techniques provided improved results in terms of cellular attachments, the use of two or more techniques to modify the surface can be time consuming and expensive. Implant coating using polymers impregnated with therapeutic agents has limitations that include fissures, cracks and waviness (undulating pattern) of the coating, inflammatory and hypersensitivity reactions as shown in Figure 2-9 [52]. The cracking and peeling of these polymeric coatings on the stents may be due to the expansion of the material beyond its elastic limit.

Most of the polymer and protein coatings are formed from large molecules with several reactive sites and hence it is difficult to introduce and control a specific chemical group. Chemical treatments with an acid or a base can offer varied surface finish (with micro pores and groves) and the introduction of a few acidic, basic and hydroxyl groups; however it is limited [120]. Heat treatment will have significant impact on the physical properties of a part but is limited to chemical modifications in conditions where the surface has to be functionalised.

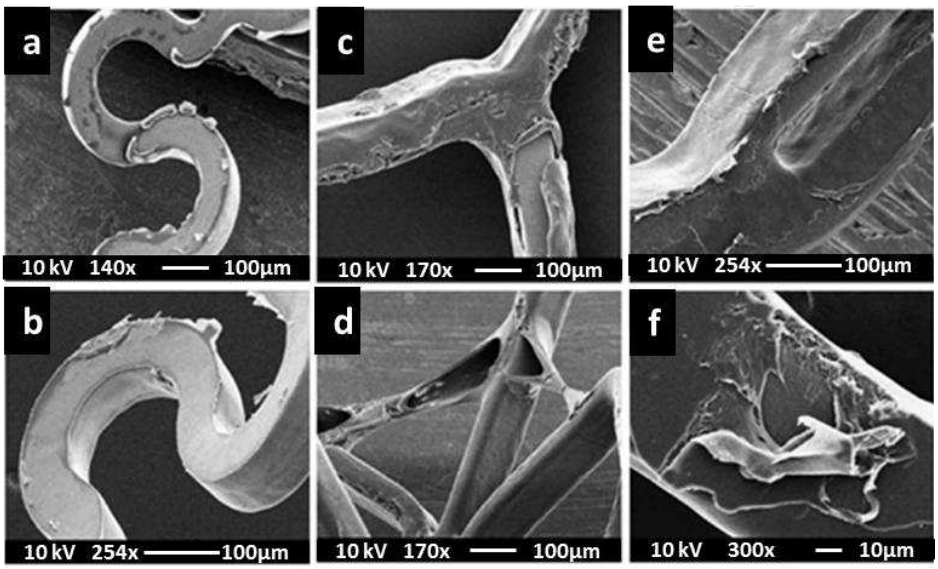

Figure 2-9 Micrographs of BiodivYsio (a, b) Taxus (c, d) and Cypher (e, f) stents commercially available for cardiovascular stenting. The stents exhibit cracking and peeling of the polymeric coatings on their expansion. Reproduced with kind permission from HMP Communications [44].

2.5. Surface Modification Using Self-Assembled Monolayers

Self-assembly is a process in which a disordered system of pre-existing component forms an organised structure or pattern due to specific local interactions among the components. Self-assembled monolayers (SAMs) are ordered molecular assemblies with a head group, a spacer and a functional tail group as represented in Figure 2-10.

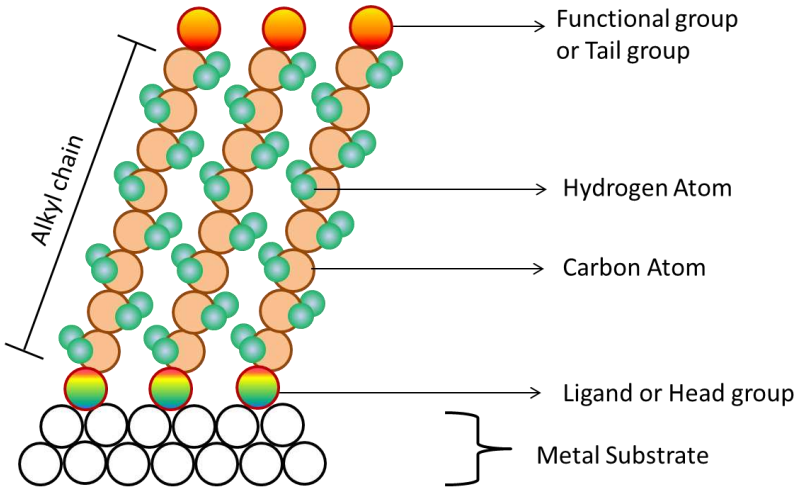

Figure 2-10 Schematic diagram of a single crystalline alkanethiol SAM formed on a metal surface.

SAMs are formed spontaneously when substrates are immersed into a solution of surface-active molecules in an appropriate solvent [121]. Usually, the head group is bound to a surface and the tail group presents a chemical functional group. This group can be modified with drugs or proteins to obtain the desired functionality such as drug delivery or cytocompatibility. The head and tail groups are separated by a spacer which is generally an alkyl chain ($-CH_2$). This organic interface provides well-defined thickness and acts as physical barrier. Also, crystallisation of this alkyl spacer layer improves monolayer stability. Hence long spacers are preferred. Commercially available tail group functionalities range from simple primary amines, hydroxyl and carboxylic groups to bulky aromatics and epoxides.

SAM coatings are usually nanosized adding only 1-10 nm thickness to the surface [58]. SAMs can be designed at molecular level to be biologically inert or active by modifying the tail group with desired functionality. SAMs can be chemisorbed to numerous materials including glass, metals (gold, copper, silver, stainless steel, titanium and its alloys, palladium and platinum) and semiconducting surfaces (silica and indium coated tin oxide) [122].

SAMs coatings are inexpensive and their ease of functionalisation with well-ordered arrays of SAMs makes them ideal systems for various applications such as the control of wetting and adhesion, corrosion protection, chemical sensing, semiconductor passivation, drug/protein delivery and nano-fabrication [59,122,123]. SAMs have wide applications in the healthcare industry including blood purification (e.g. algae removal from blood stream using SAM coated nanoparticles), drug delivery, surface modification of implants and to study the cellular properties such as interfacial reactions between cells and organelles and/or proteins and implants [124].

2.5.1. Formation of SAMs

Molecular assembly during the formation of SAMs is a thermodynamic process. Considering a system at a constant pressure and temperature, the associated Gibbs free energy (G) can be written as, $G = H - TS$, where H is the enthalpy, T is the temperature of the system and S is the entropy. The change of free energy is given by $\Delta G = \Delta H - T\Delta S$. Self-assembly is driven by the

decrease in Gibbs free energy. For the self-assembly to be spontaneous, the enthalpy of the system should be negative and in excess of the entropy of the system. Thus, when ΔG is negative i.e. $\Delta G = \Delta H - T\Delta S < 0$, self-assembly of molecules take place spontaneously. Minimisation of Gibbs free energy can be attained by the minimisation of repulsive and/or maximisation of attractive molecular interactions. Self-assembly process will become progressively less likely when the magnitude of $T\Delta S$ approaches the magnitude of ΔH and above critical temperature [125].

Deposition of monolayers on substrates offer one of the highest quality routes for preparing chemically and structurally well-defined surfaces [126]. Adsorption of SAMs on to a surface is generally performed either in polar or non-polar solvents to attain a greater flexibility in the molecular design and control over the surface properties [59]. SAMs form a covalent bond on adsorption and the interactions between the subunits (spacers) are non-covalent (involves variations of electromagnetic interactions between molecules or within a molecule) such as van der Waals forces. Non-covalent interactions are critical in maintaining the 3D structure of large molecules. Due to this non-covalent interaction between the sub-units, the SAMs have the tendency to shrink and regain their position. SAMs are adsorbed to a surface by various methods including spray deposition, electrochemical deposition or by simple immersion [127]. Spatially defined arrays of monolayers can be formed on a surface by integrating SAMs with patterning methods such as micro-contact printing and photolithography (a microfabrication technique used to pattern parts of a thin film or a bulk substrate such as circuits) [115,128].

2.5.2. Assembly of SAMs by simple immersion

The assembly of SAMs by a simple immersion method typically involves the immersion of the sample into a dilute solution (thiol, silane, phosphonic and other organic acids), allowing molecules to assemble, then removal of the sample and rinsing. The attachment and assembly processes of SAMs are schematically represented in Figure 2-11. The assembly process takes place once the sample is immersed into the solution. The amphipilic SAM-forming molecules in solution come in contact with the surface in a few seconds after

immersion leading to the organisation and packing of the molecules to form well-ordered SAMs in a few hours. As the monolayers continue to form, the non-covalent interaction between the hydrocarbon chain help in packing molecules into a well-ordered crystalline layer [129]. Since the head groups have a special affinity towards metal substrate, formation of multi-layers is not possible.

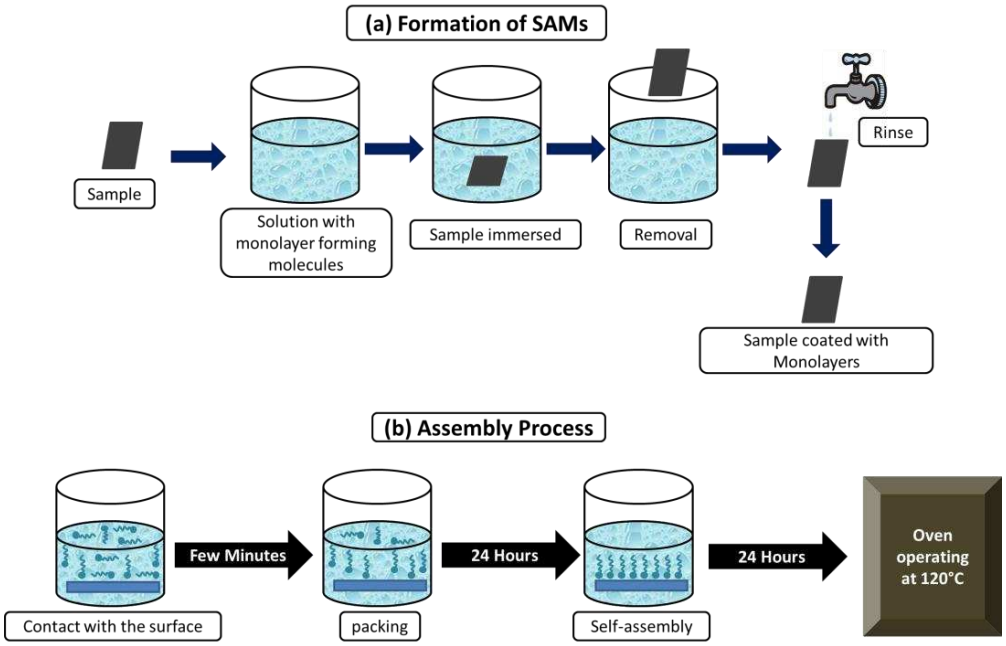

Figure 2-11 Steps involved in the adsorption (a) and assembly (b) of SAMs.

The degree of order of these monolayers is mainly determined by the length of the spacer (alkyl chain) [130]. It has been reported that SAMs with short alkyl chains (fewer than 10 carbons) lack sufficient attraction between the alkyl chains to produce well-ordered monolayers. The other important factors that determine the order of SAMs include cleanliness of the substrate, surface chemistry and purity of the solvent [58,131]. The important and problematic contaminants are hydrocarbons (oils which comes from pumps and skin), impurities on the material's surface and some polymeric contaminants from the atmosphere [132]. The quality and assembly of SAMs also depend on several factors such as head group size, its properties and assembly time. Annealing of the SAM coated specimens at 120 °C can be performed to obtain a strongly surface-bound film of monolayers [55]. A detailed explanation on the

assembly of monolayers and how these factors affect the monolayer formation are described by Schwartz [59].

2.5.3. Types of SAMs

Some of the popular monolayer self-assembly chemistries include:

- Thiols, disulfides and thiols on gold, stainless steel [58,123].
- Silanes on silicon dioxide and hydroxy functionalised surfaces [48,133].
- Fatty acids and phosph(on)ates on metal oxides [56,134].
- Isonitriles on platinum [55].

2.5.3.1. Thiols

An alkanethiol molecule has three chemical entities that determine its assembly and the general formula is $X(CH_2)_nSH$. The head group contains thiol sulfur (SH) and this acts as the driving force for the chemisorption of sulfur with the surface. The tail or terminal group (X) can feature one of several functionalities including a hydroxyl, amine and a carboxylic group. The terminal hydroxyl (OH) or carboxylic (COOH) groups of the monolayers are highly useful for the chemical transformations to achieve their desired functionality. Also, by reacting the carboxylic group of the thiol SAMs with an acid chloride ($SOCl_2$), further reactions can be attained [123]. For example, if the terminal group of the monolayer and the reacting group of the binding molecules have a carboxylic group, then in such cases, the COOH group of the monolayer can be modified to its corresponding acid chloride and the desired reaction can be achieved. Scheme 2-1 shows an example of reaction mediated using thionyl chloride.

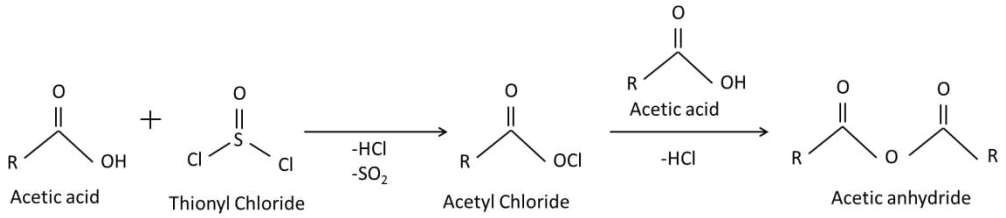

Scheme 2-1 Reaction scheme showing the conversion of acetic acid to acetic anhydride using thionyl chloride

Thiols have been mainly used to modify gold surfaces since 1983 and their attachment has been well-studied and reported [58,127,131]. However, thiols have also been used to modify other metallic surfaces including iron and stainless steel. The alkanethiol monolayers formed on 316L stainless steel (the letter 'L' represents low carbon content of 0.03% max. in the composition) were not as stable as they are on gold surfaces due to the complex surface chemistry of 316L SS [58]. Thiols have been used for a variety of applications including corrosion protection, semi-conductors, biomaterial and biosensing applications [128,135].

2.5.3.2. Silanes

Similar to thiols on gold, the use of trichlorosilane monolayers on silica surfaces is popular owing to their excellent grafting properties to silica surfaces [134]. Silanes are also used in chromatographic techniques for the separation of molecules. Chlorine in the silane monolayer reacts with the hydroxylated surface to form a stable siloxane (Si-O-Si) bond. The use of silane monolayers on metal oxide surfaces such as glass, titanium, aluminium and cobalt-chromium were also studied in recent years for drug delivery [118,136,137]. Trichlorosilane monomers were observed to be highly reactive towards glass surfaces [120].

One of the problematic conditions for researchers with silane monolayers is to synthesise and purify these silane monomers. When the silane monolayers are assembled on a surface they display a high degree of monomer crosslinking, condensation and/or formation of multilayers due to siloxane linkages (Si-O-Si) [138]. Crosslinking was observed to be less stable compared to non-cross linked monomers and thus allowing the desorption of monolayers in a short period of time. Mani et al. [137] reported that the silane monolayers formed on a cobalt-chromium alloy surface were due to the covalent bonding of the SAMs with the alloy (Si-O-Cr and Si-O-W). However, their study reported that these monolayers remained ordered and bound to the alloy surface for only seven days under in vitro conditions [137]. Drug delivery from the implant surface for a longer period below the toxic level may be necessary for certain clinical applications. In such cases, this system cannot be used and therefore,

the use of alkoxysilanes instead of chlorosilanes (such as trialkoxysilane) may be a better option. However, their assembly requires multiple soaking and annealing steps to form well-ordered monolayers [120].

2.5.3.3. Phosphonate monolayers

Apart from thiols and silane monolayers, phosphonic acids have gained considerable interest in recent years due to their ability to bond to a range of metal oxide surfaces and their relatively improved hydrolytic stability under physiological conditions [129,139]. The use of phosphonic acid SAMs for surface modification is recent when compared to silanes and thiol SAMs [140]. Similar to thiol on gold, phosphonic acid monolayers adsorb on a metal surface with a tail-up orientation with a tilt angle (determined using evanescence reflection spectroscopy) of the hydrocarbon chains of about 30° with respect to the normal [141].

Phosphonates have three oxygens and a carbon directly attached to a phosphorous molecule. The binding mechanism of these phosphonic acid monolayers to metal oxide surfaces can be a monodentate, bidentate or tridentate as represented in Figure 2-12 [123,142]. This binding mechanism depends on both the surface and the nature of the organophosphorous compounds. Phosphonic acids bind to a metal oxide surface by the co-ordination of phosphoryl oxygen to Lewis acidic sites, followed by the condensation of P-OH groups with surface hydroxyl group or other surface oxygen species [143]. A Lewis acid is an electron-pair acceptor and a Lewis base is an electron pair donor. Thus, the Lewis theory suggests that acids react with bases to share a pair of electrons, without any change in the oxidation numbers of the atoms. Phosphonic acid SAMs form a metal phosphonate bond when adsorbed to a metal oxide surface (Ti-O-P). Adsorption of long chain alkyl phosphonic acid SAMs on metal oxides has been reported to offer densely packed and well-ordered SAMs [53,56,144,145]. Like silanes, phosphonic acid SAMs do not condense (condensation is a reaction in which two molecules or moieties combine to form a large molecule, together with the loss of a small molecule) in general due to the absence of homo-condensation

(reaction between the functional groups of the same molecule/moiety) of P-OH and P-O bonds at aqueous conditions [140].

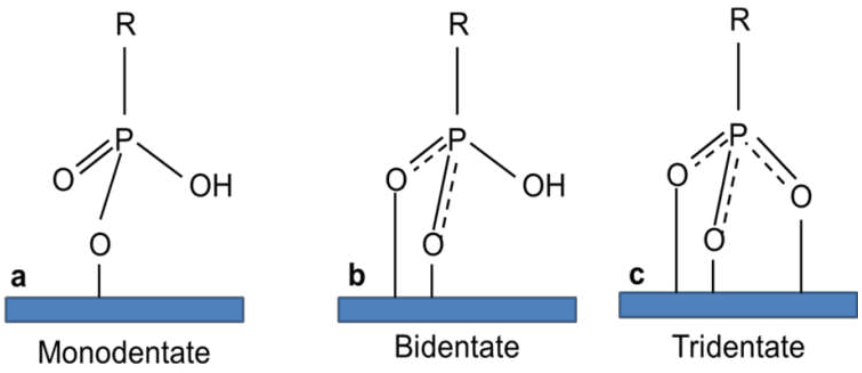

Figure 2-12 Schematic representation of the binding mechanism of phosphonic acid SAMs to a metal surface.

Although phosphonic acid SAMs were reported to exhibit high stability, it depends on various parameters including the density and degree of ordering, interaction between the monolayers, size of its head group, spacer length and the reaction method used to chemisorb the monolayers to the surface [146]. Buckholtz et al. [130] attempted to study the effect of long alkyl chains of phosphonic acid monolayers on Ti6Al4V, titanium, aluminium and vanadium surfaces. The compared long alkyl chain consisted of carbon atoms in even numbers between 18 and 30. This study showed that the results were indicative of the chain length on SAM's stability. When even numbers of carbon atoms were used, better packing of the molecules were witnessed than the odd numbers due to interdigitation (to become interlocked) [147]. Hsu et al. [148] proposed an air-liquid interface assisted method to form a smooth and a homogenous phosphonic acid SAMs on a silicon surface. However, the common method followed by most researchers is the simple immersion method since it is less complicated and in-expensive.

Tosatti et al. [149] studied the assembly of phosphate monolayers on rough and smooth titanium oxide coated glass surfaces. Their studies revealed that phosphonic SAMs were chemisorbed to both rough and smooth titanium surfaces. The structure and order of phosphonic acid based monolayers on silicon was studied by Dubey et al. [47] and compared with thiols on gold surfaces. It was reported that phosphonate monolayers can be used to form

well-ordered SAMs with methyl and hydroxyl groups for electrical and bio-sensing applications.

The stability of SAMs depends on the temperature, pH of the aqueous medium, ionic concentrations in the medium and its exposure to harsh environments such as UV or other high power radiations [123,140]. Bhure et al. [55] investigated the stability of phosphonic acid monolayers on Co-Cr surfaces and showed that the monolayers were highly stable when the surfaces were exposed to atmospheric conditions. In an another study, Kaufmann et al. [56] investigated the stability of phosphonic acid SAMs on an electropolished Co-Cr surfaces. This study concluded that the SAMs desorbed in a biphasic manner in Tris buffer solution with more desorption in the first three days followed by a slow and sustained release. Their initial fast release was accounted for by the desorption of physically bound molecules followed by the sustained release of the covalently bound molecules. An initial study by Mani et al. [53] showed that the most of the phosphonic acid SAMs adsorbed on a titanium surface desorbed in a day when immersed in Tris buffer solution at 37 °C. When exposed to ambient air, SAMs were stable for 14 days. However, in their later studies with an improved SAM adsorption procedure by heat treating the SAM coated surfaces, stable phosphonic acid SAMs were formed in solution [37]. Phosphonate monolayers are not only limited to oxide substrates; they are also used to modify hydroxyapatite and calcium carbonate [54,150]. However, the number of studies on these non-oxide surfaces is considerably lower than the oxide surfaces [140].

2.5.4. Biomedical Applications of Phosphonate SAMs

Various surfaces including silicon, titanium, cobalt-chromium, nitinol, gold, calcium phosphates have been functionalised using phosphonic acid monolayers for biomedical applications [53,56,145,151]. SAMs can be functionalised by modifying the tail group with required functionality including therapeutic drugs and proteins. This can be attained before or after the adsorption of SAMs to a surface. Although the modifications of SAMs by both of these processes have been reported, functionalisation of SAMs after its adsorption to the surface is preferred. This is because, in certain cases, it will

be difficult to control the reactivity of the head group towards the functional molecules.

There are a number of ways in which the functional group of SAMs can be modified. SAMs can be adsorbed to a surface and then dip coated with the active/functional ingredient [144]. In other ways, the functional group of SAMs are made to react directly with the molecules to be attached. When performing this, it is possible for both the monolayers and the drug to possess the same functional groups such as alcohols and carboxylic groups. In these cases, the SAMs can be converted to their corresponding acid chloride by acid chloride mediated esterification. Converting the functional group of SAMs to an acid chloride will enhance the reactivity and will effectively bind the desired molecule to the SAM. This is mainly because the reactivity of acid chloride is higher than the hydroxyl or carboxylic group.

Mani et al. [37] reported the immobilisation of flufenamic acid (as a model drug) on to gold and titanium surfaces using SAMs with carboxyl group. Thiol SAMs were used for gold whereas phosphonic acids SAMs were used for titanium. In their study, acid chloride esterification (ACE), dry heat esterification (DHE) and direct esterification (DE) reactions were performed to immobilise flufenamic acid to these surfaces. Briefly, for the ACE, 1.125 g of the drug was refluxed with 4 mL of thionyl chloride ($SOCl_2$) in an inert atmosphere. After an hour, the excess thionyl chloride was evaporated and the drug was dissolved in a solvent (THF). Sample specimens of both phosphonic SAMs on titanium and thiol SAMs on gold surfaces were immersed in this solution and incubated for 48 hours. In the DHE, both thiol and phosphonic acid SAM coated surfaces were covered with 200 µg of flufenamic acid. The specimens were then heated to 150 °C in air at a constant temperature for 4 hours. In the DE procedure, a stock solution of 525 µg of flufenamic acid in 105 mL of anhydrous toluene was prepared. SAM coated samples were immersed in 10 mL (for each sample) of the stock solution. Finally, the samples treated with the three esterification methods were rinsed with solvents and deionised water for several minutes to remove physisorbed molecules.

Surface characterisation by X-ray photoelectron spectroscopy showed the successful attachment of flufenamic acid to both thiol and phosphonic acid SAM coated surfaces. The total amount of drug loaded to the titanium surface was 0.93 ± 0.24 ng/mm^2 (DHE) and 0.61 ± 0.11 (DE) compared to 1.27 ± 0.45 ng/mm^2 (DHE) and 0.13 ± 0.02 ng/mm^2 (DE) for gold surface. According to Mani et al. [37], over all, approximately 0.1 – 1 ng/mm^2 was coated. The drug was observed to release in a biphasic manner i.e. initial burst release and a sustained release. For both DHE and DE, nearly 50% of the drug was released by day one, followed by a sustained release of the remaining drug.

The results for ACE were not presented in their study as they found significant scattering of the results for these samples which may be due to various factors as discussed below. Generally, an acid chloride will readily react with atmospheric moisture/humidity. The authors performed refluxing of the drug with thionyl chloride in an inert atmosphere to form an intermediate compound with an acid chloride group. However, after an hour, the excess of thionyl chloride was evaporated by exposing the refluxed mixture to atmosphere. During this evaporation stage, since the mixture was exposed to air, the acid chloride in the intermediate compound will react with the moisture to form flufenamic acid again (Scheme 2-2). Also, the THF used to dissolve the intermediate compound and immerse the samples was not reported to be anhydrous. Hence, the intermediate compound with acid chloride group would have reacted with any water present in the THF. Thus, these reactions would have converted the intermediate compound (refer to scheme 2-2) back into the drug, flufenamic acid.

Atomic force microscopy (AFM) images showed the high possibility for sedimentation and/or crystallisation of the drug on to the surface for most DHE and DE samples (Figure 2-13). This can be backed up with the initial burst release of more than 50% of the drug within day 1 since cleavage/hydrolysis of the drug from the monolayer is generally expected to be a slow process at a pH of 7.4. Thus, this study did not provide a suitable method to immobilise flufenamic acid and the results were inconclusive.

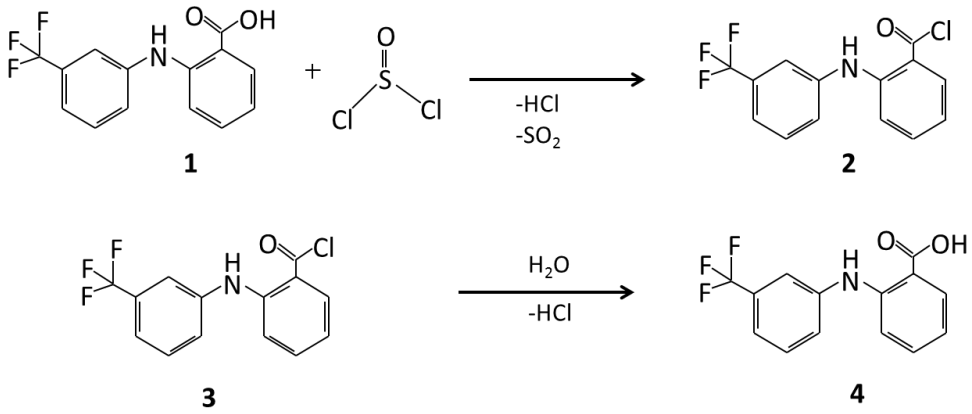

Scheme 2-2 Scheme of reactions on acid chloride esterification of flufenamic acid. Label description: Flufenamic acid reacting with thionyl chloride (1); reaction intermediate (2); reaction intermediate reacting with water (3); flufenamic acid (4).

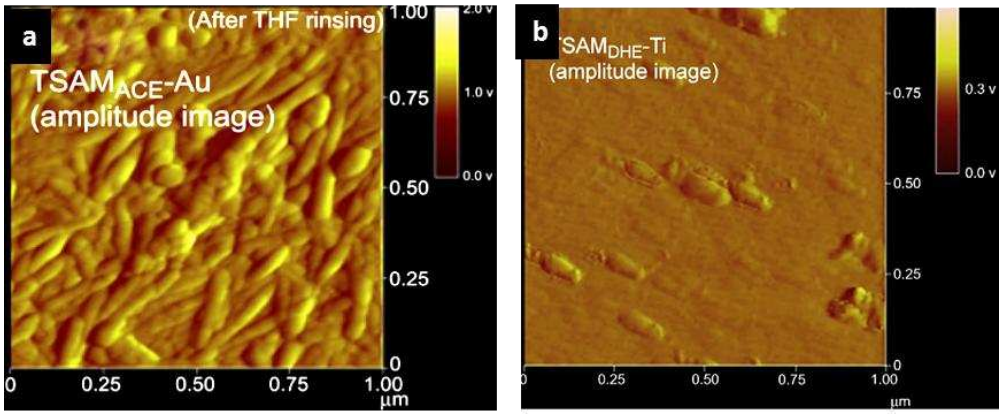

Figure 2-13 Atomic force microscope images of flufenamic acid functionalised on gold surface using acid chloride esterification (a) and flufenamic acid coated to a titanium surface by dry heat esterification method (b). Reproduced with kind permission from Elsevier [37].

Their later studies on immobilising an anti-cancer drug Paclitaxel™ on a cobalt-chromium metal surface with and without SAMs showed some interesting results [45,144]. Their method to bind Paclitaxel™ to SAM coated surfaces has a number of limitations. In their procedure, a microdrop method was used to drop the drug solution onto the cobalt-chromium surface. It was reported that from the 25 µg of drug placed on the surface (1 cm^2), only 25% of the drug was adsorbed to the surface and the rest washed away by solvent cleaning. Although a certain amount of the drug can be recovered by recycling, this method can be time-consuming and expensive. Also it should be noted that scaling up of this method will be difficult since coating drugs on implants with complex geometries using microdrop deposition would be challenging.

Furthermore, the drug adsorbed on the surface was observed to be crystallised. Their study on the delivery of Paclitaxel™ from the monolayers showed a sustained release; however, similar to their previous studies, crystals of Paclitaxel™ were formed. Crystallisation of drugs on an implant surface can potentially increase the surface roughness of the implant and may cause post-implant complications. Also due to crystallisation, controlling drug release from the implant surface will be problematic.

Torres et al. [54] reported the use of phosphonic acid monolayers to deliver an antibacterial drug from a hydroxyapatite surface to prevent bacterial infections and bio-film formation. Silver has been previously reported for its antibacterial activity [46]. In this study, phosphonic acid SAM coated surfaces were immersed in silver nitrate solution to functionalise the SAMs with silver. A significant reduction of bacterial adhesion onto the functionalised hydroxyapatite surface was observed. Apart from a therapeutic drug, functionalisation of a protein (RGD peptide) to phosphonate SAMs adsorbed on pure titanium and Ti6Al4V surfaces for osteoconductive surfaces was demonstrated by Schwartz et al. [152]. Raman et al. [153] used hydrophobic phosphonate SAMs to control the non-specific fibroblast cell adhesion and proteins on to stainless steel substrates. Using SAM patterning methods such as lithography, immobilisation of monolayers with proteins and cells to form patterned surfaces have also been explored [154].

2.6. Knowledge Gap

2.6.1. SLM

Titanium and its alloys including Ti6Al4V, Ti6Al4V ELI (extra low interstitial) and Ti6Al7Nb are commercially used to build implants for orthopaedic, dental and vascular applications due to their excellent corrosion resistance, mechanical properties, high strength-to-weight ratio and inertness [109,155]. A thin and stable passive titanium oxide (TiO_2) layer (3-10 nm range) is formed when the surface is exposed to ambient air or water and contributes to the chemical inertness of titanium and its alloys [156]. Due to the ability of Ti and its alloys to form this passive and stable oxide layer, it has wide application in harsh and corrosive environments [157]. The stability of

this surface oxide layer can be influenced by several factors including crystalline structure and thickness; however, surface chemistry plays a pivotal role [155].

In the SLM process, the powder material is melted and cooled rapidly. Hence, there is a high possibility for an SLM fabricated part to differ in its surface chemistry and microstructure compared to conventionally manufactured parts (e.g. those made by casting and forging). A selective remelting strategy proposed in the literature [93] may benefit the part to improve its density, surface morphology and mechanical property but at the same time, it may lead to varied surface chemistry and distribution of the alloying element within the part. When a high amount of heat is applied especially to an alloy (by remelting of the layers), the alloy may be superheated and will reach a high temperature. Precipitation of the alloyed elements is possible if the alloy remains at such high temperature for a long time. For example, it has been shown that segregation of Al can occur during the SLM of Ti6Al4V due to rapid melting and cooling of the alloy [158]. Such segregation of alloying elements can potentially alter the surface chemistry significantly by altering the surface oxide composition leading to surface heterogeneity.

Surface heterogeneity due to the impact of the laser can have a significant impact on biomedical applications. A biomaterial interacts with the biological environment at a bio-interface. Bio-interphases are affected by the nature of the biomaterials including its surface energy, surface chemistry, surface morphology and surface roughness [1,4,13]. Without a good understanding of the surface chemistry, the interaction of cells at the interfaces will be poorly understood.

Surface chemistry of a part mainly depends on the distribution of its alloying elements on the surface and the atmosphere to which the part is exposed to. Inclusion and discontinuity spots that arise due to surface heterogeneity may affect the biocompatibility [159]. For example, in the case of Ti6Al4V, the presence of aluminium or vanadium on the surface may form their corresponding oxides and reduce the stability of the surface oxide layer which can affect the cytocompatibility that may lead to cytotoxicity and poor cell

adhesion under in vivo conditions [3,132]. The presence of alloying elements on the implant surface can influence the dissolution of ions in to the biological environment. Clinical experience has shown the release of vanadium ions from implants made of Ti6Al4V to the body [160]. These metal ions interfere with cell differentiation and contribute to periprosthetic osteolysis by impairing osteogenesis [161]. Hence surface modification of Ti6Al4V components or the adoption of a different biocompatible material is required.

Although several surface modification techniques such as passivation, chemical etching, ion-implantation and chemical coatings are available to improve and modify the surface chemistry of an implant [1,4,117], the principle source of those surfaces is the manufacturing process. The knowledge on the surface chemistry of a SLM fabricated part and the impact of laser power on its surface chemistry is limited. Hence a study on the surface chemistry of SLM fabricated parts is central for a better understanding of its biocompatibility and the possible risk associated with the use of biomedical implants fabricated using SLM into the human body.

2.6.2. SAMs

Although a few studies have reported on the assembly of monolayers to rough and smooth surfaces, there is little literature that reports on the chemisorption and stability of phosphonic acid SAMs to highly porous and rough surfaces. As SAMs can serve as a localised drug delivery system, the use of SAMs to attach drugs to biomedical implants is gaining considerable interest. Although the delivery of drugs using phosphonic acid SAMs have been achieved by a few researchers, most of these drugs are either physisorbed or both physisorbed and covalently bound leading to a burst release. In situations where a sustained release is preferred, burst release can significantly affect the requirement. One-to-one chemical binding of a drug with a monolayer can control and prevent the initial burst release of the drug. Although the acid chloride esterification method used by Mani et al. [37] is inconclusive due to their exposure to atmospheric air, further optimisation of this method may potentially render the required binding of drugs to monolayers.

It may be difficult to functionalise SAMs with a drug using a micro-drop method where the geometry of the part is complex. Using the micro drop method in such cases may not render a homogenous coating. For example, the use of micro drop method to coat drugs to cardiovascular stenting applications will be highly complicated since their typical strut thickness is only 100 µm. Also, the use of this method for porous implants with complex internal and external geometries would be difficult. Hence a simple and efficient method to functionalise drugs to monolayers is required.

Most previous literature has discussed the coating methods, attachment, stability and release profile of the immobilised drug to SAMs. However, the knowledge on the activity of the drug upon its delivery from SAMs is limited. For example, instead of the drug, if the monolayer desorbs from the surface together with the drug, this will not produce the required activity. Hence it is important to study if the functionalised drug is active upon its release from the monolayer.

In addition to these current knowledge gaps, according to the best knowledge of the author, the use of phosphonic acid monolayers to functionalise SLM fabricated Ti6Al4V surfaces with therapeutic drugs has not been reported.

2.7. Summary

The selective laser melting process has been identified as one of the best routes to fabricate customised/patient-fitting biomedical devices. The versatility of phosphonic acid monolayers to form densely packed, well-ordered and highly stable SAMs on metal oxide surfaces makes them ideal for these biomedical applications. Delivery of drugs from monolayers attached to metal surfaces produced by various conventional manufacturing methods has previously been studied. However, to date, there have not been reports in the literature that has explored the possibility to attach monolayers to a SLM fabricated surface to the best of the author's knowledge. Hence research on integrating these two processes is required to address the knowledge gap and bridge these technologies to fabricate customised implants with drug delivery options.

3. RESEARCH HYPOTHESIS AND NOVELTY

3.1. Aim of the Research

To evaluate the potential to combine selective laser melting (SLM) to fabricate customised implants with surface modification using self-assembled monolayers (SAMs) for precise drug delivery.

3.2. Objectives

- To study the surface morphology and surface chemistry of Ti6Al4V components fabricated by SLM.
- To coat phosphonic acid SAMs onto SLM fabricated surfaces.
- To investigate the in vitro stability of SAMs on the SLM as-fabricated and mechanically polished surfaces.
- To develop an approach to functionalise the SAMs adsorbed on a SLM fabricated surface with therapeutically active substances.
- To determine the amount of drug coated and the stability (including oxidative exposure and in vitro) and biological activity of the immobilised drug molecule.

3.3. Research Novelty and Contribution to Existing Knowledge

This research presents a novel multi-disciplinary approach to fabricate and functionalise complex biomedical implants by integrating SLM with surface modification using SAMs for precise drug/protein delivery to improve mechanical and biological properties.

Although there is significant understanding of SLM process conditions and process parameters, there is very limited awareness of the surface chemistry of the SLM fabricated surfaces. By exploring the surface chemistry of a SLM fabricated Ti6Al4V surface and comparing it to a conventional surface, this research contributes to furthering the knowledge of this AM process. Currently there is no literature on the surface modification of SLM fabricated Ti6Al4V parts in terms of altering its surface chemistry using phosphonic acid SAMs to

deliver therapeutics on-site. This will be the first study according to the best knowledge of the author. The process-optimised acid chloride esterification reaction used in this study to immobilise therapeutic drugs to phosphonic acid SAMs will contribute to the knowledge available for functionalising SAMs with drugs. Previous studies on immobilisation of a drug to monolayers did not show the therapeutic activity of the released drug from the monolayers. In this thesis, the activity of the drug is examined.

4. RESEARCH METHODOLOGY

4.1. Summary of Experimental Procedure

Initially tracheobronchial stents (cylindrical meshes used to maintain airway patency in trachea and bronchi) were fabricated using SLM and surface modified using SAMs. Stents were successfully fabricated from 316L stainless steel (316L SS), one of the materials used commercially to produce stents. Although SLM was capable of fabricating stents of 300 µm strut thickness, the SLM-produced stents were rough due to partial sintering of particles to the struts. Electropolishing was performed to remove the sintered particles and mechanical testing was performed to determine the compressive strength of the SLM fabricated stents. Electropolishing yielded a relatively smooth surface, however, it removed nearly 30% of the material from the stent. On mechanical testing, the stents deformed plastically. From the results, it was identified that the SLM as-fabricated stents did not possess the required mechanical and surface properties and needed more post-processing than the conventionally produced stents using laser cutting. Also, coating of monolayers to this thin stent struts and characterisation of the stent struts using X-ray photoelectron spectroscopy (XPS) and surface wettability measurements were not straightforward. Hence, it was decided to perform research on the attachment of SAMs to the SLM fabricated cuboid surfaces and functionalise the SAMs attached to these surfaces using therapeutic agents. A detailed report on the fabrication and mechanical testing of tracheobronchial stents using SLM is annexed in appendix 1.

Later, an experiment was performed to surface modify SLM fabricated 316L SS cuboid samples using thiol monolayers. Consistent with previous literature on SAM modification of 316L SS surfaces, the adsorbed SAMs were not stable. Studies conducted on the available monolayers to modify metal oxide surfaces revealed phosphonic acid SAMs as one of the best candidates for the purpose. To examine this, cuboidal samples were fabricated in a SLM machine using three commonly used metallic biomaterials 316L SS, Ti6Al4V (titanium alloy) and L605 cobalt-chromium alloy. Surface modification of these as-

fabricated surfaces was performed using phosphonic acid monolayers. XPS characterisation confirmed the adsorption of SAMs to all three surfaces (Appendix 2). Since phosphonic acid SAMs showed the covalent attachment to all three metal oxide surfaces, it was decided that the use of all these three surfaces to address the aim was not essential. Also, studies on all three surfaces would increase the number of samples to be characterised and would be time consuming. Hence, to narrow down the research, one material was selected as the candidate member to address the aim.

Ti6Al4V, a grade 5 titanium alloy, is a material that can be processed relatively easily by SLM and is being researched extensively for biomedical applications [14,15,162]. Titanium and its alloys are ranked the best for corrosion resistance (due to its stable surface oxide layer), than cobalt, nickel titanium alloys and stainless steel [111]. It is also preferred for load bearing application due to its excellent strength-to-weight ratio compared to 316L SS and Co-Cr alloy. In addition to this, previous studies reported the successful adsorption of phosphonic acid SAMs to Ti6Al4V surfaces fabricated by conventional methods. Hence, Ti6Al4V was selected as the material for this research.

Figure 4-1 shows a schematic of the research methodology used in this study. To begin with, the surface chemistry of Ti6Al4V virgin powder and recycled powder (in an AM 250 SLM machine) was examined using XPS to determine any changes in the surface chemistry of the virgin powder. Since no significant change was observed, cuboid samples were then fabricated using the recycled Ti6Al4V in the AM 250 machine (previously SLM 250). The surface chemistry of the SLM as-fabricated (SLM-AF) and mechanically polished (SLM-MP) samples were studied and compared with a conventionally forged Ti6Al4V sample. The impact of laser power and selective laser re-melting on the surface chemistry of SLM fabricated samples was also studied.

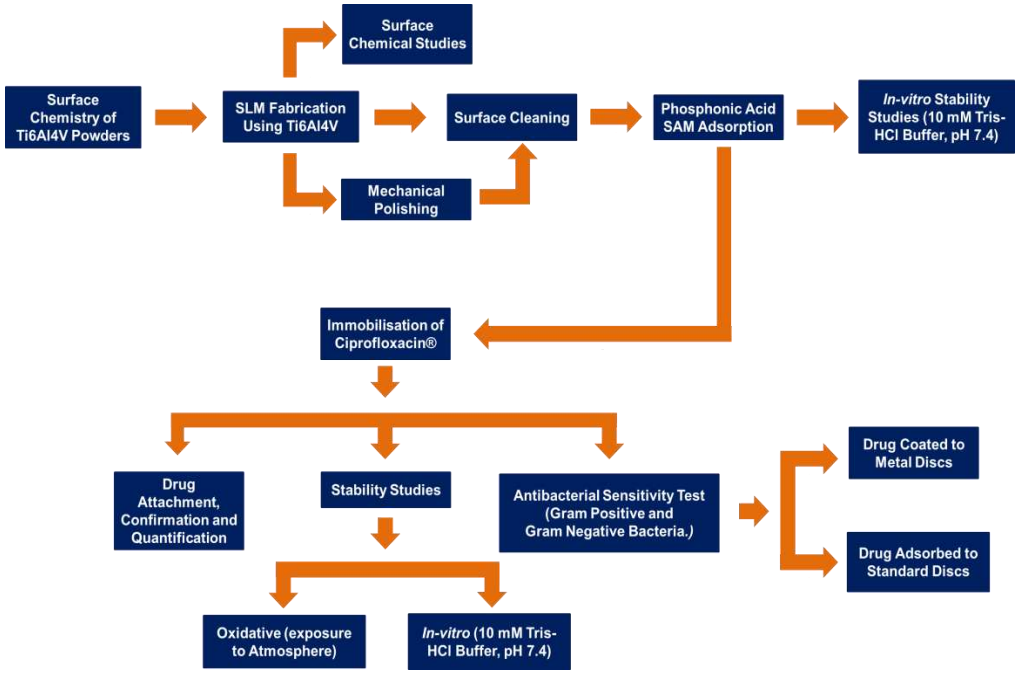

Figure 4-1 Schematic of the research methodology

A set of SLM fabricated samples were polished mechanically and surface cleaned to remove contaminants. Phosphonic acid SAMs were used to modify SLM fabricated Ti6Al4V parts due to their versatility and increased stability on metal oxide surfaces. Carboxylic terminated phosphonic acid SAMs were adsorbed to the SLM-AF and SLM-MP samples. In vitro stability of the carboxylic acid terminated SAMs on both SLM-AF and SLM-MP surfaces were investigated in Tris-HCl buffer solution of pH 7.4. On studying the in vitro stability, mechanically polished samples were used for drug attachment and other further studies. This is because, the electron counts for SLM-MP was better than SLM-AF. The presence of partially melted particles on the SLM-AF surface was observed to affect the number of electrons reaching the detector and thus reducing the signal.

Paracetamol was initially used as the model drug to functionalise the SAMs, followed later by Ciprofloxacin®. On successful attachment of Ciprofloxacin®, quantification of the drug immobilised, oxidative and in vitro stabilities, drug release profile and antibacterial activity of the immobilised drug were determined.

4.1.1. Materials

The materials and chemicals used during this research are tabulated in Table 4-1.

Table 4-1 List of materials/chemicals used.

Material/Chemical Name	**Chemical Formula**	**Supplier**	**Purity/ Grade**
Titanium alloy powder (Ti6Al4V)	-	LPW Technology Ltd., UK.	ASTM F136
Hot forged Ti6Al4V plate	-	TIMET UK Ltd., UK.	N/A
Silicon carbide grits	-	Buehler, UK.	N/A
Diamond pastes (6 µm and 1 µm)	-	Buehler, UK.	N/A
Extender solution	-	Buehler, UK.	N/A
Dichloromethane (DCM)	CH_2Cl_2	Sigma Aldrich, UK.	99.5%
Methanol	CH_3OH	Sigma Aldrich, UK.	99.8%
Ethanol	C_2H_5OH	Sigma Aldrich, UK.	> 99.5%
Hydrogen peroxide	H_2O_2	Fisher Scientific, UK	30%
Sulfuric acid	H_2SO_4	Sigma Aldrich, UK.	95 – 98%
Hydrochloric acid	HCl	Sigma Aldrich, UK.	37%
Sodium hydroxide	NaOH	Sigma Aldrich, UK.	≥ 98%
Thionyl Chloride	$SOCl_2$	Sigma Aldrich, UK.	≥ 99%
Tetrahydrofuran (THF)	C_4H_8O	Sigma Aldrich, UK.	≥ 99.9%
16-Phosphanohexadecanoic acid (16-PhDA)	$HOOC(CH_2)_{15}PO_2H$	Sigma Aldrich, UK.	97%
Octadecylphosphonic acid (ODPA)	$C_{18}H_{39}O_3P$	Sigma Aldrich, UK	97%
Tris(hydroxymethyl)aminomethane	$NH_2C(CH_2OH)_3$	Sigma Aldrich, UK	≥ 99.8%
Paracetamol	$C_8H_9NO_2$	Sigma Aldrich, UK.	≥ 99%
Ciprofloxacin®	$C_{17}H_{18}FN_3O_3$	Sigma Aldrich, UK.	≥ 98%
Carbon film/tape	-	Agar Scientific, UK.	N/A
Muller-Hinton Agar	-	Sigma Aldrich, UK.	For micro-biology
Sterile filter paper disc 10 mm diameter	-	Sigma Aldrich, UK.	Micro-biology

4.1.2. Equipment

4.1.2.1. *Selective Laser Melting*

Ti6Al4V components were fabricated in a Renishaw AM 250. The machine was equipped with a fibre modulated pulse laser with a maximum power of 200 W and wavelength (λ) of 1070 nm. The AM 250 machine consists of a hopper, a wiper, an elevator that lowers the substrate to adjust the layer thickness and a lens that focuses the laser (200 W maximum) to the build area (250 x 250 x 300 mm). Before SLM, the Ti6Al4V powder from which the part was to be fabricated was spread over the build platform from the hopper to a pre-defined layer thickness. After the layer had been spread, the laser beam scanned and fused the powder in the areas specified by the layer of the CAD file.

4.1.2.2. Malvern Mastersizer

Particle size distributions (PSDs) were measured using a Malvern Mastersizer 3000 (Malvern, Worchestershire, UK) by adopting a dry dispersion method. This equipment works on the principle of laser diffraction. Laser diffraction measures PSDs by measuring the angular variation in the intensity of light scattered as a laser beam passes through a dispensed particulate sample. This angular scattering intensity data is then analysed to calculate the size of the particles responsible for creating the scattering pattern. To measure the PSD, the Ti6Al4V powder feed rate was set to 25% and the dispersion pressure was 1 bar. PSDs were obtained for five sets of sample dispersion and averaged. Built-in software was used to calculate the PSDs.

4.1.2.3. Scanning Electron Microscope

A Philips (PW 6800/70) scanning electron microscope was used to obtain the surface morphology of the SLM fabricated Ti6Al4V surface. The scanning electron microscope (SEM) was operated at a voltage of 20 kV, spot size of 10 nm and morphologies of SLM-fabricated surfaces were obtained at various magnifications such as 100x, 250x and 500x.

4.1.2.4. Surface Profilometer

Surface roughness (Ra) patterns of the SLM as-fabricated samples and mechanically polished samples were obtained using an Alicona InfiniteFocus® optical 3D measurement device. The Ra value was calculated by averaging the values obtained for five different samples from 175 μm^2 of each sample.

4.1.2.5. Contact Angle Goniometer

The surface wettability of the sample was characterised using contact angle goniometry. Static water contact angle measurements were performed using an OCA 20 contact angle goniometer (DataPhysics, Filderstadt, Germany) at ambient temperature. A drop volume of 5 µL deionised water (pH ~ 6.8) was placed on an arbitrary spot of the surface and allowed to settle for five seconds. Images were acquired at standard atmospheric temperature and pressure using the inbuilt software and the contact angles were measured. The static water contact angles have been reported in this work as a mean ± standard error of the mean of three distinct spots on five different samples.

4.1.2.6. X-ray photoelectron spectroscopy

The surface chemistry of the samples was examined using X-ray photoelectron spectroscopy (XPS), also called electron spectroscopy for chemical analysis (ESCA). An XPS is built with an X-ray source to produce photoelectrons, a sample stage to place the sample, a lens, an ion gun to etch the sample, a detector to collect the electrons and an analyser to produce the result [163]. XPS analysis was performed at a high vacuum pressure of 10^{-8} Pa so that the electrons can travel to the detector. Monochromators were used to increase the energy resolution and to eliminate satellite signals from $K\alpha_3$ and $K\alpha_4$ X-rays. In XPS, the sample is irradiated with soft X-rays. Kinetic energy (E_k) of the emitted electrons due to irradiation is measured. The binding energy (E_B) of the photoelectrons can be calculated using the equation $\mathbf{E_B = h\nu - Ek - \varphi}$, where, hν is the energy of the X-ray photon and φ is the spectrometer work function. The most commonly used X-ray sources are Al Kα (1486.6 eV) and Mg Kα (1253.6 eV). XPS can determine the surface chemistry of a sample to a

depth of the first 10 nm and is considered as a vital tool for surface chemical analysis [164,165].

In this research, a Thermo Scientific K-Alpha XPS was used to obtain the surface chemistry of the Ti6Al4V surface. Depth profiling was performed to study the elemental composition and the oxide layer thickness of the SLM fabricated Ti6Al4V surface. Depth profiles were obtained by sputtering the specimen at a rate of approximately 1.35 $Å s^{-1}$ (for titanium) using an argon ion gun. The probing spot size used to obtain the measurement was 400 µm. Aluminium (Al) Kα monochromated radiation at 1486.6 eV was used and photoelectrons were collected at a take-off angle of 90°. Survey spectra were collected at a pass energy of 100 eV in a constant energy analyser mode. High resolution spectra were obtained at a pass energy of 20 eV. Peak deconvolution was performed using Gaussian-Lorentzian curves and was used to investigate the different chemical states. A built-in Thermo Avantage data system was used for data acquisition and processing. The national institute of standards and technology (NIST) database and previously reported literature were used to identify the unknown spectral lines. The thickness of the oxide film was estimated by two methods. In method 1, the thickness was calculated from the depth at which the oxygen content decreased to half of its maximum value during depth profiling. In method 2, the thickness was estimated from the depth at which the major alloying element Ti intersects the O in the depth profile [166].

The possible errors in the atomic percentage due to peak fitting uncertainties were calculated using CasaXPS software. The software calculates the standard deviation of a peak using a Monte Carlo method [167]. During this calculation, fitting trials are conducted in which synthetic noise is added to the measured data, followed by a peak fit. This analysis was performed for all detected peaks in a survey spectrum. The standard deviation of the fitted areas is used as the area error. Fractional area error was calculated as the ratio between the actual area of the peak to the area error. This fractional area error was multiplied with the atomic percentage of detected elements to obtain the final error. The estimated error percentage was between 0.02 and 0.11 for

different elements (i.e. 2 – 11%). Henss et al. [168] also accounted the XPS quantification error as ± 10%. Thus the instrumental error due to calibration for this study was taken as ± 10% in addition to the reported mean ± standard error of the mean.

4.1.2.7. Fourier Transform Infrared Spectroscopy

Perkin Elmer Spectrum 100 FTIR was used to characterise the Ciprofloxacin® coated on the SLM fabricated Ti6Al4V substrates (Figure 4-2). Initially, the crystal area of the Spectrum 100 FTIR was cleaned with soft tissue dipped with ethanol. The FTIR was operated under Attenuated Total Reflectance (ATR) mode. A background scan was collected and the cleanliness of the diamond stage was ensured. The Ti6Al4V substrate whose surface is to be characterised is placed on the diamond stage. Once the sample was placed, a pressure arm in the instrument was screwed down on to the sample placed over the prism (diamond) stage. The pressure arm was locked into the precise position above the diamond crystal. The pressure arm applies a small amount of force (~ 80 N) to the sample, pushing the sample on to the diamond surface using the pressure arm. This pressure ensures a good contact between the sample surface and the diamond stage, and prevents the sample from moving during the characterisation. A force gauge is present in the instrument to warn when too much of pressure is applied to the stage. A control Ti6Al4Vsurface without any drug coating was characterised and used as background for the drug coated samples. All samples were analysed from 4000 cm^{-1} to 380 cm-1 with a spectral resolution of 4 cm^{-1}.

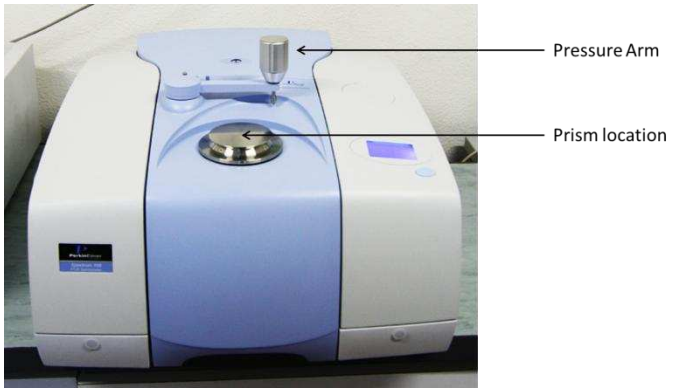

Figure 4-2 Spectrum 100 Fourier Transform Infrared spectrometer fitted with a pressure arm (with the kind permission from Perkin Elmer).

4.1.2.8. UV-Vis spectrophotometers

UV-Vis spectrophotometers are used to measure the absorbance of UV or visible light by a sample either at a single wavelength or perform a scan over a range in the spectrum. UV-Vis spectroscopy is the measurement of light when it passes through a sample and its principle is based on the ability of a molecule to absorb ultraviolet and visible light. This technique can be used both quantitatively and qualitatively. A schematic diagram of a UV-visible spectrometer is shown above in Figure 4-3.

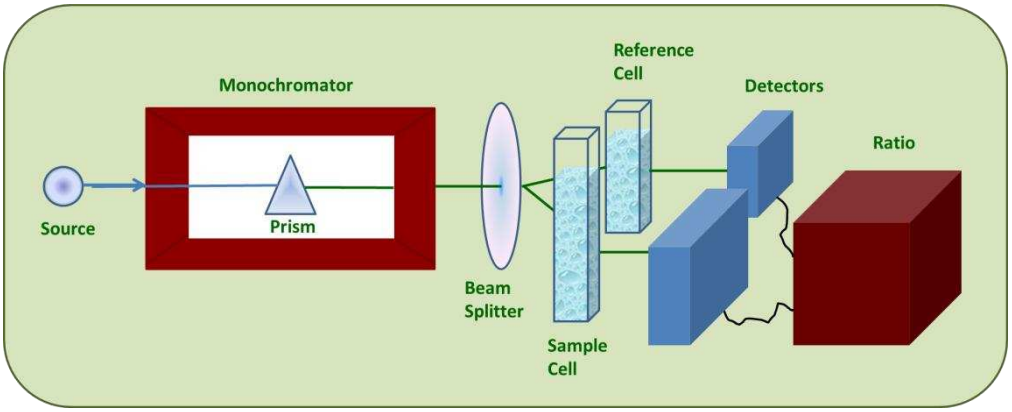

Figure 4-3 Schematic of a UV-Visual Spectrophotometer

The UV region ranges from 190 to 400 nm and the visible region from 400 to 800 nm. The light source (a combination of tungsten/halogen and deuterium lamps) provides the visible and near ultraviolet radiation covering the 200 – 800 nm region. The output from the light source is focused onto the diffraction grating which splits the incoming light into its component colours of different wavelengths, like a prism (shown above in Figure 4-3) but more efficiently.

For liquids, the sample is held in an optically flat, transparent container called a cell or cuvette. The reference cell or cuvette contains the solvent/solution in which the sample is dissolved and this is commonly referred to as the blank. The sample cell contains the solution whose concentration is to be measured. For each wavelength the intensity of light passing through both a reference cell (I_o) and the sample cell (I) is measured. If I is less than I_o, then the sample has absorbed some of the light. The absorbance (A) of the sample is related to I and I_o according to the following equation:

$$\mathbf{A = Log_{10}\ l_0/l}$$

The detector converts the incoming light into a current, the higher the current the greater the intensity. Then the absorbance is plotted against wavelength (nm) in the UV and visible section of the electromagnetic spectrum.

According to Beer's law, absorption is proportional to the number of absorbing molecules and Lambert's law tells us that the fraction of radiation absorbed is independent of the intensity of the radiation. Combining these two laws,

$$\boldsymbol{A = \varepsilon c l}$$

where 'A' is the absorbance, 'ε' is the molar absorptivity and expressed in units L mol-1 cm^{-1}, 'C' is the concentration of the sample (compound) and expressed as mol L^{-1} and 'l' is length of cell and expressed in units cm. If the absorbance of a series of sample solutions of known concentrations are measured and plotted against their corresponding concentrations, the plot of absorbance versus concentration should be linear if the Beer-Lambert Law is obeyed. This graph is known as a calibration graph. A calibration graph can be used to determine the concentration of an unknown sample solution by measuring its absorbance.

4.1.3. Methods

4.1.3.1. CAD Model

Sample parts with dimensions of 10 mm x 10 mm x 3 mm were designed using Magics 14.1 (Materialise) software and saved in STL file format. This design was then replicated to fabricate the required number of samples. Figure 4-4 represents the build platform with replicated models (in red) and the meander laser scan strategy used (right-hand side). For antibacterial susceptibility testing, cuboid samples of 25 x 30 x 2 mm were designed using Magics.

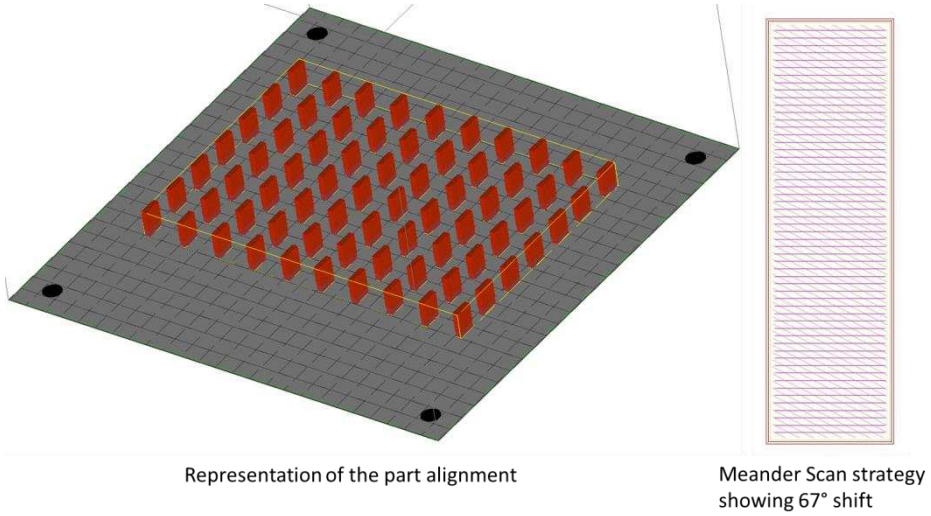

Figure 4-4 Representation of sample models aligned in the build platform and the Meander scan strategy used for fabrication (right hand corner)

4.1.3.2. *Sample Fabrication*

Parts were fabricated using a SLM machine (AM 250). Previously optimised SLM process parameters used for the study are tabulated in Table 4-2. A multi-directional meander scan strategy (Figure 4-3) was used where the laser scan direction was rotated by 67° for each layer to reduce the residual stress. The components were built on a Ti6Al4V metal substrate preheated to 80 °C. The build chamber was filled with argon gas to maintain an inert atmosphere. The temperature of the build chamber during the process was measured to be 34 – 36 °C. Parts were fabricated with skin scan (re-melting of the top surface using laser to improve the surface quality) for a better surface quality. However, to study the effect of skin scan on the surface chemistry, parts without skin scan were also fabricated. Apart from this, all other parameters were constant. The SLM fabricated samples were removed from the substrate upon fabrication.

Table 4-2 Summarised SLM Process Parameters

Laser Power P (W)	200
Hatch Spacing (µm)	100
Point Distance (µm)	50
Exposure Time (µs)	220
Layer Thickness (µm)	50
Scan Strategy	Meander
Build Plate Temperature (°C)	80

4.1.3.3. Sample Preparation

The SLM fabricated samples were sonicated in dichloromethane (DCM), methanol, ethanol and deionised water for 10 minutes each to remove loosely bound Ti6Al4V particles from the sample surface and contaminants that might be on the surface. The substrates were then dried using compressed air. The cuboid samples with 10 mm x 10 mm x 3 mm dimensions were used for the surface chemical, surface modification and functionalisation studies. For antibacterial susceptibility testing, discs of 8 mm diameter were laser cut from the cuboid samples (25 mm x 30 mm x 2 mm) fabricated by SLM.

4.1.3.4. Mechanical Polishing

The rinsed and dried samples were mechanically polished on only one side (10 mm x 10 mm) using a series of silicon carbide grits (P200, P400, P600, P800 and P1200) for 5 minutes each. These samples were then polished using diamond paste of 6 µm and 1 µm for 3 minutes each. Mechanical polishing was performed to make the surface smooth for characterisation purposes and to study the surface chemistry of a mechanically polished SLM fabricated surface. It should be noted that the cuboid samples were hand held while polishing and not clamped (difficult to hold the sample in place while polishing) or mounted using any resins. This is because the use of resins may affect the surface chemistry of the sample and may lead to contamination. The polishing fluid may also contribute to a certain level of contamination to the surface. This is cleaned using solvents and acids as described in the sample cleaning section below. Also, removal of the sample from the mount can be tedious. The discs for the antibacterial susceptibility testing were also polished in the same manner i.e. hand held. Samples polished using the above mentioned procedure rendered the surface roughness of 590 ± 13.5 nm.

4.1.3.5. Surface Cleaning

The purity and cleanliness of a sample's surface plays an important role in the assembly of SAMs since the assembly of monolayers are affected by the presence of contaminants [58,131]. In order to attain well-ordered monolayers, freshly prepared surfaces are recommended. Hence cleaning of SLM fabricated

samples was performed to ensure the cleanliness and purity of the surfaces before assembling monolayers.

Several cleaning techniques have been reported in the literature for assembling monolayers. A mixture of solution was prepared with concentrated sulfuric acid, hydrogen peroxide (30%) and water in the ratio of 1:1:5. Sulfuric acid was added to water followed by hydrogen peroxide. Addition of water or hydrogen peroxide to Sulfuric acid is exothermic and the resultant heat may increase the sample temperature above 100 °C. Hence, care should be taken. The samples were immersed in this solution for 15 minutes to remove any surface contaminants. The samples were then rinsed in deionised water for 30 minutes twice to remove any residues of the chemical mixture. The samples cleaned using this technique rendered a highly wettable surface (21° ± 0.9°) compared to solvent cleaning mentioned in the sample preparation section. Hence, this method was used throughout the study.

4.1.3.6. Preparation and adsorption of SAMs

Two types of phosphonic acid SAMs including a carboxylic acid terminated 16-phosphanohexadecanoic acid (16-PhDA; SAMs) and a methyl terminated octadecylphosphonic acid (ODPA) SAMs were used. 1mmols of 16-PhDA and ODPA SAMs were prepared separately in dry THF and coated on the Ti6Al4V surface using a solution immersion deposition method previously reported [56]. Briefly, the cleaned samples were rinsed with THF and immersed in the SAM solutions immediately. After 24 hours, the samples were removed from the THF and the residual SAM solution on the surfaces was allowed to evaporate in air. The samples were then transferred to an oven at 120 °C without rinsing. After 24 hours, the samples were removed from the oven and allowed to cool at room temperature. Finally, the samples were sonicated in THF and deionised water for 1 minute each to remove any physisorbed SAMs.

4.1.3.7. Functionalisation of SAMs with Ciprofloxacin®

Both 16-PhDA and ODPA coated SAMs were functionalised with Ciprofloxacin® separately to avoid cross contamination. As ODPA has a methyl terminal group, Ciprofloxacin® cannot be attached to the terminal end

of these monolayers whereas 16-PhDA has a carboxylic group in its terminal end that can be functionalised. Hence, the ODPA coated surfaces were used as a control sample to prove the surface reaction of Ciprofloxacin®. The apparatus include a round bottomed flask (RBF) and a reflux condenser with a constant flow of nitrogen gas into the RBF to perform the reaction under an inert atmosphere. The apparatus was dried using a flame/heat gun to avoid the presence of moisture. A sonicator was used to agitate the sample. The reaction steps that followed to coat and functionalise the 16-PhDA SAMs with Ciprofloxacin® are shown in Scheme 4-1.

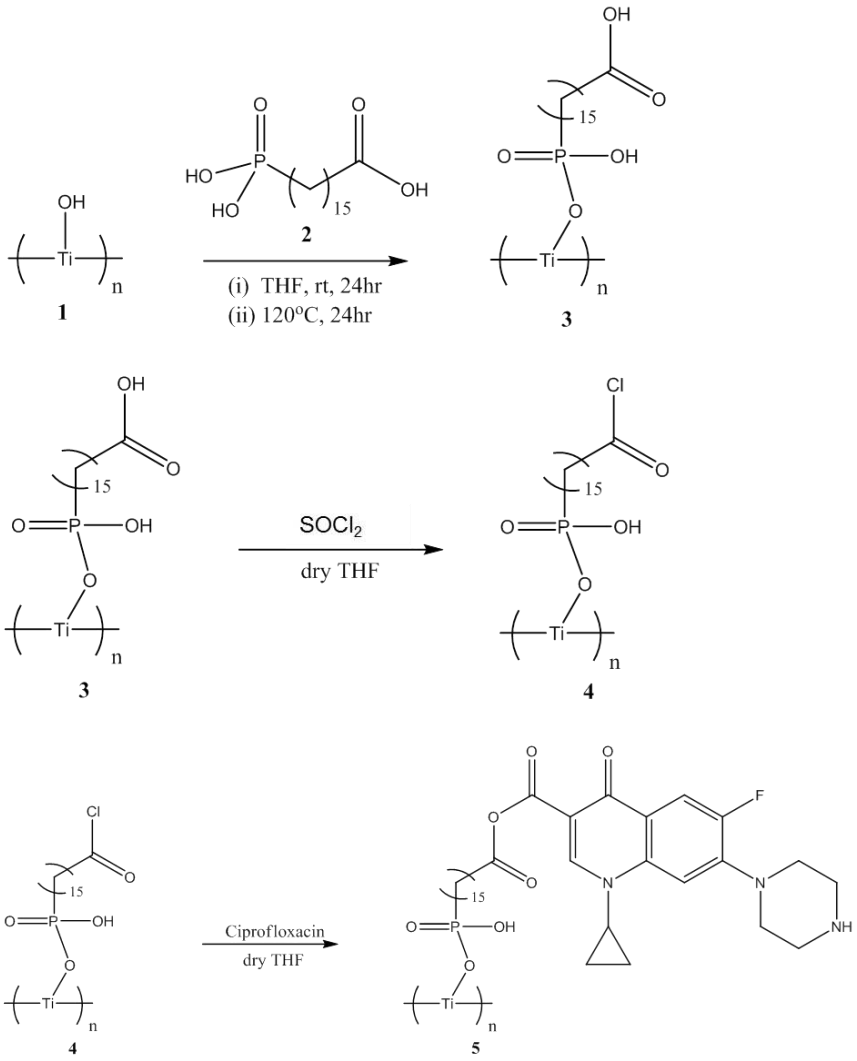

Scheme 4-1 General scheme of reactions to coat 16-PhDA monolayers to Ti6Al4V surface and to functionalise the monolayers with Ciprofloxacin®. Label description: Hydroxylated titanium surface (1), 16-Phosphanohexadecanoic acid (2), SAMs adsorbed on titanium surface (3), reaction intermediate formed as a result of acid chloride esterification (4) and Ciprofloxacin® immobilised to SAMs.

Firstly, the 16-PhDA SAM coated Ti6Al4V surfaces were transferred to the RBF with the SAM coated surface facing upwards. 3 mM of thionyl chloride ($SOCl_2$) in anhydrous THF was added to the RBF and the apparatus was sonicated for an hour. Care was taken to ensure that the solution covered the samples to obtain a uniform reaction. After one hour, the solution in the RBF was syringed out and the Ti6Al4V surfaces were sonicated thrice for 3 minutes by adding an excess of anhydrous THF to the RBF each time. After this step, 10 mM of Ciprofloxacin® in anhydrous THF was added to the RBF and sonicated for an hour. Finally, the Ciprofloxacin® solution was syringed out and the samples were sonicated with an excess of anhydrous THF and deionised water (twice for 2 minutes each). The same procedure was followed to coat Ciprofloxacin® to ODPA SAM coated Ti6Al4V surfaces.

Reaction Mechanism

The reaction scheme in Scheme 4-1 shows the binding of Ciprofloxacin® to the SAMs through its carboxylic end. Azema et al. [169], Cormier et al. [170] and Sharma et al. [171] reported the reaction of Ciprofloxacin® with acyl chlorides. In all these reported procedures, the reaction mainly occurred at the amine group of the Ciprofloxacin® rather than the carboxylic group to afford the corresponding amide. This was due to the fact that during all of these reported reactions a base, triethylamine (R:Et_3N), was used. For the synthesis of amide from acid chlorides via Schotten-Baumann reaction, a base is essential. This is because the formation of amides from acid chlorides and amines is accompanied by the production of one equivalent of HCl. This HCl should be neutralised by a base (such as NaOH and triethylamine0 for the reaction to proceed further. Thus, by using a base, the reaction can be controlled to occur through the amine group.

Anions (RCO_2^-) are better nucleophiles than a neutral nucleophile (-NH-) [172]. According to the reaction mechanism proposed in this study, the anions will attack the carbonyl group leading to the formation of Cl^- and H^+. These ions will protonate the amine group of Ciprofloxacin®. As a result of this protonation, the amine group will acquire a positive charge and become unreactive. During this attack, the acid will protonate the amine in

Ciprofloxacin® since carboxylate is a poor electrophile and the ammonium ion is not nucleophilic. Hence the reaction between the acyl chloride and the drug, Ciprofloxacin® is most likely to occur through the carboxylic group and lead to the formation of acid anhydride. If the same reaction is considered in the presence of a base, the acyl chloride will react with the amine, since the HCl produced during the reaction is neutralised by the base. This will then lead to the formation of amide rather than acid anhydride.

4.1.3.8. Stability Studies

The stability of the anti-bacterial drug under oxidative exposure and in vitro conditions was studied for 16-PhDA SAM coated surfaces immobilised with Ciprofloxacin®.

a) Oxidative Condition

Oxidative stability was determined by exposing the Ciprofloxacin® coated Ti6Al4V surfaces to ambient laboratory conditions for 7, 14, 28 and 42 days following a previously reported procedure [58]. After oxidative exposure, the samples were rinsed in de-ionised water for 1 minute and dried using compressed air before characterisation. A total of three samples were used to study the stability at each time interval using an XPS and static water contact angle goniometry. Survey spectra and high resolution spectra for C 1s, O 1s, N 1s and F 1s were collected using an XPS for all samples and the relative atomic percentages were averaged. Static contact angles obtained for each sample were averaged.

b) In vitro Condition

In vitro stability of the drug attached to 16-PhDA SAM coated surfaces was investigated by immersing each sample in 5 mL of 10 mM Tris-HCl buffer solution [Tris-HCl solution was prepared by dissolving 1.214 g Tris(hydroxymethyl)aminomethane in 900 mL of deionised water, adjusting the pH to 7.4 and making-up the final volume to 1L] and incubated at 37 °C for 42 days. The immersed samples were removed from the buffer solution at 7, 14, 28 and 42 day time intervals. The surfaces were rinsed for 1 minute with deionised water and dried using compressed air before characterisation using

XPS and static-contact angle goniometry. Three samples were used for characterisation from each time interval and the obtained results were averaged. Similar to the oxidative study, survey and high resolution spectra were collected for all the samples in each time interval.

4.1.3.9. Drug quantification

It should be noted that the amount of drug coated to the SAM modified Ti6Al4V surfaces was not calculated based on the difference in the concentration of the drug (in reaction mixture) before and after functionalisation. This was mainly because the amount of drug functionalised to the Ti6Al4V surfaces would be expected in nano-grams. Some amount of drug may be physisorbed to the surface. Thus, drug quantification by this method would affect the result. Hence, the total amount of Ciprofloxacin® functionalised onto SAM coated Ti6Al4V metal surfaces was quantified using a base hydrolysis method reported previously [37].

The drug coated samples (n=5) were immersed in a 10 mL of 10 mM NaOH solution (pH ~ 9) and incubated at 37°C. The immersion time interval to hydrolyse nearly all drug molecules was previously optimised by immersing the samples for 1 and 2 week time intervals. When characterised using XPS, after 1 week, a small amount of drug was observed on the Ti6Al4V surface whereas after 2 weeks of immersion, no drug was observed. Hence the 2 week time interval was used. The drug eluted solution was adjusted to pH 7.4 using 1 M HCl. A standard stock solution of Ciprofloxacin® (1 mg/mL) was prepared in 10 mM NaOH buffer solution of pH ~ 7.4. Working solutions including 1 ng/mL, 10 ng/mL, 50 ng/mL, 100 ng/mL, 250 ng/mL, 500 ng/mL and 1 µg/mL were prepared with pH ~ 7.4 by diluting the stock solution with the 10 mM NaOH.

Using a PerkinElmer LAMBDA 35 UV-Visual spectrophotometer (UV-Vis), the drug dispersed solution was scanned between the wavelengths of 200 to 500 nm. The maximum absorbance value obtained in the UV spectra (λ_{max}) was 272 nm (Figure 4-5) and is consistent with the previously reported literature [173–176]. Shoulders were also observed at 217 nm and 325 nm, close to the theoretical values of 222 nm and 320 nm [177]. The absorbance

peak in the figure 4-5 correlates to the transition of n/π electrons to the π* excited state. The shoulder towards the higher binding energy is not a double peak. From the relative absorbance, a calibration curve was plotted for the working solutions (1 ng/mL – 1 µg/mL of Ciprofloxacin® in 10 mM NaOH of pH ~ 7.4).

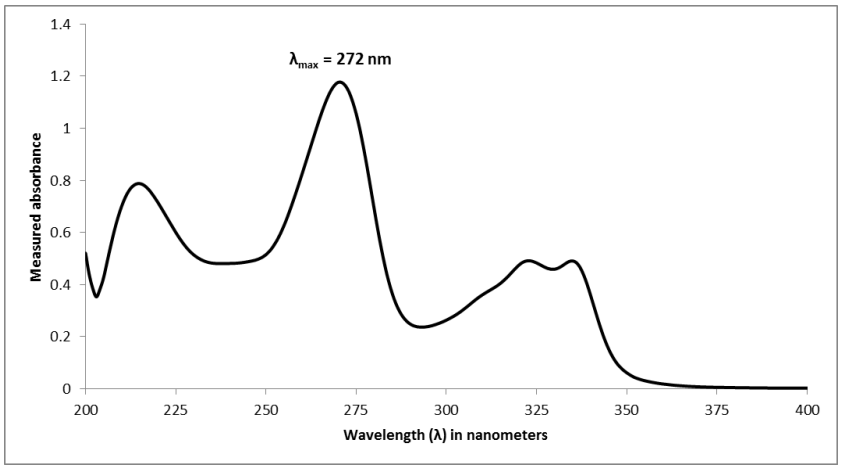

Figure 4-5 Maximum absorbance observed for Ciprofloxacin®

The calibration plot was linear as shown in Figure 4-6 and obeyed Beer-Lambert's law. The equation of the line will be Y = Mx + C, where Y is the absorbance at a given wavelength, M is the slope, x is the concentration and C is the intercept. Substituting the absorbance value of the unknown concentration in this equation will give the concentration. By using this concentration, the total amount of drug was quantified.

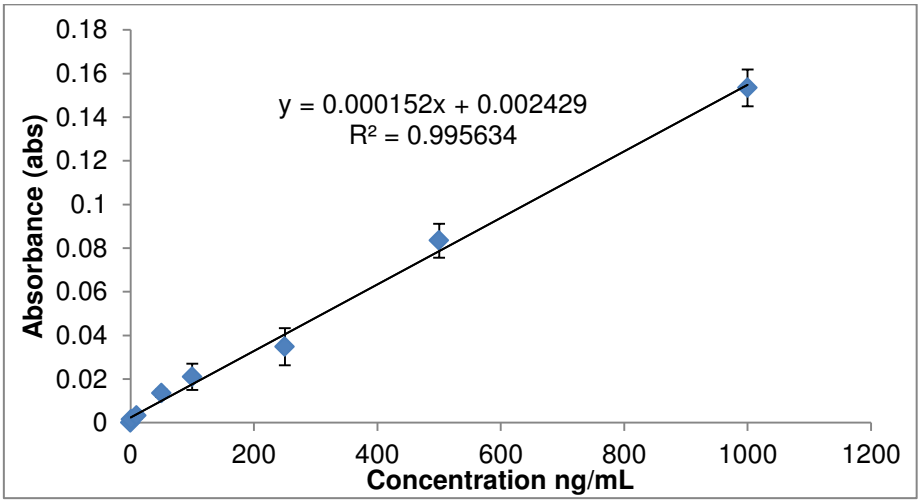

Figure 4-6 Calibration Graph for UV-Vis spectrophotometer to determine the unknown concentration for the drug quantification experiment.

4.1.3.10. Drug elution studies

Ciprofloxacin® coated Ti6Al4V samples (n=3 for each time interval) were immersed in 5 mL of 10 mM Tris-HCl buffer solution (pH ~ 7.4) and incubated at 37 °C for 7, 14, 28 and 42 weeks. Samples were taken out at these predetermined time intervals. A standard stock solution of Ciprofloxacin (1 mg/mL) was prepared in Tris-HCl buffer solution of pH ~ 7.4. Working solutions including 1 ng/mL, 10 ng/mL, 50 ng/mL, 100 ng/mL, 250 ng/mL, 500 ng/mL and 1 µg/mL were prepared by diluting the stock solution with the Tris-HCl buffer.

A calibration curve was plotted (absorbance versus concentration) by measuring the absorbance values for these standard working solutions (1 ng/mL, 10 ng/mL, 100 ng/mL, 250 ng/mL, 500 ng/mL and 1 µg/mL of Ciprofloxacin® in 10 mM NaOH of pH ~ 7.4) at the maximum absorbance of 272 nm. The Ciprofloxacin® concentration in the buffer solution was then calculated by substituting the absorbance of the unknown concentration in the obtained equation (Figure 4-7).

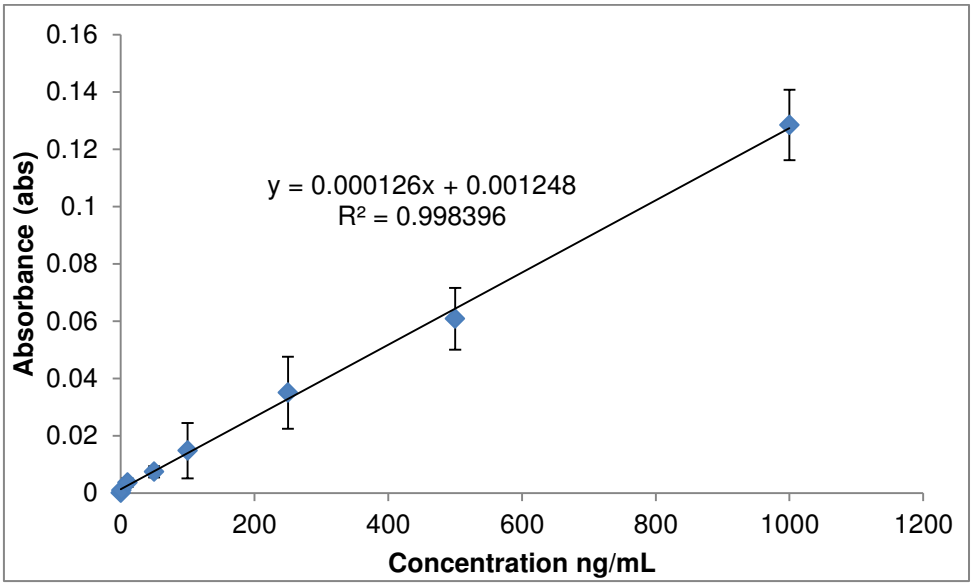

Figure 4-7 Calibration Graph for UV-Vis spectrophotometer to determine unknown concentration for the drug elution experiment.

4.1.3.11. Antibacterial susceptibility test

Infections associated with implants are mainly due to microbial contamination. Some of the most common organisms causing infections are Staphylococcus

aureus, Staphylococcus epidermidis Pseudomonas aeruginosa and Escherichia coli [1,178]. Ciprofloxacin®, being a broad spectrum antibiotic, will inhibit the growth of the majority of the both Gram positive (G+) and Gram negative bacteria (G-). G+ bacteria are primitive cell organisms that lack a membrane-bound nucleus. G- bacteria have well-organised cell organelles enclosed within cell membranes. Hence in this study, the antibacterial susceptibility test was tested against a G+ bacterium, S. aureus (ATCC 25923) and a G- bacterium, E. coli (ATCC 25922). The antibacterial susceptibility tests were performed to qualitatively investigate whether the released Ciprofloxacin® had retained its active form upon its release and produced a therapeutic effect. It should be noted that this study does not aim to quantify the drug concentration by this test or study the minimum inhibitory concentration (MIC) for the bacteria.

a) Test-1

In test-1, Ciprofloxacin® was functionalised to SAM-coated SLM-fabricated and mechanically polished Ti6Al4V discs of 8 mm diameter using the procedure for functionalisation mentioned in (4.1.3.7). Among the four discs used for each plate, two were standard filter paper discs and the other two were metal discs. Of these four discs one of each metal and the standard disc served as control with no drug on it. However, they were dipped in ethanol and dried at 80 °C prior to placing them on the inoculated agar plate. Among the other two discs, the standard control filter paper disc was coated with approximately 1 ml of 1 mmols (approximately 330 µg/mL) Ciprofloxacin® in ethanol. The remaining metal disc was coated with Ciprofloxacin® using previously mentioned procedure in this thesis (4.1.3.7).

Sub-cultures of S. aureus and E. coli were prepared 24 hours prior to inoculating to the Mueller-Hinton agar plate. Test specimens/discs were placed on the inoculated plates as shown in Figure 4-8. The plates inoculated with S. aureus were incubated at 30 °C and the plates inoculated with E. coli were incubated at 37.5 °C since they are the optimum growth temperature for the corresponding bacteria [179]. The plates (five for each bacterium) were examined after 24 hours and zones of inhibitions were measured using a calliper.

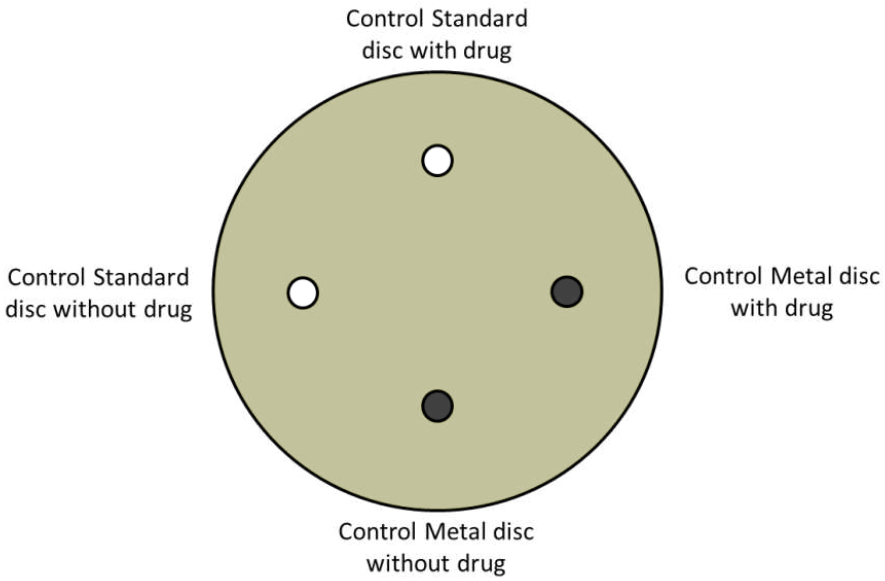

Figure 4-8 Schematic representation of test specimens placed on a culture plate

b) Test-2

Antibacterial sensitivity of the Ciprofloxacin® released to the Tris-HCl buffer solution was tested against S. aureus (ATCC 25923) and E. coli (ATCC 25922). Drug coated Ti6Al4V cuboid specimens were immersed in 5 ml of Tris-HCl buffer solution for 7, 14, 28 and 42 days. After these time intervals the specimens were taken out and the drug eluted buffer solution was used to determine the sensitivity of the eluted drug. 1 ml of the drug eluted Tris-HCl buffer solution was syringed out and added drop-by-drop to a standard filter paper disc. The excess solution was evaporated by drying the specimen in an oven operating at 80 °C for an hour. A similar procedure was followed to adsorb the Ciprofloxacin® eluted to the Tris-HCl buffer at different time intervals to the standard discs. In this study, 3 control discs were used. One was immersed in ethanol and dried and the other was immersed in Tris-HCl buffer and dried. The third control disc was coated with 1 ml of 1 mM (approximately 330 µg/mL) Ciprofloxacin® in ethanol. After drying, the filter paper disks impregnated with Ciprofloxacin® and the control discs were placed on the agar plate inoculated with the test bacteria (as shown in Figure 4-9) to test their susceptibility. Since the study is qualitative, the author did not aim to quantify the amount of drug present in the discs. The susceptibility test with these discs was performed using the procedure described in Test-1.

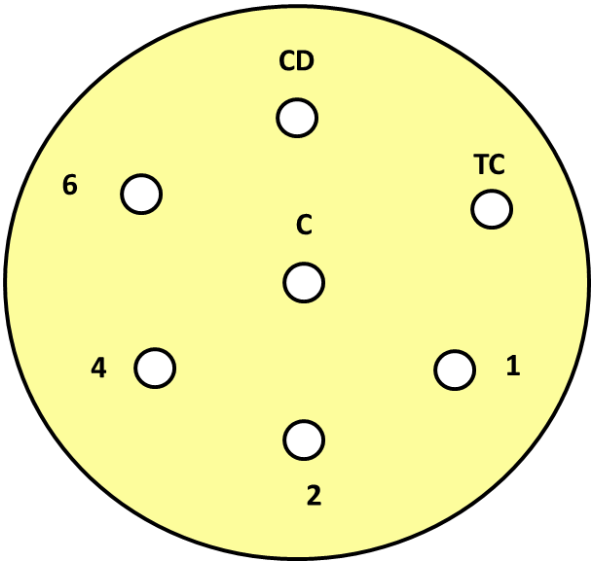

Figure 4-9 Schematic representation of test specimens placed on a culture plate. Label description: C- control disc with no drug; CD – control with drug on; TC: Control disc coated with Tris-HCl buffer; 1, 2, 4, 6 – immersion time intervals (in weeks) of the samples in buffer solution.

4.1.3.12. Statistical Analysis

The experimental results reported in this thesis represent mean ± standard error of the mean. Standard error was calculated from the results obtained for 5 different samples for contact angle measurement, surface roughness measurement, particle size analysis and anti-bacterial sensitivity tests, and 3 different samples for the XPS and UV-Vis. The mean and the standard error of the mean were calculated using Microsoft™ Excel 2013.

5. SURFACE MORPHOLOGY AND SURFACE CHEMISTRY

5.1. Introduction

This chapter concentrates on the surface morphology and surface chemistry of the Ti6Al4V powders used and the parts that were fabricated by SLM. Surface morphological and surface chemical effects of recycling Ti6Al4V powders in a SLM process is discussed. Later, the surface morphology and surface roughness profile of SLM as-fabricated (SLM-AF) surface is stated. Comparisons of SLM-AF's surface chemistry with a SLM fabricated and mechanically polished (SLM-MP) and a conventionally forged and mechanically polished (FGD-MP) surfaces are discussed in detail. Finally the surface chemistries of a laser scanned area, skin scanned and non-skin scanned areas top and side surfaces, are discussed.

5.2. Effect of Aging of Ti6Al4V Powders

5.2.1. Surface Morphology

Gas atomised Ti6Al4V powders are often used to fabricate samples in SLM due to their reduced oxide content and their ability to yield high density parts. In the SLM process, any unused powder material during the process is recycled to fabricate new parts. Since this exposed powder material is recycled several times, it is important to study the surface morphology and chemistry of the powders to investigate if there is any change in their surface properties due to aging.

The surface morphology of Ti6Al4V powders used to fabricate the samples were surface characterised before processing in an SLM machine. Figure 5-1 represents the typical surface morphology of virgin and recycled (more than 500 processing hours) powders obtained using an SEM. From the figure it can be observed that the gas atomised virgin particles had a spherical shape with a broad size distribution. However, satellites were observed on most of these spherical particles. The recycled Ti6Al4V powders depicted a small deformation in this morphology (5-1c and 5-1d). These deformations are due

to the partial melting of particles by the absorption of laser energy. Although, the observed deformations in the sphericity were not significant, this may affect the particle size, flow properties of the powder and thus induce porosities within a part fabricated using these powders. Sieving of the recycled powder before processing can be beneficial to remove such large lumps of particles.

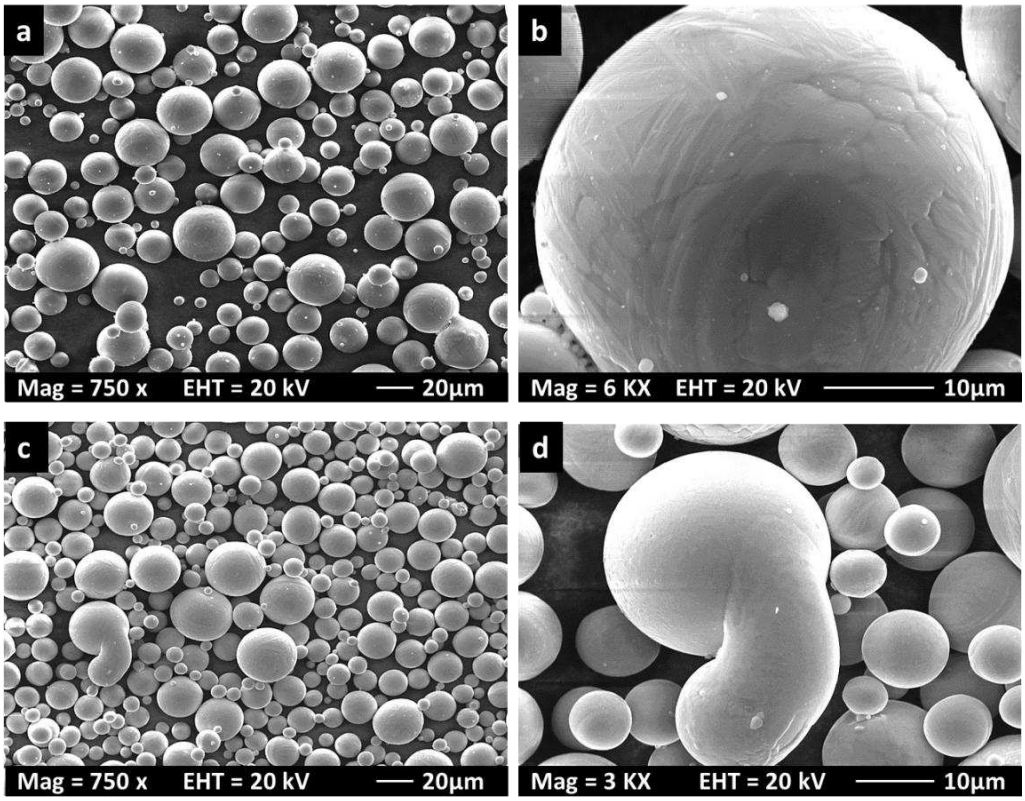

Figure 5-1 Surface morphology of virgin (a and b) and recycled (c and d) Ti6Al4V particles obtained using SEM at different magnifications.

Figure 5-2 shows the morphology of particles retained after sieving the recycled powders with a mesh size of 63 µm. From the figure it is clear that the SLM process increases the particle size and affects the particle shape and sphericity. Agglomeration, partial melting and fusion of particles can be observed. Although the amount of these retained particles on sieving is low, sieving is essential to remove these large irregular partially melted particles to obtain an improved packing density.

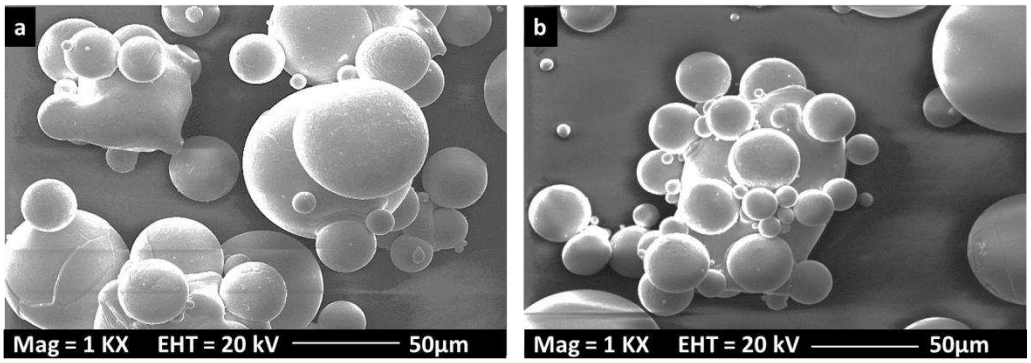

Figure 5-2 SEM micrographs of Ti6Al4V recycled powders retained after sieving using a sieve of diameter of 63 µm.

5.2.2. Particle Size Distribution

The particle size distributions of the virgin, recycled and the sieve-retained recycled powders were measured using a Malvern Mastersizer to determine if there was a change on laser processing. It can be observed from the Figure 5-3 that the virgin powders have a slightly narrower size distribution compared to the recycled powder. Also, the typical size distribution of the retained powder was significantly higher than the virgin and the recycled powders. As it is discussed in section 5.2.1, the increase in the size is mainly due to the partial melting of particles by the absorption of laser energy, presumably on the fringes of the build area.

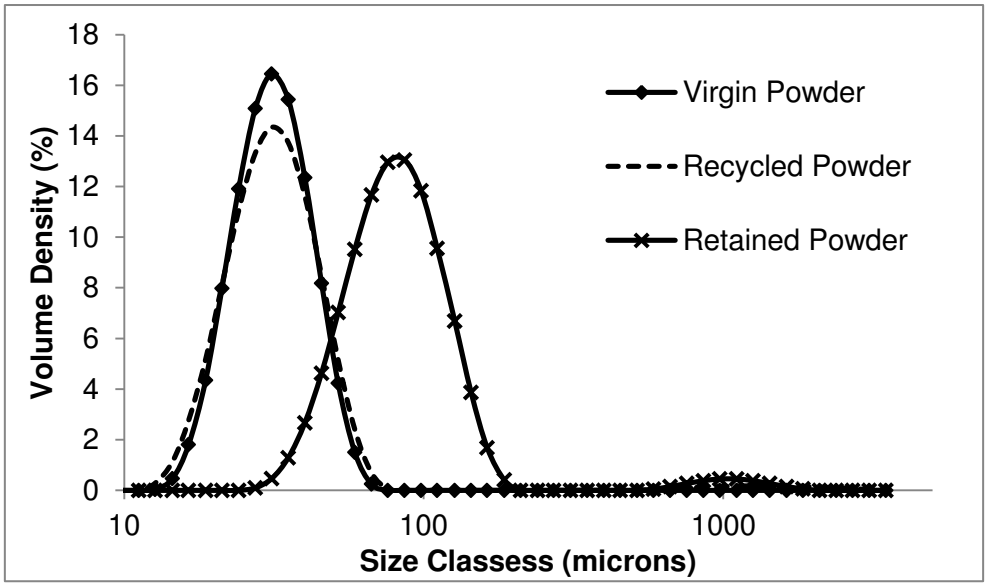

Figure 5-3 Comparison of particle size distribution obtained for virgin, recycled and sieve retained Ti6Al4V particles.

The particle size below which the 10% (Dv 10), 50% (Dv 50) and 90% (Dv 90) of the total volume of the sample exists was calculated to determine the two points of the distribution that describes the coarsest and finest particles of the distribution, shown in Table 5-1. Span is the width of the distribution based on the 10%, 50% and 90% quantile and is calculated using the equation [(Dv 90 - Dv 10) / Dv 50]. These calculations have also shown an increase in PSD on recycling. The sieve retained sample showed 10% of the particles to be over 140 µm which is predominantly due to the partial melting of particles.

Table 5-1 Calculated particle size distributions obtained for virgin, recycled and sieve retained powders using a Malvern Mastersizer (average of 5 measurements).

Size Parameter	Virgin Powder	Recycled Powder	Retained Powder
Dv 10	22.4 (µm)	21.4 (µm)	52.6 (µm)
Dv 50	33.2 (µm)	33.4 (µm)	86.1 (µm)
Dv 90	48.7 (µm)	51.8 (µm)	140 (µm)
Mean size, based on surface area (D[3,2])	31.7 (µm)	31.8 (µm)	80.9 (µm)
Mean size, based on volume (D[4,3])	34.5 (µm)	60.1 (µm)	117 (µm)
Span	0.79	0.91	1.02

The results show that on recycling the median size of the particles has increased due to the partial melting of particles. This partial melting could be due to several factors including the absorption of thermal energy by the surrounding particles in the build area. Another possible reason could be in cases where SLM failed to produce parts due to the lack of support structures. For example, if there are no supports to hold the particles in position, then, the laser beam will melt particles in the build area but will not sinter this to a previously scanned layer/solid structure. Hence, particles will float and will lead to the formation of lumps of particles.

Partial melting was observed to affect the sphericity and lead to irregularly-shaped particles. Although this change in size distribution and morphology was not significant, there is a chance that these particles, if present on the build area, may affect the part's density by inducing pores. A particle size distribution of 20 µm – 50 µm has been observed to render a high flowability

and highly packed powder bed density since the smaller particles filled in the gaps between the relatively large particle sizes [81]. A similar increase in the PSDs of Ti6Al4V processed in a SLM machine was also witnessed by Seyda et al. [83]. Hence sieving of particles before processing is required.

5.2.3. Surface Chemistry

The surface chemistry of virgin and recycled Ti6Al4V powders was studied using XPS to investigate the effect of aging on the surface chemistry of the Ti6Al4V powders. Figure 5-4 shows the survey spectra of virgin and recycled Ti6Al4V powders obtained using XPS. The spectra show the presence of major alloying elements titanium and aluminium. Vanadium (V) was not observed in the virgin powder whereas a very small concentration was observed on the surface of recycled powders. The relative atomic percentages obtained for virgin and recycled powders obtained using XPS were tabulated in Table 5-2. Figure 5-5 shows the high resolution XPS spectra for C 1s, O 1s and N 1s regions for both virgin and recycled powders.

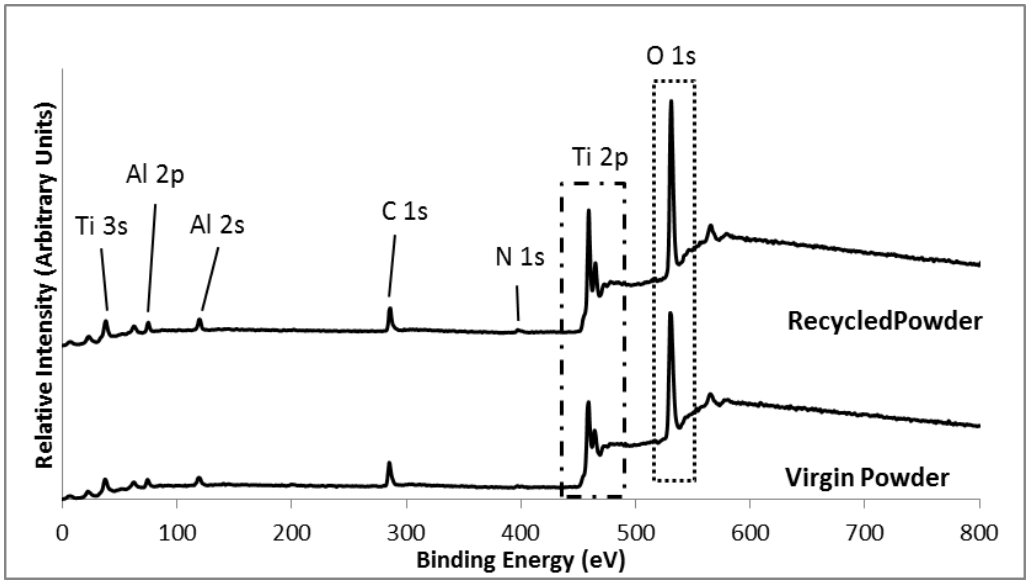

Figure 5-4 Survey Spectra obtained for virgin and recycled Ti6Al4V powders using XPS.

Table 5-2 Relative atomic percentages obtained for virgin and recycled powders using XPS. The calibration error during peak integration is ± 10%.

Metal	Relative atomic percentage	
	Virgin	Recycled
Al 2p	9.41 ± 0.2	9.16 ± 0.6
C 1s	18.95 ± 0.9	23.75 ± 1
V 2p	0	0.31 ± 0.21
O 1s	55.12 ± 0.6	50.5 ± 0.1
Ti 2p	15.13 ± 0.5	14.21 ± 1
N 1s	1.15 ± 0.2	2.06 ± 0.2

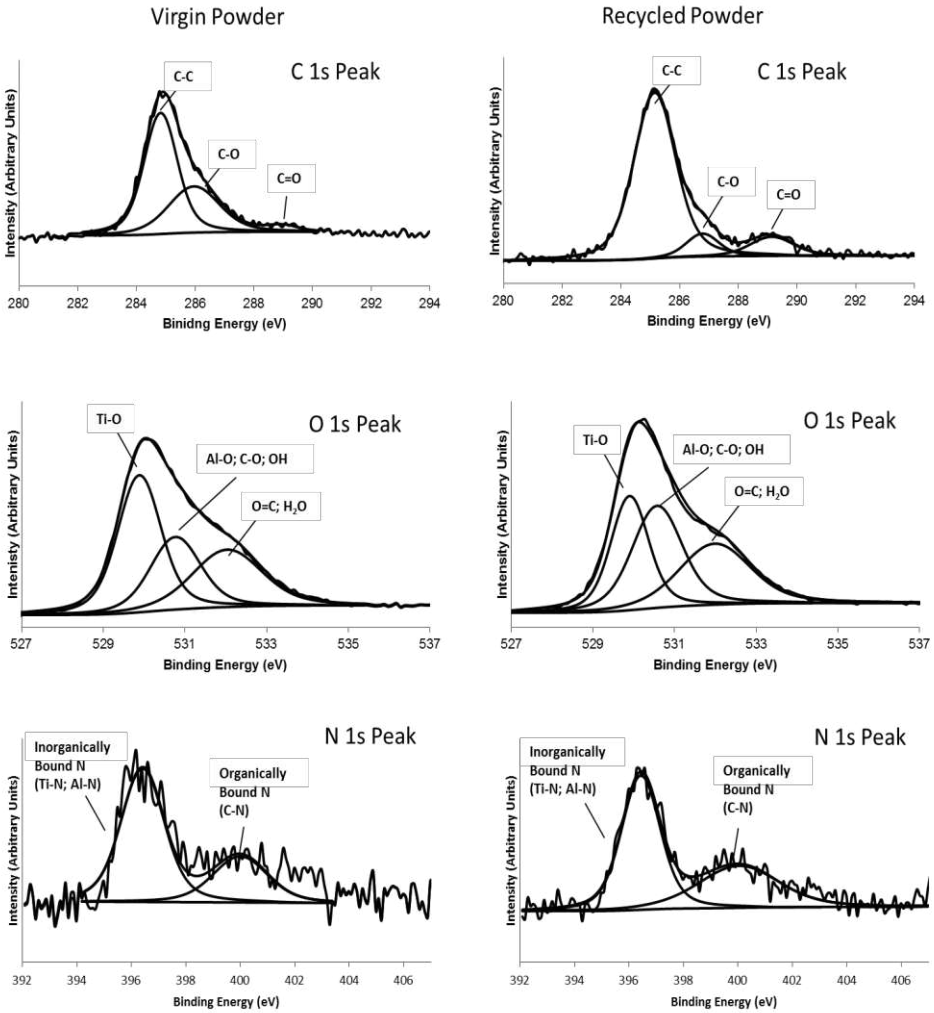

Figure 5-5 High resolution spectra of C 1s, O 1s and N 1s regions obtained for virgin and recycled Ti6Al4V powders using XPS.

It can be observed from the figure that for both virgin and recycled Ti6Al4V powders, the deconvoluted C 1s spectra showed the possibility for peaks at 285 ± 0.2 eV, 286.6 ± 0.1 eV and 289.2 ± 0.2 eV. These peaks correspond to C-C, C-O and O-C=O which are mainly due to contamination of the powders by hydrocarbons [144,180]. For O 1s, the peaks observed at 530.2 ± 0.1 eV, 530.8 ± 0.1 eV and at 532 ± 0.3 eV can be attributed to metal oxide (titanium oxide), Al-O and/or C-O and O-H and/or C=O respectively [155]. The N 1s peak at 396.6 ± 0.1 eV is due to metal nitride and 400.1 ± 0.1 eV can be attributed to C-N surface contaminants [181]. An increase in the C and N (marked with dotted lines in the Figure 5-6) observed for recycled Ti6Al4V powders are mainly due to contamination.

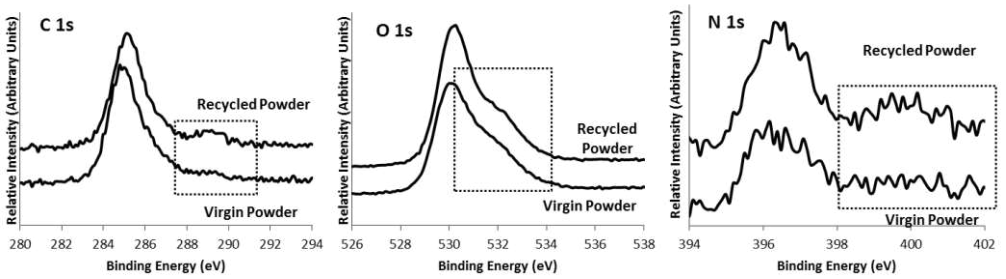

Figure 5-6 Comparison of high resolution spectra of C 1s, O 1s and N 1s regions obtained for virgin and recycled Ti6Al4V powders using XPS. The dotted lines show a possible change in the elemental composition of recycled powders due to contamination from the atmosphere.

Figure 5-7 shows the deconvoluted high resolution XPS spectra for Ti 2p, Al 2p and V 2p regions of both virgin and recycled powders. Deconvoluted Ti 2p peak showed the presence of titanium in both their metallic and oxidation states. A significant contribution from TiO_2 was observed due to the characteristic doublet Ti^{4+} peak at 458.8 ± 0.1 eV and 464.3 ± 0.1 eV for both virgin and the recycled powder. Ti^{2+} (455.7 ± 0.1 and 460.2 ± 0.1 eV) and the underlying $Ti^{metallic}$ at 454 ± 0.1 eV and 460 ± 0.1 eV were also witnessed. According to previous literature, the presence of Ti^{3+} would be expected on both Ti6Al4V powders, whereas the deconvoluted peaks did not show their existence [155]. This may be due to differences in the peak deconvolution.

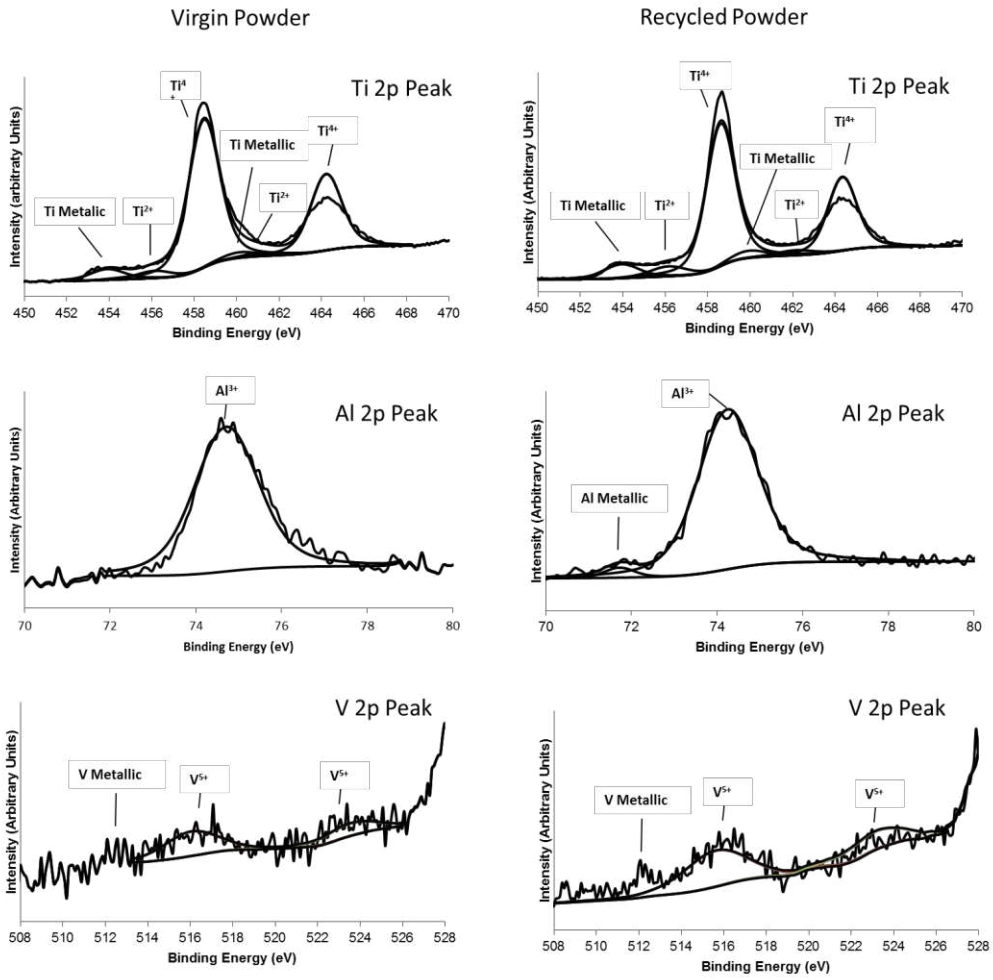

Figure 5-7 High resolution spectra of Ti 2p, Al 2p and V 2p regions obtained for virgin and recycled Ti6Al4V powders using XPS.

Aluminium observed on the virgin powder was in its sapphire form of Al_2O_3 (74.4 eV) whereas the recycled powder showed Al to be both in its metallic (71.9 eV) and sapphire form (74.5 eV). The survey spectrum of virgin powder did not show the existence of vanadium whereas the high resolution V 2p peak showed the possibility for the occurrence of vanadium in its oxide form on the virgin power. Due to the lower intensity of the peak compared to the recycled powders, the survey spectrum did not exhibit the presence of vanadium. However, the concentration of V on the recycled powder was higher than for the virgin powder and hence the survey spectrum predicted the existence of V on the recycled powder. The observed V on both powders was predominantly from its oxide; however, an inference for the existence of V in its metallic form (at 512. 1 eV) was observed.

The surface characterisation using XPS showed no significant change in the chemistry of the virgin and recycled powders apart from contamination. The increase in the C and N observed for recycled Ti6Al4V powders were mainly due to contamination [132]. The formation of titanium nitride and $Ti_xO_yN_z$ (titanium-oxy-nitride) may be due to the contamination in the gas/atmosphere to which the powders were exposed to. Contamination of powders is possible due to atmospheric contaminants and other possible contaminants such as oils (from pump/motor) from the SLM machine and manual handling [146]. Previous studies suggest that entrapment of carbon monoxide and carbon dioxide due to the oxidation of carbon was observed to induce porosity [91]. Also, titanium is highly reactive and can form titanium carbide [182]. This can affect the wettability of the fabricated layer and in turn affect the mechanical properties of the part manufactured by SLM. Since parts are produced additively in the SLM process, wettability of the surface will have a significant impact on the density of a part [92].

5.3. SLM Surface Characterisation

5.3.1. Surface Morphology and Roughness

Figure 5-8 shows the surface morphology of a SLM-AF surface at various magnifications. From the micrograph it is can be noted that loosely bound and partially melted particles are present on the surface. These partially melted particles will add to the thickness of the part and thus increasing its wall thickness and surface area. The presence of partially melted particles on the part surface is inevitable in SLM, with the magnitude of this problem being dependent on both material and process parameters. Some of the parameters that influence the partial melted /surface roughness of SLM fabricated parts are material, powder particle size, layer thickness, laser type and power, scan parameters and scan strategy [61,95].

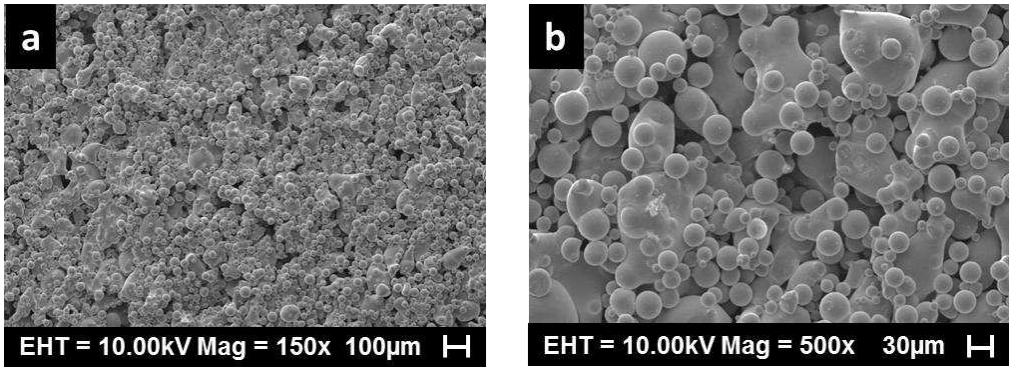

Figure 5-8 SEM images showing the surface morphology of an as-fabricated Ti6Al4V surface fabricated using SLM. The figure clearly depicts the rough and porous nature of the SLM-AF surface.

The observed surface roughness pattern and the surface roughness (Ra) obtained using a surface profilometer was 17.6 ± 1.66 µm. However, it was observed to be difficult to characterise the roughness in certain areas of the part due to the presence of large voids as shown in Figure 5-9. The white voids in the figure represent the areas from which signals were not obtained during surface profiling.

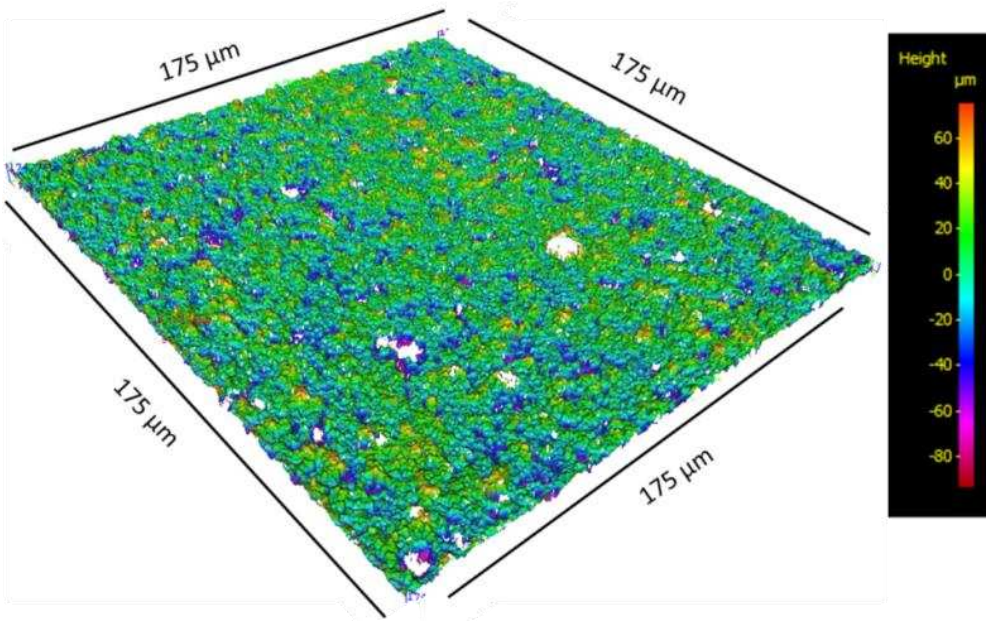

Figure 5-9 Surface Topography of an SLM as-fabricated Ti6Al4V surface obtained using a surface profilometer. The measured surface area was 175 µm^2.

The microstructure of the SLM fabricated part was not studied since it was out of this project scope. However, previous literature reported that SLM

fabricated components consist of α martensitic phase precipitated from β columnar grains [88].

5.3.2. Surface Chemistry

5.3.2.1. Surface film

The surface chemistry of SLM as-fabricated (SLM-AF), SLM fabricated and mechanically polished (SLM-MP) Ti6Al4V components were studied and compared with a forged and mechanically polished (FGD-MP) Ti6Al4V component. The surface chemistry of a vertical planar face (side face) of the cuboid samples was studied using XPS.

Initially, survey spectra for the SLM-AF, SLM-MP and FGD-MP samples were obtained to determine their surface chemistry. Figure 5-10 shows the survey spectra of the detected elements for all three samples. It is evident from the spectra that the elements C, N, O, Ti and Al are present in all three samples. A weak signal (≥ 0.3%) for vanadium was observed on the mechanically polished samples (SLM-MP and FGD-MP) and not on the SLM-AF. Since the SLM-AF samples were rough, this would have reduced the signal by reducing the electron counts reaching the detector during XPS characterisation and hence lead to lack of evidence for no vanadium on the SLM-AF surface.

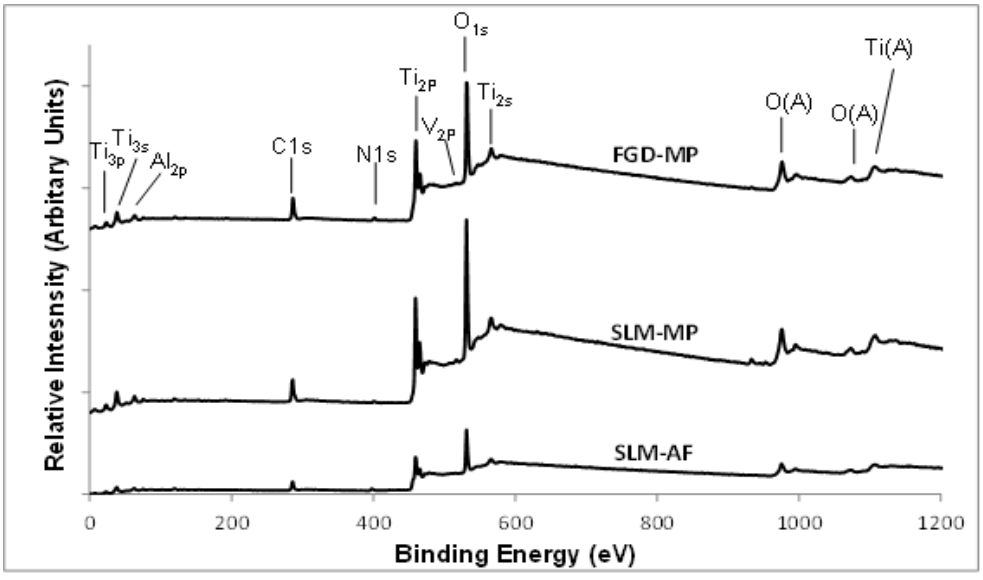

Figure 5-10 Survey spectra of SLM as-fabricated (SLM-AF), SLM mechanically polished (SLM-MP) and forged mechanically polished (FGD-MP) Ti6Al4V surface.

Table 5-3 shows the relative atomic percentages of all detected elements. As can be observed from the table, the dominant signals of the spectra for all three samples are Ti, O and C with a weak contribution from Al and N. The ratio of Ti:O observed for SLM-AF (0.32 ± 0.03), SLM-MP (0.27 ± 0.03) and FGD-MP (0.26 ± 0.02) were higher than Al:O (0.11 ± 0.01, 0.1 ± 0.01 and 0.06 ± 0.01 for SLM-AF, SLM-MP and FGD-MP) ratio. As the Ti:O ratio for all three samples was higher than its corresponding Al:O ratios, this revealed that the surface film of all three samples mainly composed of titanium oxide. To investigate the surface chemistry in detail and to determine the oxidation states of alloying elements, high resolution spectra of C, O, Al, Ti and V on the SLM-AF, SLM-MP and FGD-MP samples were obtained. Depth profiling was performed to investigate the distribution of the detected elements and their chemical states in the first few nanometres of the Ti6Al4V components.

Table 5-3 Relative atomic percentage of elements detected using XPS for SLM-AF, SLM-MP and FGD-MP samples. The calibration error during peak integration is ± 10%.

Sample Type	**Relative Atomic Percentage**					
	Al 2p	C 1s	N 1s	O 1s	Ti 2p	V 2p
SLM-AF	**5.4** ± 0.5	**25.8** ± 2.1	**3.2** ± 0.8	**49.8** ± 1.6	**15.8** ± 0.9	**0**
SLM-MP	**6.0** ± 0.6	**17.2** ± 2.7	**1.2** ± 0.5	**59.1** ± 2.1	**16.1** ± 0.5	**0.4** ± 0.1
FGD-MP	**3.0** ± 0.9	**32.6** ± 2.3	**1.8** ± 0.3	**49.2** ± 1.4	**13.2** ± 1.2	**0.3** ± 0.2

5.3.2.2. Depth Profiling

Figure 5-11 shows the high resolution and depth profiling spectra of C and O for all three SLM-AF, SLM-MP and FGD-MP samples. Bulk metals react with air and form their corresponding oxides, carbides and nitrides depending on the atmospheric conditions [183]. Although the SLM process is carried out in an argon atmosphere with oxygen concentration < 1 ppm, there is the possibility of titanium reacting with the available oxygen and forming its oxide. Also, there is less control of carbon dioxide/nitrogen during the SLM process and the actual amount of these elements present in the build atmosphere/chamber remains unknown. Although Ti6Al4V has 0.08% (max) carbon in its actual composition, a considerable amount of carbon is present in the powder due to atmospheric contamination. Characterising a surface in XPS without carbon contamination is almost impossible.

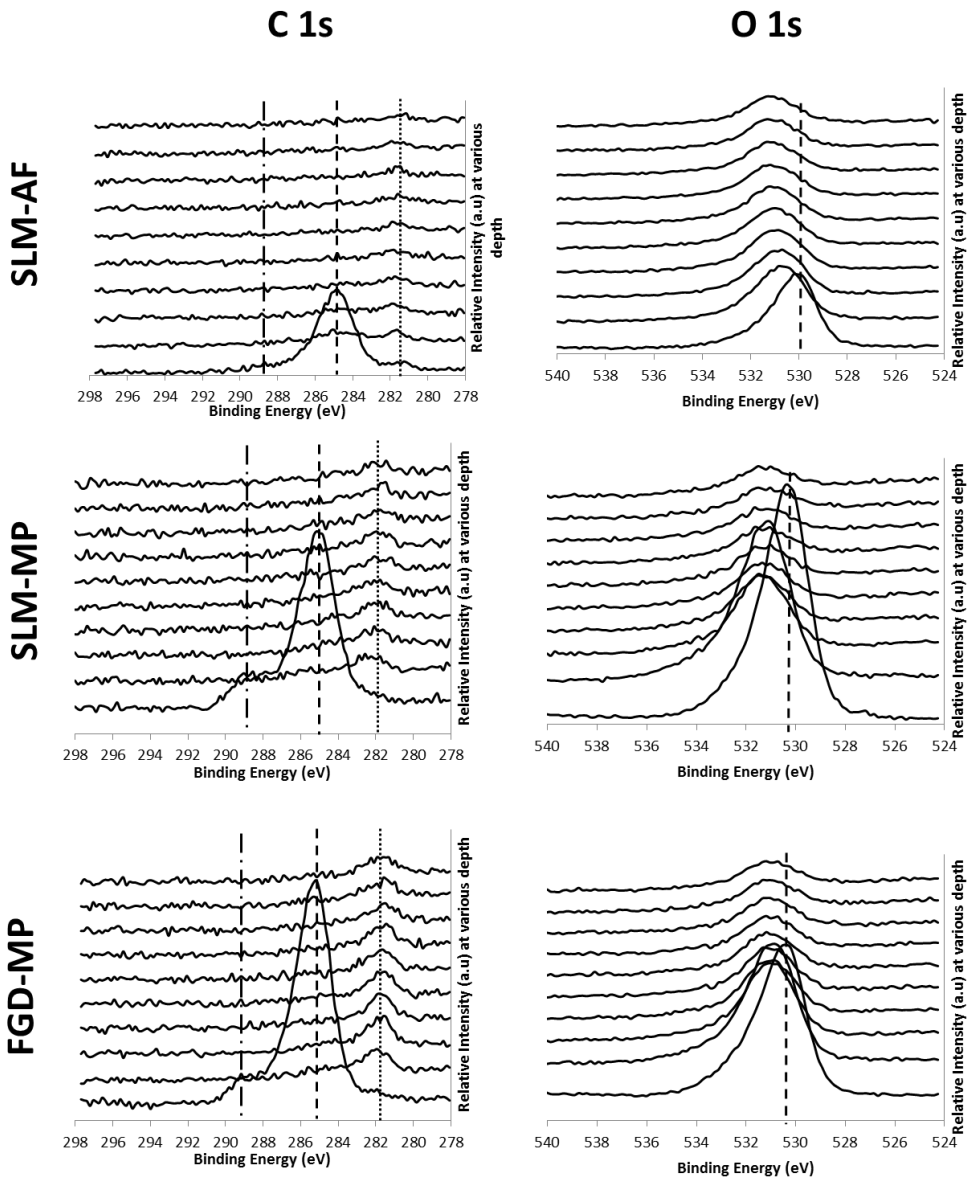

Figure 5-11 Depth profile spectra of C 1s and O 1s regions for SLM-AF, SLM-MP and FGD-MP samples. Depth profiling was performed every 30 seconds (~ 4 nm) from 0 to 270 seconds. C 1s spectra show the disappearance of the initially observed peak after 30 seconds of etching which is attributed to surface contamination. Reduction in the intensity of O 1s peak on increasing depth can also be witnessed from the figure.

Before etching the sample, the C 1s peak showed the possibility for the existence of metal carbide (281.7 ± 0.2 eV), C-C (285 ± 0.1 eV) and O=C-O (288.9 ± 0.3 eV) bonds for all three samples [155]. Since Ti6Al4V is an alloy of Ti, Al and V, the observed metal carbide may have contributions from all three metals. However, since Ti is highly reactive and is present on the surface at a higher concentration, most of the observed metal carbide may have been due to titanium carbide. After etching the samples for 30 seconds (~ 4 nm),

SLM-AF showed a reduction of C-C and C-O peaks whereas in SLM-MP and FGD-MP samples, the C-C and C-O peaks disappeared. The XPS detected C-C, O-C=O bonds can be due to hydrocarbons from air, manual handling, solvents used for cleaning purposes [183,184]. Since solvents including dichloromethane, methanol and ethanol were used for cleaning purposes, these solvents may have left behind some carbon residues that were not washed away by deionised water. Also, there is the possibility for contamination due to adventitious carbon in the atmosphere while mechanical polishing, mounting and transferring the sample into the XPS machine [181]. On sputtering the surface, the concentration of carbon decreased significantly in the first few nanometres. This clearly suggests that they are mainly from contamination. A slower decrease in the C for SLM-AF might be due to the rough nature of the SLM-AF surface. On depth profiling the sample, only the metal carbide peak was observed. Thus, depth profiling of the sample provided a powerful way to separate out the carbon contribution from atmospheric contamination.

The metal carbide peak (at 281.7 ± 0.2 eV) was witnessed even after etching all three samples to several nanometres. This shows the possibility for their formation during a laser scan and is not purely from contamination. Due to the higher reactivity of Ti, it may readily react with carbon in the build chamber to form its carbide. An exothermic formation of oxides and carbides of Ti during SLM process was previously reported to play a significant role in the instability of the melt pool [91]. As a result, the formation of irregular pores was witnessed.

The survey spectra (Figure 5-10) showed the presence of N on all three samples in addition to C. Previous studies have shown that the contribution to the nitrogen peak can be from organically and inorganically bound N. the presence nitrogen in the feed powder has been discussed in section 5.2. Inorganically bound N may originate from a small amount of TiN_x or $Ti_xO_xN_x$ in the surface film since titanium readily reacts with nitrogen. Organically bound nitrogen could be from organic contaminants such as proteins from manual handling or the atmosphere [183]. However, similar to C, the observed metal nitride may also have contributions from Al and V in addition to Ti.

On examining the high resolution O 1s spectra, the possibility of peaks at 530.2 ± 0.1 eV and 532.3 ± 0.2 eV were observed (Figure 5-11). The initial peak is due to Ti-O and the peak observed at 532.3 ± 0.2 eV may be due to C=O, aluminium oxide and adsorbed water molecules [155]. The presence of adsorbed H_2O or hydroxyl molecules could be due to the final cleaning procedure (using deionised water) or from atmospheric moisture. The Ti-O bond is due to the thin TiO film formed on the surface and C=O may be due to the contamination of the surface with carbon containing molecules [183]. From the depth profiles, the concentration of Ti-O can be observed to decrease rapidly with depth for the SLM-MP and FGD-MP samples while it reduces slowly for the SLM-AF. The possible reasons for this sudden and slow drop of oxygen concentration are due to the effect of surface roughness pattern and are discussed in section 5.3.2.3.

Figure 5-12 shows the high resolution Ti 2p peak for SLM-AF and Figure 5-13 shows its evolution on depth profiling. SLM-MP and FGD-MP also showed a similar high resolution Ti 2p peak to SLM-AF. A characteristic doublet peak shape and position observed at 459.1 ± 0.2 and 465.5 ± 0.2 eV for all three samples showed that Ti is mainly present on the surface as Ti^{4+} [183]. Hence, it is evident that the surface of the samples is dominated by TiO_2. Minor fractions of its sub-oxides Ti_2O_3 (457.8 ± 0.2 and 464.2 ± 0.1) and TiO (455.1 ± 0.2 eV and 460.9 ± 0.1 eV) were observed from the intensity of Ti 2P peak revealing their presence in the metal-oxide interface [155]. A small contribution from the Ti 2p metal (453.8 ± 0.1 eV and 460.1 ± 0.2 eV) was witnessed and this is due to the fact that the oxide is thinner than the electron escape depth [183]. On depth profiling of the samples, a clear shift of the TiO_2 peak to pure Ti metal doublet peak at 454.5 ± 0.1 eV and 460.6 ± 0.2 eV could be witnessed (Figure 5-13). This confirms that TiO was only present in the first few nanometres.

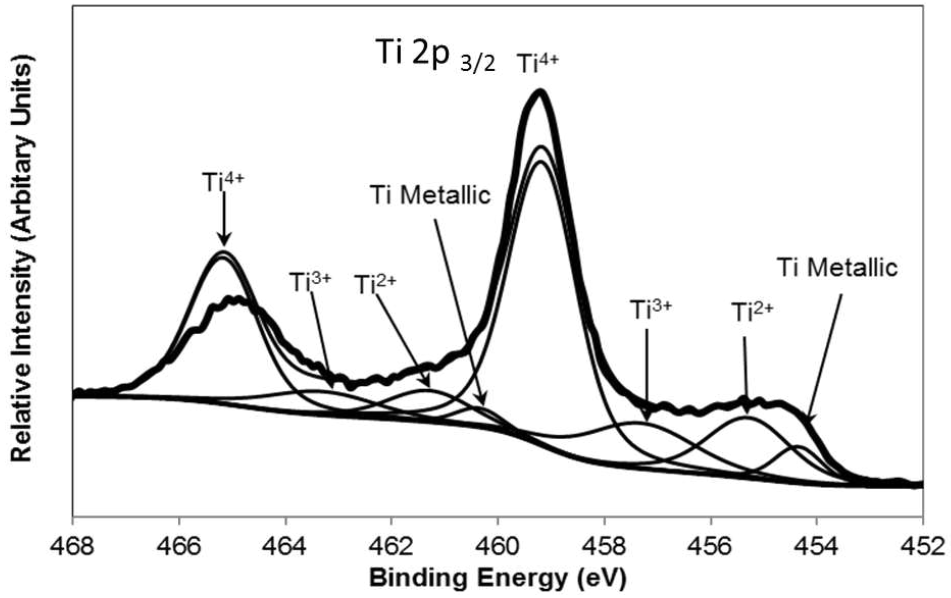

Figure 5-12 High resolution XPS scan of Ti 2p region showing the oxidation states of titanium on a Ti6Al4V SLM-AF surface.

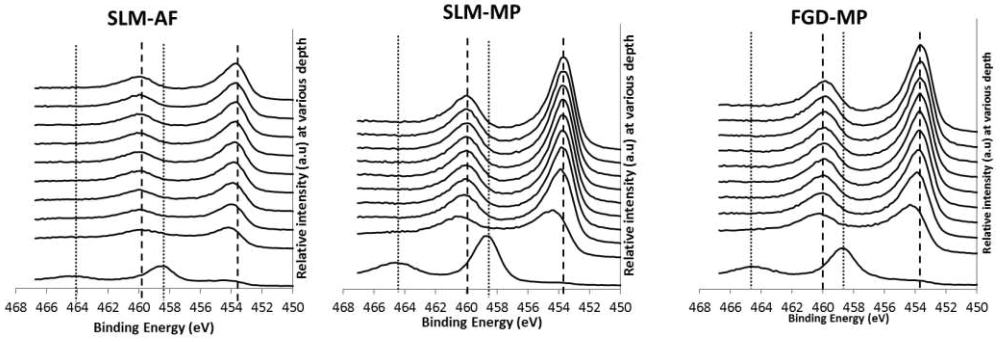

Figure 5-13 Depth profiles obtained for titanium 2p region using XPS for SLM-AF, SLM-MP and FGD-MP surfaces. Depth profiling was performed at every 30 seconds (approximately 4 nm) from 0 to 270 seconds.

Ti has a high affinity towards O and moreover O has high solubility in Ti [185]. When Ti is exposed to O, it forms a monolayer of oxygen on the metal surface. The oxide is then formed by the diffusion of O atoms into the metal and/or metal ion diffusion on to the surface. After nucleation, oxide grows laterally to cover the whole surface [185]. This reaction continues until the diffusion of O ceases leading to the formation of a passive oxide film. Since SLM-AF surface is porous (17.6 ± 1.66 µm), it is possible that there is a greater chance for more oxygen to diffuse into the metal and increase the oxide layer thickness. A previous study revealed that recycling of Ti6Al4V powders

in an additive manufacturing machine increased the thickness of its surface oxide layer from 96 Å to 112 Å [163].

The spectra obtained for Al in the Al_{2P} region shows the possibility for the presence of Al both in its metallic and oxide form for all three samples (Figure 5-14). Peaks observed at 71.8 ± 0.1 revealed the presence of metallic aluminium from the underlying bulk metal alloy and 74.6 ± 0.2 showed the presence of Al_{2P3} in the sapphire form of Al^{3+} (Al_2O_3) [155]. Also this Al^{3+} ion may exist as interstitial or substitutional ions in the TiO_2 matrix [155]. Similar to the Ti 2p peak, on depth profiling, an increase in the metallic Al and a decrease in its oxide form was observed for all three samples. However, the SLM-MP and FGD-MP showed a sudden shift from the oxide form to metallic Al whereas SLM-AF witnessed a slower change. The transformation of Al^{3+} ion to metallic Al on depth profiling revealed the presence of aluminium oxide only in the first few atomic layers.

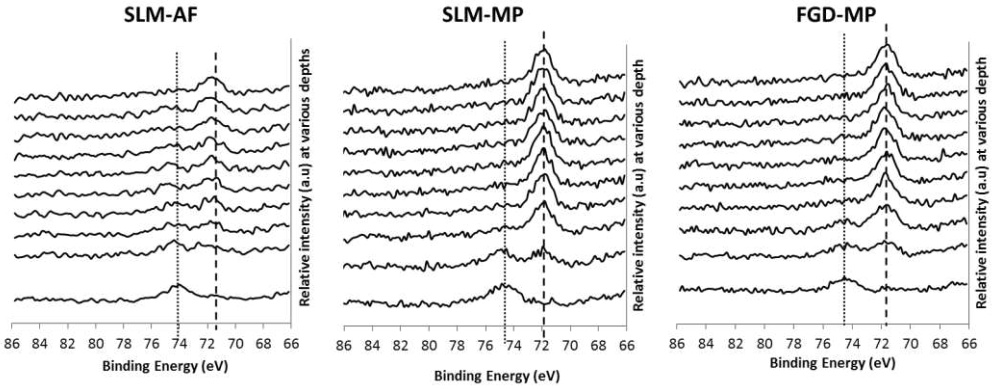

Figure 5-14 Depth profiles obtained for aluminium 2p region using XPS for SLM-AF, SLM-MP and FGD-MP surfaces. Depth profiling was performed at every 30 seconds (approximately 4 nm) from 0 to 270 seconds.

From Figure 5-15, it can be observed that there is no V on the SLM-AF surface whereas it is observed on the SLM-MP and FGD-MP surfaces in low concentration. This could be due to the fact that the SLM-AF surface has comparatively higher Ti and Al concentration than the V concentration. With this very low concentration, the signals generated would be very low and this might have also been affected by the rough nature of the surface. Although V was not observed on the SLM-AF surface, after mechanical polishing, the

alloying element is exposed to the atmosphere form its corresponding oxides (V_2O_3 and V_2O_5).

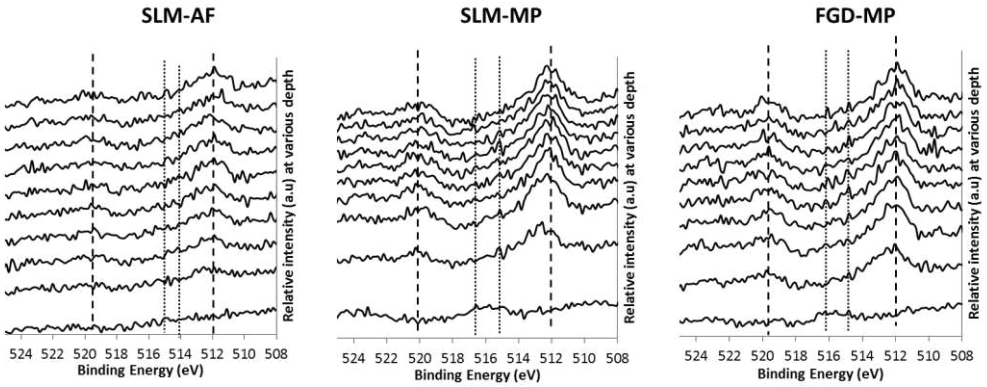

Figure 5-15 Depth profiles obtained for vanadium 2p region using XPS for SLM-AF, SLM-MP and FGD-MP surfaces. Depth profiling was performed at every 30 seconds (approximately 4 nm) from 0 to 270 seconds.

The concentration of V on the SLM-MP was lower than the concentration of V on FGD-MP. However, most of the V observed on the surface was recorded to be in its oxide form (V_2O_3 and V_2O_5) at 514.7 ± 0.2 eV and 516.8 ± 0.3 eV for both SLM-MP and FGD-MP [183]. On depth profiling, XPS detected V in the SLM-AF sample (after sputtering ~ 4 nm) and the concentration of metallic vanadium (512 ± 0.1 eV) could be observed to increase for all three samples as a function of sputtering time.

5.3.2.3. Estimation of oxide layer thickness

All three surfaces were observed to have TiO_2 as the dominant surface film. Due to the presence of Al^{3+} ions on all three surfaces, it is likely that the surfaces also contain Al_2O_3 [155,183,185]. However, the implied concentration of Al_2O_3 on all these surfaces was lower than the implied concentration of TiO_2. The presence of Al_2O_3 on the surface film will add to the corrosion resistance of Ti6Al4V. Vanadium was not observed on the SLM-AF, whereas SLM-MP and FGD-MP surfaces were observed to have vanadium on their surface as V_2O_3 and V_2O_5.

Figure 5-16 shows the graphical representation of the elemental distribution observed for SLM-AF, SLM-MP and FGD-MP samples on depth profiling. Since O concentration reduced slowly for SLM-AF due to the rough nature of

the surface, the actual thickness of its oxide layer is difficult to calculate by both of these methods. Also, it should be noted that the methods used for estimating the oxide layer thickness do not produce directly comparable results; however, comparison may be made between the samples using the results obtained by one method.

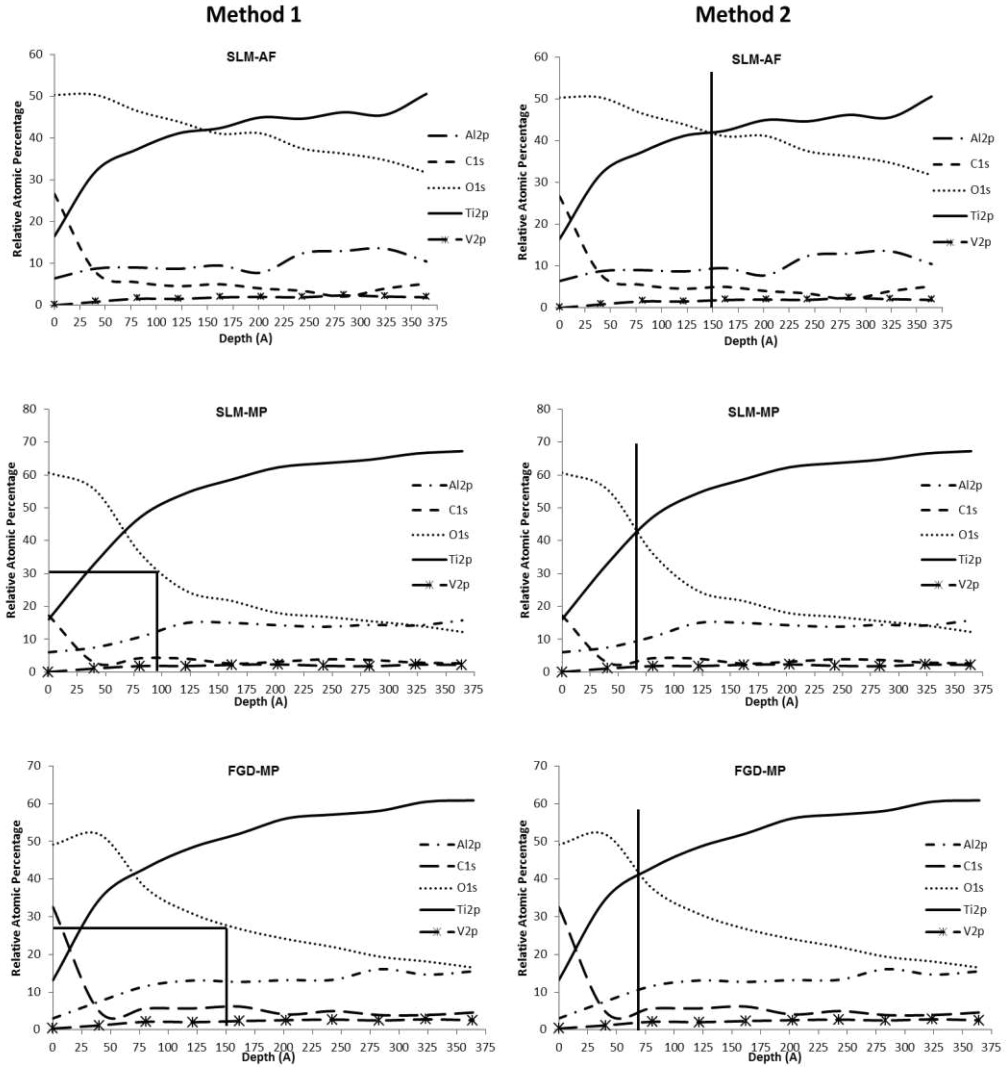

Figure 5-16 Estimation of oxide later thickness for SLM-AF, SLM-MP and FGD-MP samples using two different methods. Data points at every 40 angstroms.

The rough nature of the SLM-AF surface is due to the partial melting of particles. On mechanical polishing of the as-fabricated part, these partially melted particles can be removed from the surface. The rough and porous nature of the SLM-AF is likely to affect the XPS measurement. An important parameter to consider while estimating the oxide film thickness would be sensitivity of XPS to rough surfaces. During the measurement, the number of

counts obtained for a rough surface (SLM-AF) was considerably lower than the counts obtained for a polished surface (SLM-MP and FGD-MP). Since the surface is highly porous and uneven due to partially melted particles, this gives varied incident angles for the XPS beam (see Figure 5-17). Hence, the number of photoelectrons that pass through the analyser will be significantly lower when compared to a polished surface. When the surface morphology is uneven, it is difficult to sputter the surface equally due to a shadowing effect. As a result, some elements present on the outermost surface can still be detected even in a deeper location in the depth profile. Due to this shadowing effect and uneven etching of the sample surface, the SLM-AF samples showed a gradual change in its detected elemental composition.

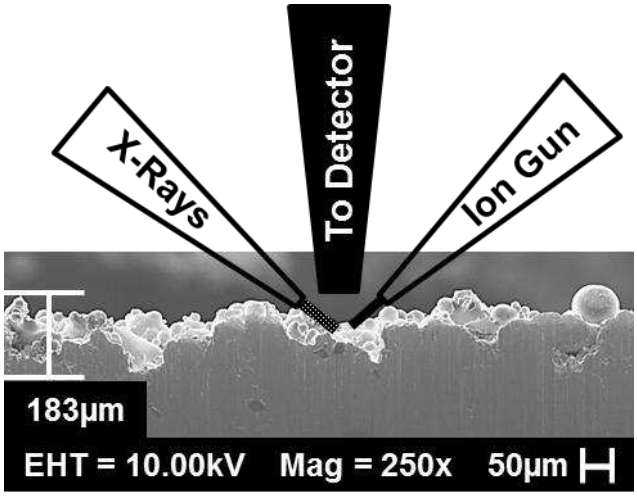

Figure 5-17 Schematic of XPS probing on a rough SLM-AF Ti6Al4V component.

The values obtained for SLM-AF using method 1 shows it has a thick oxide layer (> 35 nm). In the SLM process, parts are built layer-by-layer and this means that every layer will be exposed to the atmosphere within the build chamber for few seconds until a fresh layer is laid. Although argon gas is used to inert the SLM process chamber, there is still the possibility for the presence of oxygen at a very small concentration (less than 8 ppm). This oxygen may react with the laser scanned area to saturate the layer whereas this may not be the case in forging. Hence the process conditions might be a reason for the formation of thick oxide on the SLM fabricated samples. However, the gradual change in the elemental composition of Ti and O compared to the mechanically polished surfaces (SLM-MP and SLM-AF) during depth

profiling shows that XPS characterisation of the sample was affected by the rough nature of the SLM-AF. Thus, the oxide layer thickness of SLM-AF was observed to be higher than mechanically polished surfaces.

On comparing the oxide layer thickness for the mechanically polished samples using method 1, FGD-MP showed thicker oxide layer (~ 15 nm) than SLM-MP (~ 10 nm). Although this may be true, one of the reasons for this might have been the effect of high carbon contamination observed on the FGD-MP surface. The carbon contaminant present above the surface oxide layer might have masked certain concentration of the oxygen initially. This masking effect can be clearly observed from the depth profiling of FGD-MP (an increase in the oxygen concentration as carbon concentration drops). Thus depth profiling/etching of a metal sample's surface renders useful information to examine if the carbon present on the surface is due to contamination or from its alloy.

In method 2, SLM-MP (~ 6.5 nm) and FGD-MP (~ 7 nm) showed nearly similar thickness value and lesser than SLM-AF (~ 15 nm). Since these SLM-MP and FGD-MP samples were mechanically polished, the oxide layer formed may not be representative of the true oxide layer formed during the manufacturing process. Also, due to mechanical polishing of the samples, there will be no or very minimal shadowing effect caused due to partially melted particles during etching and hence their values are closer. The oxide layer thickness observed for SLM-MP and FGD-MP were nearly consistent with literature showing an oxide layer of 1 – 10 nm [186] for un-treated Ti6Al4V substrates. Thus the surface composition was in the order of metal oxides leading to bulk metal.

The presence of surface oxide layer on both the SLM-AF and SLM-MP Ti6Al4V surfaces will be the key for the corrosion resistance of the SLM fabricated surfaces. The mechanically polished surfaces show a similar oxide thickness as the conventionally fabricated parts (without any treatment) [186]. However, the SLM-AF shows a thick oxide layer and this could be beneficial for various applications. If required, to improve the surface oxide thickness, further surface modifications can be performed. Surface treatments such as

chemical etching, passivation, ion implantation and thermal oxidation are performed to enhance this oxide layer thickness for biomedical applications [4,183].

Variola et al. [155] etched Ti6Al4V surface with a mixture of sulphuric acid and hydrogen peroxide to enhance the oxide layer thickness from 10 nm to 45 nm. Their study reported an enhanced growth of osteoblast cells on the Ti6Al4V samples with a thick surface oxide film. Anodic oxidation of Ti6Al4V ELI using an electrolyte solution of 0.5 M H_3PO_4 was reported to yield oxide layers in the range of 30 – 120 nm depending on the anodising current density [187]. Velten et al. [188] performed a thermal oxidation of Ti6Al4V substrates between 400 and 600 °C for 5 – 500 minutes and reported the formation of 190 nm thick oxide layer. They have also reported the formation of oxide films of more than 100 nm thick on the Ti6Al4V surfaces by anodic oxidation and sol-gel process. Although the SLM-MP parts had an oxide thickness of less than 10 nm, if a thickness of > 10 nm is required, then these can be improved by adopting a suitable chemical treatment method. However, the SLM-AF surfaces show an oxide layer thickness of 15 nm which is better than the oxide-layer thickness of the SLM-MP and FGD-MP surfaces.

5.4. Surface Chemistry Comparisons

5.4.1. Effect of skin scanning

Surface Morphology

Skin scanning or selective remelting of the top layer of a SLM fabricated component is performed to increase the surface quality [93]. During skin scanning, the top/final layer is scanned twice. Figure 5-18 shows the surface morphology of a non-skin scanned and skin scanned part fabricated using SLM. Partial melting of particles to the build during SLM (side surface) can be observed. The non-skin scanned part had more particles sintered to the laser scanned surface than the skin scanned part. The surface morphology also clearly shows the laser scan track during the SLM process. An elevated ridge of the solidified material on the edges of both the NSK and SK parts can be observed from Figure 5-19. This is mainly because the remelted material is

partially pushed by the laser beam to the contour of the part. A similar effect has been reported by Kruth et al. [51] for SLM produced parts.

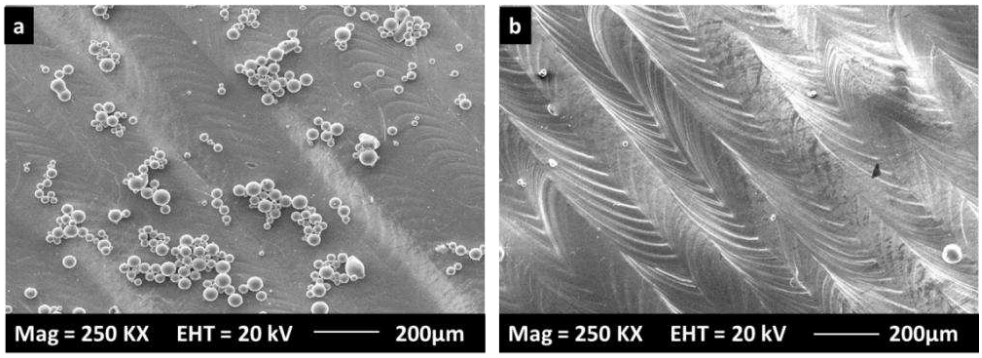

Figure 5-18 Surface morphology of non-skin scanned and skin scanned Ti6Al4V SLM surfaces depicting the laser scan tracts.

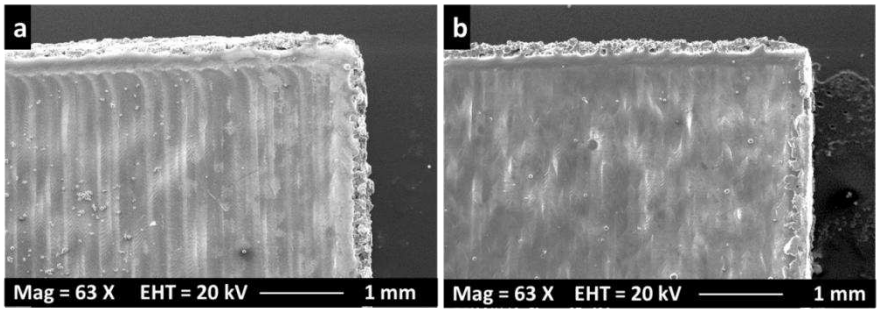

Figure 5-19 Surface morphology of a non-skin scanned (NSK) (a) and skin scanned (SK) (b) Ti6Al4V part fabricated by SLM.

Skin scanning or selective re-melting of layers during SLM is performed to increase the surface quality and density of the fabricated part [93]. This is achieved by remelting the laser-scanned layer to form an even surface. When the surface is even, the distribution of powder to build the next layer will be more homogenous and hence will reduce the entrapment of air. Hence, highly dense parts can be produced. In this study, both the NSK and SK parts fabricated using the AM 250 were observed to be rough (Ra = 3.4 µm ± 0.24 µm for NSK and Ra = 2.2 µm ± 0.16 µm for SK) due to the presence of partially melted particles and the laser scan pattern.

Apart from the partially sintered particles, laser scan tracks are clearly visible in the surface morphology of the NSK and especially in the SK surfaces (Figure 5-18). Since the SK surfaces are scanned by the laser twice (using a meander scan strategy i.e. rotating the laser scan to 67°), a relatively smooth

(Ra = 2.2 µm ± 0.2) surface compared to the NSK (Ra = 3.4 µm ± 0.2 µm) surface was obtained. However, it should also be noted that this re-melting leaves a laser scan track that might potentially affect the surface profile. Although optimising the hatch distance may potentially reduce the laser scan track, this is almost difficult to overcome.

Surface Chemistry

Figures 5-20 shows the high resolution C 1s, N 1s and O 1s spectral regions revealing the evolution of these constituent elements over the first few atomic layers (56 nm) of the NSK and SK components. On deconvoluting the C 1s region (Figure 3) of NSK and SK surfaces, peaks were observed at 285 ± 0.2 eV, 286.7 ± 0.1 eV and 288.2 ± 0.2 eV. These peaks were attributed to C-C, C-O/C-N and C=O [155]. For both NSK and SK surfaces, carbon observed in their outermost layer vanished on etching the surface for ~ 4 nm. As mentioned in the previous section, the disappearance of the C-C, O/C-N and C=O peaks after etching confirms that the carbon is mainly from contamination of the surface [132]. However a peak at 282 eV was observed for both NSK and SK sample after etching their outermost layer. This peak was attributed to metal carbide [183].

The N 1s region on deconvolution exhibited the possibility for peaks at 396.5 ± 0.2 eV and 400.2 ± 0.2 eV which corresponds to inorganically (metal-nitrogen) and organically (C-N) bound nitrogen to the surface [181]. On etching the surface for approximately 4 nm, the organically bound nitrogen disappeared. This reveals that this organic nitrogen is from nitrogen containing carbon contaminants (oil from pumps). The deconvoluted O 1s peak exhibited the possibility for presence of TiO_x, C-O and adsorbed water molecules for both NSK and SK samples. From the Figure 5-20, in addition to the formation of metal oxides, on depth profiling, the formation of metal carbide and metal nitride on both NSK and SK surfaces was observed. Although argon is used to make the chamber inert, there is the possibility for the presence of traces of C and N in addition to oxygen. AM 250 has a built-in sensor to quantify the amount of oxygen in the chamber; but not for C and N. Also, C and N are present in the atmosphere as organic contaminants and as gases (CO/CO_2 and

N_2). These elements were observed on the Ti6Al4V powders as contaminants (discussed in section 5.2). Due to the high reactivity of Ti and Al towards carbon and nitrogen these metal carbides and nitrides are formed [183].

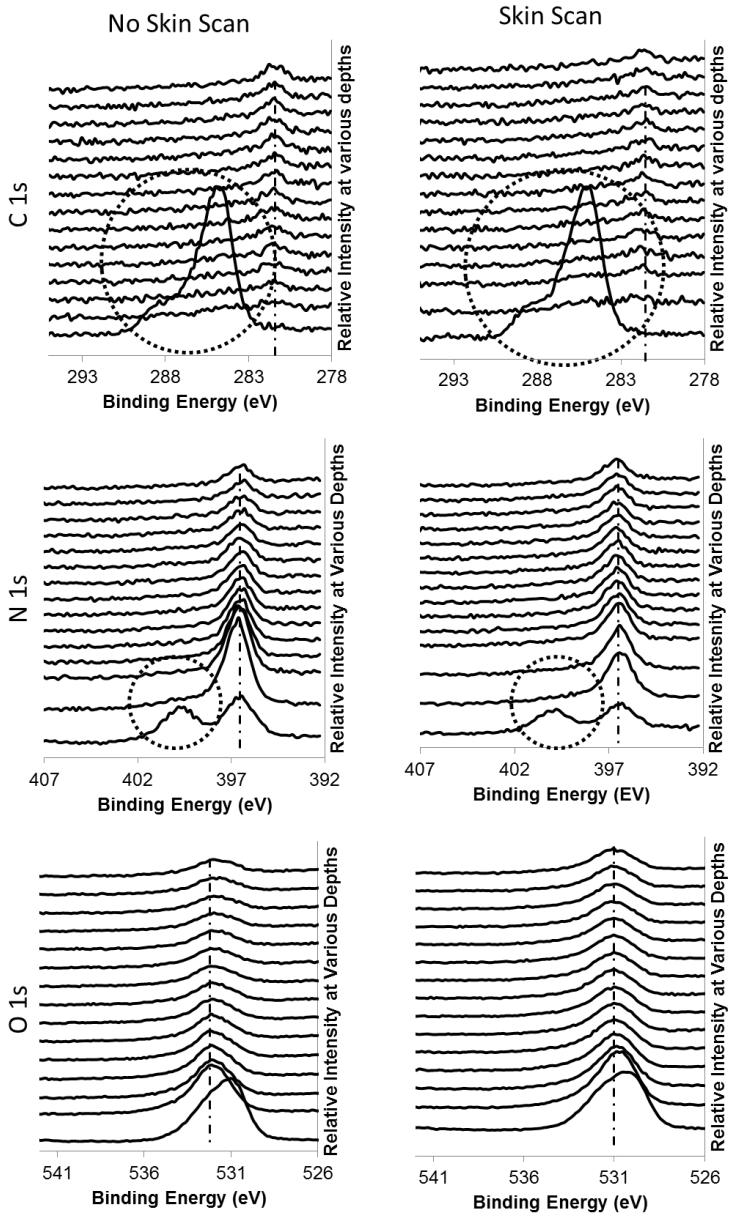

Figure 5-20 XPS spectra of C 1s, N 1s and O 1s regions for the non-skin scanned (NSK) and skin scanned (SK) Ti6Al4V surfaces fabricated by SLM. The dotted lines shows the peaks that disappeared on etching the surface.

Figures 5-21 shows the high resolution Ti 2p, Al 2p and V 2p spectral regions on depth profiling the NSK and SK components. On depth profiling, a clear transition of the metal oxide to pure metal was observed (circled with dotted lines in Figure 5-21) for both NSK and SK surfaces. However, the

transformation of Al oxide to aluminium was more gradual for SK compared to NSK (circled in Figure 5-21 with dotted lines). This slow transition may be due to the formation of thick oxide of aluminium.

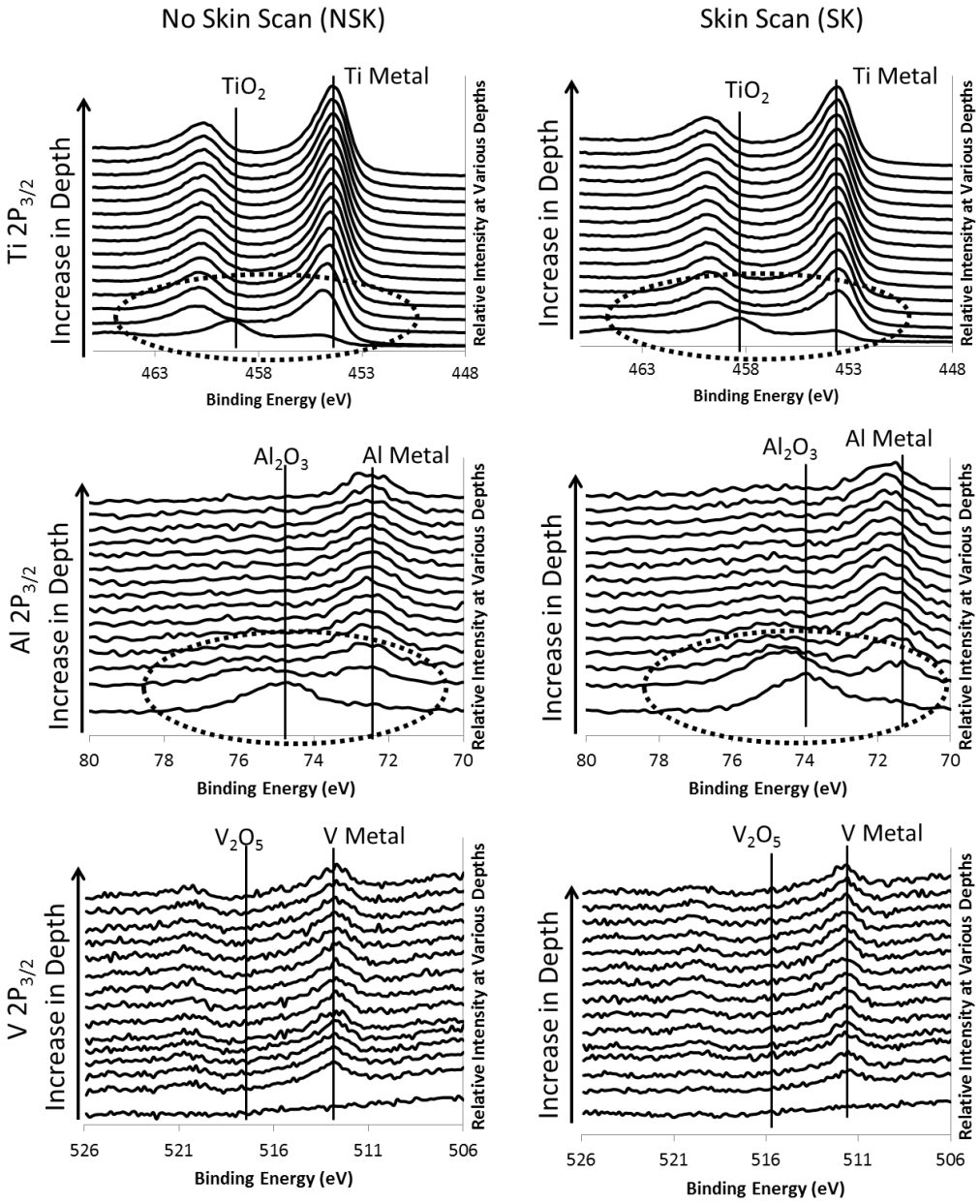

Figure 5-21 XPS spectra of Ti 2p, Al 2p and V 2p regions for the non-skin scanned (NSK) and skin scanned (SK) Ti6Al4V surfaces fabricated by SLM. The dotted lines show the transition of metal oxides from the outermost layer to pure metals.

Figure 5-22 shows the evolution of elements on depth profiling of NSK and SK Ti6Al4V samples using XPS. From the figure it can be observed that on skin scanning, the concentration of aluminium on the surface increases (nearly doubled). The thickness of the oxide layer was measured by two different

methods. As mentioned previously, in the first method, the thickness was measured based on the point at which the concentration of the major alloying element Ti was equal to that of oxygen. In the other method, the thickness was taken as the point at which the maximum observed concentration of oxygen has reduced to half. Using the initial method, the NSK showed a thickness of approximately 7 nm whereas the SK part showed approximately 14 nm which is nearly double that of the NSK's oxide layer thickness. In method 2, for the NSK surface, the initially observed maximum O concentration of 46% reduced to 23% at nearly 35 nm; whereas for the SK surface, the initial maximum O concentration of nearly 47% did not reduce to half until the sampling depth of 56 nm. Thus the oxide layer thickness and the evolution of elements including Ti, C, N and O on the NSK and SK surfaces were observed to be significantly different.

Previous literature has suggested the use of skin scanning (re-melting) for improved surface quality and mechanical properties. However, the surface chemistry of such skin scanned surfaces has not been discussed [91]. During skin scanning or re-melting, the top/final layer is scanned twice. Hence during this scanning period, a high amount of energy will be transferred to re-melt and solidify the upper most surface. On re-melting, due to the increase in temperature, segregation of elements in an alloy is possible. For example, segregation of aluminium was reported due to rapid cooling/solidification [51].

This study observed a high concentration of aluminium in the SK surface compared to the NSK surface. Although the Ti6Al4V alloy has only 6% Al, more than 10% on the surface and over 15% into the SK component was observed; whereas for the NSK component, Al was relatively less abundant near the surface. Since the solubility of Al in Ti is very low, precipitation of a Ti_3Al phase is possible as the temperature reaches 500-600℃. On re-melting the previously scanned layer, the material will remain at a high temperature for a long time leading to precipitation [51]. However, the XPS determined surface concentration did not show an increase in the metallic titanium concentration.

Both NSK and SK surfaces mainly consisted of oxides Ti and Al; however, their concentrations were significantly different when compared to each other. Ti6Al4V alloy is preferred for various biomedical applications because of the high cytocompatibility offered by the presence of corrosion resistant TiO_2 film. Also, SLM is considered to be one of the viable processes for making customised metallic implants with complex structures. The application of SLM to fabricate implants will be limited if the process affects the surface chemical composition. Small changes in the chemical composition may cause catastrophic loss of ductility, corrosion resistance, toxicity and cytocompatibility [3,51].

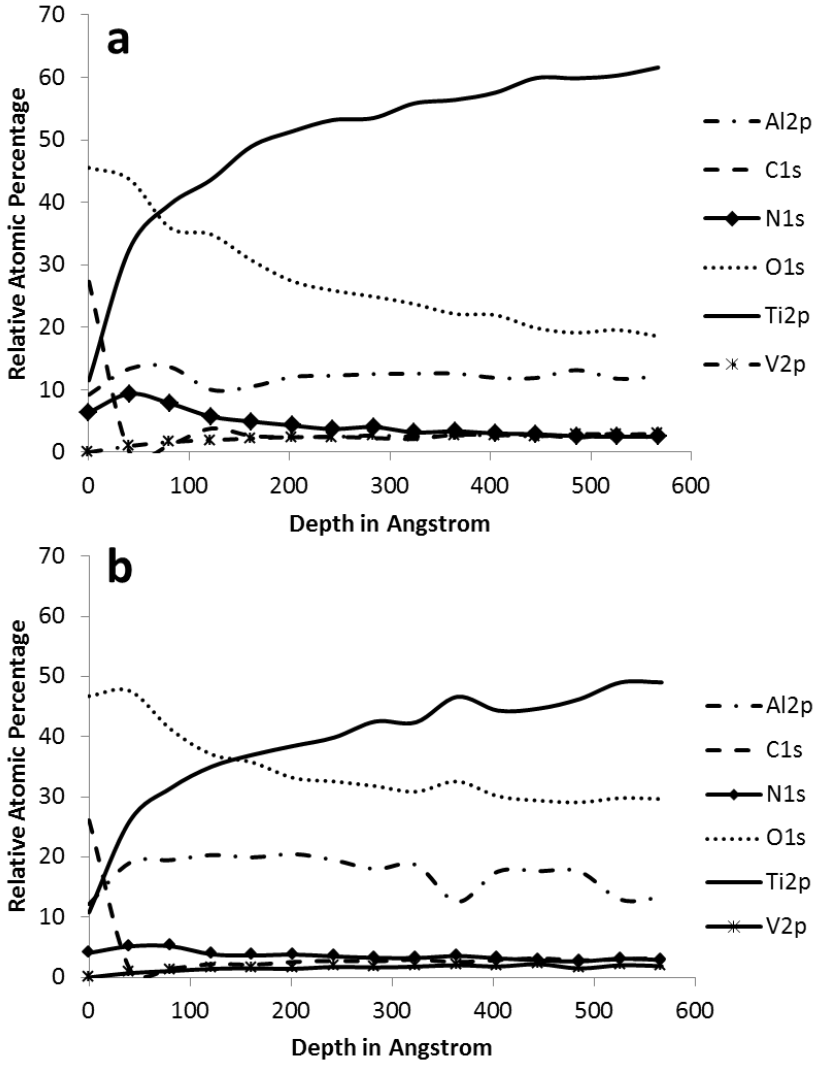

Figure 5-22 Evolution of the surface chemistry of non-skin scanned (a) and skin scanned (b) SLM fabricated surface.

Thus selective remelting of the final layer may be advantageous in terms of rendering a better surface finish. However, it should be noted that it may also alter the surface chemical composition and surface oxide layer. The presence of TiO_2 as the predominant surface oxide layer on Ti6Al4V surface is responsible for its corrosion resistance and cytocompatibility. Since selective remelting alters this composition by increasing aluminium oxide concentration on the surface, cytocompatibility of these components may be reduced and should be properly investigated.

5.4.2. Top Surface and Side Surface

The surface morphology of a side surface and a top surface are shown in Figure 5-23. It can be observed from the figure that the side surface is very rough and porous compared to the top surface. As described earlier in section 5.3.1, this is mainly due to the partial melting of particles from the powder bed to the build. However, the top surface was also accounted for a small number of partially melted particles. These particles might have been blown away by the gassing unit after laser scanning on these areas. In addition to the sintered particles, peaks and valleys due to laser scanning and laser scan tracks can also be seen in the Figure 5-23b.

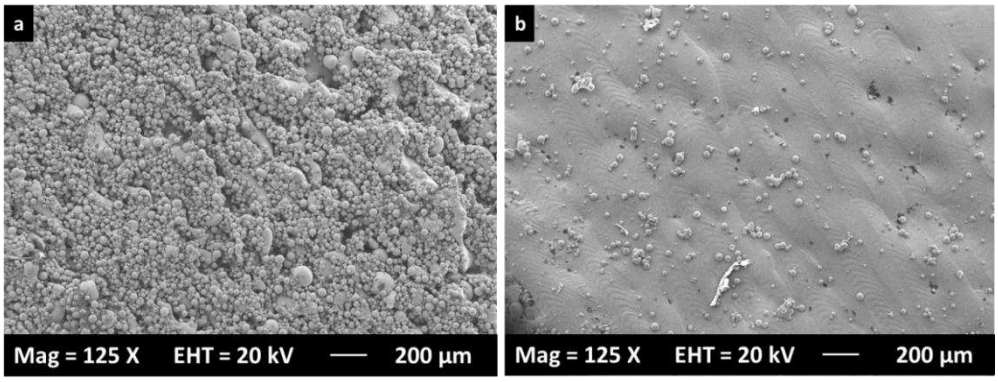

Figure 5-23 SEM micrographs of a side surface (a) and top surface (b).

The surface chemistry of the side surface and the top surface was examined using XPS to determine if there had been any change in the surface chemistry (Table 5-4). Both surfaces showed high carbon and nitrogen contamination. The side surface showed the titanium oxide as its major surface oxide film with a minor contribution from aluminium oxide (Ti:O = 0.32 ± 0.02; Al:O =

0.11 ± 0.01). On the other hand, the oxide film on the top surface (laser scanned area) was observed to have nearly the same contribution from both titanium oxides and aluminium oxides (Ti:O = 0.26 ± 0.03; Al:O = 0.24 ± 0.02). On comparing the oxide films of top and side surfaces, it was clear that the aluminium oxide concentration significantly increased for the top surface. The reason for more aluminium on the top surface may be due to the segregation of the metal during laser scanning [51]. The existence of vanadium on the top surface was observed but not on the side surface. Thus the surface morphology and surface chemistry of the top surface and the side surfaces were significantly different. However, it should be noted that the high surface roughness of the side surface might have affected the XPS results in determining the exact surface chemistry. Further characterisation of these surfaces using SEM with energy dispersive X-ray, X-ray diffraction and transmission electron microscopy is essential to understand the surface properties in detail.

Table 5-4 Relative atomic percentage of elemental contributions obtained using an XPS. The calibration error during peak integration is ± 10%.

Sample Type	**Relative Atomic Percentage**					
	Al 2p	C 1s	N 1s	O 1s	Ti 2p	V 2p
Side Surface	**5.4** ± 0.5	**25.8** ± 2.1	**3.2** ± 0.6	**49.8** ± 1.6	**15.8** ± 0.9	**0**
Top Surface	**10.4** ± 0.9	**27.9** ± 1.5	**6.0** ± 0.7	**44.2** ± 1.1	**11.3** ± 0.9	**0.3** ± 0.1

5.4.3. Recycled powders Vs side surface

The side surfaces of the SLM fabricated components had more particles sintered to them. Hence a comparison of the surface chemistry of the particles used for fabrication and the surface chemistry of the side surface was examined to study the difference in their surface chemistry. Figure 5-24 shows the surface morphologies of the powders used to fabricate the part and the side surface of the part fabricated by SLM. From the figure it can be witnessed that the feed particles are partially melted and bound to the laser melted zones. Thus, the side surface of the SLM sample is contained with the feed particles and the laser melted zones.

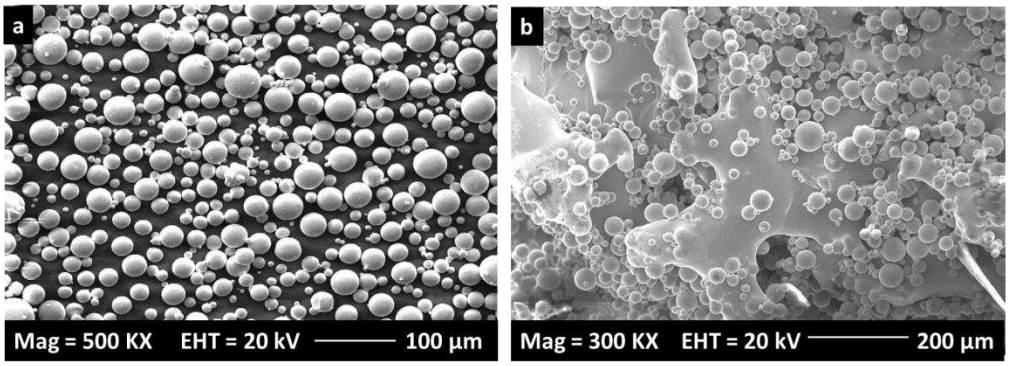

Figure 5-24 Surface morphology of recycled powders used to fabricate the part (a) and the side surface with partially sintered particles (b).

The relative atomic percentage of the elements detected during XPS measurement of the feed powder and the side surface is given in Table 5-5. Compared to the powders, the side surface showed a relatively high degree of carbon and nitrogen contamination due to their high surface area. However, another possible reason for the increased carbon and nitrogen levels might be due to the formation of more metal carbide and nitride on the SLM surface. A small contribution to the carbon may also be possible from the carbon tape used to stick the Ti6Al4V powder particles for characterisation. Since the surface and the powders had varying levels of contamination, the ratio of metal to oxygen was used to interpret their surface chemistry.

Table 5-5 Relative atomic percentage of elements detected during XPS characterisation of Ti6Al4V powders and side surface. The calibration error during peak integration is ± 10%.

Sample Type	**Relative Atomic Percentage**					
	Al 2p	C 1s	N 1s	O 1s	Ti 2p	V 2p
Recycled Powder	**9.2** ± 0.6	**23.8** ± 1	**2.1** ± 0.2	**50.5** ± 0.6	**14.2** ± 1	**0.3** ± 0.1
Side Surface	**5.4** ± 0.5	**25.8** ± 2.1	**3.2** ± 0.8	**49.8** ± 1.6	**15.8** ± 0.9	0

On comparing the metal to oxygen ratio of the major alloying elements Ti and Al, it was observed that the Ti:O and Al:O ratios of the powders and the side surface were significantly different with varying levels of surface oxide compositions (Figure 5-25). The ratio of Ti:O for the Ti6Al4V powder was lower than the ratio of the side surface. This implies that on laser processing of the Ti6Al4V powders, the ratio of Ti:O increases. In contrast, the Al:O ratio

observed for the powders were higher than the ratio witnessed for the side surface.

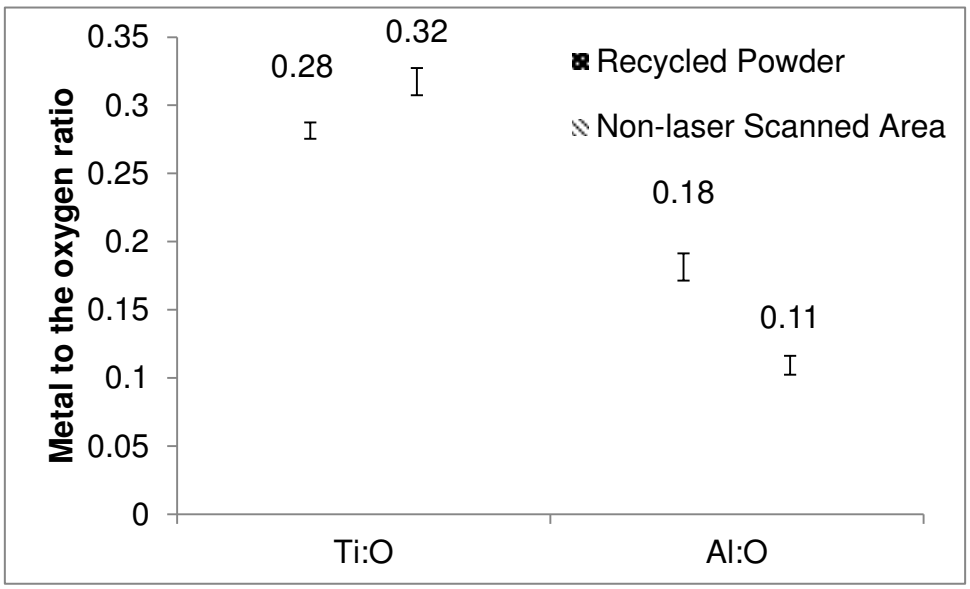

Figure 5-25 Elemental ratio of titanium and aluminium to oxygen in the recycled powder and the side surface.

These clearly show that although a significant amount of particles are partially melted and bound to the side surface, the surfaces do not exhibit the surface chemistry of the feed powders. Since the presence of both SLM melted zones and partially melted powders are observed on the surface, its surface chemistry is most possibly contributed to by both of these factors. Also, controlling the surface chemistry of a SLM surface with both partially sintered particles and laser melted zones can be difficult.

5.5. Summary

SLM fabricated Ti6Al4V samples were observed to be rough and porous due to partially melted particles on the surface. Disappearance of carbon on etching the surface by approximately 4 nm revealed most of the carbon observed on all three surfaces was likely due to contamination. As revealed by the depth profiling, the present study showed differences in the surface chemistry of SLM-AF, SLM-MP and FGD-MP with respect to the distribution of elements and its composition on the surface. Vanadium was not observed on the SLM-AF surface and hence the surface oxide film of SLM-AF was made of oxides of titanium and aluminium. Due to the existence of vanadium, the surface

oxide film of SLM-MP and FGD-MP was made of all three alloying elements (Ti, Al and V). Although SLM-AF showed a high oxide film thickness, this could have been due to the effect of partially melted particles on the surface. A SLM fabricated part with a smooth surface will be ideal to determine its oxide layer thickness accurately using XPS. On comparing the impact of laser power on the surface chemistry, when skin scanning was performed, a possible increase in the surface oxide layer and segregation of aluminium on the surface was observed. The study on the top and side surfaces showed differences in their surface chemistries due to the varied elemental distributions. Thus, the SLM fabricated parts showcased a non-homogeneous surface chemistry on its surfaces and the laser power was observed to influence the surface chemistry of the SLM fabricated parts. Due to this non-homogeneous surface chemistry, surface modification is required to prevent the release of metal ions by which corrosion resistance and cytocompatibility of the SLM fabricated Ti6Al4V components can be enhanced for biomedical applications.

6. SURFACE MODIFICATION USING SAMs

6.1. Introduction

In chapter 5, the SLM fabricated surfaces were shown to have a non-homogenous surface chemistry and require surface modification. In this chapter, surface modification by the adsorption of SAMs and in vitro stability of the attached phosphonic acid monolayers formed on SLM fabricated surfaces are described. The impact of surface roughness on the stability of the chemisorbed monolayers is also presented.

6.2. SAM Attachment

Previous studies on the attachment of phosphonic acid monolayers have been performed mostly on polished surfaces [53–56,58,137,144,189] with only a very few having been performed on rough surfaces [149]. For biomedical use, some applications require a smooth surface (such as stents) and some require a porous surface to promote cell adhesion and tissue integration/regeneration[4]. Prior examples of the attachment of monolayers to an SLM fabricated surface have not been reported. Hence, the attachment of 16-PhDA phosphonic acid SAMs (with COOH termination/functionality) to a rough SLM as-fabricated Ti6Al4V surface (SLM-AF) and a smooth mechanically polished (SLM-MP) surface was performed. The surface roughness (Ra) of the SLM-MP after polishing was measured to be 590 ± 13.5 nm. In vitro stability of phosphonic acid monolayers on these rough and smooth surfaces and the impact of surface roughness on SAM's stability were investigated.

Since one batch of the samples was rough (SLM-AF), the commonly used techniques to characterise SAMs including atomic force microscopy (AFM) and ellipsometry could not be employed in this study. Also the presence of irregular pores on the mechanically polished surfaces affected AFM measurements. Hence, XPS was used as the main characterisation technique along with contact angle goniometry to confirm the attachment and stability of the monolayers.

6.2.1. Surface chemistry

Figure 6-1shows the XPS spectra of the SLM-AF and SLM-MP Ti6Al4V surfaces before and after 16-PhDA SAM coating. It can be observed that there is a significant change in the carbon 1s peak at 285 eV after surface modification using SAMs for both SLM-AF and SLM-MP. This increase in carbon is consistent with the presence of the 16 carbon atoms of 16-PhDA. Also after surface modification, a significant amount of phosphorous was observed on the SAM-modified surface for both SLM-AF and SLM-MP. Although a ratio of 16:1 would be expected, the observed C:P atomic ratio was approximately 13:1 for SLM-AF and 12.4:1 for SLM-MP. This may be due to peak fitting uncertainties (calculated error was ± 10%). Also, since XPS measurement is sensitive to surface contaminants, it is believed that contamination of the sample might have affected the ratio. For example, contamination of the surface due to oxygen and nitrogen based contaminants can alter the atomic percentage of elements. A small difference in the C:P ratio due to surface contaminants has been reported in literature [190]. However, it should be noted that the atomic percentage of phosphorous is much less than that of carbon, and is consistent with the presence of only one phosphorous atom in 16-PhDA.

The observed low concentrations of aluminium (SLM-MP) and nitrogen (for SLM-AF) on the Ti6Al4V surfaces before SAM attachment further reduced after SAM formation. The observed nitrogen might be due to contamination of the surface due to atmospheric contaminants such as oils. Also the concentration of titanium and oxygen observed before SAM attachment decreased after surface modification, since the limited penetration depth of XPS is now sampling less of the underlying substrate. The detection of titanium and oxygen through the 16-PhDA layer confirms that this layer is thin (i.e. less than the typical XPS sampling depth of 5-10 nm). A similar decrease in the bulk material's composition was reported in previous literature after the assembly of SAMs [144]. All observed changes in the surface chemistry of the SLM-AF and SLM-MP surfaces are consistent with previously reported literature for the formation of SAMs on the SLM fabricated Ti6Al4V surfaces

[37]. Thus the XPS data is consistent with the coating of 16-PhDA SAMs on both the SLM-AF and SLM-MP surfaces.

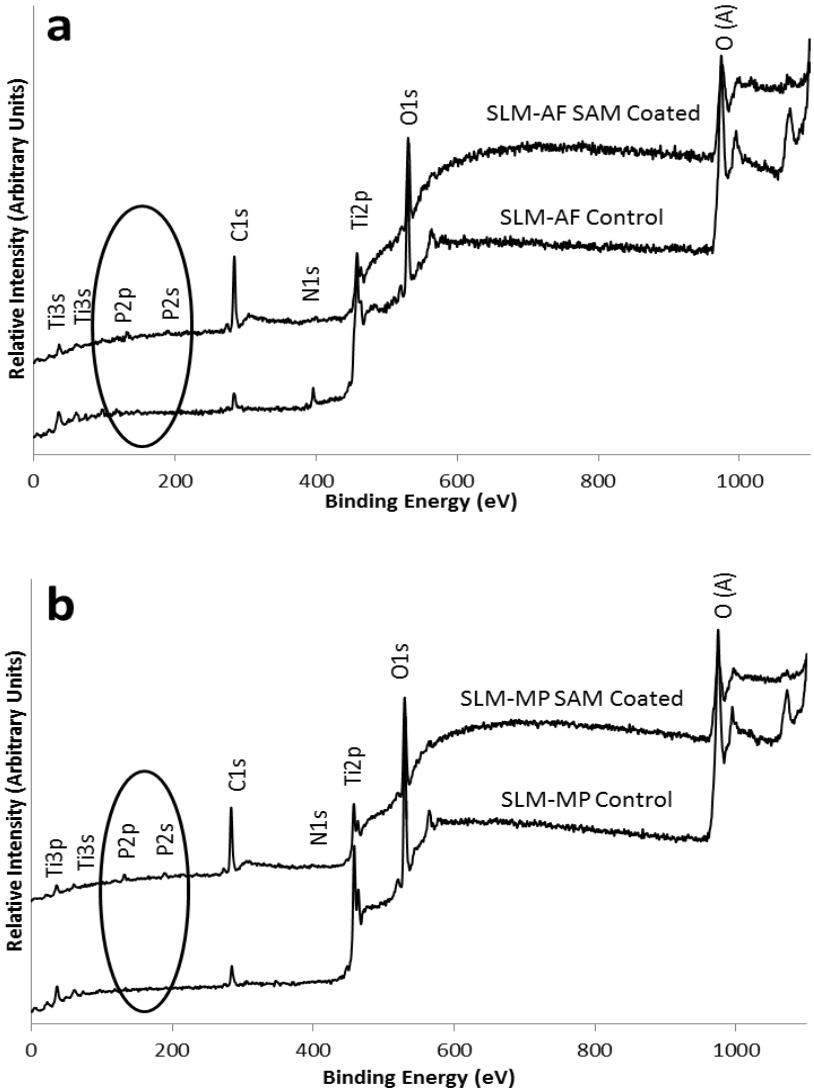

Figure 6-1 XPS spectra before and after surface modification of a) SLM-AF and b) SLM-MP by adsorption of a 16-PhDA monolayer.

6.2.2. Surface wettability

The contact angle formed by a liquid at an interface can provide a measure of surface wettability, SAM order and uniformity [55]. Figure 6-2 shows the surface wettability of SLM-AF and SLM-MP surfaces after different surface treatments. It can be observed that the contact angle reduced after surface cleaning. The high contact angle value before surface cleaning is likely due to the presence of contaminants on the surface. The important and problematic contaminants are hydrocarbons (oils from pumps and skin) and impurities on

the material surface. These contaminants are mainly due to manual handling and exposure to the atmosphere [1,132].

On cleaning these contaminants were effectively removed from the surface thus yielding lower contact angles (due to high surface energy) for both SLM-AF and SLM-MP surfaces. After surface modification using SAMs, the contact angle reduced further. This was because the employed SAMs were hydrophilic, possessing a carboxylic acid (COOH) group. This change in the contact angle further supports the formation of a monolayer on both the SLM-AF and SLM-MP surfaces. Differences between the measured contact angles for the two surfaces were most likely due to the effect of the different surface roughnesses of SLM-AF (17.6 ± 1.66 µm) and SLM-MP (0.59 ± 0.01 µm). Due to the presence of voids in certain areas of the SLM-AF surface, measurement of contact angles on those areas were impossible. Hence, an alternate area (without voids) was selected on the sample for wettability measurement.

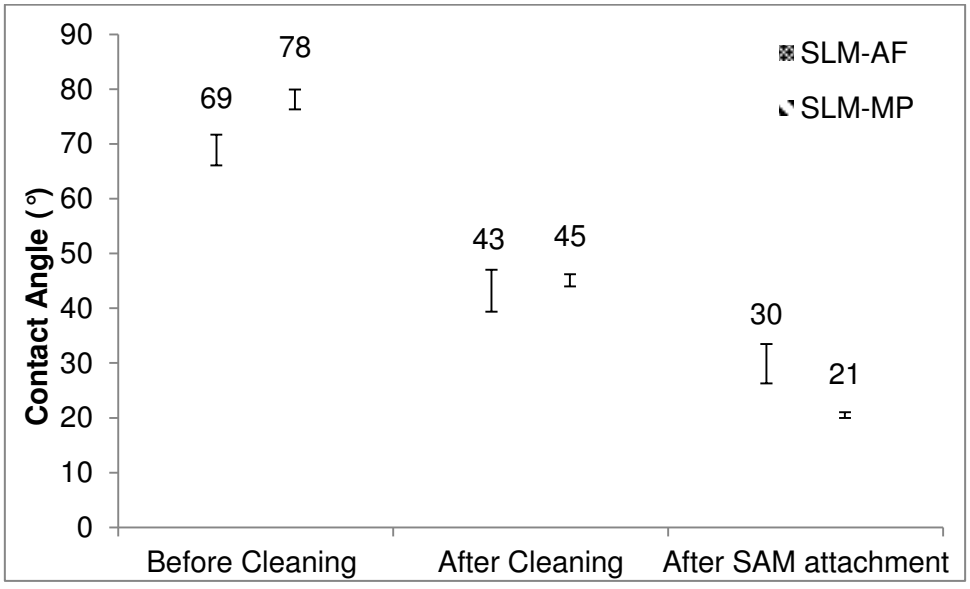

Figure 6-2 Static water contact angle measurements on SLM-AF and SLM-MP surfaces, after cleaning and SAM attachment.

Although both substrates were modified with SAMs on the same time, in addition to their roughness profile, their varying levels of surface contamination could affect their surface wettability. Previous literature reported contact angle values ranging from 45° to 62° for the assembly of

hydrophilic phosphonic acid SAMs [53,56,153,191]. However, the contact angle observed in this study was lower than the values reported in literature. This difference in the contact angle can be attributed to the monolayer arrangement and the cleanliness of the substrate [146]. Also, surface roughness pattern can affect the monolayer arrangement and the surface wettability. Tosatti et al. [149] demonstrated the surface wettability of SAM modified titanium surface to vary with their varied roughness patterns. In their study, the rough surface (Ra = 2.5 ± 0.2 µm) showed a advancing contact angle of 150° for methyl terminated SAM; whereas, the smooth surface (Ra = 3 ± 0.3 nm) depicted 110°. Thus surface roughness patter can affect the contact angle measurements. However, since the phosphonic SAMs used in this study bears –COOH functionality, a hydrophilic group, the surface remained hydrophilic. This confirms the surface modification of SLM-AF and SLM-MP Ti6Al4V surfaces using 16-PhDA SAMs.

6.3. Stability Studies

6.3.1. Surface chemistry

Figure 6-3 shows the high resolution XPS spectra for the phosphorous 2p region of the samples soaked in the buffer solution for different time intervals. It can be witnessed from the spectra that the metal phosphonate peak at 133.3 ± 0.2 eV retained its position at the same binding energy for the whole duration of immersion in the buffer solution. Bhure et al. [55] reported the phosphorous 2p peak to be centred at 133.2 eV for 14 days during their stability studies (when exposed to air). Similarly, in this study, the P 2p peak was observed at 133.3 ± 0.2 eV throughout the study period. However, the intensity and relative atomic composition of P 2p peak decreased over the course of the experiment especially after four weeks, showing desorption of monolayers from the Ti6Al4V surface. Although the desorption of monolayers was noted to occur after four weeks, a small amount of monolayer was observed at the end of six weeks. On comparing the XPS P 2p spectra of SLM-AF and SLM-MP, there was no significant difference in the stability of 16-PhDA SAMs on these surfaces. This shows that the roughness pattern of the SLM-AF did not affect the stability. However, it should be noted that the peeling of partially

melted particles after SAM attachment can affect the monolayer assembly and may lead to the formation of islands without monolayers.

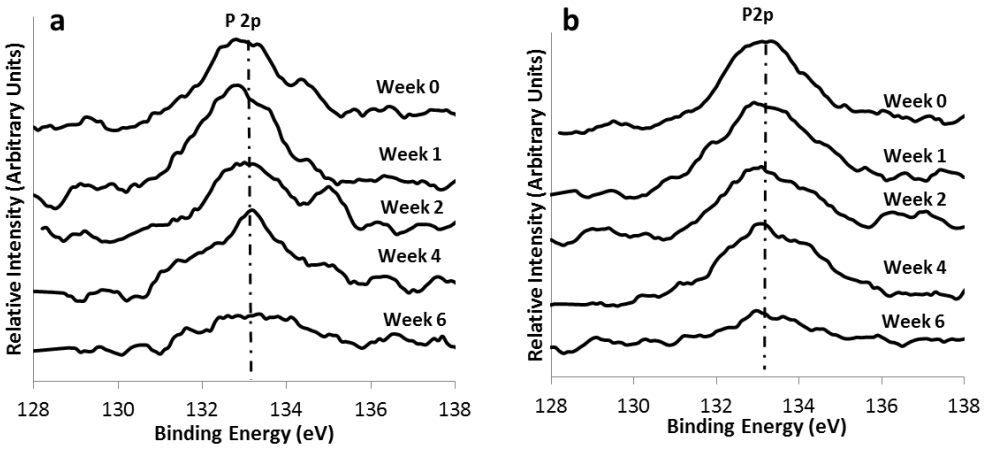

Figure 6-3 XPS spectra for the in vitro stability of SAMs on SLM-AF (a) and SLM-MP (b) surfaces after immersing in Tris-HCl buffer solution for various time intervals.

6.3.2. Surface wettability

A gradual increase in the contact angle was noted after immersing the samples in Tris-HCl buffer solution (although this change has low significance compared to the standard deviations of individual measurements). This may be attributed to a small amount of desorption (Figure 6-4) leading to the change in the assembly pattern of the monolayers. It can be noted from the figure that the contact angles measured for the SLM-AF samples had a high standard deviation when compared to the SLM-MP samples. This may be due to the surface roughness of the SLM-AF samples. The slight increase with time for the SLM-MP sample was observed, however this was not significant. The effect of roughness also makes these results difficult to interpret; however, the surfaces of both SLM-AF and SLM-MP remained highly wettable. Bhure et al. [55] studied the stability of phosphonic acid SAMs on cobalt-chromium surfaces by exposing it to the atmosphere and reported that the SAMs were stable for the duration of their study i.e. 14 days. Kanta et al. [192] studied the stability of phosphonic acid SAMs by exposing the SAM coated titanium surfaces to various conditions including the exposure to UV light (energy of 10.4 J/cm^2 at sample surface) for 180 minutes and heat treatment (100 °C) for 3 hours and plasma treatment with a power of 100W and frequency of 13.56 MHz. Their studies concluded that UV, heat and plasma treatment decomposed

the alkyl chain leading to the degradation of SAMs. However, there were no previous studies reporting the long-term stability (6 weeks) of the 16-PhDA monolayers assembled on to SLM fabricated Ti6Al4V surfaces (rough and smooth) under in vitro condition. Hence, it is believed that this is possibly the first study showing their stability under in vitro conditions.

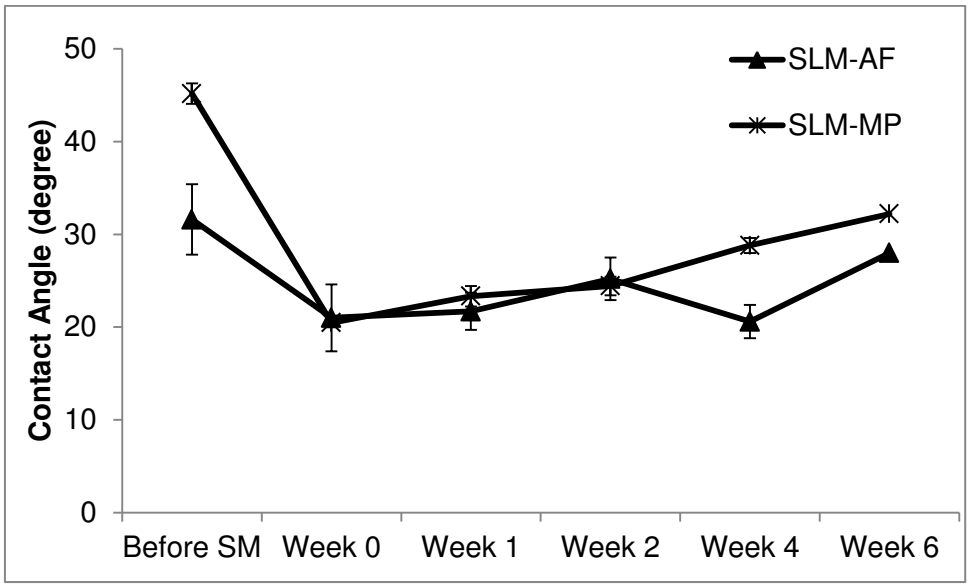

Figure 6-4 Static water contact angle measurements on SLM as-fabricated (SLM-AF) and SLM-MP surfaces for different immersion time intervals in Tris-HCl buffer solution. "Before SM" refers to samples before surface modification using SAMs and "Week 0" measurements made after surface modification.

6.4. Summary

The as-fabricated SLM surface (SLM-AF) and mechanically polished SLM surface (SLM-MP) were modified using 16-PhDA monolayers. XPS and contact angle measurements were consistent with the formation of monolayers. The surface roughness of the SLM-AF samples did not affect the monolayer formation significantly. 16-PhDA monolayers were found to be stable for over 28 days on both SLM-AF and SLM-MP surface before its desorption. However, a small amount of phosphorous was still observed on both SLM-AF and SLM-MP surface after 42 day time interval. The rough nature of the SLM-AF surface did not have a significant effect on the stability of the attached monolayers. It should be noted that XPS produced comparatively lower signals for as-fabricated SLM-AF surface compared to the mechanically polished SLM-MP surface. The rough nature of the SLM-AF surface was also observed

to affect the wettability measurements leading to scattering of data. Hence the use of a mechanically polished surface would be beneficial for improved XPS intensity and better surface wettability measurements.

7. FUNCTIONALISATION OF SAMs

7.1. Introduction

On studying the in vitro stability of phosphonic acid monolayers, functionalisation of these monolayers with Paracetamol as a model drug was performed. In this chapter, the results obtained using XPS and surface wettability measurements for the adsorption and functionalisation of SAMs on SLM fabricated surface are discussed.

7.2. SAM attachment

As discussed in previous chapters, the SLM-produced surfaces are porous due to partially melted particles. These particles could detach from the surface and can cause acute and chronic effects. If these particles detach after monolayer assembly, those areas will be left without drug attachment since there will be no underlying monolayer to functionalise. XPS was also observed to be sensitive to rough surfaces and thus reducing the signal. Hence, the SLM fabricated surfaces were mechanically polished on one of the surfaces to remove the partially-sintered particles and to attain a smooth surface before surface modification with SAMs and functionalisation with a drug. The average surface roughness (Ra) of the mechanically polished surfaces obtained using a surface profilometer was 590 ± 13.5 nm.

7.2.1. Surface chemistry

Figure 7-1 shows the survey spectra obtained from the mechanically polished Ti6Al4V surface before and after surface modification using 16-PhDA SAMs. The spectra clearly indicate the introduction of a metal phosphonate peak at 133.3 eV showing the surface has been modified with 16-PhDA monolayers. This metal phosphonate peak is due to the formation of Ti-O-P bonds after SAM attachment [56,148]. This has further been justified by an increase in the intensity of carbon and a reduction in the intensity of oxygen, titanium and aluminium after surface modification (due to the limited penetration depth of XPS measurements, less of the underlying metal and oxide is detected).

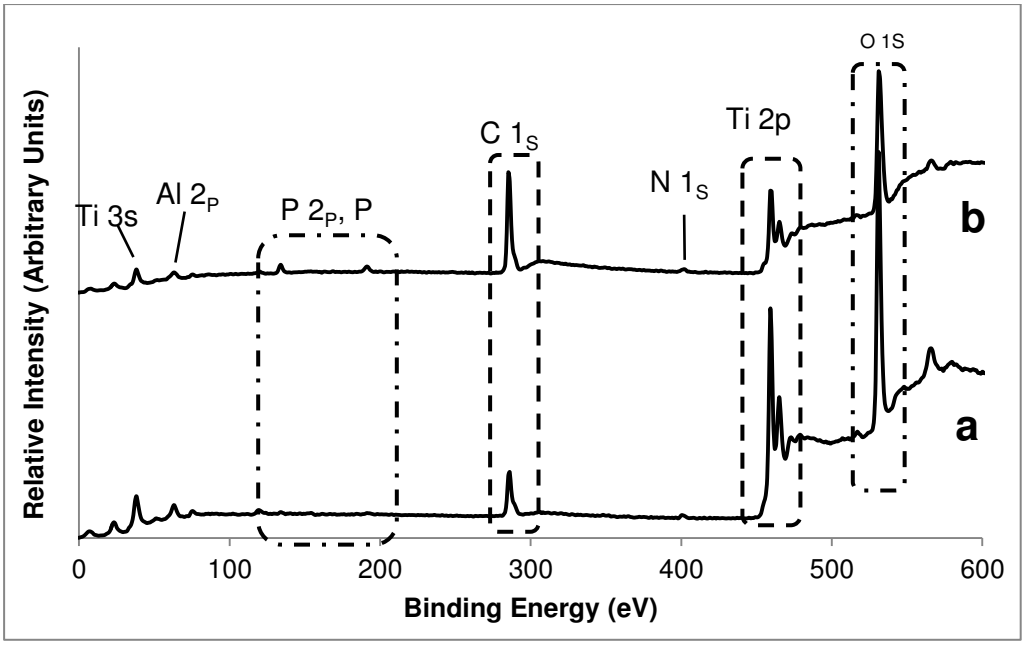

Figure 7-1 Survey spectra showing the change in surface chemistry of a Ti6Al4V surface after SAM attachment. (a) Control surface without SAM coating and (b) After 16-PhDA SAM coating.

Table 7-1 shows the relative atomic composition obtained for the Ti6Al4V surface before and after surface modification. For a surface modified using 16-PhDA, the expected ratio of C:P is 16:1 and in the current study, it is observed to be nearly the same (i.e. 15.6:1). The small variation between the actual and the expected ratio is within the instrument/calibration error (± 10%) limit. High resolution spectra obtained for the phosphorous 2p region showed the formation of a metal-phosphonate bond at 133.3 eV confirming the modification of the surface with monolayers [56].

Table 7-1 Relative atomic percentages of the elements detected in XPS. The calibration error during peak integration in XPS is ± 10%.

	Relative Atomic Percentage								
Sample	**C**	**O**	**N**	**Ti**	**Al**	**V**	**P**	**Cl**	**S**
Control	**21.8** ± 1	**54.5** ± 1.2	**0.2** ± 0.5	**18.2** ± 0.5	**4.7** ± 0.4	**0.6** ± 0.1	**0**	**0**	**0**
16-PhDA SAM	**51.1** ± 1.3	**32.9** ± 0.8	**2.0** ± 0.3	**8.7** ± 0.6	**1.8** ± 0.4	**0.3** ± 0.1	**3.3** ± 0.3	**0**	**0**

The C:P ratio obtained in this chapter for 16-PhDA SAMs was closer to the actual than the C:P ratio of SLM-AF (13:1) and SLM-MP (12:1) obtained in the previous chapter. One of the possible reasons for this difference is the concentration of carbon. An increase or decrease in the carbon concentration

can affect the C:P ratio [190]. Carbon is present in the atmosphere as contaminant. Similarly, contamination is also possible due to oxygen and nitrogen, leading to variations in the C:P ratio. Hoque et al. [190] also observed a difference in C:P ratio due to surface contamination.

7.2.2. Surface wettability

The average static contact angles obtained from the surface before and after surface modification with SAMs were 24° ± 1.3° and 35 ± 3.1° respectively. The contact angles can be observed to increase after SAM attachment showing a change in the surface wettability. A similar trend of a change in contact angle after surface modification using SAMs was previously reported [37]. This change is attributed to confirm the surface modification, since surface wettability is highly specific to the surface chemistry. However, these wettability values are different to the values reported for 'before surface modification' and 'after SAM attachment' in chapter 6. As mentioned in chapter 6, a small disorder in the assembly of monolayers can offer varied surface wettability/contact angles. Since surface profiling of the SAM attached Ti6Al4V surfaces using an AFM was not performed in this study (due to the rough nature of the sample), it is difficult to qualify the monolayer order/arrangement pattern.

Mahapatro et al. [58] reported a significant change in contact angle before cleaning (94.3°) and after cleaning (< 3°) of 316L SS surface (Ra = 0.2 ± 0.1 µm). Also, their varied surface chemical treatment provided them with varied contact angles. On treating bare metal surface with 70% ethanol, acetone and 40% nitric acid separately, their contact angle was 64°. However, this reduced to < 3° on plasma treatment of the chemically treated surface. This shows that varied chemical treatment will provide varied contact angles. Faucheux et al. [48] reported contact angles between 48° and 62° for COOH SAMs for silica and glass substrates (Ra 0.3 nm); whereas, the contact angle observed in the current work was low. This can be due to various factors including surface roughness and monolayer arrangement pattern, varying levels of surface contamination, differences in the purity and pH of water used to measure the contact angle. However, since 16-PhDA SAMs are hydrophilic, possessing a

carboxylic acid (COOH) terminal group, the surface remained highly wettable after surface modification.

7.3. SAMs Functionalisation with Paracetamol

7.3.1. Surface chemistry

After studying the stability of 16-PhDA monolayers on the SLM fabricated Ti6Al4V surface, a sample drug (Paracetamol) was used to functionalise the SAMs. Paracetamol was only used as a model drug to test the reaction mechanism. As described in the methodology, the carboxylic acid group at the terminal end of 16-PhDA SAMs was reacted with thionyl chloride ($SOCl_2$) to form an intermediate acid chloride compound with –COCl as the terminal group. Other than $SOCl_2$ to form an acid chloride, phosphorous trichloride (PCl_3) or phosphorous pentachloride (PCl_5) can also be used. After forming the acyl chloride, this group was then allowed to react with the hydroxyl (–OH) group of Paracetamol to bind the drug covalently to the monolayers. The whole reaction step was performed in an inert atmosphere to prevent the $SOCl_2$ reacting with moisture in the atmosphere to form HCl that could hydrolyse the –COCl to inactive –COOH. It should be noted that no base was used during this reaction.

Scheme 7-2 shows the reaction schemes for the immobilisation of Paracetamol to SLM fabricated Ti6Al4V surface. Figure 7-2 shows the survey spectra for the Ti6Al4V sample before and after drug attachment. The corresponding atomic percentages are given in Table 7-2. It can be clearly noted that there is a significant change in the surface chemistry of the SAM-coated Ti6Al4V surface after the immobilisation of Paracetamol. The ratio of C:P was 15.6 for SAM coated surface and after the attachment of Paracetamol the ratio of C:P was 41. Also, there is an increase in the atomic percentage of nitrogen. These suggest the addition of Paracetamol to the SAM coated surface. This addition of material is likely to be Paracetamol.

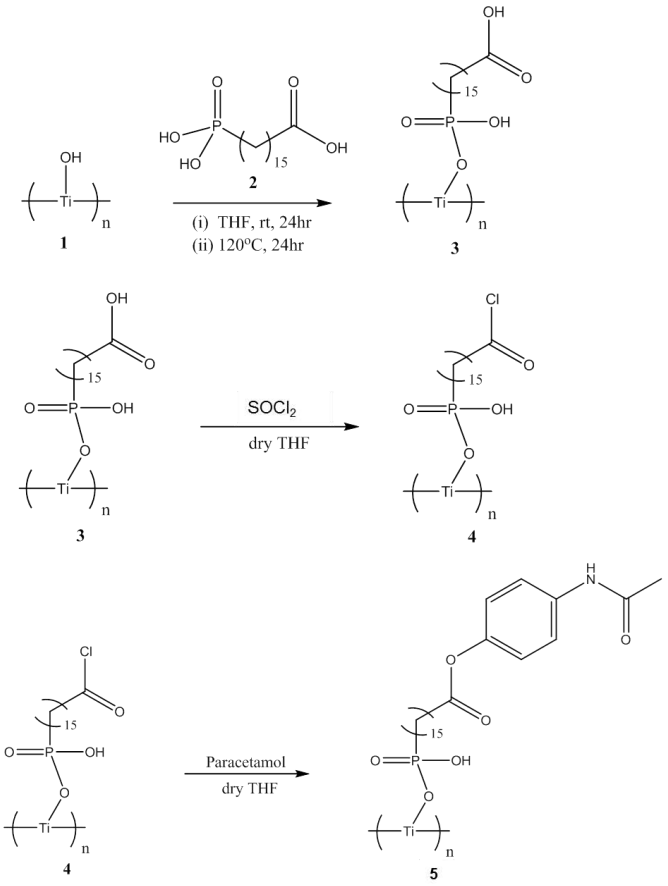

Scheme 7-1 Scheme of reactions to coat 16-PhDA monolayers to a Ti6Al4V surface and to functionalise the monolayers with Paracetamol. Label description: hydroxylated Ti6Al4V surface (1); 16-PhDA SAMs (2); 16-PhDA SAMs chemisorbed to Ti6Al4V surface (3); reaction intermediate (4); Paracetamol immobilised to SAMs (5).

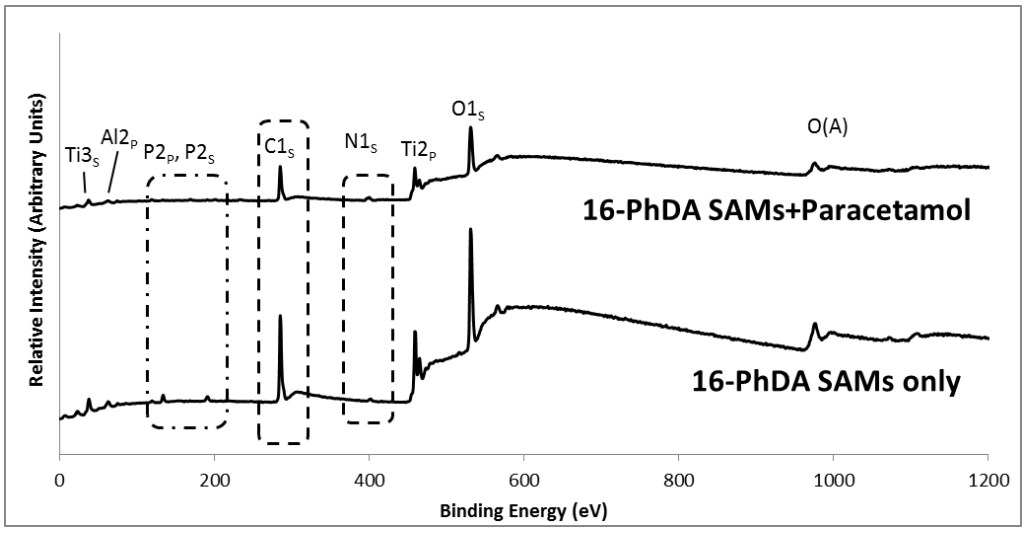

Figure 7-2 Survey spectra obtained using XPS for the SAM coated and Paracetamol coated surfaces. The changes in the intensity of the detected elements before and after drug coating indicate a change in the surface chemistry.

Table 7-2 Relative atomic percentages of elements detected by the XPS in SAM coated and Paracetamol coated Ti6Al4V surfaces. The calibration error during peak integration in XPS is ± 10%.

Sample	Relative Atomic Percentage								
	C	**O**	**N**	**Ti**	**Al**	**V**	**P**	**Cl**	**S**
16-PhDA SAM	**51.1** ± 1.3	**32.9** ± 0.8	**2.0** ± 0.3	**8.7** ± 0.6	**1.8** ± 0.4	**0.3** ± 0.1	**3.3** ± 0.3	**0**	**0**
SAM + Paracetamol	**48.1** ± 1	**35.8** ± 0.9	**4.5** ± 0.4	**7.8** ± 0.7	**1.1** ± 0.3	**0**	**1.2** ± 0.2	**0.8** ± 0.1	**0.9** ± 0.1

Due to the presence of nitrogen in Paracetamol, its concentration was noted to increase; however, this is not a large increase since the drug molecule contains only one nitrogen atom. The concentration of phosphorous (from 16-PhDA) and the underlying metals (titanium, aluminium and vanadium) were observed to decrease and this further confirms the functionalisation of SAMs with Paracetamol. A very small contribution from chlorine and Sulfur was observed after the attachment of Paracetamol and this is likely to be added from the $SOCl_2$ used in the intermediate step.

Carbon contamination is unavoidable as it is present as a contaminant in the atmosphere and in the solvent THF. However, a small amount of nitrogen was also observed on the Ti6Al4V sample as a contaminant in both the control and SAM coated surfaces. The presence of these elements on the metal oxide surface as contaminants has been reported in literature [45,56]. Hence the ratio of carbon to the underlying metal composition of the surface has been used to determine the adsorption of SAMs and Paracetamol to the metal surface.

Figure 7-3 shows the ratio of carbon and oxygen to the underlying metals (titanium + aluminium and vanadium) and the ratio of carbon to oxygen for all three samples (control, SAM attached and Paracetamol coated). It can be observed that the carbon and oxygen concentration increased after SAM attachment and functionalisation showing the attachment of the Paracetamol to the tail group of 16-PhDA monolayers. A similar reduction in the base metal composition after surface modification was reported previously [45].

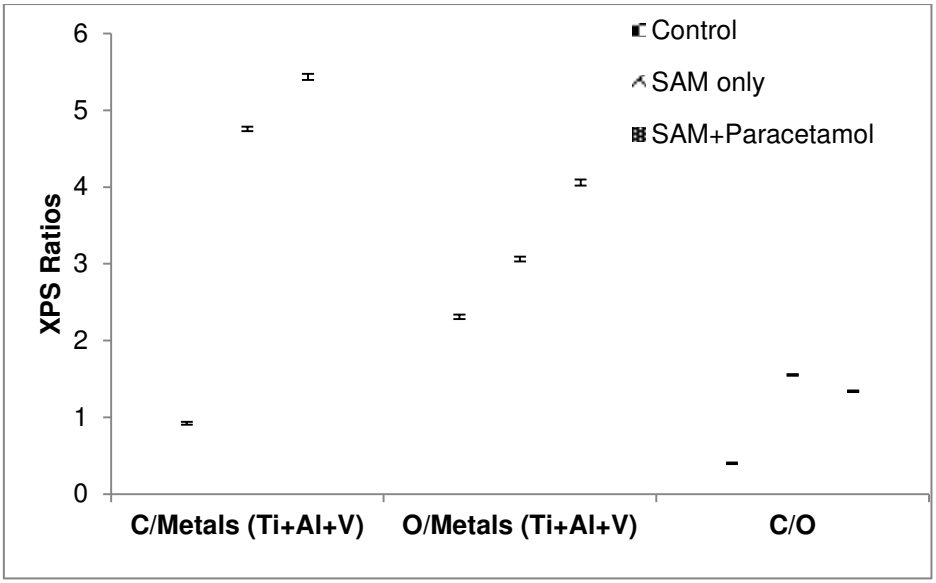

Figure 7-3 Ratio of carbon and oxygen to its underlying metals and C/O ratio for control, SAM coated and Paracetamol coated surfaces.

A comparison of the C 1s spectra obtained for the control, 16-PhDA SAM coated and SAMs functionalised with Paracetamol is shown in Figure 7-4. High-resolution spectrum of C 1s for the control sample was deconvoluted into two components. Peaks formed at 285.3 eV and 286.2 eV were assigned to C-C and C-O of hydrocarbon contaminants. Adsorption of hydrocarbon as a contaminant to metal oxide surfaces have been discussed in previous literature and the major source for this contaminant is adventitious carbon in air, solvents (used for cleaning) and from hydrocarbons (containing proteins and oils) due to manual handling [181,184,193,194].

The C 1s spectrum for the SAM coated Ti6Al4V surface was deconvoluted into three components (Figure 7-4b). The peaks observed at 284.9 eV, 286.5 eV and 289.3 eV were assigned to C-C, C-O and C=O [45]. A significant increase in the relative C-C peak intensity when compared to the control surface was due to the 16 membered carbon chain [$HOOC(CH_2)_{15}PO(OH)_2$] in the 16-PhDA molecule. The C-O and C=O are also from the 16-PhDA molecule, present in the head and tail group of the chain. The significant change in the intensity of C-C, C-O and the introduction of C=O peak confirms the modification of SLM fabricated Ti6Al4V surface with 16-PhDA monolayers.

On characterising the Ti6Al4V surface functionalised with Paracetamol (Figure 7-4c), the deconvoluted C 1s spectrum rendered four components at 284.7 eV, 285.8 eV, 286.9 eV and 289.1 eV. These peaks can be assigned to C-C, C-O, C-N and C=O, respectively [45,144]. Comparing this to the SAM coated surface, the peak intensity of C-C and C=O has changed. Also the introduction of C-N peak at 286.9 eV was observed. This C-N peak is from the amide group in Paracetamol.

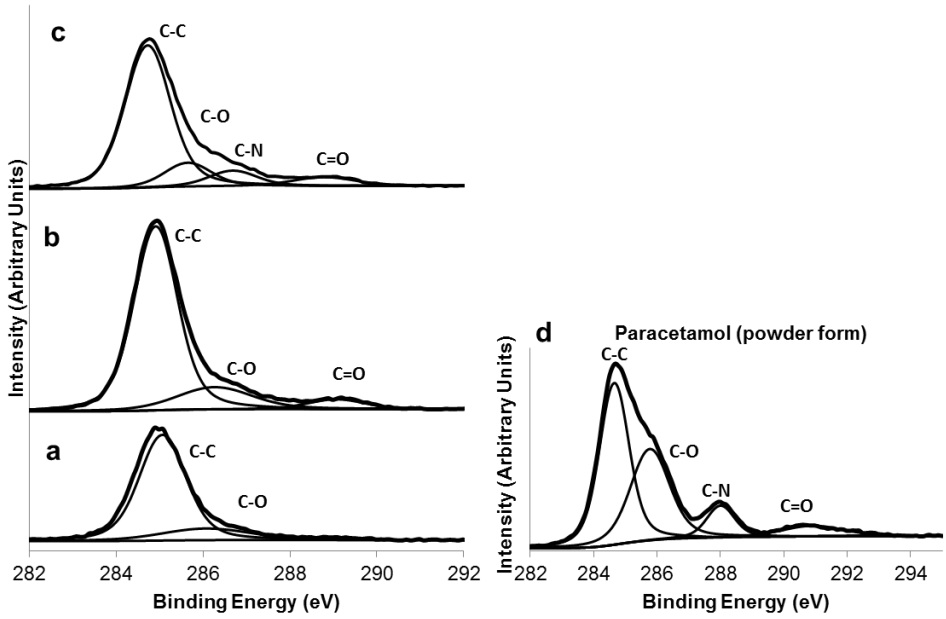

Figure 7-4 High resolution spectra of carbon 1s region obtained for (a) control, (b) SAM attached, (c) Paracetamol coated samples, (d) shows the C 1s region for Paracetamol powder characterised using XPS.

Paracetamol powder in its pure from (as purchased) was characterised using XPS to obtain the spectrum for C 1s region (Figure 7-4d). The deconvoluted spectrum showed the existence of four components C-C (284.7 eV), C-O (286 eV), C-N (288.2 eV) and C=O (291.2 eV) [45,160]. These peaks can be assigned to carbon atoms in hydrocarbon, hydroxyl, amide and ester groups of Paracetamol. The XPS results obtained for Paracetamol coated Ti6Al4V surface were in good agreement with the results obtained for the C 1s region of Paracetamol powder. However, a small change in the peak binding energies was noted and this could be due to errors in peak integration during deconvolution (± 0.1 %) and might also be due to sample charging (± 0.3 eV) of the Paracetamol powder.

The O 1s region spectrum obtained using XPS for the control sample (Figure 7-5a) was deconvoluted into two components, metal oxide at 530.5 eV and oxygen atoms in O-C at 532.1 eV [156,183,195]. The metal oxide peak observed at 530.5 eV is likely to be mostly due to titanium oxide; however, a small proportion of aluminium and vanadium oxides is also possible due to the presence of these elements in Ti6Al4V alloy. In agreement with the C 1s spectrum, the O 1s spectrum also showed the existence of O-C species on the control sample as contaminants.

On deconvoluting the O 1s spectrum for the 16PhDA SAM coated Ti6Al4V surface, three components were obtained (Figure 7-5b). The peaks formed at 530.4 eV, 531.9 eV and 533.2 eV were assigned to metal oxides, O-C and O=C, respectively [156,183,196]; however, there is also the possibility for a small contribution from aluminium oxide for the peak observed at 531 eV. The relative intensity of metal oxide peak at 530.4 eV for the SAM coated sample can be observed to decrease and the O=C peak at 533.2 eV to increase when compared to the control sample. The introduction of O=C at 533.2 eV should mostly derive from the carboxylic group at the terminal end of the 16-PhDA molecule. These observed changes compared with the control sample can be attributed to the adsorption of 16-PhDA monolayers on to the SLM fabricated Ti6Al4V surfaces.

After functionalising SAMs with Paracetamol, the deconvoluted O 1s XPS spectrum rendered three components metal oxide (530.8 eV), O-C (532.1 eV) and O=C (533.4 eV) and are shown in Figure 7-5c. Although the O-C and O=C are expected only from Paracetamol, a small contribution from the underlying monolayers is possible (see 7-5b). The XPS characterisation of Paracetamol powder for the O 1s region rendered two components including O-C (531.7 eV) and O=C (533.1 eV) on deconvolution [183] as shown in Figure 7-5d. On comparing the deconvoluted O 1s peaks obtained for the Paracetamol coated surface with the O 1s peaks obtained for the Paracetamol powder, both the peaks were in good agreement. However, there was a slight variation in the binding energies. This further confirms the attachment of Paracetamol to the 16-PhDA adsorbed Ti6Al4V surface.

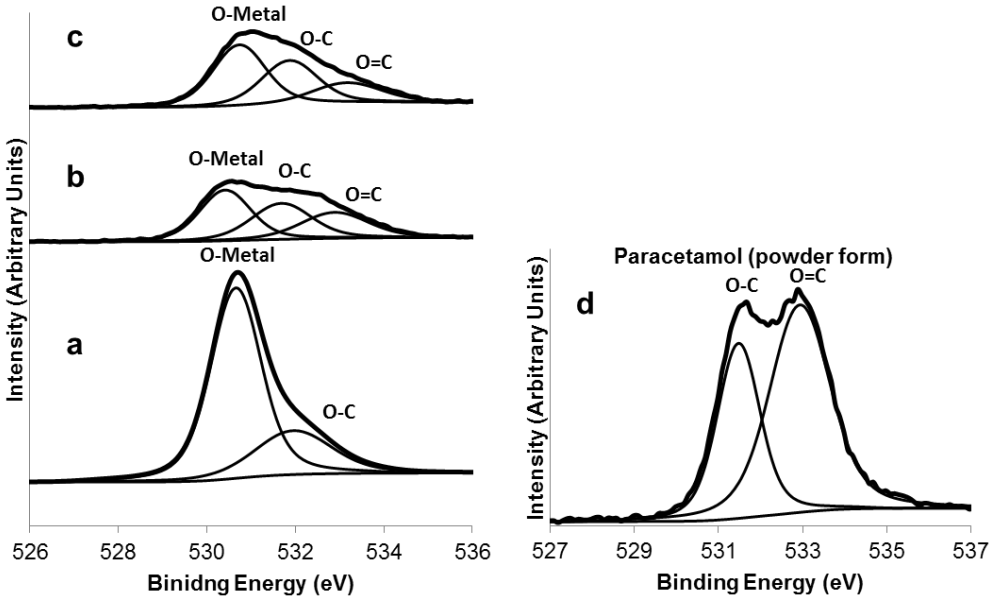

Figure 7-5 XPS spectra obtained for the oxygen 1s region for (a) control, (b) SAM attached, (c) Paracetamol coated samples, (d) shows the O 1s region for Paracetamol powder characterised using XPS.

Deconvoluted N 1s spectrum showed the presence of N-C and N-O at 400.3 eV and 402.6 eV respectively on the control surface (Figure 7-6a). Although nitrogen is not expected on the Ti6Al4V surface (as it is not in the composition), a small amount of nitrogen was observed. Similar to carbon, nitrogen also has strong affinity towards metal oxides and their presence on metal oxide surfaces could be from nitrogen containing carbon contaminants [45]. Similar to the control sample, the SAM coated surface also showed the existence of nitrogen at 400.1 eV (N-C) and 402.3 eV (N-O) after deconvolution (Figure 7-6b) [181]. This could also be from contamination of the surface as the peaks were observed similar to the control samples. Furthermore, the 16-PhDA SAMs do not have nitrogen in their structure.

The deconvoluted N 1s spectrum for the Paracetamol coated Ti6Al4V surface also showed two components, N-C at 400.1 eV and Ti-Ox-Ny at 401.9 eV (Figure 7-6c). Although a small contribution to these peak from contaminants is possible since the other samples (control and SAM coated) were shown to have contaminants, the N-C peak is distinct and increased in relative intensity.

XPS characterisation of Paracetamol powder for the N 1s region showed a single N-C peak at 400.3 eV (Figure 7-6d).

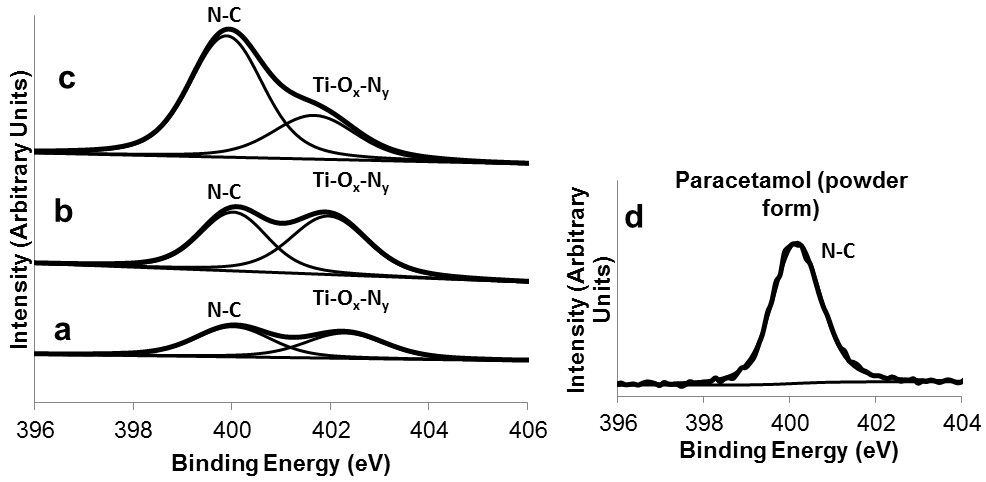

Figure 7-6 N 1s region for (a) control, (b) SAM attached, (c) Paracetamol coated samples, (d) Paracetamol powder, characterised using XPS.

7.3.2. Surface wettability

Static contact angles obtained for the control, 16-PhDA SAM attached and Paracetamol coated surfaces are shown in Figure 7-7. Figure 7-8 shows the contact angle values obtained graphically. It can be observed that the control and 16-PhDA SAM deposited surfaces were highly wettable whereas the Paracetamol coated surface was more hydrophobic. The wettability of the control surface was due to the presence of metal oxides which impart a high surface energy. Wettability of the 16-PhDA SAM coated surfaces was due to the presence of carboxylic acid in their terminal group. A similar increase in contact angle after SAM modification was reported in literature [54,58]. The difference in the contact angle is due to the change in surface chemistry. Control Ti6Al4V surface will present hydroxylated surface oxide layer, and COOH-SAM modified Ti6Al4V surface will also present hydroxylated surface. However, it is not always possible to get a very well packed SAMs. Even if there is a small change in the ordering, this will affect the contact angle. Hence this might be the reason for the difference in contact angle before and after SAM attachment. Since the SAM coated surface was functionalised with Paracetamol, it would be expected that a methyl group ($-CH_3$) is exposed as the terminal group leading to a lower energy surface. In agreement with

this, the measured contact angles showed the Paracetamol coated surface to be more hydrophobic with a contact angle higher than 90°. Mahapatro et al. [197] reported a change in the surface wettability from hydrophilic to hydrophobic surface after the attachment of Ibuprofen to SAMs. Thus the change in surface wettability is consistent with the functionalisation of Paracetamol to 16-PhDA SAMs coated on the SLM fabricated Ti6Al4V surfaces.

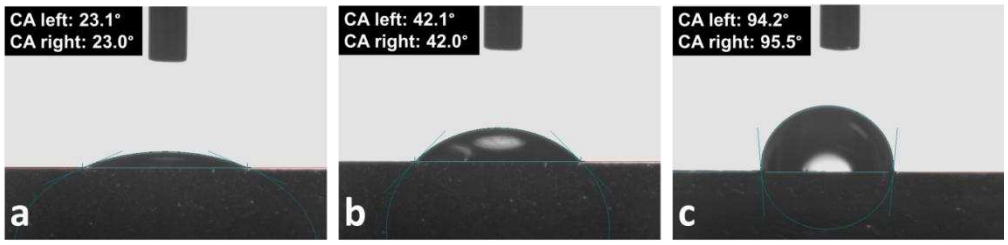

Figure 7-7 Contact angles obtained for SLM fabricated Ti6Al4V surfaces after cleaning (a), 16-PhDA SAM attachment (b) and Paracetamol attachment (c).

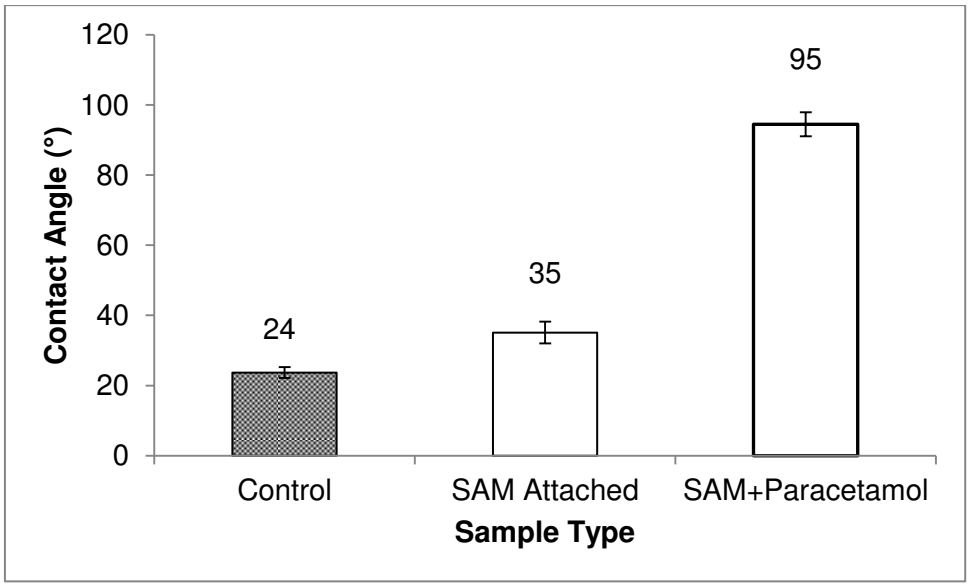

Figure 7-8 Static water contact angle obtained for Control, SAM coated and Paracetamol coated Ti6Al4V samples.

Although the changes in the surface chemistries of Ti6Al4V surfaces revealed the functionalisation of Paracetamol to SAMs, the use of Paracetamol as a model drug may not be advisable. This is mainly because of two reasons. The first being, Paracetamol does not have a distinct element that could easily be characterised. The elements constituting Paracetamol are carbon, nitrogen,

oxygen and hydrogen. All of these elements are present in the atmosphere as contaminants. Hence, the use of these elements to confirm the reaction may lead to false results. The second reason is, Paracetamol is a phenolic compound. On functionalising Paracetamol to COOH SAMs, a phenolic ester is formed. In general phenolic esters will hydrolyse readily in the presence of a hydroxyl group to form an alcohol and carboxylic acid [172]. Hence, moisture in the atmosphere can hydrolyse the drug. Thus they have poor oxidative stability and will also show a rapid release under physiological conditions. Thus Paracetamol may not be the best choice of drug for these reasons.

Pyrene derivatives such as hydroxy-pyrenes, amino-pyrenes can be used to study the functionalisation since they have a better hydrolytic stability than phenolic esters. In addition to this, they are fluorescent compounds and hence they could be easily characterised using a fluorescence microscopy. However, these compounds mainly constitute carbon and nitrogen, which are present in atmosphere. This could limit the use of characterisation equipment such as XPS.

Fluoroquinolone compounds such as Ciprofloxacin®, Levofloxacin®, Ofloxacin® may be a better choice than Paracetamol and Pyrene derivatives since they have a distinct fluorine atom (not usually present in air as contaminant) attached to the central benzene ring that could easily be characterised in FTIR and XPS. Also, most of the fluoroquinolones exhibit fluorescence property, which could then be used for characterisation in fluorescence microscopy to determine the surface coverage of the compound [198]. Since these compounds being antibiotic, simple biological tests can be performed to confirm the drug attachment and its activity. Thus a careful consideration is required when selecting a model drug.

7.4. Summary

Changes observed in the surface chemistry of the Ti6Al4V surface at each stage through XPS characterisation and surface wettability measurements are consistent with the functionalisation of monolayers with Paracetamol. This chapter showed the successful immobilisation of Paracetamol to 16-PhDA SAMs attached to a SLM fabricated Ti6al4V surface. However, nitrogen alone

cannot be used as a key element to confirm Paracetamol attachment, since it is present on the surfaces as a contaminant and may affect the result. Also, phenolic esters hydrolyse readily. Hence, the use of compounds with distinct elements that is unlikely to be present in the atmosphere as contaminants should be used to prevent contamination affecting the results of future studies.

8. IMMOBILISATION OF CIPROFLOXACIN®

8.1. Introduction

In this chapter, immobilisation of an anti-bacterial drug, Ciprofloxacin®, to SAMs using the previously stated procedure for Paracetamol is described. Drug quantification studies, in vitro and oxidative stability of the drug, drug release profile and antibacterial susceptibility of Ciprofloxacin® adsorbed to a SLM fabricated Ti6Al4V surface are presented.

8.2. SAM attachment

8.2.1. Surface chemistry

XPS survey spectra for the control octadecylphosphonic acid (ODPA) SAM coated and 16-phosphanohexadecanoic acid (16-PhDA) SAM coated Ti6Al4V samples are shown in Figure 8-1. Peaks for the major alloying elements Ti and Al are clearly visible from the spectra. Since the Ti6Al4V surface predominantly contained oxides of Ti and Al, the amount of V observed on the surface was considerably less (<0.3%). Hence the V peak is not clearly visible in the spectra. The relative atomic percentages of the detected elements before and after surface modification are shown in Table 8-1.

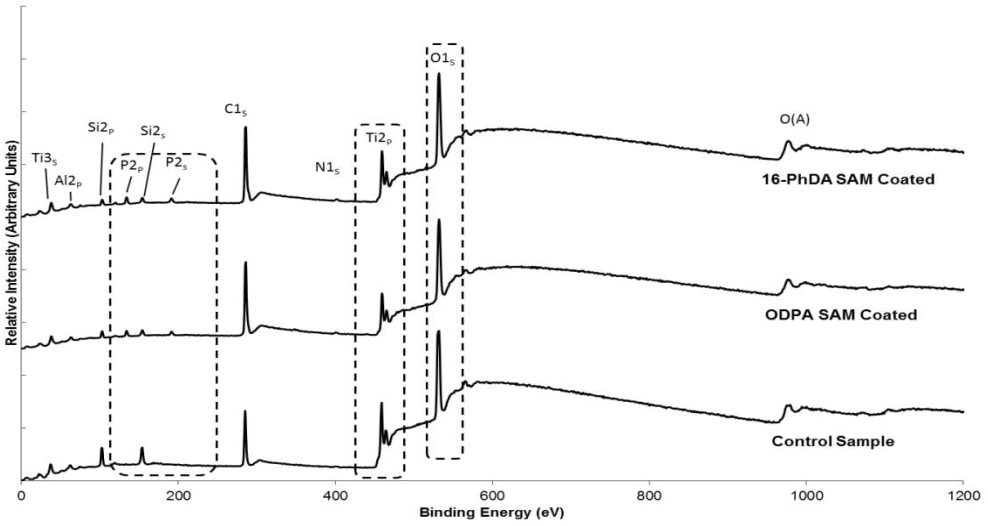

Figure 8-1 Survey spectra shows the change in the intensity of C 1s peak before and after SAM attachment and the introduction of P 2p peak after SAM attachment thus confirming the attachment of 16-PhDA SAMs and ODPA SAMs to the Ti6Al4V surface.

Table 8-1 Relative atomic percentage of the elements detected by XPS after different surface treatments. The calibration error during peak integration in XPS is ± 10%.

Detected Elements		Sample Type				
		Control	**16-PhDA SAM Coated**	**16-PhDA SAM + Drug Coated**	**ODPA SAM Coated**	**ODPA SAM + Drug Coated**
Al 2p	**Mean**	**4.19**	**2.39**	**1.24**	**2.44**	**2.26**
	S.E	± 0.4	± 0.2	± 0.1	± 0.1	± 0.2
Ti 2p	**Mean**	**17.72**	**7.57**	**4.68**	**5.7**	**4.55**
	S.E	± 0.6	± 0.4	± 0.3	± 0.4	± 0.2
V 2p	**Mean**	**0.63**	**0**	**0**	**0**	**0**
	S.E	± 0.1	0	0	0	0
C 1s	**Mean**	**22.61**	**53.68**	**60.57**	**54.18**	**56.87**
	S.E	± 1	± 0.5	± 0.7	± 0.5	± 0.7
O 1s	**Mean**	**50.93**	**31.05**	**24.84**	**31.87**	**28.27**
	S.E	± 1	± 0.4	± 0.8	± 0.5	± 0.6
N 1s	**Mean**	**1.19**	**0.82**	**4.1**	**1.4**	**2.38**
	S.E	± 0.1	± 0.1	± 0.5	± 0.2	± 0.1
F 1s	**Mean**	**0**	**0**	**1.5**	**0**	**0.63**
	S.E	0	0	± 0.1	0	± 0.1
P 2p	**Mean**	**0**	**3.51**	**2.29**	**3.02**	**2.38**
	S.E	0	± 0.2	± 0.1	± 0.21	± 0.2
Cl 2p	**Mean**	**0**	**0**	**0.41**	**0**	**0.28**
	S.E	0	0	± 0.1	0	± 0.1
S 2p	**Mean**	**0**	**0**	**0.37**	**0**	**1.35**
	S.E	0	0	± 0.01	0	± 0.1
Si 2p	**Mean**	**2.73**	**1.98**	**0**	**1.39**	**1.03**
	S.E	± 0.8	± 0.6	0	± 0.6	± 0.5

On comparing the spectra obtained for 16-PhDA and ODPA SAM coated samples with the control spectrum, the intensity of C 1s peak is significantly higher for the SAM coated samples. Also the intensities of O 1s and Ti 2p

peaks were lower for the SAM coated samples compared to the control sample. The presence of phosphorous from 16-PhDA and ODPA SAMs was confirmed by the existence of P 2p (133.3 eV) and P 2s (193.1 eV) peaks on the SAM coated surfaces but not on the control surface. The atomic percentage of phosphorous was much lower than that of carbon, consistent with the presence of only one phosphorous atom in 16-PhDA. The obtained C:P atomic ratio for the Ti6Al4V surface coated with 16-PhDA SAMs was 15.3:1; however, a ratio of 16:1 would be expected. This small difference in the ratio lies within the error limit of ± 10% due to the integration the P 2p peak.

Similarly, for the ODPA SAM coated surface a ratio of 18:1 would be expected and the obtained ratio was 17.9:1. These values are in good agreement with the literature previously reported for the modification of metal surfaces with 16-PhDA and ODPA SAMs [54,55,148]. Thus, the XPS results confirmed the successful deposition of 16-PhDA and ODPA SAMs on the SLM fabricated Ti6Al4V surface. Carbon contamination of the control surface was witnessed by XPS and this could be from the adventitious carbon present in the atmosphere [183]. A small amount of silicon was observed on the Ti6Al4V surface at all stages. This may be attributed to the contamination of the samples during polishing with silicon carbide grits or during further processing or characterisation.

8.2.2. Surface wettability

The contact angle formed at an interface is sensitive to the molecular structure of the surface and renders a measure of hydrophobicity or hydrophilicity of the surface. These can also be attributed to the SAM arrangement and uniformity of the surface coverage [55]. Hence, static water contact angle measurements were performed using a contact angle goniometer to determine the change in surface chemistry before and after surface modification with SAMs. Figure 8-2 shows the static water contact angles measured for the control, 16-PhDA SAM coated and ODPA SAM coated samples.

The contact angle value obtained for the control sample (after cleaning) showed the hydrophilic nature of the Ti6Al4V surface. After surface

modification with SAMs, this was observed to change. The 16-PhDA SAM coated surface exhibited a hydrophilic nature due to the presence of a carboxylic acid (-COOH) group in its terminal end (figure 8-2). On the other hand, the ODPA SAM coated surface rendered a hydrophobic surface due to the presence of a methyl group ($-CH_3$) in its terminal group. Previous literature showed the contact angle for ODPA SAM coated surface between 90° – 120° [54,55,190]. The obtained contact angles for the ODPA SAMs were in agreement with the previously reported values.

On comparing the obtained contact angles with chapter 7, the contact angle for the Ti6Al4V substrate after cleaning was observed to be the same; however, the contact angle of 16-PhDA SAM coated surface was different. As discussed in previous chapters, the deviation in contact angle can be due to various factors including SAM arrangement, surface cleanliness, surface roughness and more importantly, the surface contamination. In agreement with the XPS data, the change in surface wettability also confirmed the adsorption of 16-PhDA and ODPA SAMs to the Ti6Al4V surfaces.

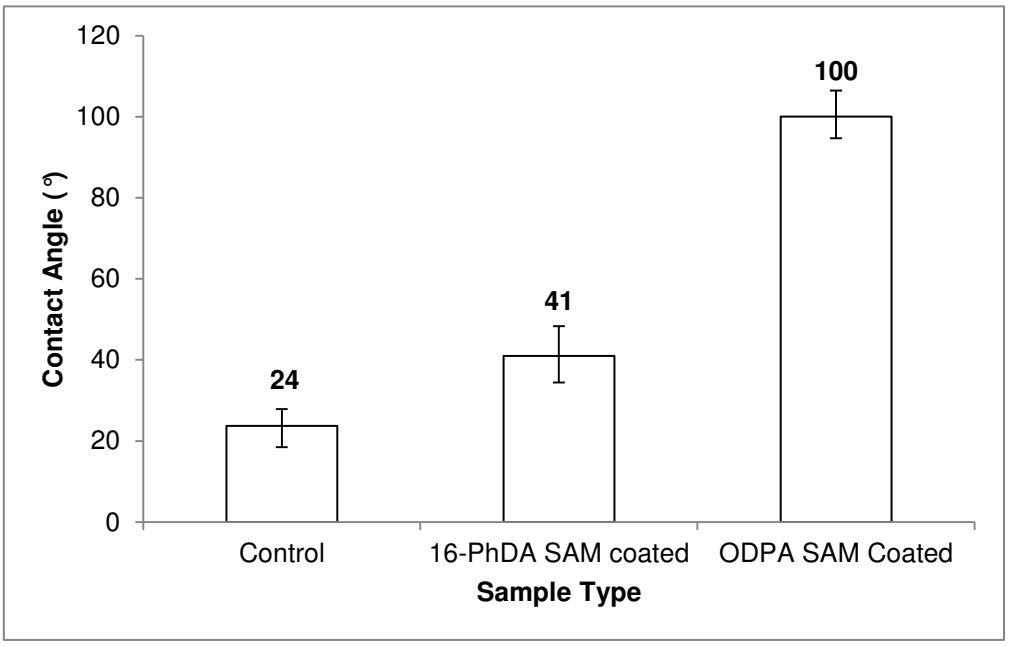

Figure 8-2 Static water contact angle showing a change in the wettability of the surface after coating the surfaces with monolayers.

8.3. Functionalisation of SAMs with Ciprofloxacin®

8.3.1. Surface chemistry

The relative atomic percentages of elements detected before and after surface modification with SAMs and Ciprofloxacin® have been shown in Table 8-1. From the table, changes in the relative atom percentage of elements were observed for both 16-PhDA and ODPA SAMs after functionalising with Ciprofloxacin®. However, 16-PhDA SAMs functionalised with Ciprofloxacin® showed a more significant change than the ODPA SAMs functionalised with the drug. After functionalising 16-PhDA SAMs with Ciprofloxacin, a C:F ratio of 33:1 would be expected and the obtained results were approximately 40:1. This difference in the ratio is believed to be due the ± 10% error in the peak integration and surface contamination before and during surface characterisation. Also, the carbon contamination of the drug coated surface might also be a contributing factor.

Although a small increase in the relative atomic percentage of C, N and a decrease in the relative atomic percentage of Al, Ti, O and P was observed for ODPA SAMs functionalised with the drug, this is not considered to be significant (Table 8-1). This is because the atomic percentage of fluorine obtained for ODPA SAMs functionalised with the drug was less than half of the relative atomic percentage of F for 16-PhDA SAMs functionalised with the drug. A C:F ratio of 35:1 would be expected for ODPA SAMs functionalised with Ciprofloxacin®; however, the obtained ratio was nearly 90:1. This is possibly because the tail group of the ODPA SAMs were not functionalised with the drug due to the unavailability of a reactive group (such as –OH, -COOH and -NH-) in ODPA SAM's tail end. This shows that the small change in the relative intensities and relative atomic percentage for the ODPA SAMs after treating with Ciprofloxacin® may be due to the physisorbed drug molecule on the surface.

Figure 8-3 shows the XPS spectra of the ODPA SAM coated Ti6Al4V before and after functionalisation with Ciprofloxacin®. Whilst functionalisation of methyl (-CH_3) terminated SAMs with Ciprofloxacin® are not possible, a small

change in the surface chemistry of the ODPA SAM coated surface after functionalisation can be observed from the spectra. A change in the intensity of C, Ti, N and Al was observed along with the addition of fluorine at 688.2 eV. These changes can be due to the physisorption of Ciprofloxacin® to the ODPA SAM coated surface. There is also the possibility for the drug to displace some ODPA and bond directly to the metal surface or perhaps fill the gaps in the monolayer by binding to the surface. Similar to the functionalisation of 16-PhDA SAMs with Ciprofloxacin®, the ODPA SAMs functionalised with the drug also showed the physisorption of chlorine and Sulfur to its surface from the intermediate step. The other potential binding site for Ciprofloxacin® is through the amine group [171]. However, as previously discussed in the methodology, since no base was used in this reaction, the reaction is believed to occur through the carboxylic group to form acid anhydride rather than an amide.

As the functional group of both Ciprofloxacin® and the 16-PhDA SAMs is a carboxylic group (-COOH), they will not react with each other under normal condition. Hence in order to provide favourable reactive conditions, the 16-PhDA SAM coated surfaces were treated with thionyl chloride ($SOCl_2$) in an inert atmosphere to form an acid chloride. Now, the reactive –COOH group in Ciprofloxacin® will readily react with the –OCl group of SAMs to immobilise Ciprofloxacin® to SAMs (depending on the reaction conditions the amine group in the Ciprofloxacin® molecule may also react with the SAMs). However this is not possible with the ODPA SAMs since they do not have a reactive terminal group.

Figure 8-4 shows the XPS survey spectra for 16-PhDA SAMs coated Ti6Al4V surface functionalised with Ciprofloxacin®. The spectra clearly indicate a change in the surface chemistry after functionalising the 16-PhDA SAM coated surface. The intensity of carbon at 285 eV was observed to increase after the drug attachment compared to the 16-PhDA SAM coated surface. This increase is due to the presence of carbon in Ciprofloxacin®. The intensity of nitrogen at 400.1 eV was also observed to increase due to the presence of N

(one secondary amine and 2 tertiary amines) in the chemical structure of Ciprofloxacin®.

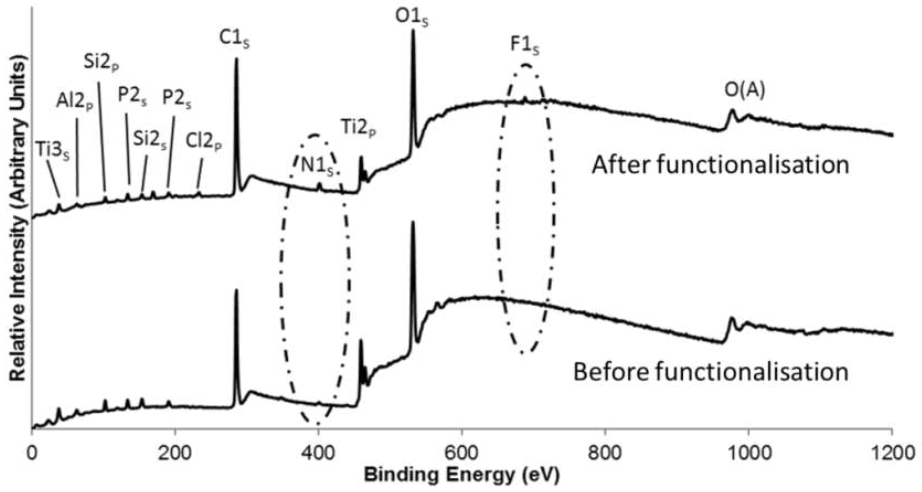

Figure 8-3 XPS survey spectra before (bottom) and after (top) functionalisation of a ODPA SAM coated surface.

After functionalising the 16-PhDA SAMs with the drug, an addition of fluorine (at 687.6 eV) to the SAM coated surface was observed. This fluorine is from fluorocarbon present in the drug molecule. A small amount of silicon observed on the SAM coated surface was noted to further decrease after the drug attachment. Further to these changes, the decrease in the intensity of Al 2p, Ti 2p, O 1s and P 2p after drug attachment also confirmed the successful functionalisation of 16-PhDA SAMs with Ciprofloxacin®. A very small amount of sulfur in its oxidised form at 168 eV and chlorine at 193.9 eV was observed. These sulfur and chlorine atoms were bound to the surface as contaminants from the intermediate step in which $SOCl_2$ was used to convert the carboxylic group of the 16-PhDA SAMs.

High resolution C 1s (a), O 1s (b), N 1s (c) and F 1s (d) spectra obtained for the control, 16-PhDA SAM coated and 16-PhDA SAMs functionalised with Ciprofloxacin® were deconvoluted and are shown in Figure 8-5. The position of the peak and the contribution of a particular spectra peak depend on the type of substrate and the chemical deposited on it. From the C 1s spectra, the control C 1s spectrum was deconvoluted into two components and the peaks at 285.1 eV and 286.6 eV were assigned to C-C and C-O species of the hydrocarbon [144].

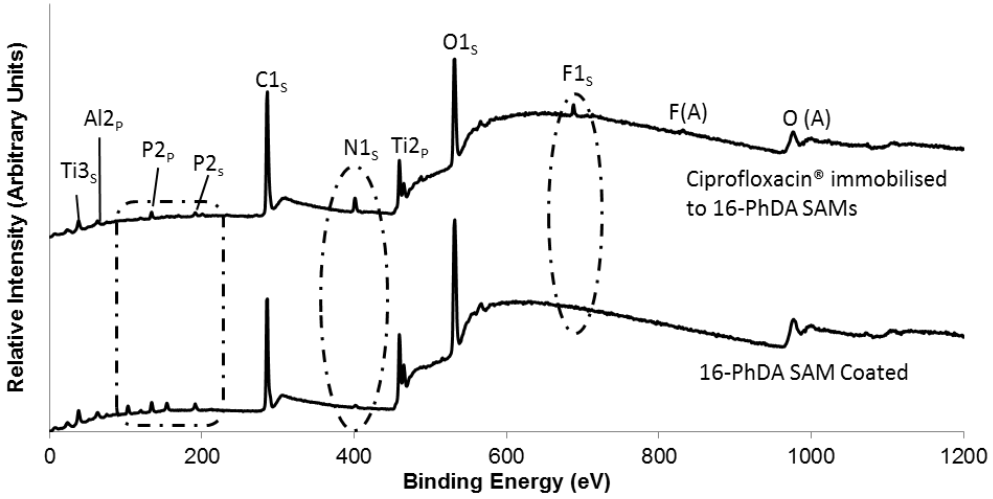

Figure 8-4 XPS survey spectra showing the change in the surface chemistry after functionalising 16-PhDA SAMs with Ciprofloxacin®. Note the presence of F 1s peak at 687.6 eV and increase in the intensity of N 1s peak at 400.7 eV.

The C 1s spectrum of the 16-PhDA SAM coated Ti6Al4V surface was deconvoluted into three components. The peaks formed at 285 eV, 286.7 eV and 289.4 eV were assigned to C-C, C-O and C=O species of the 16-PhDA SAM molecule [137,156,196]. The deconvoluted C 1s spectrum of SAMs functionalised with Ciprofloxacin® also rendered three components at 284.8 eV, 286.3 eV and 288.9 eV and are assigned to C-C, C-O and C=O species [45]. On comparing the C 1s spectra for all three samples, an introduction of C=O species was observed after SAM coating and drug coating. This carbonyl (C=O) peak was not observed for the control surface showing that the peak should essentially be from the SAM and drug molecule. Furthermore, an increase in the intensity of the C-O peak after functionalising the SAM coated surface with the drug shows the possibility for the attachment of Ciprofloxacin® to the 16-PhDA SAMs.

The O 1s peak for the control Ti6Al4V surface was deconvoluted into two components and the peaks at 530.5 eV and 532.7 eV were assigned to metal oxide and hydroxyl groups, respectively. On surface modification with 16-PhDA SAMs, the deconvoluted O 1s spectrum showed three components including metal oxide (530.3 eV), O-C (531.2 eV) and O=C (532.5 eV) [144]. A small contribution from the P=O at 531.2 eV and P-O at 532.5 eV is also possible [55]. Also, on functionalisation with Ciprofloxacin®, similar groups were observed at 530 eV (metal oxides), 531.3 eV (C-O) and 532.6 eV (C=O).

In agreement with C 1s spectra, the O 1s spectra also showed a significant change confirming the change in surface chemistry.

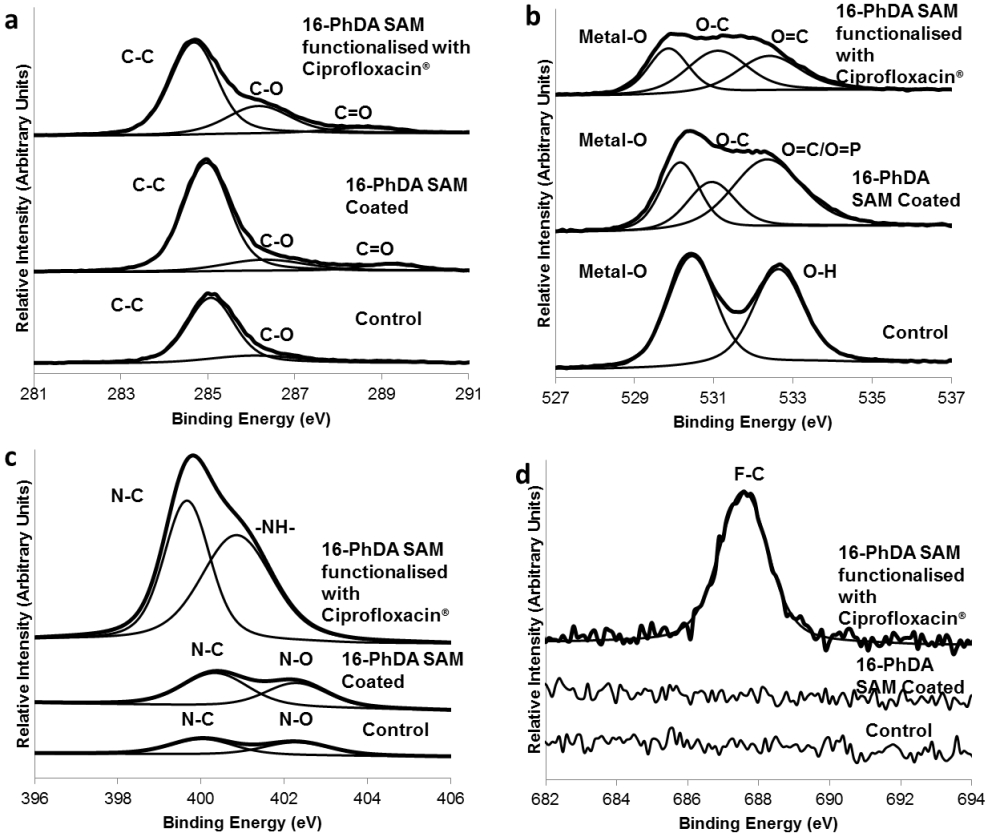

Figure 8-5 Deconvoluted a) C 1s, b) O 1s, c) N 1s and d) F 1s spectra obtained using XPS for control, SAM coated and drug coated surfaces.

The deconvoluted N 1s spectrum for the control and SAM coated Ti6Al4V surfaces showed nitrogen in the form of contaminants (N-C and N-O) [45,132,181]. On functionalising the SAMs with Ciprofloxacin, the deconvoluted spectrum showed a significant change. The N-C at 399.8 eV and amine group (-NH-) at 401.2 eV corresponds to the amino carbons in the Ciprofloxacin® molecule. High resolution F 1s spectra showed the presence of fluorine atom only on the Ciprofloxacin functionalised surface and not on the control and SAM coated surface. These changes in the C 1s, O 1s, N 1s and F 1s confirm the successful functionalisation of 16-PhDA SAMs with Ciprofloxacin®.

Figure 8-6 shows the C 1s and O 1s spectra obtained for the pure Ciprofloxacin® powder. Deconvoluted C 1s spectrum showed the presence of

C-C (285 eV), C-O (286.3 eV) and C=O (287.8 eV) [181]. The deconvoluted O 1s spectra showed O-C and O=C peaks at 531 eV and 532.6 eV [45,132,181,183]. Also, the Ciprofloxacin® powder showed a single N 1s peak at 400.7 eV and F 1s peak at 687.5 eV. On comparing these spectra with the C 1s and O 1s spectra obtained for 16-PhDA SAMs functionalised with Ciprofloxacin®, a good agreement of the peaks were observed. This further confirmed the successful attachment of Ciprofloxacin® to the 16-PhDA SAMs coated on SLM fabricated Ti6Al4V surface.

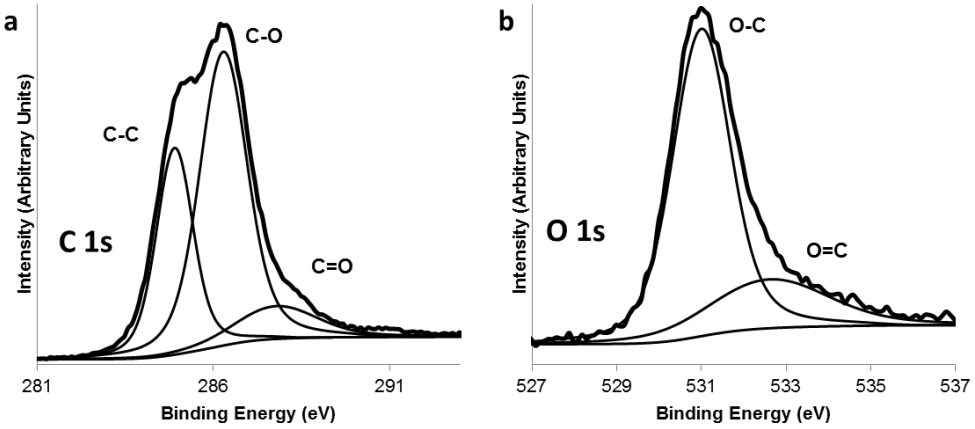

Figure 8-6 Deconvoluted C 1s and O 1s spectra for Ciprofloxacin® powder obtained using XPS.

The FTIR characterisation results obtained for the drug coated Ti6Al4V substrates were inconclusive. No significant peak for the expected amide (1640 – 1609 cm^{-1} or anhydride (1830 – 1800 cm^{-1} and 1775 – 1740 cm^{-1}) was observed in the spectra (see appendix 3). The major factor for this could be the sample roughness. In FTIR, after the infrared light hits the sample, the reflected infrared light between the prism and sample provides the information about the sample's surface chemistry. In order to get a good signal, a good contact between the surface of the substrate and the prism is essential. Although the pressure arm helps ensuring this contact, surface roughness of the Ti6Al4V substrates could have significantly affected this contact. Also, the roughness pattern could have affected the beam reflection. As a result of these issues, the FTIR did not show any significant result to confirm the drug coating. Hence, analysing rough metal sample surfaces using this pressure arm

supported FTIR may not be the best choice. However, further studies can be performed by functionalising Ciprofloxacin® to a smooth surface.

8.3.2. Surface wettability

In addition to the XPS results, the static contact angle measurements also confirmed the functionalisation of 16-PhDA SAMs with Ciprofloxacin®. The transformation of wettable (hydrophilic) surface observed before surface modification to a non-wettable surface (hydrophobic) after drug attachment shows a change in the surface wettability (Figure 8-7). This hydrophobic nature can be attributed to the presence of hydrocarbon in the terminal group of Ciprofloxacin® molecules. The ODPA SAMs functionalised with Ciprofloxacin® did not show a significant difference since the surface was already hydrophobic. Also, as stated earlier, due to the non-availability of a functional group in the terminal end, the ODPA SAMs cannot be functionalised with Ciprofloxacin®.

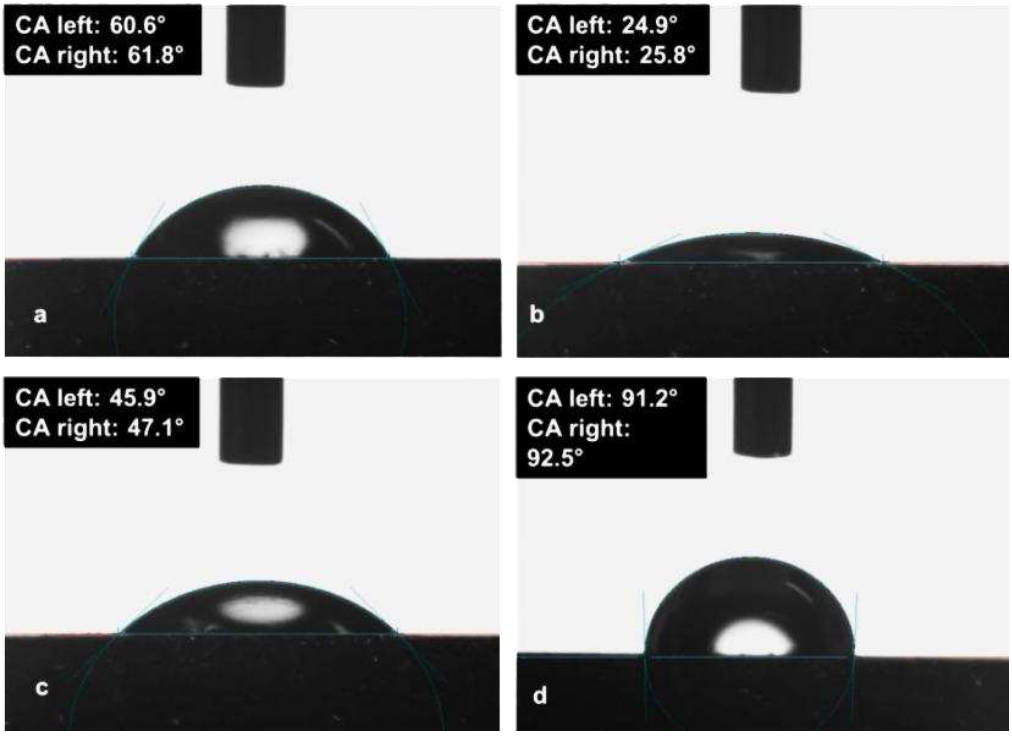

Figure 8-7 Static contact angle measurements using a contact angle goniometer. a) Before cleaning; b) after cleaning; c) after 16-PhDA SAM attachment and d) after immobilisation of 16-PhDA SAMs with Ciprofloxacin®.

8.4. Stability Studies

8.4.1. Oxidative stability of Ciprofloxacin®

8.4.1.1. Surface chemistry

Figure 8-8 gives detailed high resolution XPS spectra of the convoluted peaks for the C 1s, O 1s, N 1s and F 1s regions under oxidative conditions. The peaks for all elements were observed to be very consistent for the whole duration of the oxidative exposure.

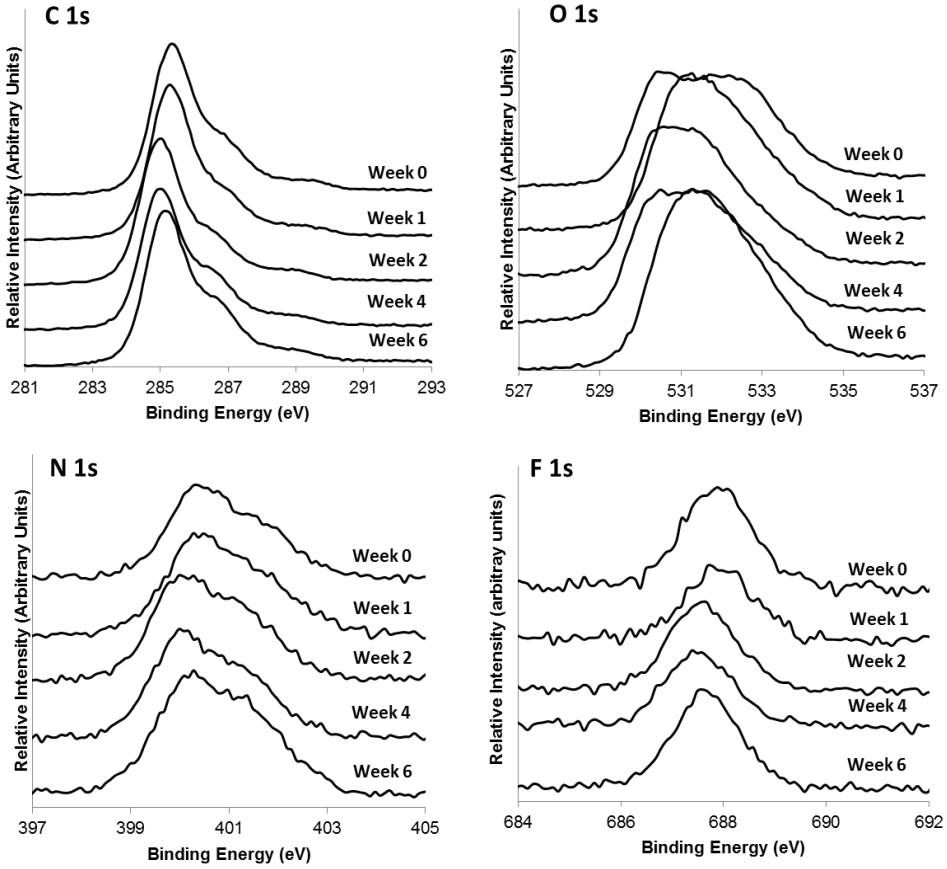

Figure 8-8 Relative intensity of C 1s, O 1s, N 1s and F 1s spectra obtained using XPS for samples exposed to oxidative conditions for different time intervals.

Table 8-2 XPS determined relative atomic percentages of elements detected for different oxidative exposure time intervals. The calibration error during peak integration in XPS is ± 10%.

Detected Elements		Relative Atomic Percentage (%)				
		After Immobilisation	**7 Days**	**14 Days**	**28 Days**	**42 Days**
Al 2p	**Mean**	**1.24**	**1.06**	**0.86**	**0.96**	**1.01**
	S.E	± 0.1	± 0.2	± 0.2	± 0.2	± 0.1
Ti 2p	**Mean**	**4.68**	**3.9**	**4.29**	**3.87**	**3.7**
	S.E	± 0.3	± 0.5	± 0.4	± 0.3	± 0.2
C 1s	**Mean**	**60.59**	**62.55**	**61.75**	**61.12**	**63.03**
	S.E	± 1.1	± 1	± 0.6	± 0.7	± 1.5
F 1s	**Mean**	**1.5**	**1.58**	**1.28**	**1.2**	**1.34**
	S.E	± 0.1	± 0.1	± 0.1	± 0.2	± 0.1
N 1s	**Mean**	**4.14**	**3.5**	**4.07**	**4.22**	**3.46**
	S.E	± 0.3	± 0.3	± 0.1	± 0.3	± 0.5
O 1s	**Mean**	**24.84**	**24.4**	**24.63**	**25.57**	**24.87**
	S.E	± 0.5	± 0.6	± 1	± 0.4	± 1
P 2p	**Mean**	**2.23**	**2.1**	**2.39**	**2.03**	**1.94**
	S.E	± 0.3	± 0.1	± 0.2	± 0.1	± 0.1
S 2p	**Mean**	**0.37**	**0.39**	**0.32**	**0.61**	**0.31**
	S.E	± 0.1	± 0.1	± 0.1	± 0.1	± 0.1
Cl 2p	**Mean**	**0.41**	**0.44**	**0.41**	**0.44**	**0.33**
	S.E	± 0.1	± 0.1	± 0.1	± 0.1	± 0.1

8.4.1.2. Surface wettability

The wettability of the Ciprofloxacin® coated surfaces was measured to determine the stability of the drug under oxidative conditions. The surfaces remained hydrophobic during all oxidative exposure time intervals and their

respective contact angles are shown in Figure 8-9. As explained earlier, the hydrophobic nature of the surface is due to the presence of hydrocarbons (from the drug) on the outer most surface. Surface wettability measurements showed that the drug is highly stable and remain attached to the 16-PhDA SAM coated Ti6Al4V surface under oxidative (ambient air) conditions. Bhure et al. [55] also observed a small change in the contact angle (~ 10°) within the hydrophobicity limit during their oxidative stability measurement. Although a small change was observed in the present study, this was not significant. Hence, this confirms that the attached Ciprofloxacin® is stable under oxidative condition used in this study.

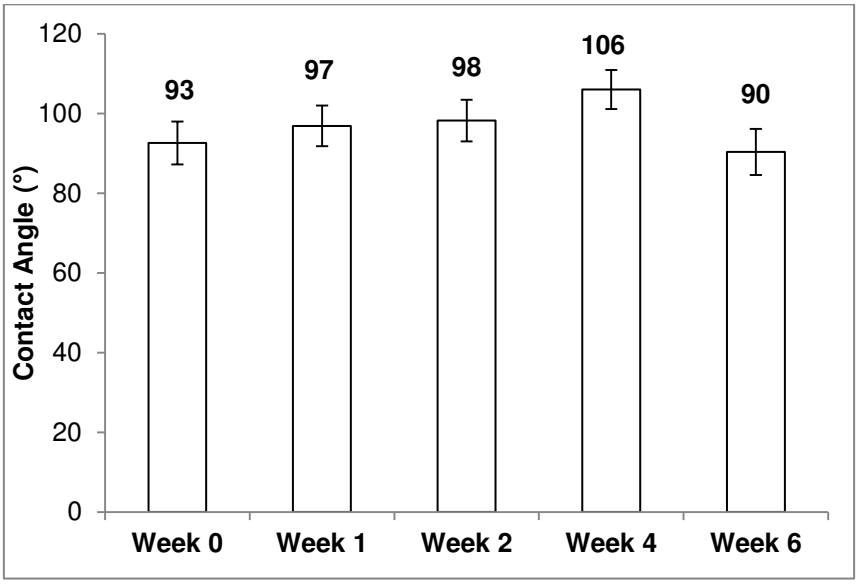

Figure 8-9 Static water contact angles obtained to determine the stability of Ciprofloxacin® under oxidative conditions at different time intervals.

8.4.2. In vitro stability of Ciprofloxacin®

8.4.2.1. Surface chemistry

The reaction mechanism for the release of Ciprofloxacin® under in vitro condition is hydrolysis. As a result, the immobilised drug will release from the SAM molecule and regain its structure to produce therapeutic effect. Table 8-3 shows a change in the XPS determined relative atomic percentage of elements after soaking the Ciprofloxacin® coated surface in Tris-HCl buffer solution at different time intervals. It can be observed from the table that the concentration of C and F decreased with the increase in the immersion time period.

Concurrently, the elemental concentration of Ti, O and Al increased. This suggests the hydrolysis of drug from the terminal end of 16-PhDA SAMs.

Table 8-3 XPS determined relative atomic percentages of elements detected for different immersion time interval in Tris-HCl buffer solution. The calibration error due to XPS peak integration is ± 10%.

Detected Elements		**Relative Atomic Percentage (%)**					
		Drug Immobilisation		**7 Days**	**14 Days**	**28 Days**	**42 Days**
		Before	**After**				
Al 2p	**Mean**	**2.39**	**1.24**	**1.16**	**1.57**	**1.5**	**2**
	S.E	± 0.2	± 0.2	± 0.2	± 0.1	± 0.2	± 0.1
Ti 2p	**Mean**	**7.57**	**4.68**	**5.54**	**5.88**	**6.44**	**6.88**
	S.E	± 0.4	± 0.2	± 0.1	± 0.2	± 0.8	± 0.6
C 1s	**Mean**	**53.68**	**60.59**	**58.17**	**56.55**	**56.7**	**55.12**
	S.E	± 0.5	± 1.1	± 0.1	± 0.9	± 1.6	± 0.3
F 1s	**Mean**	**0**	**1.5**	**1.18**	**1.15**	**1.16**	**0.92**
	S.E	0	± 0.1	± 0.1	± 0.1	± 0.1	± 0.1
N 1s	**Mean**	**0.82**	**4.14**	**3.84**	**4.05**	**3.97**	**4.01**
	S.E	± 0.1	± 0.2	± 0.1	± 0.4	± 0.3	± 0.3
O 1s	**Mean**	**31.05**	**24.84**	**27.85**	**27.99**	**27.5**	**28.46**
	S.E	± 0.4	± 0.5	± 0.2	± 0.6	± 1	± 0.3
P 2p	**Mean**	**3.51**	**2.23**	**2**	**2.34**	**1.9**	**1.76**
	S.E	± 0.2	± 0.3	± 0.1	± 0.2	± 0.2	± 0.1
Si 2p	**Mean**	**1.98**	**0**	**0.14**	**0.35**	**0.6**	**0.6**
	S.E	± 0.6	0	± 0.1	± 0.1	± 0.2	± 0.1
S 2p	**Mean**	**0**	**0.37**	**0**	**0**	**0**	**0**
	S.E	0	± 0.1	0	0	0	0
Cl 2p	**Mean**	**0**	**0.41**	**0**	**0**	**0**	**0**
	S.E	0	± 0.1	0	0	0	0
Ba 3d	**Mean**	**0**	**0**	**0.11**	**0.14**	**0.25**	**0.25**
	S.E	0	0	± 0.1	± 0.1	± 0.1	± 0.1

Figure 8-10 shows the high resolution spectra of C 1s, O 1s, N 1s and F 1s region obtained after different immersion time intervals. From the C 1s region, reduction in the intensity of C-C, C-O and C=O peaks with an increase in immersion time was observed; whereas, the O 1s region showed an increase in the intensity of the metal oxide peak at 530 eV and a decrease in the O-C peak. The N 1s region showed a change in the intensity but a clear trend was not

observed. This may be due to the adsorption of nitrogenous contaminants from air and Tris-HCl buffer. The relative intensity of the fluorocarbon peak obtained at 687.5 ± 0.2 eV was observed to decrease with the increase in immersion time and clearly shows the desorption of Ciprofloxacin® from the SAM coated surface. It can be observed from the F 1s spectra that nearly half of the drug was desorbed after 28 days with some drug remaining after 42 days. A small amount of barium was observed only for the samples soaked in buffer solution. This barium may be contamination from the glass vial used to immerse the samples in Tris-HCl buffer solution.

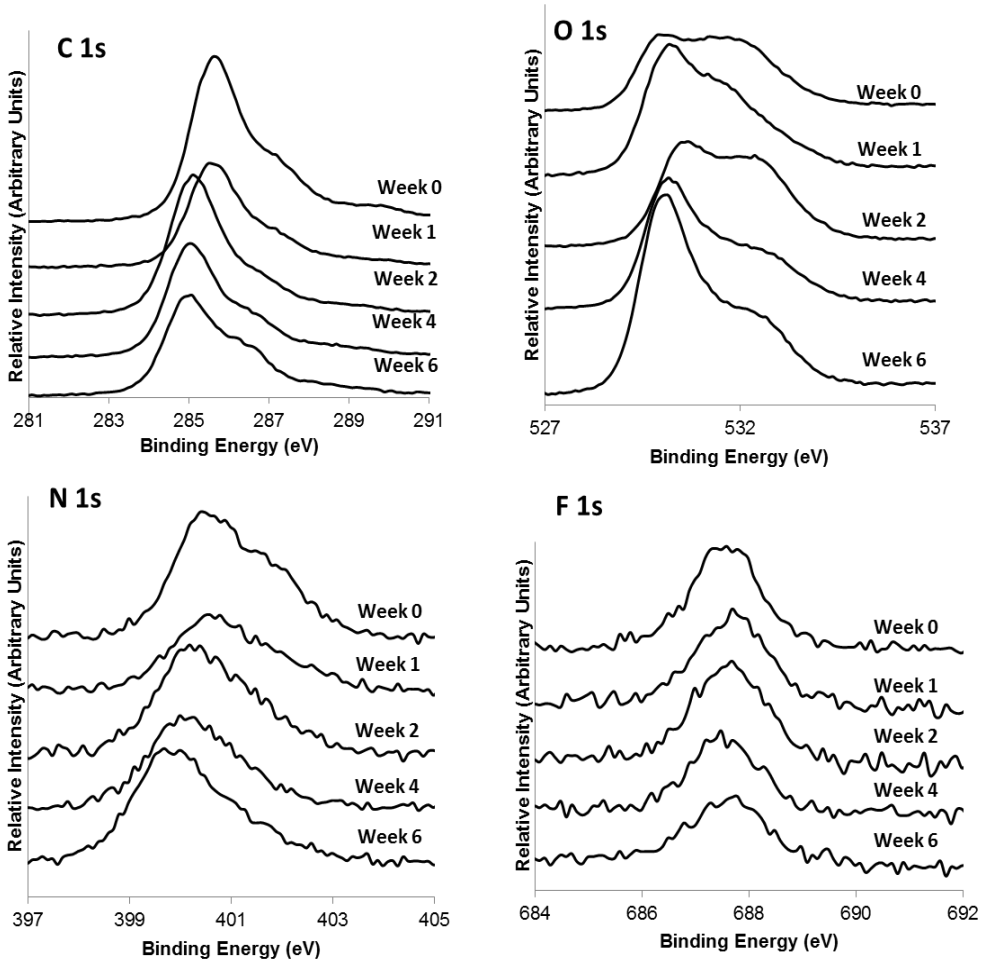

Figure 8-10 High resolution XPS spectra of C 1s, O 1s, N 1s and F 1s regions showing their relative intensities after the immersion of Ciprofloxacin® coated surfaces for different time intervals.

8.4.2.2. Surface wettability

Under in vitro conditions, the stability of Ciprofloxacin® on the 16-PhDA SAM coated Ti6Al4V surface was significantly different to its stability under

oxidative condition. After incubating the drug coated surfaces in Tris-HCl buffer solution, the contact angle values changed with respect to its initial value before immersion (Figure 8-11). This change can be attributed to the cleaving of Ciprofloxacin® molecules from the tail group of SAMs to the Tris-HCl buffer solution. On desorption of Ciprofloxacin® from the surface, the surface will be expected to be hydrophilic. This is due to the fact that a bare Ti6Al4V metal surfaces and 16-PhDA SAM coated metal surfaces are hydrophilic.

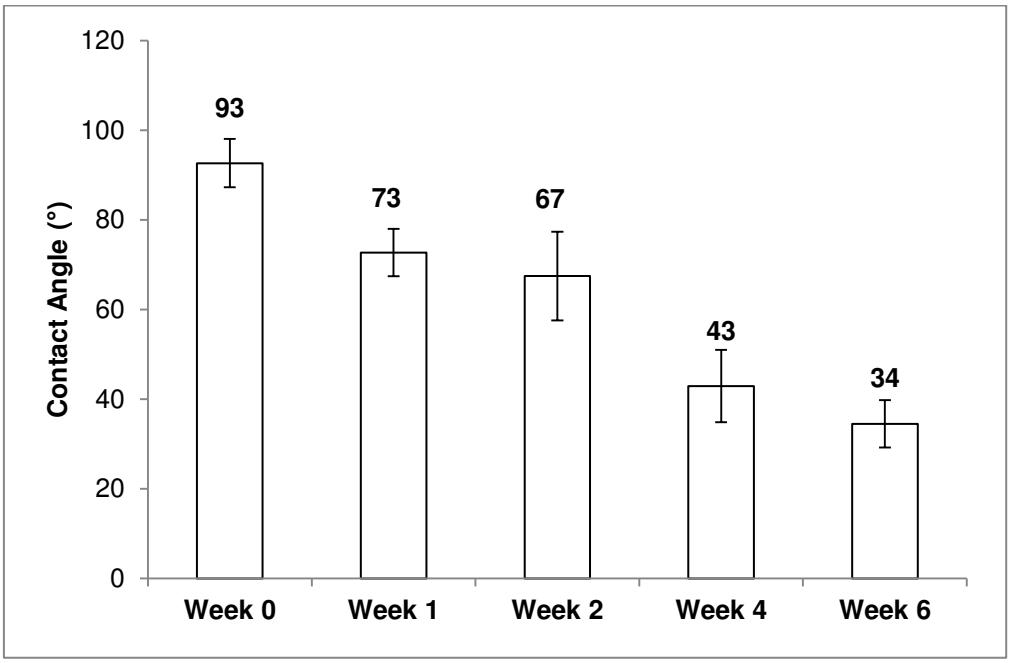

Figure 8-11 Static water contact angle exhibiting a change in the surface wettability after the immersion of Ciprofloxacin® coated surface in Tris-HCl buffer solution for different time intervals.

In the present study, after the immersion of the drug coated surfaces in Tris-HCl buffer solution, the contact angles were observed to decrease compared to their initial values after drug coating (Figure 8-11). The wettability measurement showed desorption of drugs from the surface with a clear trend. The contact angles decreased with the increase in immersion time revealing desorption of Ciprofloxacin®. However, the calculated standard deviations were high. This is likely to be due to the presence of Ciprofloxacin® in a few islands and not on the other. This can be due to an irregular assembly and cleaving of monolayers after they are exposed to in vitro solution.

8.5. Drug Quantification

The total amount of drug loaded was calculated using UV-Vis spectrophotometry. A calibration curve was plotted for Ciprofloxacin® in 10 mM NaOH (pH ~ 7.4) for the concentration range from 1 ng/mL to 1 µg/mL. The regression equation was determined as $y = 2.34x \times 10^{-4} + 2.4 \times 10^{-3}$ ($R^2 = 0.996$). The total amount of Ciprofloxacin® immobilised to SAMs was determined to be from 1.17 ± 0.1 µg/cm^2 (assuming the surface area of the sample is 3.2 cm^2). Previous literature showed the immobilisation of ~100 ng/cm^2 of Paclitaxel™ to 16-PhDA SAMs [144]. However, in the case of this study a drug loading ten times greater was obtained. This variation is more likely due to the surface roughness pattern of the SLM fabricated sample. Although the top surface was mechanically polished, the other faces remained rough. The change in the surface area can influence the amount of SAM adsorption which will then directly influence the total amount of drug loaded. Also, the Paclitaxel™ (853.91 g/mole) drug has a molecular mass more than twice that of the Ciprofloxacin® (331.35 g/mole). Ajami et al. [136] reported the attachment of Ciprofloxacin® to SAMs, but the amount of drug coated was not quantified. However, this study shows that by increasing the surface area, more drugs can be immobilised to 16-PhDA SAMs.

8.6. Drug Elution Studies

Figure 8-12 shows the percentage of drug eluted to the Tris-HCl buffer solution at 7, 14, 28 and 42 day time intervals. The calibration curve was obtained for Ciprofloxacin® in Tris-HCl buffer over the concentration range from 1 ng/mL to 1 µg/mL and the regression equation for Ciprofloxacin® in Tris-HCl buffer (pH ~ 7.4) was determined as $y = 10x \times 10^{-5} + 1.2 \times 10^{-3}$ ($R^2 = 0.998$). UV-Vis determined drug release profile showed a sustained release profile. Previously reported studies have shown the possibility for the surface to have both covalently bound drug and a reservoir of drug as the surface is rough [136,144]. In the present study, such formation of reservoir of Ciprofloxacin® was not witnessed. This may be because the samples after the immobilisation of Ciprofloxacin® were sonicated with anhydrous tetrahydrofuran and deionised water twice for two minutes. During this

procedure, it can be expected that most of the physisorbed drug molecule would be removed. Also the amount of drug used for immobilisation is less. Despite these reasons, there is the possibility for some physisorbed drug molecule to be present. If there was a reservoir of drug, a bulk release of the drug should have been witnessed during the UV-Vis spectroscopic measurement. However, the 42 days in vitro studies revealed no such bulk release of the drug. This shows that the presence of a reservoir of Ciprofloxacin® on the samples is less likely. Thus, as there was no initial burst release, it can be stated that most of the drug molecules were covalently bound.

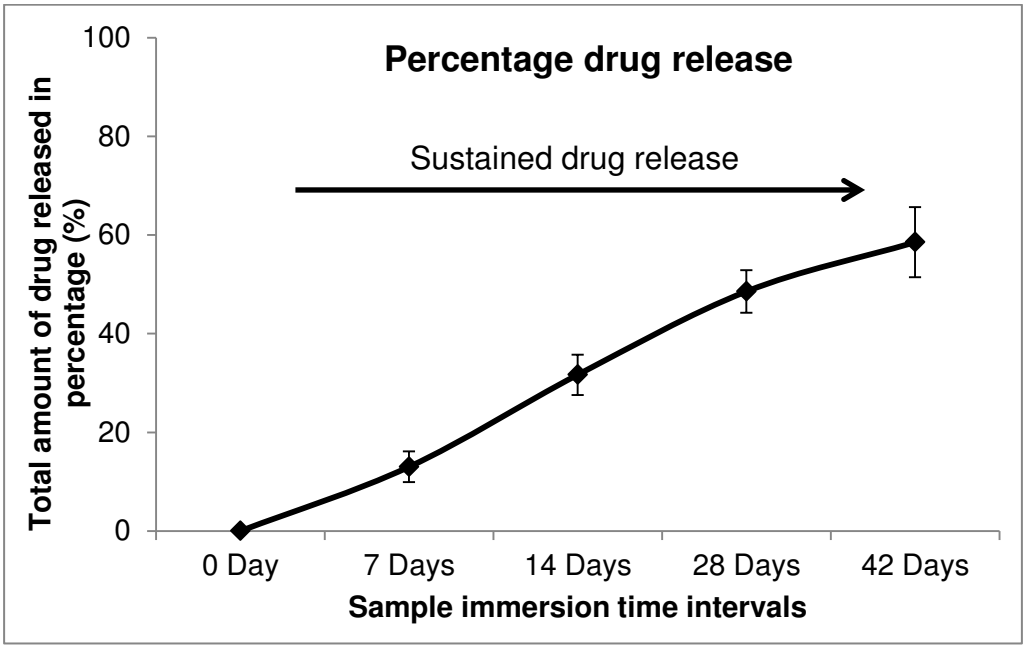

Figure 8-12 Percentage drug released at different time intervals determined using UV-Visual Spectrophotometer.

After immersing the sample in the buffer solution for 7 days, nearly 13% of the drug eluted whereas after a 28 day interval, nearly 50% of the drug had been released. However, after 42 days of immersion, nearly 40% of the drug was still observed to be eluted from the surface. The UV-Vis determined release profile was observed to be in good agreement with the XPS determined in vitro stability. This may suit biomedical applications where a sustained release of the drug is required over a period of time. However, it should be noted that Ciprofloxacin® will be inactive when it is immobilised to the monolayers and will only be active upon its release from the monolayer. The release of the drug in its active form from the monolayer can be attained by hydrolysis.

Ajami et al. [136] reported the release of Ciprofloxacin® from a silane SAMs. In their study, more than 50% of the drug was observed to release within 5 days in 20 mL of high purity water (18.2MΩ.cm) maintained at 37 °C. They have also observed 80% release in 26 days. There is a high possibility for this release profile to be faster in physiological condition than in water. Release profile reported by Mani et al. [37] for flufenamic acid showed an initial burst release followed by a sustained release of the drug. In an another study reported by Mani et al. [144], they observed a burst release of Paclitaxel™ in 7 days followed by a sustained release for up to 35 days. Comparing the release profiles reported by these researchers with this study, the drug release is slow and exhibits the potential to use this system for long-term release (more than 6 weeks) of drug from an implant's surface. As mentioned before, the slow release is mainly due to the covalent bonding of the drug and non-availability of physisorbed drug on the surface.

This release profile further confirms the formation of an anhydride rather than amide and shows possibility for the attachment of Ciprofloxacin® to the acyl chloride via a carboxylic group. This is because amide is a poor leaving group with a pKa of about 25. Hence, hydrolysis of amides requires vigorous reaction conditions (such as addition of catalysts and high temperature ~ 100 °C) [172]. In this study, the drug coated implants were immersed in Tris-HCl buffer solution of pH 7.4 at 37.5 °C. This pH is slightly towards the basic condition and the temperature used is relatively low. Under this mild condition, hydrolysis of amides is less favourable, whereas, anhydrides will readily hydrolyse (since pKa of anhydrides is about 5) in water to form corresponding carboxylic acid [172]. Thus the formation of anhydrides rather than amides is most expected.

8.7. Antibacterial Susceptibility

8.7.1. Test-1

The susceptibility test was performed to determine if the immobilised drug was releasing and to investigate activity of the drug after hydrolysing from the monolayers. Figure 8-13 shows the photographic images of the zone of

inhibition for the control discs and discs coated with Ciprofloxacin®. Release of the drug from the standard filter paper disc coated with the drug was observed to inhibit the growth of S. aureus whereas the metal disc coated with drug did not show any drug elution and inhibition. In contrast, the metal discs coated with Ciprofloxacin® were observed to inhibit the growth of E.coli. A similar trend was followed in all five sets for both bacteria. It may be argued that the metal discs placed on S. aureus were not coated with the drug, but this may not be the case. All metal discs used for both S. aureus and E. coli were from the same batch. Also, the XPS studies on the drug coated metal discs confirmed the functionalisation of Ciprofloxacin® (Figure 8-14).

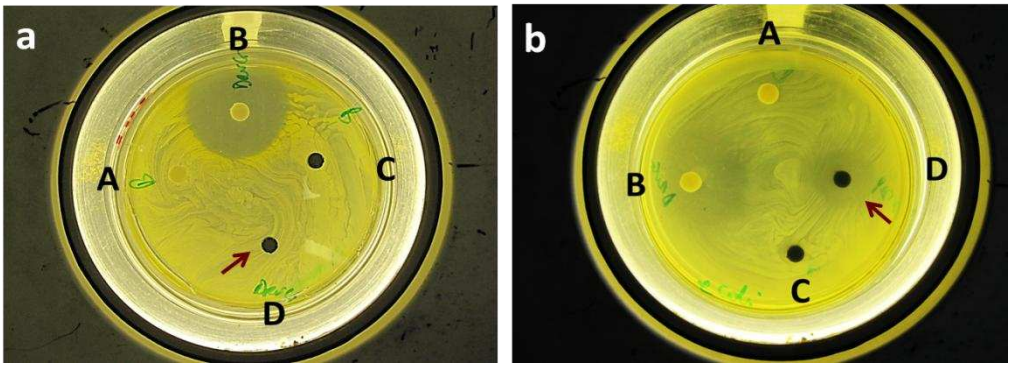

Figure 8-13 Antibacterial susceptibility test against S. aureus (a) and E. coli (b). Label description: A - control standard filter paper disc without drug, B - standard filter paper disc with drug; C - Control Ti6Al4V metal disc without drug; D - metal disc coated with drug.

Ciprofloxacin®, being a wide spectrum antibiotic, should inhibit the growth of S. aureus and previous studies have proved this [175]. Whereas, the results obtained in this study for S. aureus are unclear. One possible reason for not inhibiting the growth may be due to the temperature used to incubate the culture plates after placing the discs. Since the S. aureus inoculated plates were maintained at 30 °C, this might have affected the hydrolysis of the drug from the monolayer. Since the drugs on the standard filter paper discs were physisorbed, it has released the drug and inhibited the growth. The temperature used to incubate E. coli (37.5 °C) was observed to hydrolyse the drug from the metal disc and inhibit the bacterial growth. Thus the temperature might have been the factor that affected the drug release.

After the experimentation time, the samples were removed from the culture plate and rinsed with ethanol for 2 minutes before examining the presence of

Ciprofloxacin® using XPS on these discs. Figure 8-14 shows the XPS spectra obtained for a control, drug coated, drug coated metal disc from S. aureus culture and drug coated metal disc from on E. coli culture.

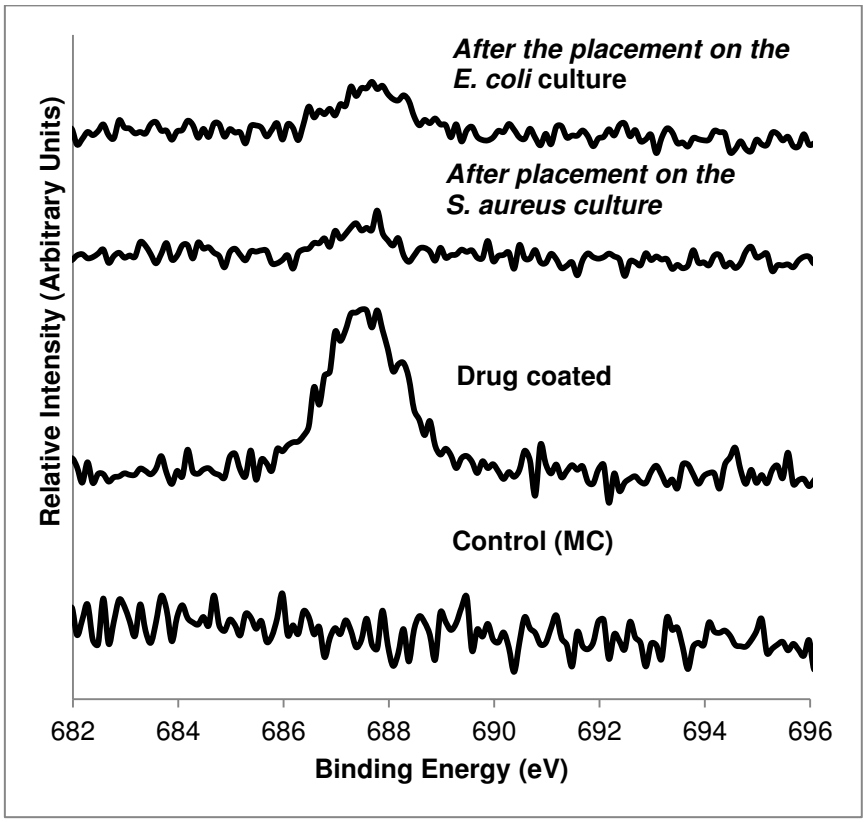

Figure 8-14 XPS spectra of F 1s region for control, drug coated and drug coated discs placed on S. aureus and E. coli bacteria.

The spectra clearly show the existence of the drug on the surface of the Ti6Al4V discs placed on the culture medium; however, their intensities varied. The variation in the intensities might be due to the fact that after placing on the medium, adherence of the agar medium to the metal discs are possible. Since XPS probes typically 1-10 nm of the surface, the adhered medium might have reduced the penetration depth of the photoelectrons. Although the results showed the drug released from the metal substrate is active for E. coli, no activity was observed for S. aureus and the reason for this should be further explored. In addition to the drug release profile, the release of drug in this bacterial culture (again a mild condition) further shows the possibility for the formation of anhydrides rather than amide during the reaction between the acyl chloride and Ciprofloxacin®.

8.7.2. Test-2

Since the drug eluted from the metal discs did not show any activity against the gram positive bacteria S. aureus, this test was mainly performed to investigate antibacterial susceptibility of Ciprofloxacin® released from the metal samples in Tris-HCl buffer. This test was also performed to qualitatively observe if there was an increase in the inhibition zone diameter with respect to immersion time intervals in the Tris-HCl buffer solution. Theoretically, as the immersion time of the drug coated sample in Tris-HCl is increased, the amount of drug eluted from the metal surface should increase. As the concentration of the drug in Tris-HCl buffer increases, there should be an increase in the diameter of the inhibition zone. Figure 8-15 shows the photographic images of the zone of inhibition for the discs coated with Ciprofloxacin® eluted at different time intervals.

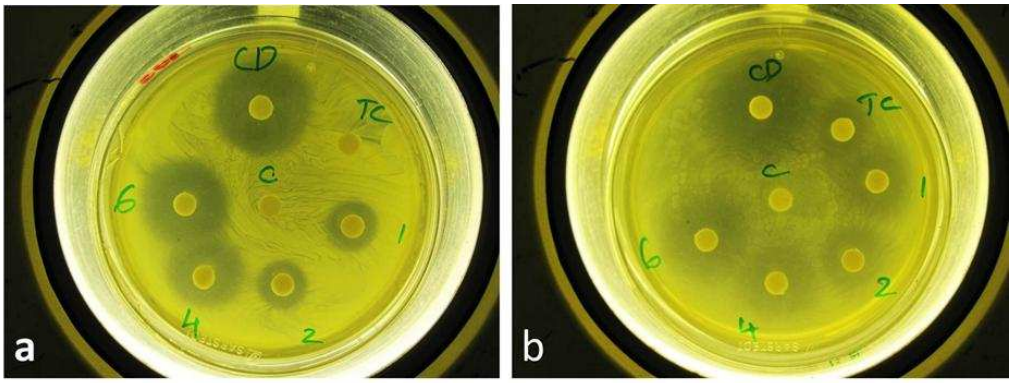

Figure 8-15 Antibacterial susceptibility test against a) S. aureus and b) E. coli. Label description: C- control disc with no drug; CD – control with drug on; TC: discs coated with Tris-HCl buffer; 1, 2, 4, 6 – immersion time intervals (in weeks) of the samples in Tris-HCl buffer solution.

It can be observed from the graph that the discs coated with the drug showed anti-bacterial activity confirming the drug was active upon their release. Furthermore, the discs coated with drugs eluted at different time intervals showed an increased zone of inhibition diameter (Figure 8-16) for both S. aureus and E.coli. As expected this may be due to the fact that as the sample immersion time was increased, more Ciprofloxacin® molecules eluted from the surface to the buffer solution thereby increasing the drug concentration. This study qualitatively showed the release of the drug and its antibacterial

activity. Since the present study did not use standard discs coated with Ciprofloxacin®, the MIC for S. aureus and E. coli was not determined.

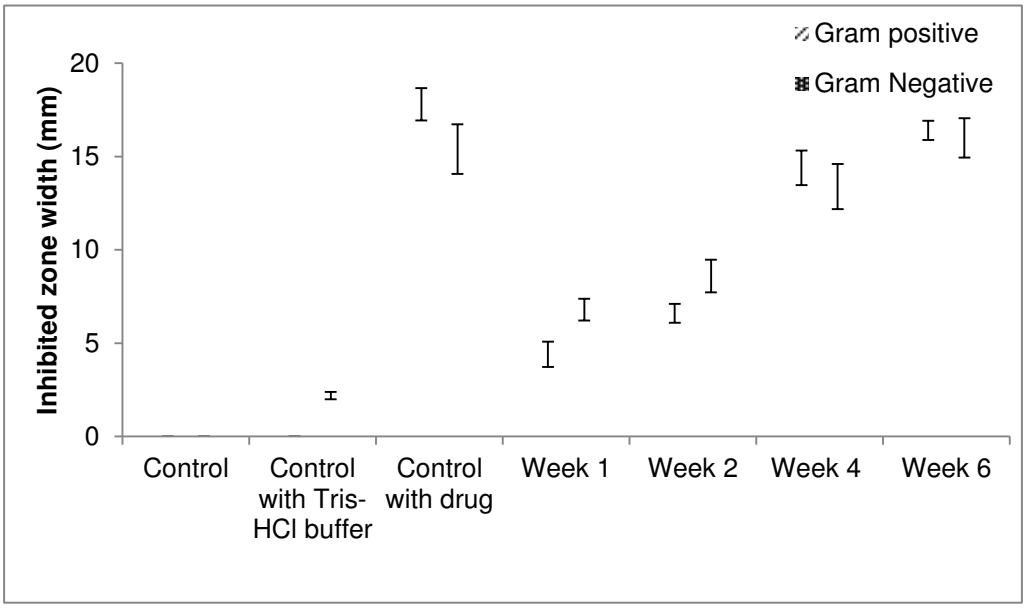

Figure 8-16 Inhibited zone diameters for S. aureus and E. coli.

8.8. Summary

The use of 16-PhDA monolayers to modify SLM fabricated structures to deliver therapeutics has been demonstrated. Experimental results showed a covalent attachment of the Ciprofloxacin® molecules to SAMs and sustained release in Tris-HCl buffer solution. The total drug immobilised to the monolayers was estimated to be approximately 1.2 ± 0.1 µg/cm^2. The antibacterial susceptibility study revealed that the drug was active upon its release. Thus the attachment, stability and the delivery of Ciprofloxacin® from SLM fabricated surface shows the potential to use this approach to deliver therapeutics directly from customised implant surfaces.

9. CONCLUSION AND FUTURE WORK

9.1. Conclusion

This research concludes the potential to integrate SLM with SAM based surface modification to deliver therapeutics directly from customised implant surfaces fabricated by SLM. Based on the experimental studies, this research has also arrived at the following conclusions.

- The surface chemistry of the SLM fabricated parts was not homogeneous and varied depending on their exposure to the laser beam. Aluminium rich areas were witnessed on the SLM fabricated Ti6Al4V parts when a high laser energy density was applied. The surface chemistries of the SLM-AF and SLM-MP were different with a varied elemental contribution.
- 16-PhDA SAMs were covalently bound to both the SLM-AF and SLM-MP Ti6Al4V surfaces and were stable for 28 days on these surfaces. The surface roughness of the SLM-AF did not have a significant impact on the in vitro stability of the 16-PhDA SAMs.
- The use of acid chloride esterification was successful to immobilise the Paracetamol to the 16-PhDA SAMs. However, the use of Paracetamol may not be the best choice to prove the accomplishment of the reaction due to the possibility that the results may be affected by atmospheric contaminants. For example, a drug molecule with distinct elements such as fluorine and bromine that are unlikely to be present in the atmosphere can prevent contamination affecting the results. Also, Paracetamol (phenolic esters) can easily hydrolyse from the SAM molecules in the presence of moisture or water molecules. Thus, a careful consideration is required when choosing a model drug.
- The total amount of Ciprofloxacin® coated on the SLM-MP Ti6Al4V was estimated to be approximately 1.2 $\mu g/cm^2$. The drug was observed to be highly stable under oxidative conditions for over 42 days. The in vitro release of the drug in Tris-HCl buffer solution showed the covalent attachment of the drug to the monolayers and exhibited the

potential to use this model for applications requiring a sustained release pattern. Upon release from the monolayer, the drug was active and inhibited the growth of bacteria.

- Contamination of Ti6Al4V powder due to atmospheric contaminants including carbon and nitrogen was witnessed upon recycling the powders in a SLM machine.

9.2. Future Work

This work, being the first study of its kind in AM, has opened up future studies in various directions. The following are some recommendations to extend the knowledge beyond that performed in this work.

- This study compared the surface chemistry of Ti6Al4V surface using XPS only. These results can be compared with other surface chemical characterisation techniques such as AES for improved understanding.
- Estimating the oxide layer thickness and surface chemistry of the SLM as-fabricated surface in this study was limited due to the sensitivity of XPS to rough surfaces. However, there are other SLM machines such as EOSINT M 280, EOS M 400 which provide a better surface finish. Studies on the surface chemistry of these parts could be used for comparison.
- Electron beam melting (EBM), an AM technique, is also used for the fabrication of biomedical devices. Comparison of the surface chemistries obtained by EBM and SLM would be beneficial.
- This study showed the attachment and functionalisation of 16-PhDA monolayers only. Other phosphonic acid monolayers could be used and their stability could be analysed and compared.
- Although the surface modification and functionalisation were performed by immersing the whole SLM fabricated part into the SAM and drug solution, only the top surface was studied and characterised. Implants often have complex geometries and not just a flat surface. Hence, a study on the immobilisation of drugs to SAMs adsorbed on the whole of the surface is required.

- This study proposes the reaction of acyl chloride with carboxylic acid to form an anhydride but not the reaction of acyl chloride with amine to form an amide. This has to be further confirmed by the use of FTIR-ATR to know the exact reaction mechanism.
- The amount of drug functionalised to SAMs in this study may be low for certain applications and hence methods need to be developed to increase the amount of drug loading, for example, growing multi-layers by using polymer brushes can be explored.
- Although the sustained release pattern of the drug is convincing, a shorter time gap between the intervals over the study period will generate improved knowledge on the drug release profile.
- Metal discs coated with Ciprofloxacin® and incubated at 30°C for evaluation of its antibacterial susceptibility did not show drug release. Although temperature might have been a factor, this should be further explored.
- This study proposed the attachment of only therapeutic drugs to SAMs. The SAM attached SLM fabricated Ti6Al4V surfaces can be explored for the immobilisation of proteins which would be useful for various biomedical applications.
- A similar procedure can be used to functionalise other metallic biomaterial surfaces (including 316L SS and Co-Cr) and their stability can be tested.
- Often, for biomedical applications, more than one type of drug is required and/or delivery of drug from a particular area is preferred. Hence, patterning of SLM fabricated surfaces with SAMs and functionalising the SAMs with various drugs would be beneficial.

REFERENCES

1. Ratner BD. A history of biomaterials. In: Ratner BD, Hoffman A s, Schoen FJ, Lemons JE, editors. Biomater. Sci. an Introd. to Mater. Med. second edi. London: Elsevier; 2004. p. 10–23.

2. Grillo HC. Diseases and results of treatment. In: Grillo HC, editor. Surg. trachea bronchi. London: BC Decker Inc, USA; 2004. p. 173–429.

3. Manivasagam G, Dhinasekaran D, Rajamanickam A. Biomedical implants : corrosion and its prevention - a review. Recent Patents Corros. Sci. 2010;2:40–54.

4. Paital SR, Dahotre NB. Calcium phosphate coatings for bio-implant applications: Materials, performance factors, and methodologies. Mater. Sci. Eng. R Reports. 2009;66(1-3):1–70.

5. Hassler C, Boretius T, Stieglitz T. Polymers for neural implants. J. Polym. Sci. Part B Polym. Phys. 2011 Jan 1;49(1):18–33.

6. 10th Annual Report. National Registry for England, Wales and Northern Ireland [Internet]. 2013. Available from: http://www.njrcentre.org.uk/njrcentre/Portals/0/Documents/England/Reports/10th_annual_report/NJR 10th Annual Report 2013 B.pdf

7. Miller RS. Increasing incidence of joint replacements burdens healthcare system. Med. Device Marketpl. Rev. 2008 p. 1–3.

8. Paxton EW, Inacio M, Slipchenko T, Fithian DC. The kaiser permanente national total joint replacement registry. Perm. J. 2008;12(3):12–6.

9. King M. The future of the orthopedic devices market to 2012 [Internet]. 2008. Available from: http://www.hipresurfacingnews.com/archives/265-The-Future-of-the-Orthopedic-Devices-Market-to-2012.html. Accessed on 30th January, 2012.

10. Singhatanadgit W. Biological responses to new advanced surface modifications of endosseous medical implants. Bone Tissue Regen. Insights. 2009;2:1–11.

11. Anderson JM. Biological responses to materials. Annu. Rev. Mater. Res. 2001;31:81–110.

12. Anderson JM, Rodriguez A, Chang DT. Foreign body reaction to biomaterials. Semin. Immunol. 2008;20(2):86–100.

13. Castner DG, Ratner BD. Biomedical surface science: foundations to frontiers. Surf. Sci. 2002;500(1-3):28–60.

14. Eyers D, Dotchev K. Technology review for mass customisation using rapid manufacturing. Assem. Autom. 2010;30(1):39–46.

15. Hao L, Harris R. Customised implants for bone replacement and growth. In: Bartolo P, Bidanda B, editors. Bio-materials Prototyp. Appl. Med. Springer US; 2008. p. 79–107.

16. Taylor M, Tanner KE. Fatigue failure of cancellous bone: a possible cause of implant migration and loosening. J. bone Jt. surgery. 1997;79-B(2):181–2.

17. Freitag L. Airway stents. Eur Respir Mon. 2010;48:190–217.

18. Huddleston J, Gobezie R, Rubash H. Custom Implants in Revision Total Knee Arthroplasty. In: Bono J V, Scott RD, editors. Revis. Total Knee Arthroplast. Springer US; 2005. p. 105–16.

19. Freeman R, Plante-bordeneuve P. Early migration and late aseptic failure of proximal femoral prostheses. J. bone Jt. surgery. 1994;76:432–8.

20. Wholey MH, Ferral H, Reyes R, Lopera J, Castan W. Retrieval of migrated colonic stents from the rectum. Cardiovasc. Intervent. Radiol. 1997;20:477–80.

21. Galindo-Moreno P, Padial-Molina M, Sánchez-Fernández E, Hernández-Cortés P, Wang H-L, O'Valle F. Dental implant migration in grafted maxillary sinus. Implant Dent. 2011;20(6):400–5.

22. Hebel KS, Gajjar RC. Cement-retained versus screw-retained implant restorations: achieving optimal occlusion and esthetics in implant dentistry. J. Prosthet. Dent. 1997;77(1):28–35.

23. Shadid R, Sadaqa N. A comparison between screw- and cement-retained implant prostheses. A literature review. J. Oral Implantol. 2012;38(3):298–307.

24. Chaar MS, Att W, Strub JR. Prosthetic outcome of cement-retained implant-supported fixed dental restorations: a systematic review. J. Oral Rehabil. 2011;38(9):697–711.

25. Natali AN, Carniel EL, Pavan PG. Dental implants press fit phenomena: biomechanical analysis considering bone inelastic response. Dent. Mater. 2009;25(5):573–81.

26. Lu J. Orthopaedic bone cements. In: Poitout DG, editor. Biomech. Biomater. Orthop. First. Springer New York; 2004. p. 96.

27. Bibb R, Eggbeer D, Evans P. Rapid prototyping technologies in soft tissue facial prosthetics: current state of the art. Rapid Prototyp. J. 2010;16(2):130–7.

28. Wood D. Tracheal and Bronchial Stenting. In: Grillo H, editor. Surg. Trachea Bronchi. Ontario: BC Decker Inc, Hamilton, Ontario; 2004. p. 763–90.

29. Stoeckel D, Pelton A, Duerig T. Self-expanding nitinol stents: material and design considerations. Eur. Radiol. 2004;14(2):292–301.

30. Kurella A, Dahotre NB. Review paper: surface modification for bioimplants: the role of laser surface engineering. J. Biomater. Appl. 2005;20(1):5–50.

31. Aksakal B, Yildirim O., Gul H. Metallurgical failure analysis of various implant materials used in orthopedic applications. J. Fail. Anal. Prev. 2004;4(3):17–23.

32. Bhola R, Bhola SM, Mishra B, Olson DL. Corrosion in titanium dental implants / prostheses - a review. Trends Biomater Artif Organs. 2011;25(1):34–46.

33. Pye D, Lockhart DE, Dawson MP, Murray C, Smith J. A review of dental implants and infection. J. Hosp. Infect. 2009;72(2):104–10.

34. Knobben BS, van Horn JR, van der Mei HC, Busscher HJ. Evaluation of measures to decrease intra-operative bacterial contamination in orthopaedic implant surgery. J. Hosp. Infect. 2006;62(2):174–80.

35. Leung JW. History of bile duct stenting: rigid prostheses. In: Kozarek R, Baron T, Song H-Y, editors. Self-expandable Stents Gastrointest. Tract. New York, NY: Springer New York; 2013. p. 15–31.

36. Noppen M, Piérard D, Meysman M, Claes I, Vincken W. Bacterial colonization of central airways after stenting. Am. J. Respir. Crit. Care Med. 1999;160(2):672–7.

37. Mani G, Johnson DM, Marton D, Feldman MD, Patel D, Ayon A and Agarwal M. Drug delivery from gold and titanium surfaces using self-assembled monolayers. Biomaterials. 2008;29(34):4561–73.

38. An YH, Dickinson RB, Doyle RJ. Mechanisms of bacterial adhesion and pathogenesis of implant and tissue infections. In: An YH, Friedman RJ, editors. Handb. Bact. Adhes. Princ. Methods Appl. New Jersy: Humana Press Inc; 2002. p. 1–27.

39. Harris LG, Richards RG. Staphylococci and implant surfaces: a review. Injury. 2006;37 Suppl 2:S3–14.

40. Garvin K, Feschuk C. Polylactide-polyglycolide antibiotic implants. Clin. Orthop. Related. Res. 2005;437:105–10.

41. Schmidmaier R, Simsek M, Baumann M, Emmerich P, Meinhardt G. Synergistic antimyeloma effects of zoledronate and simvastatin. Anticancer Drugs. 2006;17(6):621–30.

42. Stone RM, O'Donnell MR, Sekeres MA. Acute myeloid leukemia. Am. Soc. Hematol. 2004;98–117.

43. Levy Y, Mandler D, Weinberger J, Domb AJ. Evaluation of drug-eluting stents' coating durability - clinical and regulatory implications. J. Biomed. Mater. Res. B. Appl. Biomater. 2009;91(1):441–51.

44. Otsuka Y, Chronos N, Apkarian R, Robinson K. Scanning electron microscopic analysis of defects in polymer coatings of three commercially available stents: comparison of BiodivYsio, Taxus and Cypher stents. J. Invasive Cardiol. 2007;19(2):71–6.

45. Mani G, Macias CE, Feldman MD, Marton D, Oh S, Mauli Agrawal C. Delivery of paclitaxel from cobalt-chromium alloy surfaces without polymeric carriers. Biomaterials. 2010;31(20):5372–84.

46. Knetsch MLW, Koole LH. New strategies in the development of antimicrobial coatings: The example of increasing usage of silver and silver nanoparticles. Polymers (Basel). 2011 Jan 26;3(4):340–66.

47. Dubey M, Weidner T, Gamble LJ, Castner DG. Structure and order of phosphonic acid-based self-assembled monolayers on Si(100). Langmuir. 2010;26(18):14747–54.

48. Faucheux N, Schweiss R, Lützow K, Werner C, Groth T. Self-assembled monolayers with different terminating groups as model substrates for cell adhesion studies. Biomaterials. 2004;25(14):2721–30.

49. Arabnejad Khanoki S, Pasini D. Multiscale design and multiobjective optimization of orthopedic hip implants with functionally graded cellular material. J. Biomech. Eng. 2012;134(3):031004–10.

50. Chahine G, Atharifar H, Smith P, Kovacevic R. Design optimization of a customized dental implant manufactured via Electron Beam Melting ® Int. Solid Free. Fabr. Symp. 2009. p. 631–40.

51. Kruth J, Badrossamay M, Yasa E, Deckers J, Thijs L, Humbeeck J Van. Part and material properties in selective laser melting of metals. 16th International Symposium on Electromachining. 2010. p. 1–12.

52. Mani G, Feldman MD, Patel D, Agrawal CM. Coronary stents: a materials perspective. Biomaterials. 2007;28(9):1689–710.

53. Mani G, Johnson DM, Marton D, Dougherty VL, Feldman MD, Patel D, and Ayon A. Stability of self-assembled monolayers on titanium and gold. Langmuir. 2008;24(13):6774–84.

54. Torres N, Oh S, Appleford M, Dean DD, Jorgensen JH, Ong JL, Agarwal MC and Mani G. Stability of antibacterial self-assembled monolayers on hydroxyapatite. Acta Biomater. 2010;6(8):3242–55.

55. Bhure R, Abdel-Fattah TM, Bonner C, Hall F, Mahapatro A. Stability of phosphonic self assembled monolayers (SAMs) on cobalt chromium (Co-Cr) alloy under oxidative conditions. Appl. Surf. Sci. 2011;257(13):5605–12.

56. Kaufmann C, Mani G, Marton D, Johnson D, Agrawal CM. Long-term stability of self-assembled monolayers on electropolished L605 cobalt chromium alloy for stent applications. J. Biomed. Mater. Res-A. 2011;98B(2):280–9.

57. Tegoulia V, Cooper S. Staphylococcus aureus adhesion to self-assembled monolayers: effect of surface chemistry and fibrinogen presence. Colloids Surfaces B Biointerfaces. 2002;24(3-4):217–28.

58. Mahapatro A, Johnson DM, Patel DN, Feldman MD, Ayon A, Agrawal CM. The use of alkanethiol self-assembled monolayers on 316L stainless steel for coronary artery stent nanomedicine applications: an oxidative and in vitro stability study. Nanomedicine. 2006;2(3):182–90.

59. Schwartz DK. Mechanisms and kinetics of self -assembled monolayer formation. Annu. Rev. Phys. Chem. 2001;52:107–37.

60. Lindner M, Hoeges S, Meiners W, Wissenbach K, Smeets R, Telle R, Poprawe Reinhart and Fischer Horst. Manufacturing of individual biodegradable bone substitute implants using selective laser melting technique. J. Biomed. Mater. Res-A. 2011;97(4):466–71.

61. Yadroitsev I, Smurov I. Surface morphology in selective laser melting of metal powders. Phys. Procedia. 2011;12:264–70.

62. ASTM-F2792. Standard Terminology for Additive Manufacturing Technologies. Standard Terminologies for Additive Manufacturing. Technology, ASTM International, West Conshohocken, PA, 2003; 2010.

63. Gibson I, Rosen DW, Stucker B. Additive Manufacturing Technologies. Boston, MA: Springer US; 2010.

64. Santos E, Shiomi M, Osakada K, Laoui T. Rapid manufacturing of metal components by laser forming. Int. J. Mach. Tools Manuf. 2006;46(12-13):1459–68.

65. Schleifenbaum H, Meiners W, Wissenbach K, Hinke C. Individualized production by means of high power Selective Laser Melting. CIRP J. Manuf. Sci. Technol. CIRP; 2010;2(3):161–9.

66. Tuck C, Hague R. The pivotal role of rapid manufacturing in the production of cost effective customised products. Int. J. Mass Cust. 2006;1(3):360–73.

67. Hopkinson N, Hague RJ, Dickens PM. Rapid Manufacturing: An Industrial Revolution for the Digital Age. 1st ed. Hopkinson N, Hague RJ, Dickens PM, editors. John Wiley and Sons Ltd., West Sussex, UK.; 2006.

68. Li R, Shi Y, Wang Z, Wang L, Liu J, Jiang W. Densification behavior of gas and water atomized 316L stainless steel powder during selective laser melting. Appl. Surf. Sci. 2010;256(13):4350–6.

69. Murr LE, Martinez E, Hernandez J, Collins S, Amato KN, Gaytan SM and Shindo Patrick W. Microstructures and properties of 17-4 PH stainless steel fabricated by selective laser melting. J. Mater. Res. Technol. 2012;1(3):167–77.

70. Badrossamay M, Childs THC. Layer formation studies in selective laser melting of steel powders. International Solid Freeform Fabrication Symposium. University of Texas, Austin; 2006. p. 268–79.

71. Hauser C, Childs THC, Taylor CM, Badrossamay M, Xie J, Fox P and Neil WO. Direct selective laser sintering of tool steel powders to high density part: effects of laser beam width and scan strategy. International Solid Freeform Fabrication Symposium. University of Texas, Austin; 2003. p. 644–55.

72. Kempen K, Thijs L, Yasa E, Badrossamay M, Verheecke W, Kruth J. Process optimisation and microstructural analysis for selective laser melting of AlSi10Mg. International Solid Freeform Fabrication Symposium. University of Texas, Austin; 2011. p. 484–95.

73. Vora P, Derguti F, Mumtaz K, Todd I, Hopkinson N. Investigating a semi-solid processing technique using metal powder bed additive manufacturing processes. International Solid Freeform Fabrication Symposium. University of Texas, Austin; 2013. p. 454–62.

74. Yadroitsev I, Smurov I. Selective laser melting technology: From the single laser melted track stability to 3D parts of complex shape. Phys. Procedia. 2010;5:551–60.

75. De Peppo GM, Palmquist A, Borchardt P, Lennerås M, Hyllner J, Snis A,Lausmaa J, Thomsen P and Karlsson C. Free-form-fabricated commercially pure Ti and Ti6Al4V porous scaffolds support the growth

of human embryonic stem cell-derived mesodermal progenitors. Sci. World J. 2012;2012:1–14.

76. Yadroitsev I, Bertrand P, Smurov I. Parametric analysis of the selective laser melting process. Appl. Surf. Sci. 2007;253(19):8064–9.

77. Mumtaz K, Hopkinson N. Selective laser melting of Inconel 625 using pulse shaping. Rapid Prototyp. J. 2010;16(4):248–57.

78. Ng CC, Savalani M, Man HC. Fabrication of magnesium using selective laser melting technique. Rapid Prototyp. J. 2011;17(6):479–90.

79. Shishkovsky I, Yadroitsev I, Smurov I. Direct selective laser melting of nitinol powder. Phys. Procedia. 2012;39:447–54.

80. Vision Systems Design Magazine. 2011;16.

81. Liu B. Further Process Understanding and Prediction on Selective Laser Melting of Stainless Steel 316L [PhD Thesis]. Loughborough University, UK; 2013.

82. Kruth JP, Mercelis P, Froyen L, Rombouts M. Binding Mechanisms in Selective Laser Sintering and Selective Laser Melting. Rapid Prototyp. J. 2005;11(1):25–36.

83. Seyda V, Kaufmann N, Emmelmann C. Investigation of aging processes of Ti-6Al-4 V powder material in laser melting. Phys. Procedia. 2012;39:425–31.

84. Khan M. Selective laser melting (SLM) of gold (Au) [PhD Thesis]. Loughborough University, UK.; 2010. p. 1–152.

85. Marcu T, Todea M, Gligor I, Berce P, Popa C. Effect of surface conditioning on the flowability of Ti6Al7Nb powder for selective laser melting applications. Appl. Surf. Sci.; 2012 Jan;258(7):3276–82.

86. Mumtaz K, Hopkinson N. Selective laser melting of thin wall parts using pulse shaping. J. Mater. Process. Technol. 2010;210(2):279–87.

87. Alkahari MR, Furumoto T, Ueda T, Hosokawa A, Tanaka R, Aziz A and Sanusi M. Thermal Conductivity of Metal Powder and Consolidated Material Fabricated via Selective Laser Melting. Key Eng. Mater. 2012 Nov;523-524:244–9.

88. Simonelli M, Tse Y, Tuck C. Further Understanding of Ti-6Al-4V Selective Laser Melting Using Texture Analysis. International Solid Freeform Fabrication Symposium. University of Texas, Austin; 2012. p. 480–9.

89. Shiomi M, Osakada K, Nakamura K, Yamashita K, Abe F. Residual stress within metallic model made by selective laser melting process. CIRP Ann. - Manuf. Technol. 2004;53(1):195–8.

90. Neikov O d, Naboychenko SS, Dowson G. Atomisation and granulation. In: Neikov O, Naboychenko SS, Mourachova I, Gopienko V, Frishberg I, Lotsko D, editors. Handb. non-ferrous Met. Technol. Appl. First edit. Elsevier Ltd; Amsterdam; 2009. p. 122–5.

91. Rombouts M, Kruth JP, Froyen L, Mercelis P. Fundamentals of selective laser melting of alloyed steel powders. CIRP Ann. - Manuf. Technol. 2006;55(1):187–92.

92. Morgan R, Sutcliffe CJ, O'Neill W. Density analysis of direct metal laser re-melted 316L stainless steel cubic primitives. J. Mater. Sci. 2004;39(4):1195–205.

93. Yasa E, Kruth J. Application of laser re-melting on selective laser melting parts. Adv. Prod. Eng. Manag. 2011;6(4):259–70.

94. Yadroitsev I, Gusarov A, Yadroitsava I, Smurov I. Single track formation in selective laser melting of metal powders. J. Mater. Process. Technol. 2010;210(12):1624–31.

95. Vandenbroucke B, Kruth J-P. Selective laser melting of biocompatible metals for rapid manufacturing of medical parts. Rapid Prototyp. J. 2007;13(4):196–203.

96. Tolosa I, Garciandía F, Zubiri F, Zapirain F, Esnaola A. Study of mechanical properties of AISI 316 stainless steel processed by "selective laser melting", following different manufacturing strategies. Int. J. Adv. Manuf. Technol. 2010;51(5-8):639–47.

97. Craeghs T, Bechmann F, Kruth J. Feedback control of selective laser melting using optical sensors. Phys. Procedia. 2010;00:1–8.

98. Lott P, Schleifenbaum H, Meiners W, Wissenbach K, Hinke C, Bültmann J. Design of an optical system for the in-situ process monitoring of selective laser melting (SLM). Phys. Procedia. 2011;12:683–90.

99. Gusarov A, Yadroitsev I, Bertrand P, Smurov I. Heat transfer modelling and stability analysis of selective laser melting. Appl. Surf. Sci. 2007;254(4):975–9.

100. Gibson I. Advanced Manufacturing Technology for Medical Applications. Gibson I, editor. Sussex, England: John Wiley & Sons Ltd.; 2005.

101. Huang SH, Liu P, Mokasdar A, Hou L. Additive manufacturing and its societal impact: a literature review. Int. J. Adv. Manuf. Technol. 2012;67(5-8):1191–203.

102. Bibb R, Eggbeer D, Evans P, Bocca A, Sugar A. Rapid manufacture of custom-fitting surgical guides. Rapid Prototyp. J. 2009;15(5):346–54.

103. Wehmoller M, Warnke P, Zilian C, Eufinger H. Implant design and production—a new approach by selective laser melting. Int. Congr. Ser. 2005 May;1281:690–5.

104. Reeves P, Tuck C, Hague R. Additive manufacturing for mass customisation. In: Fogliatto FS., da Silveira GJC, editors. Mass Customisation. Engineering and Managing Global Operations. First edit. Springer Verlag; 2011. p. 275–89.

105. Ryan G, Pandit A, Apatsidis DP. Fabrication methods of porous metals for use in orthopaedic applications. Biomaterials. 2006;27(13):2651–70.

106. Pattanayak DK, Fukuda A, Matsushita T, Takemoto M, Fujibayashi S, Sasaki K, Nishida N, Nakamura T and Kukubo T. Bioactive Ti metal analogous to human cancellous bone : fabrication by selective laser melting and chemical treatments. Acta Biomater. 2011;7(3):1398–406.

107. Pattanayak DK, Matsushita T, Takadama H, Fukuda A, Takemoto M, Fujibayashi S, Sasaki K, Nishida N, Nakamura T and Kukubo T. Fabrication of bioactive porous Ti metal with structure similar to human cancellous bone by selective laser melting. Bioceram. Dev. Appl. 2011;2:1–3.

108. Fukuda A, Takemoto M, Saito T, Fujibayashi S, Neo M, Pattanayak DK, Matsushita T, Sasaki K, Nishida N, Nakamura T and Kukubo T. Osteoinduction of porous Ti implants with a channel structure fabricated by selective laser melting. Acta Biomater. 2011;7(5):2327–36.

109. Warnke PH, Douglas T, Wollny P, Sherry E, Steiner M, Galonska S and Sivanathan S. Rapid prototyping : porous titanium alloy scaffolds produced by selective laser melting for bone tissue engineering. Tissue Eng. Part C. 2009;15(2):115–24.

110. Traini T, Mangano C, Sammons RL, Mangano F, Macchi A, Piattelli A. Direct laser metal sintering as a new approach to fabrication of an isoelastic functionally graded material for manufacture of porous titanium dental implants. Dent. Mater. 2008;24(11):1525–33.

111. Zieliński A, Sobieszczyk S, Seramak T, Serbiński W, Świeczko-Żurek B, Ossowska A. Biocompatibility and bioactivity of load-bearing metallic implants. Adv. Mater. Sci. 2010;10(4):21–31.

112. Drstvensek I, Hren NI, Strojnik T, Brajlih T, Valentan B. Applications of rapid prototyping in cranio-maxilofacial surgery procedures. Int J Biol Biomed Eng. 2008;2(1):29–38.

113. Figliuzzi M, Mangano F, Mangano C. A novel root analogue dental implant using CT scan and CAD/CAM: selective laser melting technology. Int. J. Oral Maxillofac. Surg. 2012;41(7):858–62.

114. Almeida EO, Júnior ACF, Bonfante E a, Silva NRF a, Coelho PG. Reliability evaluation of alumina-blasted/acid-etched versus laser-sintered dental implants. Lasers Med. Sci. 2013;28(3):851–8.

115. Castner DG, Ratner BD. Biomedical surface science: foundations to frontiers. Surf. Sci. 2002;500(1-3):28–60.

116. Goddard J, Hotchkiss J. Polymer surface modification for the attachment of bioactive compounds. Prog. Polym. Sci. 2007;32(7):698–725.

117. Stanford CM. Surface modification of biomedical and dental implants and the processes of inflammation, wound healing and bone formation. Int. J. Mol. Sci. 2010;11(1):354–69.

118. Raynor JE, Petrie T, Fears KP, Latour R, García AJ, Collard DM. Saccharide polymer brushes to control protein and cell adhesion to titanium. Biomacromolecules. 2009;10(4):748–55.

119. Kim H, Choi S-H, Ryu J-J, Koh S-Y, Park J-H, Lee I-S. The biocompatibility of SLA-treated titanium implants. Biomed. Mater. 2008;3(2):1–6.

120. Lafranzo NA. Use of self-assembled monolayers to tailor surface properties : from lubrication to neuronal development [PhD Thesis]. Washington University; 2013.

121. Alford K. Polymers and peptides attached to terminally functionalised self-assembled monolayers: synthesis, characterisation and molecular architecture [Master's Thesis]. Washington State University; 2005.

122. Chaki NK, Aslam M, Sharma J, Vijayamohanan K. Applications of self-assembled monolayers in materials chemistry. J. Chem. Sci. 2001;113(5-6):659–70.

123. Ulman A. Formation and structure of self-assembled monolayers. Chem. Rev. 1996;96(4):1533–54.

124. Yung CW, Fiering J, Mueller AJ, Ingber DE. Micromagnetic-microfluidic blood cleansing device. Lab Chip. 2009;9(9):1171–7.

125. Mahony CT, Richard FA, Goshal T, Holmes JD, Morris MA. Thermodynamics - Systems in Equilibrium and Non-Equilibrium. 1st ed. Moreno Pirajn JC, editor. Thermodyn. Syst. Equilib. Non-equilibrium. InTech; 2011. p. 279–306.

126. Shustak G, Domb AJ, Mandler D. Preparation and characterization of n-alkanoic acid self-assembled monolayers adsorbed on 316L stainless steel. Langmuir. 2004;20(18):7499–506.

127. Schreiber F. Structure and growth of self-assembling monolayers. Prog. Surf. Sci. 2000;65(5-8):151–257.

128. Whitesides GM. The "right" size in nanobiotechnology. Nat. Biotechnol. 2003;21(10):1161–5.

129. Mastrangelo F, Fioravanti G, Quaresima R, Raffaele V, Gherlone E. Self-assembled monolayers (SAMs): which perspectives in implant dentistry? J. Biomater. Nanobiotechnol. 2011;02(05):533–43.

130. Buckholtz GA, Gawalt ES. Effect of alkyl chain length on carboxylic acid SAMs on Ti-6Al-4V. Materials (Basel). 2012;5(12):1206–18.

131. Thebault P, Taffin de Givenchy E, Guittard F, Guimon C, Geribaldi S. Self-assembled monolayers of semi-fluorinated thiols and disulfides with a potentially antibacterial terminal fragment on gold surfaces. Thin Solid Films. 2008;516(8):1765–72.

132. Aronsson BO, Lausmaa J, Kasemo B. Glow discharge plasma treatment for surface cleaning and modification of metallic biomaterials. J. Biomed. Mater. Res. 1997;35(1):49–73.

133. Metwalli E, Haines D, Becker O, Conzone S, Pantano CG. Surface characterizations of mono-, di-, and tri-aminosilane treated glass substrates. J. Colloid Interface Sci. 2006;298(2):825–31.

134. Durmaz F. A modular approach to functional self-assembled monolayers [PhD Thesis (16942)]. Swizz Federal Institute of Technology; 2006. p. 1–118.

135. Pardo L, Boland T. A quantitative approach to studying structures and orientation at self-assembled monolayer/fluid interfaces. J. Colloid Interface Sci. 2003;257(1):116–20.

136. Ajami E, Aguey-zinsou K. Functionalization of electropolished titanium surfaces with silane-based self-assembled monolayers and their application in drug delivery. J. Colloid Interface Sci. 2012;385:258–67.

137. Mani G, Feldman MD, Oh S, Agrawal CM. Surface modification of cobalt–chromium–tungsten–nickel alloy using octadecyltrichlorosilanes. Appl. Surf. Sci. 2009;255(11):5961–70.

138. Raynor JE. Surface modification of titanium substrates with polymer brushes to control cell adhesion for bioapplications [PhD Thesis]. Georgia Institute of Technology; 2008.

139. Pellerite MJ, Dunbar TD, Boardman LD, Wood EJ. Effects of fluorination on self-assembled monolayer formation from alkanephosphonic acids on aluminum: kinetics and structure. J. Phys. Chem. B. 2003;107(42):11726–36.

140. Guerrero G, Alauzun JG, Granier M, Laurencin D, Mutin PH. Phosphonate coupling molecules for the control of surface/interface properties and the synthesis of nanomaterials. Dalton Trans. 2013;42(35):12569–85.

141. Michel R, Lussi JW, Csucs G, Reviakine I, Danuser G, Ketterer B, Hubbel J, Textor M and Spencer N. Selective molecular assembly patterning: a new approach to micro- and nanochemical patterning of surfaces for biological applications. Langmuir. 2002;18(8):3281–7.

142. Gao W, Dickinson L, Grozinger C, Frederick M, Reven L. Self-assembled monolayers of alkylphosphonic acids on metal oxides. Langmuir. 1996;12(26):6429–35.

143. Feng G. The synthesis and characterisation of phosphonic acids for the surface modification study on indium tin oxide [Master's Thesis]. Georgia Institute of Technology; 2012.

144. Mani G, Torres N, Oh S. Paclitaxel delivery from cobalt-chromium alloy surfaces using self-assembled monolayers. Biointerphases. 2011;6(2):33–42.

145. Pawsey S, Yach K, Reven L. Self-assembly of carboxyalkylphosphonic acids on metal oxide powders. Langmuir. 2002;18(13):5205–12.

146. Biddle M. An Introduction to SAMs: Self-Assembled Monolayers in Organic Chemistry [Internet]. chem.wisc.edu. 2001 [cited 2011 Aug 29]. Available from: http://www.chem.wisc.edu/areas/organic/studsemin/biddle/biddle-abs.pdf

147. Allen MT, Diele S, Harris KD., Hegmann T, Kariuki BM, Preece JA and Tschierske C. Intermolecular organisation of triphenylene-based discotic mesogens by interdigitation of alkyl chain. J. Mater. Chem. 2001;11:302–11.

148. Hsu C-W, Liou H-R, Su W-F, Wang L. Self-assembled monolayers of 2-(thienyl)hexylphosphonic acid on native oxide surface of silicon fabricated by air-liquid interface-assisted method. J Colloid Interf. Sci. 2008;324(1-2):236–9.

149. Tosatti S, Michel R, Textor M, Spencer ND. Self-assembled monolayers of dodecyl and hydroxy-dodecyl phosphates on both smooth and rough titanium and titanium oxide surfaces. Langmuir. 2002;3858(7):3537–48.

150. Malti W El, Laurencin D, Guerrero G, Smith ME, Mutin PH. Surface modification of calcium carbonate with phosphonic acids. J. Mater. Chem. 2012;22:1212–8.

151. Dadafarin H, Katic J, Metikos-Hukovic M, Omanovic S. Functionalization of a NiTi surface with phosphonic acid self-assembled monolayers. 219th Electrochem. Soc. Meet. The Electrochemical Society; 2011. p. 120.

152. Schwartz J, Avaltroni MJ, Danahy MP, Silverman BM, Hanson EL, Schwarzbauer JE, Midwood K and Gawalt E . Cell attachment and spreading on metal implant materials. Mater. Sci. Eng. C. 2003;23:395–400.

153. Raman A, Gawalt E. Reduction of 3T3 fibroblast adhesion on SS316L by methyl-terminated SAMs. Mater. Sci. Eng. C. 2011;30(8):1157–61.

154. Mrksich M, Whitesides GM. Using self-assembled monolayers to understand the interactions of man-made surfaces with proteins and cells. Annu. Rev. Biophys. Biomol. Struct. 1996;25:55–78.

155. Variola F, Yi J-H, Richert L, Wuest JD, Rosei F, Nanci A. Tailoring the surface properties of Ti6Al4V by controlled chemical oxidation. Biomaterials. 2008;29(10):1285–98.

156. Chang E, Lee TM. Effect of surface chemistries and characteristics of Ti6Al4V on the Ca and P adsorption and ion dissolution in Hank's ethylene diamine tetra-acetic acid solution. Biomaterials. 2002;23:2917–25.

157. Heakal FE, Awad KA. Electrochemical corrosion and passivation behavior of titanium and its Ti-6Al-4V alloy in low and highly concentrated HBr solutions. Int. J. Electrochem. Sci. 2011;6:6483–502.

158. Kruth J, Vandenbroucke B, Van Vaerenbergh J, Mercelis P. Benchmarking of different SLS/SLM processes as rapid manufacturing techniques. International Conference on Polymer Moulds and Innovation. Ghent, Belgium; 2005. p. 1–7.

159. Hryniewicz T, Rokicki R, Rokosz K. Magnetoelectropolished titanium biomaterial. In: Pignatello R, editor. Biomater. Sci. Eng. First edit. Intech; 2011. p. 227–47.

160. Szewczenko J, Walke W, Nowinska K, Marciniak J. Corrosion resistance of Ti-6Al-4V alloy after diverse surface treatments. Corrosion. 2010;41(5):360–71.

161. El-ghannam A, Starr L, Jones J. Laminin-5 coating enhances epithelial cell attachment spreading and hemidesmosome assembly on Ti-6Al-4V implant material in vitro. J. Biomed. Mater. Res. 1998;41(1):30–40.

162. Kruth J, Vandenbroucke B, Van Vaerenbergh J, Naert I. Rapid manufacturing of dental prostheses by means of selective laser sintering / melting. J. Dent. Technol. 2007;(2):24–32.

163. Axelsson S. Surface characterization of titanium powders with X-ray photoelectron spectroscopy [Diploma Thesis]. Chalmers University of Technology, Sweden; 2012. p. 1–56.

164. Wagner C, Riggs W, Davis L, Moulder J. Handbook of X-Ray Photoelectron Spectroscopy. Perkin-Elmer Corporation, Minnesota; 1979.

165. Olefjord I. X-ray photoelectron spectroscopy. In: Brune D, Hellborg R, Whitlow H, Hunderi O, editors. Surf. Characterisation A users source B. WILEY, Weinheim; 1997. p. 291–319.

166. Sundgren J, Bodo P, Lundstrom I. Auger electron spectroscopic studies of the interface between human tissue and implants of titanium and stainless steel. J. Colloid Interface Sci. 1986 Mar;110(1):9–20.

167. Principal axes and peak fitting uncertainities - CasaXPS Manual 2.3.16 rev 1.0. 2010 p. 1–18.

168. Henss A, Rohnke M, Knaack S, Kleine-Boymann M, Leichtweiss T, Schmitz P, El Khassawna T, Gelinsky M, Heiss C and Janek J. Quantification of calcium content in bone by using ToF-SIMS--a first approach. Biointerphases. 2013 Dec;8(1):31.

169. Azéma J, Guidetti B, Dewelle J, Le Calve B, Mijatovic T, Korolyov A,Vaysee J, Malet-Martino M, Martino R and Kiss R. 7-((4-Substituted)piperazin-1-yl) derivatives of ciprofloxacin: synthesis and in vitro biological evaluation as potential antitumor agents. Bioorg. Med. Chem. 2009 Aug 1;17(15):5396–407.

170. Cormier R, Burda WN, Harrington L, Edlinger J, Kodigepalli KM, Thomas J, Kapolka R, Roma G, Anderson BE and Turos E. Studies on the antimicrobial properties of N-acylated ciprofloxacins. Bioorg. Med. Chem. Lett. 2012 Oct 15;22(20):6513–20.

171. Sharma P, Jain S. Synthesis and antibacterial activity if certain novel 1-cyclopropyl-6-fluoro-1,4-dihydro-7,4-substituted-piperazin-1-yl-4-oxoquinoline-3-carboxylates. Acta Pharm. Sci. 2008;50(1):35–40.

172. Clayden J, Greeves N, Warren S. Organic Chemistry. second. Clayden J, Greeves N, Warren S, editors. Oxford University Press; 2012. p. 197–230.

173. Zupan M, Turel I, Bukovec P, White AJP, Williams DJ. Synthesis and characterization of two novel zinc (II) complexes with Ciprofloxacin. Croat. Chem. acta. 2001;74(1):61–74.

174. Cristina E, Cazedey L, Regina H, Salgado N. Spectrophotometric determination of Ciprofloxacin hydrochloride in ophthalmic solution. Adv. Anal. Chem. 2012;2(6):74–9.

175. Mäkinen TJ, Veiranto M, Lankinen P, Moritz N, Jalava J, Törmälä P and Aro HT. In vitro and in vivo release of ciprofloxacin from osteoconductive bone defect filler. J. Antimicrob. Chemoth. 2005;56(6):1063–8.

176. Ma X, Li L, Xu C, Wei H, Wang X, Yang X. Spectroscopy and speciation studies on the interactions of aluminum (III) with ciprofloxacin and β-nicotinamide adenine dinucleotide phosphate in aqueous solutions. Molecules. 2012;17(8):9379–96.

177. Shamraiz S. Optical Spectroscopic and theoretical investigations of a series of fluoroquinolones [Master's Thesis]. Roskilde University; 2010. p. 1–33.

178. Gottlieb J, Fuehner T, Dierich M, Wiesner O, Simon a R, Welte T. Are metallic stents really safe? A long-term analysis in lung transplant recipients. Eur Respir J. 2009;34(6):1417–22.

179. Brown DF. Detection of methicillin/oxacillin resistance in staphylococci. J. Antimicrob. Chemother. 2001;48 Suppl 1:65–70.

180. Mantel M, Wightman JP. Influence of the surface chemistry on the wettability of stainless steel. Surf. Interface Anal. 1994;21:595–605.

181. Dementjev AP, Graaf A De, Sanden MCM Van De, Maslakov KI. X-Ray photoelectron spectroscopy reference data for identification of the C3 N4 phase in carbon-nitrogen films. Diam. Relat. Mater. 2000;9:1904–7.

182. Lausmaa J. Surface spectroscopic characterization of titanium implant materials. J. Electron Spectros. Relat. Phenomena. 1996;81(3):343–61.

183. Ask M, Lausmaa J, Kasemo B. Preparation and surface spectroscopic characterization of oxide films on Ti6Al4V. Appl. Surf. Sci. 1989;35(3):283–301.

184. Fu Y, Du H, Zhang S, Huang W. XPS characterization of surface and interfacial structure of sputtered TiNi films on Si substrate. Mater. Sci. Eng. A. 2005;403(1-2):25–31.

185. Leyens C. Oxidation and protection of titanium alloys and titanium aluminides. In: Peters M, Leyens C, editors. Titan. Titan. Alloy. Weinheim: Wiley Verlag GmbH & Co.; 2003. p. 187–223.

186. Zreiqat H, Valenzuela SM, Nissan B Ben, Roest R, Knabe C, Radlanski RJ, Rens H and Evans PJ. The effect of surface chemistry modification of titanium alloy on signalling pathways in human osteoblasts. Biomaterials. 2005;26(36):7579–86.

187. Krasicka-Cydzik E. Anodic layer formation on titanium and its alloys for biomedical applications. In: Nurul Amin A, editor. Titan. Alloy. - Towards acheiving enhanced properties for diversified applications. 1st ed. Coratia: Intech; 2012. p. 175–200.

188. Velten D, Biehl V, Aubertin F, Valeske B, Possart W, Breme J. Preparation of TiO 2 layers on cp-Ti and Ti6Al4V by thermal and anodic oxidation and by sol-gel coating techniques and their characterization. J. Biomed. Mater. Res. 2002;59(1):18–28.

189. Stoebner SE, Mani G. Effect of processing methods on drug release profiles of anti-restenotic self-assembled monolayers. Appl. Surf. Sci.; 2012 Apr;258(12):5061–72.

190. Hoque E, Derose J a, Hoffmann P, Mathieu HJ, Bhushan B, Cichomski M. Phosphonate self-assembled monolayers on aluminum surfaces. J. Chem. Phys. 2006 May 7;124(17):174710.

191. Quiñones R, Gawalt ES. Study of the formation of self-assembled monolayers on nitinol. Langmuir. 2007 Sep 25;23(20):10123–30.

192. Kanta a., Sedev R, Ralston J. The formation and stability of self-assembled monolayers of octadecylphosphonic acid on titania. Colloids Surfaces A Physicochem. Eng. Asp. 2006 Dec;291(1-3):51–8.

193. Deligianni DD, Katsala N, Ladas S, Sotiropoulou D, Amedee J, Missirlis YF. Effect of surface roughness of the titanium alloy Ti-6Al-4V on human bone marrow cell response and on protein adsorption. Biomaterials. 2001;22(11):1241–51.

194. Kasemo B, Lausmaa J. Biomaterial and implant surfaces: on the role of cleanliness, contamination, and preparation procedures. J. Biomed. Mater. Res. 1988;22(A2 Suppl):145–58.

195. Chrzanowski W, Szewczenko J. Influence of the anodic oxidation on the physicochemical properties of the Ti6Al4V ELI alloy. J. Mater. Process. Technol. 2005;162-163:163–8.

196. Hanawa T, Hiromoto S, Yamamoto A, Kuroda D, Asami K. XPS characterization of the surface oxide film of 316L stainless steel samples

that were located in Quasi-biological environments. Bioengineering. 2002;43(12):3088–92.

197. Mahapatro A, Johnson DM, Patel DN, Feldman MD, Ayon A a, Agrawal CM. Surface modification of functional self-assembled monolayers on 316L stainless steel via lipase catalysis. Langmuir. 2006;22(3):901–5.

198. Sowinski KM, Kays MB. Determination of ciprofloxacin concentrations in human serum and urine by HPLC with ultraviolet and fluorescence detection. J. Clin. Pharm. Ther. 2004;29(4):381–7.

APPENDIX 1

Electropolishing and Mechanical Testing of Tracheobronchial Stents Fabricated Using Selective Laser Melting

ABSTRACT

This study explores the potential of selective laser melting (SLM) to fabricate tracheobronchial stent and the effectiveness of electropolishing to polish this SLM fabricated stent. The stents were fabricated in a SLM Realizer 100 using 316L stainless steel (316L SS). SLM was found to be capable of fabricating tracheobronchial stents although it afforded a rough surface and the stents exhibited non-elastic behaviour. The observed roughness was due to partially sintered 316L SS particles on the stent surface and stepped profiles due to layer-by-layer fabrication. A weight loss of 27.9% was observed on electropolishing for two minutes and 48.6% on polishing for five minutes. Hence, a significant decrease in the stent strut diameter was observed. An addition of phosphorous from the electrolytic solution and a significant change in the elemental composition of carbon and oxygen were observed on the electropolished stent surface. Although electropolishing rendered a smooth surface, the compressive strength of the stent reduced after electropolishing. The reduction in compressive strength can be attributed to the removal of material during electropolishing. However, the microstructure and micro-hardness of the stent did not vary significantly after electropolishing.

INTRODUCTION

Tracheobronchial stents are hollow meshes or tubes in cylindrical, T or Y shapes used to treat obstructions (stenosis) in trachea and/or bronchi. They are made of metals or polymers or combinations of the two. Tracheobronchial stents are typically fabricated using laser cutting, knitting, braiding or die casting [1, 2]. The introduction of tracheobronchial stents has improved quality of living by prolonging life expectancy; however, post-implant complications including stent migration, fracture, bacterial colonisation, granulation tissue formation have been experienced after tracheobronchial stenting [1-5].

Although a range of materials and manufacturing techniques have been trialled and adopted, there is still not a perfect stent to treat tracheobronchial obstruction in terms of shape and manufacturability [6].

It is envisaged that customised implant designs, due to their superior fit compared to traditional off-the-shelf designs, could reduce post-implant complications by preventing implant migration and fracture. The current fabrication techniques including laser cutting, knitting and braiding do not allow economical customisation of tracheobronchial stents. Knitting and braiding of stents will impose limitations in the geometries that can be made. To obtain customised tracheobronchial stents, moulds have been produced using additive manufacturing (AM) techniques including stereolithography and selective laser sintering [7]. However, fabricating stents from moulds will increase the manufacturing time and cost involved, by adding an additional step to the manufacturing process. Also fabricating complex designs using moulds can be tedious. Hence a direct manufacturing technique that can produce customised designs and complex structures is preferred.

Melgoza et al. [6] used a Fab@home system to directly print a tracheobronchial stent from a computer aided design. The material used was silicone. The Fab@Home builds objects layer by layer, using any material than can be squeezed through a syringe and holds its shape [8]. Materials are hardened by drying, heating, UV light, and other methods as necessary. The work proposed by Melgoza et al., [6] concentrated more on developing an integrated tool for making customised tracheal stent design to meet ideal stent requirements. Since they have used Fab@home system to print their conceptual design, the mechanical properties of the stent produced by this equipment was not reported [6].

Although Fab@home system is capable of making customised design, it can only process selected materials. Its ability to produce functional biomedical parts using biocompatible metallic materials such as nitinol, 316L Stainless Steel (316L SS), titanium and cobalt-chromium alloys have not been reported. Also this system has limitations on the geometries that can be made due to its relatively low resolution and small build area. Building an implant using this

technique with its current capabilities may not produce functional biomedical implants.

Selective laser melting (SLM), a metal based AM technique is of particular interest among researchers due to its ability to fabricate customised and complex structures for biomedical applications [9]. Several implants for maxillo-facial and other orthopaedic applications have been fabricated using SLM and the capability of SLM to produce such implants is being studied [10-13]. However, the ability of SLM to produce tracheobronchial stents, in particular to process the thin struts required for these structures, has not been studied. This work therefore explores the ability of SLM to fabricated tracheobronchial stents possessing thin struts with a view to producing customised versions.

Although SLM potentially has considerable advantages over conventional methods to fabricate tracheobronchial stents, the surface quality of SLM fabricated surfaces is rough and for stenting applications, a smooth surface is required to prevent restenosis [14]. There are different techniques such as sand blasting, grinding or etching to attain a good surface finish, but not all of these techniques can be used to polish the stent surface since they can damage the thin struts.

Electro-polishing has been recognised as a suitable technique to achieve a superior surface finish in several biomedical applications including the polishing of cardiovascular stents and surgical equipment [15]. Electro-polishing is a process by which a metallic surface is smoothed by polarising it anodically in a suitable electrolyte [14]. During electropolishing, a work piece is immersed in a temperature controlled electrolytic bath. The work piece serves as anode and is connected to the positive end of the power supply. The negative terminal of the DC power supply is connected to a cathode. When current is passed through the anode, the metal on the surface is oxidised and dissolved in the electrolyte whereas at the cathode, reduction occurs. As a result of this electrolytic reaction, the surface of the work piece (anode) is polished. Although electro-polishing is currently being adopted to polish structures built by various techniques, its application to polish SLM fabricated

stent structures has not been reported. Hence, in this study, the potential of SLM to fabricate tracheobronchial stents and the ability of electropolishing to polish SLM fabricated surface is investigated.

MATERIALS AND METHODS

Materials

Gas atomised 316L stainless steel (SS) powder with an average particle size of 31 µm (LPW Technology Ltd., UK) was used to fabricate the stents. Ortho-phosphoric acid (85%) and glycerol used for electropolishing were purchased from Fisher Scientific, UK. A 316L SS plate (Hydramaster, UK) 150 mm long, 40 mm wide and 2 mm thick was used as the cathode. A SLM fabricated stent was used as the anode.

Equipment and Methods

Design and fabrication

A tracheobronchial stent of 60 mm height and 15 mm diameter with a strut diameter of 300 µm was designed using Siemens PLM NX 7.5 software. The design was exported to the SLM Realizer in STL file format for fabrication.

Tracheobronchial stents were fabricated layer-by-layer in a SLM Realizer 100 (MCP Tooling Technologies Ltd., UK). The SLM Realizer 100 machine consist of a hopper attached to a wiper, an elevator that lowers the substrate to adjust the layer thickness and a lens that focuses the laser (50 W max) to the build area (125 mm diameter). Before SLM, the powder from which the part was to be fabricated was spread over the build platform from the hopper to a pre-defined layer thickness. After the layer had been spread, the laser beam scanned and fused the powder in the areas specified by the layer of the CAD file.

Once the scan was complete, the elevator lowered by the pre-defined layer thickness (50 µm) for the powder to be spread for the next layer and this process continued until the part was completed. The principle of the SLM process has been described in detail in previous literature [16]. The parameters used to build the stents in this work included a laser power of 50 W, scan

speed of 200 mm/s, layer thickness of 50 µm and laser spot size of approximately 29 µm. After fabrication, an electrical discharge machine (EDM) from Renishaw Plc., was used to cut the stents from the build plate and sonicated in methanol, ethanol and deionised water.

Electropolishing

A schematic of the experimental set-up used for electropolishing is represented in Figure 1. A 400 ml glass beaker served as the cell for electro-polishing and a direct current (DC) rectifier (30 V and 4 amp max.) was used as the power supply. The electrolyte composition was obtained from previous literature [14] whereas, the electropolishing conditions were self-optimised for the stent design.

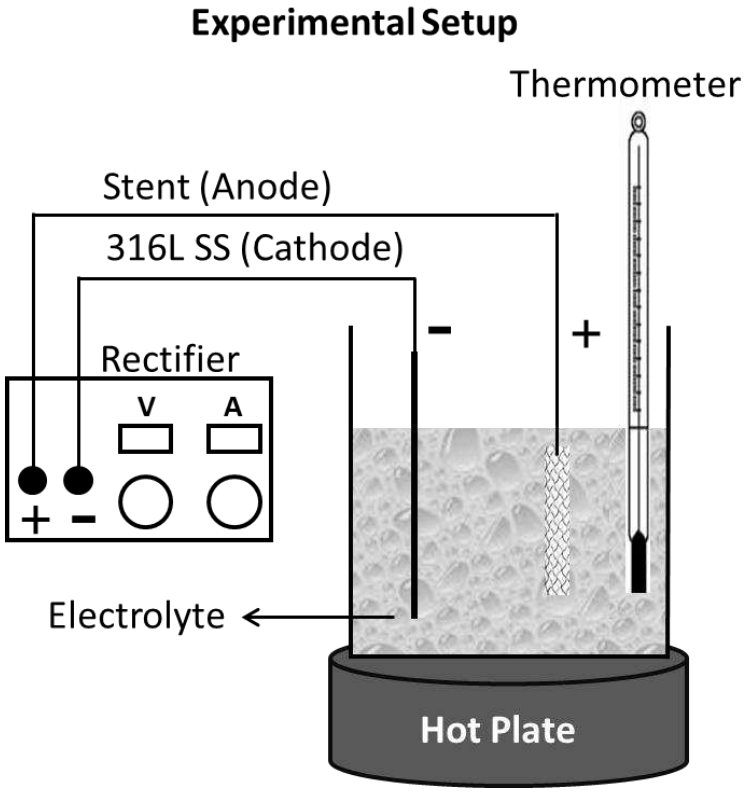

Figure 1 Schematic representation of the self-constructed electropolishing apparatus.

The electrolyte used for this experiment composed of a mixture of ortho-phosphoric acid (42%), glycerol (47%) and de-ionised water (11%). The stents were polished for 1, 2, 3, 4 and 5 minutes. With the polishing time as the only

variable, the voltage (10-12 V), current (2.4 amp) and the temperature of the bath (90-96 °C) used were kept constant.

Initially the stent was polished for a minute. The polished stent was cleaned using deionised water in a sonicator for 30 minutes (twice) and then characterised using a scanning electron microscope (SEM). Then the same stent was again electropolished for another minute and cleaned in a sonicator for 30 minutes (twice). Then the electropolished surface was characterised using SEM and X-ray photoelectron spectroscopy (XPS). Similar procedure was used until to attain a total of five minutes of electro-polishing.

Mechanical Testing

Metallographic characterisation

Metallographic characterisation was performed on the transversal section of the stents before and after electro-polishing. The stents were ground finely using silicon carbide (SiC) grit paper (220, 400, 600, and 1200) and finely polished with 6µm and 1µm diamond pastes. The samples were ultrasonically cleaned using iso-propanol and deionised water (15 minutes each) and dried. These mechanically polished samples were then etched using an etchant that comprised of 5 g of ferric chloride, 1 ml of nitric acid (con.) and 1 ml of hydrochloric acid in 100ml of deionised water. A light optical microscope (Nikon Optiphot microscope) was used to capture the microstructure patterns (using TS View software). Microstructure patterns of the stents before and after electro-polishing were captured using TS View software.

Vicker's micro-hardness test

The Vicker's micro-hardness of the stent was determined using a Buehler MMT3 equipment on the cross section of the stent strut before and after electro-polishing. The load used for the test was 100 g.

Compression test

Compression testing was performed on an Instron 3366 equipment. The load required to compress 75% of the stent diameter was calculated by compressing the stent at a rate of 5 mm/min.

Surface Characterisation

Scanning Electron Microscopy (SEM)

The surface morphology of the SLM fabricated stents before and after electropolishing was obtained using a LEO 440 SEM. The SEM was operated at a voltage of 10 kV. In-built software (INCD) for the point distance measurement was used to determine the strut thickness of the stents before and after electropolishing.

X-ray photoelectron spectroscopy (XPS)

The surface chemistry of the SLM fabricated stent was probed using XPS (VG ESCALAB Mk l). Using aluminium (Al) Kα radiation at 8 kV, high resolution spectra of all detected elements were collected at a pass energy of 100 eV. The relative intensity of the detected elements was plotted against binding energy and the chemical composition of the surface was characterised.

Measurement of weight and dimensions of the stents

An Adam ADG 3000L electronic balance was used to weigh the stents before and after electropolishing. The diameters of the stent struts were measured from the images obtained using SEM. Five measurements were performed on randomly selected struts from across the stent to determine the strut diameter before and after polishing and the corresponding mean value was calculated. The percentage weight loss and the strut diameter reduction before and after electro-polishing were calculated.

RESULTS

Surface Morphology after SLM fabrication

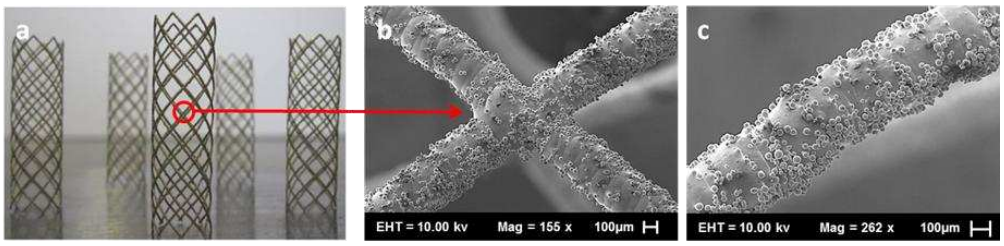

Figure 2 Photographic image of SLM fabricated stents (a) and surface morphology of the stent struts obtained using an SEM (b and c).

Figure 2a shows the SLM fabricated stent. The surface morphology of the SLM fabricated stent obtained using SEM is shown in Figures 2b and 2c. From the figure it can be observed that powder particles are partially sintered to the stent surface. This could be a natural consequence of laser melting since the beam area will naturally intersect some particles only partially. However, dissipation of energy to the powder surrounding the build during the laser scan could also be a reason. An array of segments can be observed from the figure and these segments or stepped profiles are due to layer-by-layer fabrication. SLM process parameters, including laser power, hatch distance and layer thickness, have been found to influence the part's surface morphology and have been discussed in previous papers [17, 18].

The average measured strut diameters (using SEM images) after fabrication were 308 ± 9.9 µm (including the partially sintered particles) whereas the actual designed diameter was 300 µm. This increase in strut thickness was due to the partially sintered particles on the struts and stepped profile obtained due to the layer-by-layer fabrication.

Surface morphology after electropolishing

During electro-polishing, burrs and other projections become the areas of very high current density and are preferentially removed [15]. Figure 3 shows the SLM fabricated stents struts (a) as-fabricated and b) after electropolishing for 1 minute, c) 2 minutes, d) 3 minutes, e) 4 minutes and f) 5 minutes.

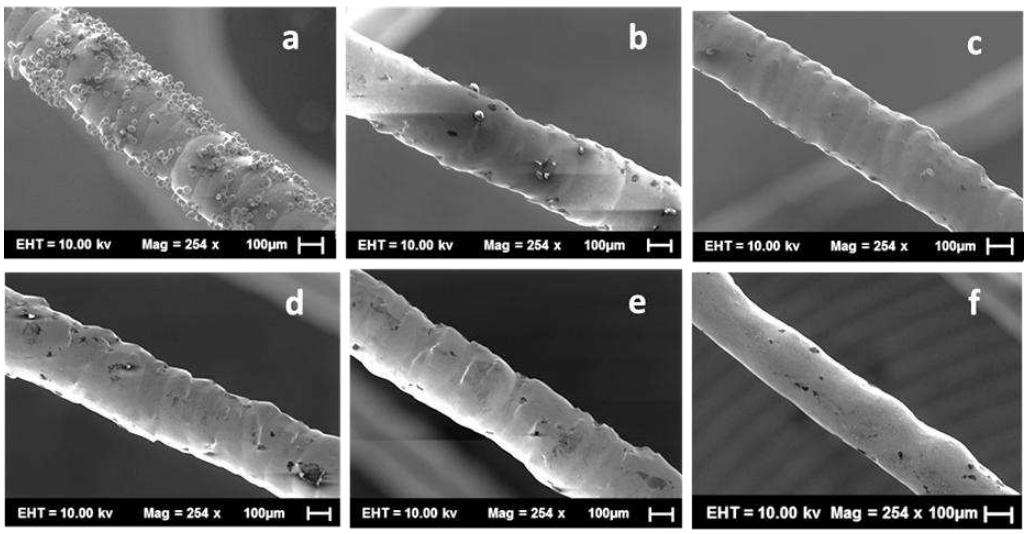

Figure 3 SLM as-fabricated stent strut (a); Stent strut after electropolishing for 1 minute (b); 2 minutes (c); 3 minutes (d); 4 minutes (e) and 5 minutes (f).

As can be observed from the Figure 3, the partially sintered particles on the stent surface were removed after electropolishing for 2 minutes. However, the stepped profile due to layer-by-layer manufacturing can still be observed on the surface until the stent was polished for 5 minutes. This will increase the stent's surface roughness. Hence, to further smooth the surface, the stent was further polished for an additional three minutes.

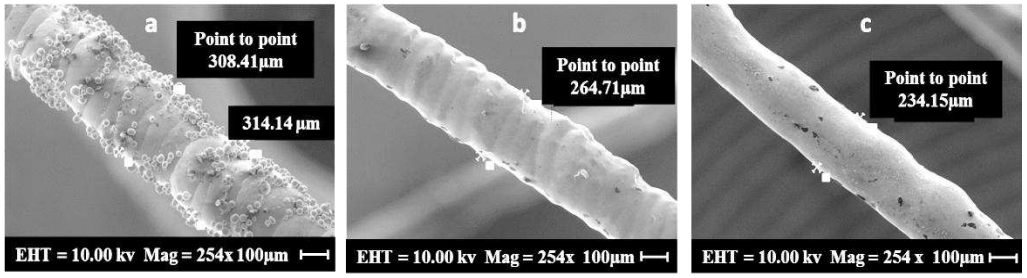

Figure 4 Strut diameter measurement using SEM. As-fabricated stent strut (a); an electropolished stent strut for 2 minutes (b) and an electropolished stent strut for 5 minutes (c).

Table 1 Mean weight, strut diameter, weight loss and reduction in strut diameter.

Stent	**Weight (mg)**	**Stent Diameter (µm)**	**Weight Loss (%)**	**Reduction in the Stent Strut Diameter (%)**	
				As-fabricated (from 308 µm)	As-designed (from 300 µm)

As-fabricated	640 ± 1.8	308 ± 2.2	-	-	-
Electro-polishing (2 minutes)	459 ± 2.7	264 ± 3.08	27.9	14.2	12
Electro-polishing (5 minutes)	327 ± 1.5	234 ± 1.4	48.6	24	22

Figure 4 shows the stent strut before and after electropolishing for 2 and 5 minutes. The strut surface can be observed to be smooth (4c) without the stepped profile that was observed after electropolishing for 2 minutes (4b). Although electropolishing was efficient in removing the sintered particles and the stepped profiles, it is important to determine the change in geometry and the amount of material removed during the process. The observed changes in weight and strut diameter before and after electropolishing procedures are tabulated in Table 1. Figure 5 shows a SEM micrograph of a magnified stent strut electropolished for 5 minutes.

After electro-polishing, a significant reduction in the stent's weight and the strut diameter was observed. The loss in the weight of the stent was contributed to by both the partially sintered particles to the stent surface and the material removed from the actual part. A loss of nearly 30% of the stent's weight was observed after electropolishing for 2 minutes with a 14.2% loss in their strut diameter. Although 48.6% loss of the stent's weight was observed after electropolishing for 5 minutes, the total reduction in the stent's diameter was only 24%.

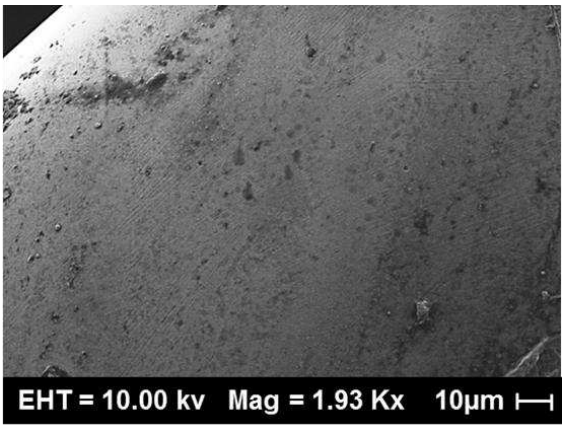

Figure 5 SEM micrograph of a magnified electropolished stent strut (1.93Kx).

By using the relationship V1M1=V2M2 (where V1 and M1 are the volume and mass of the stent before polishing whereas V2 and M2 are the volume and mass of the stent after polishing), the loss of mass after electropolishing of a stent can be expected to scale between diameter^2 (for wire) since the stent has cylindrical geometry. The obtained results nearly agreed to the relationship i.e., $M_1/M_2 = R_1^2/R_2^2$ for both electropolishing procedures. However, the slight variation observed might have been due to the presence of partially sintered (nearly spherical) particles with spherical shape on the stent struts. This shows that most of the material removed from the stent's surface was from the sintered particles. However it is difficult to exactly quantify the amount of particles sintered to the surface.

Surface Chemistry

XPS was used to probe the SLM fabricated stent before and after electropolishing for 5 minutes to determine the change in surface chemistry. Table 2 shows the atomic percentage of elemental distribution on the stent surface before and after electropolishing. Medical grade 316L SS is expected to have iron (Fe), chromium (Cr), nickel (Ni), manganese (Mn), and molybdenum (Mo) with some traces of silicon (Si), phosphorous (P) and sulfur (S). From the table it can be observed that there is a significant decrease in carbon after electropolishing. This may be because the excessive carbon present initially on the stent surface might have been from contamination [21, 22].

Table 2 Relative atomic percentage obtained using XPS

Nature of the sample	**Relative atomic percentage of the detected elements**						
	C	O	Fe	Cr	Mn	P	N
Before electropolishing	54.4	35.7	4.4	4.3	1.2	0	0
After electropolishing	11.3	57.6	7.4	7.9	1.5	11.6	2.7

Since the concentration of C is a lot less after electropolishing compared to its earlier concentration, the metal to oxygen ratio was calculated to determine the change in their surface chemistry. The as-fabricated stent surface showed its surface oxide layer to be composed of predominantly iron oxide with a

comparatively lesser contribution from chromium oxide. On electropolishing, the concentration of Cr:O increased to 0.14 whereas its initial concentration before electropolishing was 0.12. The Cr:O (0.14) ratio was observed to be higher than the Fe:O (0.13) ratio after electropolishing showing the surface is enriched with chromium oxide with a comparatively less contribution from iron oxide. After electropolishing, the Mn concentration decreased relative to its observed initial concentration.

An addition of phosphorous to the stent surface after electro-polishing was noted and this could be from the phosphoric acid present in the electrolyte. The used cleaning procedure used was not sufficient to remove this phosphorous and hence, adoption of a more suitable cleaning method is required. Nitrogen observed after electropolishing might also be due to contamination. Surface chemical analysis showed that electropolishing enhanced the concentration of chromium oxide in the stent surface. Although the presence of chromium oxide may improve the corrosion resistance, leaching of chromium ions may cause acute and/or chronic effects. is Also, the electropolished surface was previously reported to be enriched with hydroxyl group (-OH), yielding a highly wettable (hydrophilic) surface and the presence of stable oxide will increase the corrosion resistance [20].

Mechanical Properties

Metallographic characterisation

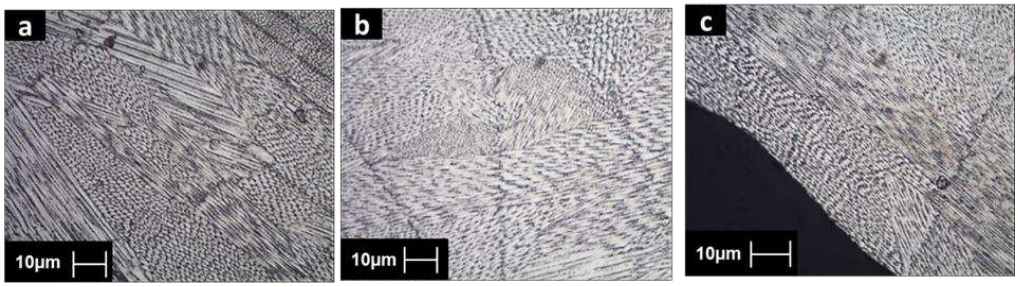

Figure 6 Microstructure patterns obtained for the stents struts fabricated using SLM. a) as-fabricated; b) after electropolishing for 5 minutes (middle of the stent strut) and c) after electropolishing for 5 minutes exhibiting the outer surface of the stent to show that the electropolishing did not affect the microstructure.

The microstructures of the struts were studied to determine the impact of electropolishing. Figure 6a shows the microstructure pattern of the stent before electropolishing whereas Figures 6b and 6c show the microstructure patterns after electropolishing. All the figures show the presence of columnar and equiaxed grains on the stent surface. These grains show different microstructure patterns to each other because they are differently oriented. The microstructure patterns did not show any significant difference before or after electropolishing confirming electropolishing does not alter the microstructural patterns.

Micro-hardness Testing

A Vickers hardness test was performed to determine the micro-hardness of the stent struts from their microstructures. The mean hardness for the struts before electro-polishing was 215.2 ± 3.47 HV and after electro-polishing was 220.06 ± 4.16 HV. The obtained results showed that there was no significant difference between the hardness observed for the struts before and after polishing. This slight deviation observed in their hardness may be due to the presence of different micro-structural orientations within the struts.

Compression Testing

A one-off compression study was performed to determine the compressive strength of the SLM fabricated stents before and after electropolishing (Figure 7). This study revealed a decrease in the compressive strength of the stent after electropolishing. Although this decrease is essentially due to the amount of material removed during electropolishing, the density of the stent could also be a factor. Since there is a high possibility for the formation of varied microstructure and generation of different levels of porosities during the SLM process, the density of the part may be slightly different [21].

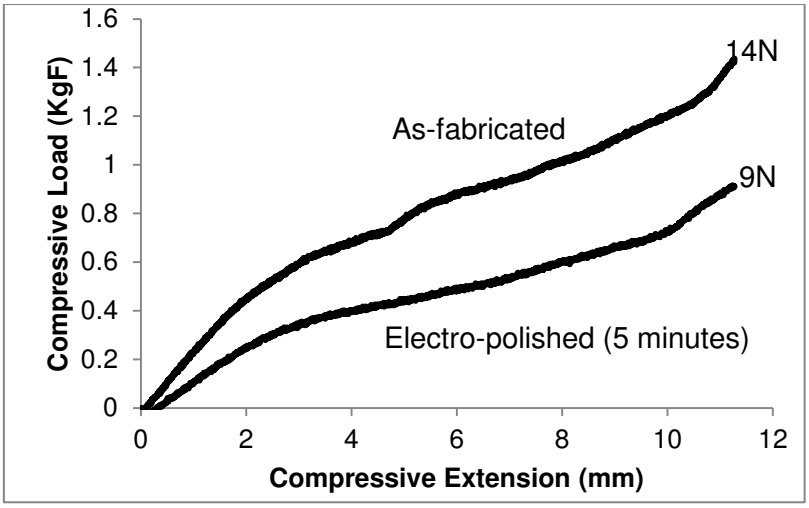

Figure 7 Compression testing of the tracheobronchial stents (before and after electropolishing) fabricated using SLM.

In compression testing, the stent fabricated by SLM was observed to deform in a non-elastic manner. For any stenting application, the stent should be capable of deforming elastically under any applied load [22]. The SLM fabricated stents did not exhibit elastic property. This could also be due to the level of porosities and micro structural patterns.

DISCUSSION

SLM was able to fabricate stents of 15 mm diameter with a strut diameter of 300µm. However, the surface rendered by this technique is not favourable for stenting applications. The partially sintered particles on the stent surface do not just increases the strut thickness and surface roughness, but they could also cause some serious disorders if the stent is implanted. For example, coughing, a reflex action that clears airways compresses stents to half of their normal size and leads to stent deformation. Also during a cough cycle, the air from the lungs flow out at high velocities [23, 24] to clear the airways. If the stents with these sintered particles were implanted, frequent deformation of the stent structure may potentially lead to the release of these partially sintered particles. This can potentially cause acute and/or chronic disorders by blocking alveolus (air sacs) in the lungs. Also the increased surface roughness due to the sintered particles may cause inflammation leading to restenosis [14, 170]. Hence it is important that the stent surface should be smooth.

Electropolishing was used to polish the rough surface in the present study to avoid any damage to the stent struts that are possible with mechanical polishing such as sand blasting. Electropolishing rendered a smooth surface and it reduced the weight and the strut diameter significantly. Most of the weight loss observed could be from the removal of sintered particles, however, the reduction in strut diameter cannot be neglected.

Previous studies reported electropolishing of cardiovascular stents that were cut using laser from a tube. During this laser cutting, they produce tiny burrs on the cutting zones and since during electropolishing, these burrs become the areas of high current densities, they get preferentially eroded. Whereas with the SLM fabricated stent, the struts have partially sintered particles with a diameter of 5 µm and 45 µm. By the time electropolishing removes these partially sintered particles, it also erodes materials in other areas where there is no sintered particles.

Although electropolishing was capable of polishing the stent without physically damaging the struts, the amount of material removed and the reduction in the strut diameter is not desirable. Removal of more material from the actual design can affect the mechanical properties of the stent [14]. Hence it is important to control material removal during electropolishing. This can be achieved by optimising the parameters (such as the current, electrolyte, bath temperature and time) that govern the electropolishing process.

Electropolishing is suitable for surfaces with small burrs but not to polish the as-fabricated SLM surface with partially sintered particles. However, electropolishing can be combined with other suitable polishing technique as the final step to polish SLM fabricated structures. Electropolishing did not alter the microstructure and grain distribution of the stent. Vicker's micro-hardness did not vary significantly showing electropolishing did not affect the micro-hardness of the stent. The observed small variation could possibly due to the microstructural patterns.

The study on the mechanical properties of the SLM fabricated tracheobronchial stents are not convincing due to its non-elastic behaviour. In

the SLM process, the powder particles are rapidly melt and cooled. This can contribute to the varied microstructural patterns. Also, since SLM is a powder bed process, there is a high possibility for uneven melting and entrapment of air in the melt pool leading to porosity [21]. All these factors could have contributed to the non-elastic property of the stent fabricated using SLM. Post processing such as annealing can be performed to improve the mechanical property of SLM fabricated stents.

CONCLUSION

This study showed the potential to fabricate tracheobronchial stents with a strut diameter of 300 µm using SLM and explored the possibility to electropolish the SLM fabricated tracheobronchial stents. This study concludes,

- The surface finish of the SLM fabricated stent was rough due to the partially sintered particles on its surface.
- Electropolishing the stents for two minutes in the electrolytic bath removed the partially sintered particles; however, on polishing for five minutes, the stepped profiles formed due to layer-by-layer building of the stent were removed.
- Although electropolishing was capable of polishing the surface, it removed a significant amount of material from the stent surface leading to reduction in the weight and strut diameter of the stent.
- The surface chemistry of the stents showed a significant change after electropolishing rendering a stable and non-corrosive surface oxide layer.
- The stents fabricated using SLM with the applied process condition did not yield highly elastic stent to meet the current requirement.
- SLM produced stents require surface finishing and hence leading to two-step process.
- Further optimisation of both the SLM and electropolishing process is required to examine the potential of SLM to fabricate customised stents with smooth surface.

REFERENCES

1. Wood D. Tracheal and Bronchial Stenting. In: Grillo H, editor. Surgery of Trachea and Bronchi. Ontario: BC Decker Inc, Hamilton, Ontario; 2004. p. 763–90.

2. Freitag L. Airway stents. Eur Respir Mon. 2010;48:190–217.

3. Ko-Pen K, Mehta A, Turner J. Flexible Bronchoscopy. Second edition. Massachusetts, USA: Blackwell Publishing Company; 2004.

4. Walser EM. Stent placement for tracheobronchial disease. Eur. J. Radiol. 2005 Sep;55(3):321–30.

5. Zilberman M, Eberhart RC. Drug-eluting bioresorbable stents for various applications. Annu. Rev. Biomed. Eng. 2006;8:153–80.

6. Melgoza EL, Serenó L, Rosell A, Ciurana J. An integrated parameterized tool for designing a customized tracheal stent. Comput. Des. 2012;44(12):1173–81.

7. Lim CS, Eng P, Lin SC, Chua CK, Lee YT. Rapid prototyping and tooling of custom-made tracheobronchial stents. Int. J. Adv. Manuf. Technol. 2002;20(1):44–9.

8. Malone E, Lipson H. Fab @ Home : the personal desktop fabricator kit. Rapid Prototyp. J. 2007;4(April):245–55.

9. Hollister SJ, Bergman TL. Biomedical applications of integrated additive/subtractive manufacturing. World Technology Evaluation Centre; 2004 p. 55–62.

10. Vandenbroucke B, Kruth J-P. Selective laser melting of biocompatible metals for rapid manufacturing of medical parts. Rapid Prototyp. J. 2007;13(4):196–203.

11. Kruth J, Vandenbroucke B, Vaerenbergh J Van, Naert I. Rapid manufacturing of dental prostheses by means of selective laser sintering / melting. J. Dent. Technol. 2007;(2):24–32.

12. Lindner M, Hoeges S, Meiners W, Wissenbach K, Smeets R, Telle R, Poprawe Reinhartm and Fischer Horst. Manufacturing of individual biodegradable bone substitute implants using selective laser melting technique. J. Biomed. Mater. Res-A. 2011;97(4):466–71.

13. Drstvensek I, Hren NI, Strojnik T, Brajlih T, Valentan B. Applications of rapid prototyping in cranio-maxilofacial surgery procedures. Int. J. Biol. Biomed. Eng. 2008;2(1):29–38.

14. Zhao H, Humbeeck J Van, Leuven KU, Sohier J, Scheerder IDE. Electrochemical polishing of 316L stainless steel slotted tube coronary stents : an investigation of material removal and surface roughness. Prog. Biomed. Res. 2003;8(2):7–9.

15. Eliaz N, Nissan O. Innovative processes for electropolishing of medical devices made of stainless steels. J. Biomed. Mater. Res. Part A. 2007;7(9).

16. Gibson I, Rosen DW, Stucker B. Additive Manufacturing Technologies. Boston, MA: Springer US; 2010.

17. Yadroitsev I, Smurov I. Surface morphology in selective laser melting of metal powders. Phys. Procedia. 2011;12:264–70.

18. Kruth J, Badrossamay M, Yasa E, Deckers J, Thijs L, Van Humbeeck J. Part and material properties in selective laser melting of metals. 16th Int. Symp. Electromachining. 2010. p. 1–12.

19. Hanawa T, Hiromoto S, Yamamoto A, Kuroda D, Asami K. XPS characterization of the surface oxide film of 316L stainless steel samples that were located in Quasi-biological environments. Bioengineering. 2002;43(12):3088–92.

20. Mantel M, Wightman JP. Influence of the surface chemistry on the wettability of stainless steel. Surf. Interface Anal. 1994;21:595–605.

21. Hautmann H, Rieger J, Huber RM, Pfeifer KJ. Elastic deformation properties of implanted endobronchial wire stents in benign and malignant bronchial disease: A radiographic in vivo evaluation. Cardiovasc. Intervent. Radiol. 1999;22(2):103–8.

22. Grillo HC. Diseases and results of treatment. In: Grillo HC, editor. Surg. trachea bronchi. London: BC Decker Inc, USA; 2004. p. 173–429.

APPENDIX 2

Surface Modification of Metallic Biomaterials Using Phosphonic Acid Monolayers

AIM

To surface modify SLM as-fabricated Ti6Al4V, 316L SS and L605 Co-Cr surfaces using 16-phosphanohexadecanoic acid monolayers.

METHODS

Ti6Al4V, 316L SS and L605 Co-Cr substrates of dimensions 10 x 10 x 3 mm were fabricated in a selective laser melting (SLM) machine using previously optimised parameters. 1 mmoles of 16-phosphonohexadecanoic acid (16-PhDA) was prepared in 20 ml of THF. Before surface modification, the as-fabricated substrates were sonicated with dichloromethane, methanol and deionised water for 15 minutes twice and dried to remove surface contaminants. These cleaned surface treated SLM substrates were then rinsed with tetrahydrofuran (THF) and immediately dipped into a solution of 1mmoles of 16-PhDA in 20 ml THF. To avoid any cross contamination, the substrates of different materials were immersed in different containers. After 24 hours, the substrates were removed and the residual solvent was allowed to evaporate at room temperature. Without rinsing, the samples were transferred to a normal air-convection oven maintained at 120 °C for 18 hours. Finally, the SAM coated substrates were allowed to cool at room temperature and sonicated in THF and deionised water for 1 minute each to remove any physisorbed molecules.

RESULTS AND DISCUSSIONS

Figure 1 represents the rough nature of the as-fabricated SLM samples in various magnifications. This is due to the partial sintering of particles to the samples during SLM process. Figure 2 represents the XPS scan (P 2p region) of the Ti6Al4V, 316L SS and L605 Co-Cr substrates before and after surface modification using SAMs. A metal-phosphonate peak observed at 133.3 eV for the SAM treated sample was absent in their respective control samples. This

confirms that adsorption of 16-PhDA monolayers to all three metal oxide surfaces.

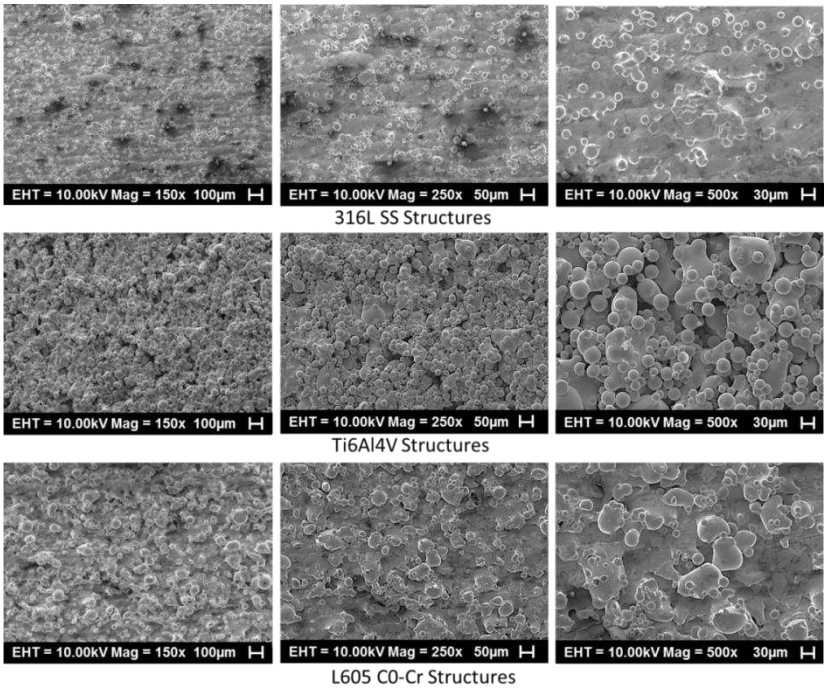

Figure 1 SEM micrograph of as fabricated surfaces.

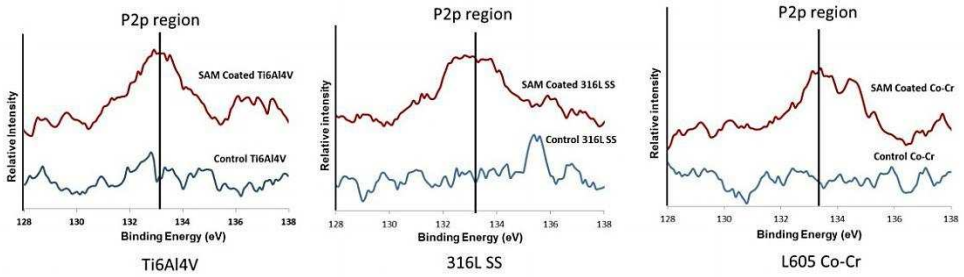

Figure 2 High resolution P 2p spectra obtained using XPS for various metal surfaces before and after surface modification using SAMs.

CONCLUSION

Adsorption of 16-PhDA monolayers on all three SLM as-fabricated surfaces shows the potential of 16-PhDA SAMs to modify metal oxide surfaces. Sintered particles on the SLM surfaces did not affect the monolayer formation significantly. However, stability of these monolayers on the rough SLM surface should be studied. Comparison of SAM attachment on both as fabricated SLM surface and mechanically polished SLM surface may generate knowledge on the effect of monolayers formation on a rough and a smooth surface.

APPENDIX 3

Fourier Transform Infrared Spectroscopy Results

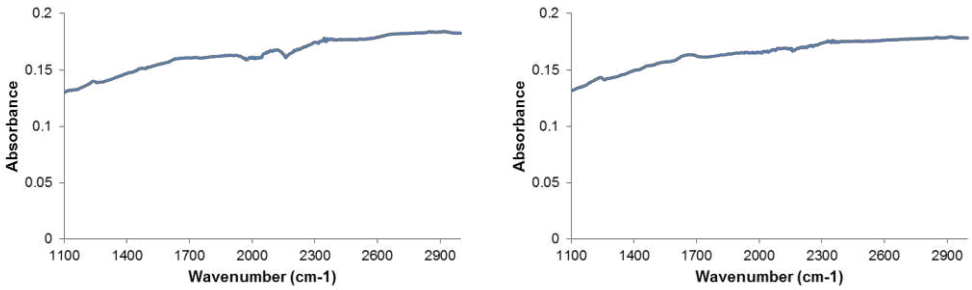

Figure 1 FTIR Spectra obtained using Perkin Elmer Spectrum 100 FTIR-ATR for two different Ti6Al4V samples coated with Ciprofloxacin®.